

**SMALL ANGLE SCATTERING  
INVESTIGATIONS OF NANO-CERAMICS AND  
NANO-COMPOSITES**

*By*

**JITENDRA BAHADUR**

**(PHYS01201004005)**

Bhabha Atomic Research Centre, Mumbai

*A thesis submitted to the*

*Board of Studies in Physical Sciences*

*In partial fulfillment of requirements*

*For the Degree of*

**DOCTOR OF PHILOSOPHY**

*of*

**HOMI BHABHA NATIONAL INSTITUTE**



**September, 2012**

# Homi Bhabha National Institute

## Recommendations of the Viva Voce Board

As members of the Viva Voce Board, we certify that we have read the dissertation prepared by **Jitendra Bahadur** entitled “*Small angle scattering investigations of nano-ceramics and nano-composites*” and recommend that it may be accepted as fulfilling the dissertation requirement for the Degree of Doctor of Philosophy.

\_\_\_\_\_ **Date:**

Chairman- **Prof. S. L. Chaplot**

\_\_\_\_\_ **Date:**

Guide / Convener- **Prof. S. Mazumder**

\_\_\_\_\_ **Date:**

External Examiner- **Prof. H. B. Bohidar**

\_\_\_\_\_ **Date:**

Member 1- **Prof. G. K. Dey**

\_\_\_\_\_ **Date:**

Member 2- **Prof. A. K. Tyagi**

Final approval and acceptance of this dissertation is contingent upon the candidate's submission of the final copies of the dissertation to HBNI.

I hereby certify that I have read this dissertation prepared under my direction and recommend that it may be accepted as fulfilling the dissertation requirement.

**Date:**

**Place:**

**Dr. S. Mazumder**

**(Guide)**

## **STATEMENT BY AUTHOR**

This dissertation has been submitted in partial fulfillment of requirements for an advanced degree at Homi Bhabha National Institute (HBNI) and is deposited in the Library to be made available to borrowers under rules of the HBNI.

Brief quotations from this dissertation are allowable without special permission, provided that accurate acknowledgement of source is made. Requests for permission for extended quotation from or reproduction of this manuscript in whole or in part may be granted by the Competent Authority of HBNI when in his or her judgment the proposed use of the material is in the interests of scholarship. In all other instances, however, permission must be obtained from the author.

**Jitendra Bahadur**

# **DECLARATION**

I, hereby declare that the investigation presented in the thesis has been carried out by me.

The work is original and has not been submitted earlier as a whole or in part for a degree / diploma at this or any other Institution / University.

**Jitendra Bahadur**

# **DECLARATION**

I, hereby declare that the queries raised by the examiners of the thesis have been incorporated as suggested.

**Dr. S. Mazumder**  
**(Guide)**

# **DEDICATIONS**

**This thesis is dedicated to my parents.**

**For their endless love, support and encouragement.....**

# ACKNOWLEDGEMENTS

First and foremost, I would like to express my deep and sincere gratitude to my thesis supervisor, Dr. S. Mazumder for his invaluable guidance, constant encouragement, inspiration, keen interest and good wishes. His wide knowledge and his logical way of thinking on critical scientific problems have been of great value for me. I am also grateful to him for being patient while critically reviewing this thesis.

This thesis would not have been possible without the guidance, help, support, critical analysis and valuable suggestions from Dr. D. Sen who has been truly invaluable to me both on an academic and a personal level, for which I am extremely grateful. I am also thankful to him for sharing his excellent knowledge and scientific understanding with me.

I also gratefully acknowledge the help rendered by all the members of Solid State Physics Division, BARC. It gives me immense pleasure to thank the members of the doctoral committee Prof. S. L. Chaplot (Chairman), Prof. G. K. Dey (Member) and Prof. A. K. Tyagi (Member) for their critical review and suggestions during the progress review and pre-synopsis viva-voce.

I would like to acknowledge my collaborators for their support in several measurements and discussions.

Finally, I owe my heartfelt gratitude and indebtedness to my parents who have always encouraged me to follow my heart and inspired my inquisitive mind throughout my childhood and study career. Above all, I would like to thank my wife Hema for her personal support and great patience at all times. I would like to take this opportunity to acknowledge my sweet little daughter who came in this world and made my life more cheerful.

I express my sincere thanks to all my friends for their numerous help, support and enjoyable company for making the life pleasant.

# CONTENTS

	<b>Page</b>
<b>Synopsis</b> .....	1-11
<b>List of Figures</b> .....	12-21
<b>List of Tables</b> .....	22-22
<b>Chapter 1: Introduction</b> .....	23
1.0. General Introduction.....	23-25
1.1. Small angle scattering.....	25-26
1.2. Interaction of radiation with matter.....	27-27
1.3. Comparing neutron and X-ray as a probe.....	28-32
1.4. Small-angle scattering theory.....	32-36
1.4.1. Small-angle scattering by a macroscopically isotropic system.....	36-37
1.4.2. Small-angle scattering by an isotropic two-phase structure.....	37-38
1.4.3. The integral of the scattering intensity in reciprocal space.....	38-38
1.4.4. Asymptotic behavior of scattering curves at high $q$ : Porod law.....	38-40
1.4.5. Small-angle scattering of a dilute system of isolated nano-objects....	40-49
1.4.6. Small-angle scattering of a concentrated set of nano-objects.....	49-53
1.5. Small angle scattering: Instrumental Considerations.....	53-54
1.5.1. Laboratory based SAXS instrument.....	54-56
1.5.2. Synchrotron based SAXS instrument.....	56-57
1.5.3. SANS instruments.....	57-59
1.5.4. Smearing effects in SAS measurements.....	59-59
1.5.5. Absolute Intensity/Scattering cross section.....	60-60
<b>Chapter 2: Probing Mesoscopic Morphology of Euclidean Nano-ceramics</b>	

<b>Aggregates</b> .....	61
2.1. Evolution of Pore Morphology in the NiO Aggregates.....	61
2.1.1. Introduction.....	61-62
2.1.2. Experimental Methods.....	62-62
2.1.3. Results and Discussion.....	62-66
2.1.4. Conclusions.....	66-66
2.2. Evolution of Pore Morphology in YCrO <sub>3</sub> Aggregates.....	66
2.2.1. Introduction.....	66-67
2.2.2. Experimental details .....	67-69
2.2.3. Data Analysis and Discussions.....	69-75
2.2.5. Conclusions.....	75-76
2.3. Investigation on TiO <sub>2</sub> and TiO <sub>2</sub> -CNT Composite Submicrospheres .....	76
2.3.1. Introduction.....	76-77
2.3.2. Experiments.....	77-78
2.3.3. Results and discussion.....	78-84
2.3.4. Conclusions.....	84-84
<b>Chapter 3: Probing Mesoscopic Morphology of the Non-Euclidean Nano-</b>	
<b>ceramics Aggregates</b> .....	85
3.0. General Introduction .....	85-86
3.1. Evolution of Y <sub>3</sub> Al <sub>5</sub> O <sub>12</sub> Fractal Aggregates under Thermal Annealing .....	86
3.1.1. Introduction.....	86-88
3.1.2. Experiments.....	88-88
3.1.3. SANS data analysis.....	89-89
3.1.4. Computer simulation.....	89-94
3.1.5. Results and discussion.....	94-95

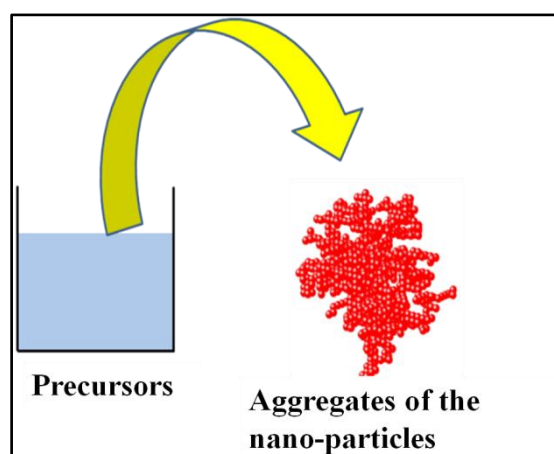
3.1.6. Conclusions.....	95-96
3.2. Smoothing of Non-Euclidean Surface of Nd <sub>2</sub> O <sub>3</sub> Doped CeO <sub>2</sub> under Sintering.....	96
3.2.1. Introduction.....	96-97
3.2.2. Experimental.....	97-97
3.2.3. Data Analysis.....	98-99
3.2.4. Monte Carlo based computer simulation and discussions.....	99-103
3.2.5. Conclusions.....	103-103
3.3. Temporal Evolution of Characteristic Length and Fractal Dimension for a Non-Euclidean System.....	103
3.3.1. Introduction.....	103-106
3.3.2. Computer Model and the results on structure evolution during cement hydration.....	106-110
3.3.3. Conclusions.....	110-110
<b>Chapter 4: Hierarchical nano-composites via evaporation induced assembly under non-buckling regime.....</b>	<b>111</b>
4.0. General Introduction.....	111-112
4.1 Evaporation-induced Self Assembly of Nanoparticles in Non-buckling Regime: Effect of Initial Colloidal Concentration.....	112
4.1.1. Introduction.....	112-113
4.1.2. Experimental methods.....	113-115
4.1.3. Results and discussion .....	116-124
4.1.4. Conclusions.....	125-125
4.2. Evaporation-induced Self assembly of Nanoparticles in Non-buckling Regime: Effect of Charge Variation of the Colloid .....	125

4.2.1. Introduction.....	125-126
4.2.2. Experimental methods.....	126-128
4.2.3. Results and Discussions.....	128-132
4.2.4. Conclusions.....	132-132
 <b>Chapter 5: Hierarchical Nano-composites via Evaporation Induced</b>	
<b>Assembly under Buckling Regime.....</b>	<b>133</b>
5.1. Origin of Buckling Phenomenon during Drying of Micrometric Colloidal Droplets.....	133
5.1.1. Introduction.....	133-134
5.1.2. Experimental.....	134-136
5.1.3. Results and discussion.....	136-143
5.1.4. Conclusions.....	143-144
5.2. Control of Buckling in Colloidal Droplets during Evaporation Induced Assembly of Nano-particles.....	144
5.2.1. Introduction.....	144-145
5.2.2. Experiments.....	146-149
5.2.3. Results and discussion.....	149-157
5.2.4. Conclusions.....	157-157
5.3. One Step Fabrication of Thermally Stable TiO <sub>2</sub> /SiO <sub>2</sub> Nanocomposite Microspheres by Evaporation Induced Self-assembly.....	157
5.3.1 Introduction.....	157-158
5.3.2. Experimental methods.....	158-159
5.3.3. Results and discussion.....	159-170
5.3.4 Conclusions.....	171-171
 <b>Chapter 6: Buckling Induced Morphological Transformation of Droplets of</b>	

<b>Mixed Colloidal Suspensions during Evaporation Induced Self assembly .....</b>	<b>172</b>
6.1. Morphological Transformation of Droplets of Silica Colloids and <i>E-coli</i> Suspensions.....	172
6.1.1. Introduction.....	172-172
6.1.2. Experimental Section.....	173-173
6.1.3. Results and Discussions.....	173-176
6.1.4. Conclusions.....	176-177
6.2. Arrest of Morphological Transformation during EISA of Mixed Colloids by Charge Tuning.....	177
6.2.1. Introduction.....	177-177
6.2.2. Experimental.....	177-178
6.2.3. Results and discussion.....	178-183
6.2.4. Conclusions.....	184-184
6.3. Nanocomposite Silica Surfactant Microcapsules by Evaporation Induced Self Assembly: Tuning the Morphological Buckling by Modifying Viscosity and Surface Charge.....	184
6.3.1. Introduction.....	184-185
6.3.2. Experimental.....	185-186
6.3.3. Results and discussions.....	186-193
6.3.4. Conclusions.....	193-193
<b>Chapter 7: Summary and Conclusions.....</b>	<b>194-198</b>
<b>References.....</b>	<b>199-217</b>
<b>List of Publications.....</b>	<b>218-221</b>

# SYNOPSIS

Nano-materials are at the leading edge of the rapidly developing field of nanotechnology. Since last decade, nano-materials in general and nano-ceramics in particular have gained tremendous importance owing to their potential technological applications. A reduction in particle size to nanometer scale results in various special and interesting properties vis-à-vis bulk properties<sup>1</sup>. The size dependent properties make these materials superior and indispensable in diverse area of human activities. Effects due to quantum size and high specific surface area are the driving force to obtain fine size particles with advanced physico-chemical properties<sup>2</sup>. Applications of nano-materials in technology have been increased enormously and also have been commercialized for diverse applications<sup>3,4</sup>. In various functional applications, like drug delivery, optical, magnetic, sensors, solid oxide fuel cell, catalysis, nano-ceramics have been playing an important role. Two major methods for synthesizing nano-materials are sol-gel and precipitation techniques<sup>5</sup>. It is often observed that these synthesis techniques give rise to aggregates of nanoparticles (**Schematic 1**).

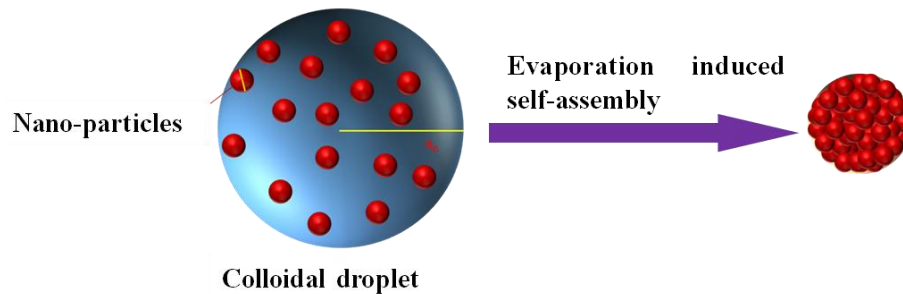


**Schematic 1** *The schematic shows the nature of the nanoparticles aggregates in the sol-gel or precipitation technique.*

These aggregates consist of loosely bound structure of nanoparticles. Because of negligible strength, the loosely bound structure of nanoparticles has limited application. Sintering is a process which binds the nanoparticles into a coherent structure imparting enough strength for its pertinent application. It has been found that ceramics with ultra fine microstructure are more ductile and have lower sintering temperature than their coarse-grained counterparts<sup>6,7</sup>. The restructuring of the mesoscopic morphology during sintering depends on various parameters such as temperature, sintering time, initial morphology and intermediate phases etc<sup>8</sup>. In present thesis, two broader aspects of the nano-ceramics have been dealt with. First aspect deals with the sintering behavior of the nano-ceramics aggregates prepared by sol-gel or precipitation route. Mesoscopic structural modifications during sintering of various important nanoceramics systems such as NiO, YCrO<sub>3</sub>, Yttrium Aluminum Garnet (YAG) and TiO<sub>2</sub> etc. have been investigated. Monte-Carlo simulations have been also performed in some systems to understand the sintering behavior.

Second aspect of the thesis deals with evaporation induced self-assembly of the nanoparticles. As discussed above, often the ceramics synthesized by sol-gel and precipitation technique results in agglomerated nano-particles. In this kind of the un-controlled aggregates, some properties arising from nanophase may get suppressed. In order to overcome the uncontrolled aggregation of nano-particles, a relatively new self assembly technique has been recently utilized to achieve controlled assembly of nano-particles. Assembly of the nanoparticles in a well controlled morphology may have potential applications in nanotechnology in wide domains, such as, photonics, electronics, sensors, energy storage, catalysis etc. Self assembly<sup>9,10</sup> is generally considered as the most promising means for designing and controlling the bottom up approach to synthesize structures with varied geometries like spheres, doughnuts, sheets, tubes, wires etc. In recent years, spray drying<sup>10-14</sup> has been found a special place in synthesizing hierarchically structured grains by atomizing a colloidal

suspension into droplets and then converting these droplets into nanostructured grains (Schematic 2).



**Schematic 2** *The schematic show the controlled assembly of nanoparticles.*

The effect of various physico-chemical parameters on the assembly of nanoparticles during drying has been studied. The micrometric grains having various morphologies have been synthesized and characterized.

At this juncture, it is important to note that the pertinent length scales, which are present in the nano-ceramic and nano-composite systems discussed above, manifest in 1-1000 nm range. Small angle scattering (SAS)<sup>15</sup> is an ideal technique to study the nano-ceramics and self-assembled materials. SAS provides structural information on inhomogeneities of colloidal dimension and are defined with respect to the scattering length density as seen by the probe radiation vis-à-vis that of the homogeneous matrix. Structures are defined by the scattering length density as a function of position, and the scattering profile by the intensity as a function of the momentum transfer vector. Structural properties include size, shape, dimensionality and interparticle spatial correlation. The probe radiations used for these studies include X-rays and neutrons depending upon the nature of the inhomogeneity like the scattering density contrast it offers to the probe radiation vis-à-vis that offered by the matrix. In present work, the sintering behavior of the nano-ceramics and self-assembled materials have been extensively studied and characterized by Small Angle Neutron/X-ray

scattering in addition to the other complimentary technique such as Scanning Electron Microscopy, Light Scattering etc. The thesis is organized into following seven Chapters.

## **Chapter 1: Introduction**

Chapter-1 of the thesis presents a general introduction of the importance of the nano-ceramics and nano-composite systems. The suitability of the small angle scattering (SAS) technique to probe these systems are also described. The chapter-1 of the thesis deals with the details of the SAS theory. The SAS using neutron and X-ray as probing radiation has been described in this section. In this chapter various information, which can be obtained by SAS experiment, has been discussed. The chapter also deals with the different instrumental aspect of the SAS technique. This chapter also gives rudiments of Small Angle Neutron Scattering (SANS) and Small Angle X-ray scattering (SAXS) instrument, which have been used for scattering measurements.

## **Chapter 2: Probing Mesoscopic Morphology of Euclidean Nano-ceramics Aggregates**

The chapter-2 of the thesis is based on the studies of sintering behavior of the nano-ceramics Euclidean aggregates. Pore structure evolution in nano-crystalline Nickel Oxide (NiO) at different sintering temperatures has been investigated using SANS. The finding of the experiments reveals scattering contributions from pore structures in two different length scales. For larger pores, reductions in pore size and polydispersity have been observed with increasing temperature. Evolution of the pore morphology has been attributed to the mass transport mechanism via diffusion during heat treatment.

The dielectric response and the pore morphology of  $\text{YCrO}_3$  have been investigated as a function of sintering temperature. A non-Debye to Debye type transition of dielectric response is observed beyond sintering temperature of  $1400^\circ\text{C}$ . Results from dielectric

measurements were explained on the basis of pore morphology, pore-size distribution and connectivity between the pores.

Mesoscopic structural evolutions of  $\text{TiO}_2$  microspheres synthesized via spray hydrolysis technique has also been investigated by SANS and SAXS. The effects of heat treatment have been studied by SAXS. It has been shown that the  $\text{TiO}_2$  microspheres are good candidates for the growth of CNTs.

### **Chapter 3: Probing Mesoscopic Morphology of the Non-Euclidean Nano-ceramics**

#### **Aggregates**

This chapter deals with the SAS investigations of the fractal aggregates of ceramics systems. Mesoscopic structural evolution under thermal annealing of Yttrium Aluminum Garnet (YAG) fractal aggregates has been investigated by SANS. Fractal dimension remains invariant with sintering temperature but the extent of fractal realm gets narrowed down significantly. A Monte Carlo simulation, based on Ostwald-ripening type of relaxation of fractal aggregates for a mass conserved system, has been attempted in order to understand the aforementioned novel observation. Predictions of the model were found to be consistent with experimental observations.

Smoothing of the fractal rough surface, in  $\text{Nd}_2\text{O}_3$  doped  $\text{CeO}_2$  ceramic, under sintering has been observed from ultra-small angle X-ray scattering investigation (USAXS). The surface-fractal dimension of 2.6 in the non-sintered specimen reduces with sintering temperature and gradually attains a value of 2.0, which corresponds to a smooth surface, at high enough sintering temperature. A Monte Carlo based computer simulation has been attempted to explain the smoothing of such fractally rough surface due to the diffusion based surface transport of the materials from region of positive curvature to that of negative curvature.

Monte-Carlo simulations on DLA cluster has been used to understand some experimental observations on temporal evolution of characteristic length and fractal dimension for a dynamical system<sup>16-18</sup>. It has been shown that the simulation corroborates well with the trend of the experimentally observed temporal evolutions of fractal dimension and characteristic length during light water hydration of calcium silicates ( $C_3S$  and  $C_2S$ ) and ordinary Portland cement (OPC).

#### **Chapter 4: Hierarchical nano-composites via evaporation induced assembly under non-buckling regime**

Chapter-4 of the thesis covers the controlled assembly of the nanoparticles via spray drying of colloids under slow drying regime. Hierarchical structures of micrometric spheres are synthesized by evaporation induced self assembly of silica colloids using spray drying technique. Effects of concentration of initial colloidal dispersion, on the packing of the nanoparticles in assembled grains in non-buckling regime of drying, has been investigated. Although, the packing of nanoparticles remains uniform in an assembled grain at smaller concentration, the same becomes non-uniform at higher concentration. Further, the average packing fraction of the nanoparticles within the assembled grains, decreases with increasing colloidal concentration. These observations have been attributed to the modification in viscosity of the initial dispersion. Electron microscopy, light scattering measurements have been performed to probe overall morphology of the dried grains, while inter-particle correlation inside the grains has been investigated by SANS.

In addition, chapter-4 also deals with the effect of alteration of charge of colloids on the assembly process. Inter-particle correlation and available specific surface area of silica and air interfaces, in the assembled grains, gets modified, keeping the overall spherical shape of the assembled grains un-altered on addition of electrolyte in initial colloidal dispersion prior

to self assembly process. While the external morphology of the assembled grains was probed by scanning electron microscopy, SANS technique has been employed to investigate the modifications in the internal structure and the inter-particle correlation inside the assembled grains. It is revealed that a sticky hard sphere type inter-particle correlation between the constituent particles gets altered to a fractal type correlation with addition of electrolyte. Further, the available specific surface area for the silica-air interface gets significantly enhanced after the electrolyte is leached out from the assembled grains.

### **Chapter 5: Hierarchical Nano-composites via Evaporation Induced Assembly under Buckling Regime**

The evaporation induced self assembly of the colloids in fast drying regime have been dealt with in chapter-5 of the thesis. It has been observed that the doughnut grains have been obtained in contrast to spherical grains in slow drying regime. An attempt has been made to understand, using electron microscopy and SANS, the origin of buckling of micrometric colloidal droplets during EISA. It has been shown that the origin of the buckling is better explained with the help of an existing hypothesis based on formation of viscoelastic shell of nanoparticles during drying. The hypothesis was further supported by the arrest of buckling by modifying the colloidal interaction in initial dispersion.

The silica dispersion has been modified with polyethylene glycol (PEG) of different molecular weights in varying concentrations. Spray drying experiment have been performed on these modified dispersions. The buckyball type of anisotropic grains has been observed and their formation could not be explained on the basis of buckling of the homogenous elastic spherical shell theory. However, these experimental observations could be understood on the basis of inhomogeneous elastic shell model.

EISA of mixed colloids has been employed to synthesize microspheres of  $\text{TiO}_2/\text{SiO}_2$  nano-composite. SANS/SAXS and electron microscopy investigations have revealed hierarchical morphology of the microspheres. Although the internal structure of the microspheres, consisting of solely silica nanoparticles, gets significantly modified with time due to reduction in high specific surface area by internal coalescence, the internal structure for the composite microspheres remains stable over aging of one year. Such temporal stability of the composite microspheres is attributed to inhibition of coalescence of the silica nanoparticles in presence of titania nanoparticles. X-ray diffraction and thermo-gravimetric results show the improved thermal stability of the composite grains against the anatase to rutile phase transition. Such thermal stability is attributed to the suppression of the growth of titania nanoparticles in presence of silica nanoparticles. The Ultraviolet-Visible spectrometry (UV-Vis) results indicate the confinement effect of the  $\text{TiO}_2$  nanoparticles in the silica matrix. A plausible mechanism has been proposed for the formation of the microspheres of different morphology during self-assembly.

## **Chapter 6: Buckling Induced Morphological Transformation of Droplets of Mixed Colloidal Suspensions during Evaporation Induced Self assembly**

Chapter-6 of the thesis deals with the morphological transformation during EISA of a mixed colloidal suspension in micrometric droplets. It is illustrated that the structural modulations get significantly amplified with enhancement in volume fraction of anisotropic soft colloidal component of the mixed colloids. It has been argued that the reduction in elastic modulus of formed shell, at the boundary of a drying droplet, and the anisotropic nature of one of the colloidal components facilitate the deformation process.

It has also been demonstrated that the buckling induced sphere to deformed-doughnut like morphological transformation in such a process can be arrested by proper tuning of the

surface charge on the colloidal components. The buckling amplitude diminishes with a reduction in stabilization force between the colloidal particles. It is established that such arrest of morphological transformation is related to an effective exposure of the surface of softer components at gas-liquid interface. A plausible mechanism regarding the arrest of morphological transformation by surface charge tuning is discussed.

Chapter-6 also deals with the synthesis of the nano-composite microcapsules of silica and surfactants via EISA. It is established using electron microscopy and measurements using SANS and SAXS that viscosity of the virgin dispersion and surface charge of colloidal components play significant role in buckling of the spray droplets during drying. Hollow spherical grains are realized at relatively lower viscosity and higher surface charge while mushroom like grains manifest at higher viscosity and lower surface charge. In the intermediate conditions, deformed doughnut shaped microcapsules are obtained. Scattering experiments establish the presence of organization of micelle like aggregates of surfactants in the dried grains and also corroborate with the observations from electron microscopy. A plausible mechanism regarding the chronological pathways of morphological transformation is illustrated.

### **Chapter7: Summary and Conclusions**

The findings of the research work have been summarized in chapter 7 of the thesis. It has been shown that SAS technique is an ideal technique to probe the mesoscopic length scale in the nano-ceramics. The sol-gel technique often used to synthesize the nano-ceramics, results into agglomerated structure of the nanoparticles. The sintering behavior can be effectively monitored using the SAS experiments. A model Monte Carlo simulation has been adopted to comprehend the experimental observations. A controlled evaporation induced assembly of the nanoparticles has been utilized to realize different kind of the morphology of the self-assembled grains. The isotropic micrometric spherical grains can be realized in slow drying

regime whereas; anisotropic grains have been realized in the fast drying regime. The SAS experiment reveals the inter-particle correlation inside the grains.

### References:

- [1] C.B. Murray, C.R. Kagan, M.G. Bawendi, *Annu. Rev. Matter Sci.* 30 (2006) 545.
- [2] G-M Chow, N. Ivanova Noskova, *Nano-structured Materials Science and Technology*. Dordrecht: Kluwer Academic publishers (1998).
- [3] L.Mazzola, *Nature biotechnology* 21 (2003) 1137.
- [4] R. Paul, J. Wolfe, P. Hebert, M .Sinkula, *Nature Biotechnology* 20 (2003) 277.
- [5] Larry L. Hench, Jon K. West, *Chem. Rev.*, 90 (1), 1990, pp 33–72
- [6] R. W.Siegel, *Physics of New Materials*, edited by F. E. Fujita (Springer-Verlag, Heidelberg) (1994) 65.
- [7] J. Karch, R. Birringer, H. Gleiter, *Nature (London)* 330 (1987) 556.
- [8] W.D. Kingery, H.K. Bowden, D.R. Uhlmann, *Introduction to Ceramics*. Sec ed. Wiley Series on the Science and Technology of the Materials.1976, New York: John Wiley & sons. 1032.
- [9] G. M. Whitesides, B. Grzybowski, *Science* 295 (2002) 2418.
- [10] R. D Kamien, *Science* 299 (2003) 1671.
- [11] K. Master, *Spray Drying Handbook*, 5th ed.; Longman Scientific & Technical: England, 1991.
- [12] D. Sen, S. Mazumder, J. S. Melo, Arshad Khan, S. Bhattacharya, and S. F. D’Souza, *Langmuir* 25 (2009) 6690.
- [13] N. Tsapis, D. Bennett, B. Jackson, D. A. Weitz, and D. A. Edwards *Proc. Natl. Acad. Sci. USA* 99 (2002) 12005.
- [14] D. Sen, O. Spalla, L. Belloni, T. Charpentier, A. Thill, *Langmuir* 22 (2006) 3798.

[15] A. Guinier, G. Fournet, B. C. Walker and L. K. Yudowith in *Small Angle Scattering of X-Rays*, Wiley, New York (1955).

[16] S. Mazumder, D. Sen, A. K. Patra, S. A. Khadilkar, R. M. Cursetji, R. Loidl, M. Baron and H. Rauch; *Phys. Rev. Lett.* 93 (2004) 255704.

[17] S. Mazumder, D. Sen, A. K. Patra, S. A. Khadilkar, R. M. Cursetji, R. Loidl, M. Baron and H. Rauch; *Phys. Rev. B* 72 (2005), 224208.

[18] S. Mazumder, R. Loidl and H. Rauch; *Phys. Rev. B* 76 (2007) 064205.

# LIST OF FIGURES

	<b>Page</b>
1.1 The schematic shows the application of the nano-materials in various areas of industry.	23
1.2 The length scales and various techniques to probe the different length scales.	25
1.3 The working principle of the microscopy and scattering experiments.	26
1.4 Interaction of the different radiation with matter.	27
1.5 Scattering of a perfect collimated radiation under a scattering potential.	28
1.6 Variation of scattering lengths of different elements with respect to X-rays and neutrons.	29
1.7 The oscillations of scattering length density at molecular length scale.	31
1.8 X- ray/neutron beam paths from the source to the detector, both elements located far away from the sample. The segment BC+AB is the optical path difference from which the phase shift is determined.	33
1.9 Schematic examples of two-phase systems (a) a set of isolated objects with a constant SLD embedded in a homogeneous matrix (b) continuous and interconnected phases, both with a constant SLD.	37
1.10 Ensemble of spherical nano-objects embedded into homogenous matrix in dilute limit.	44
1.11 The modeled scattered intensity from a monodisperse spheres of 10 and 20 nm. Inset show the Porod plot of the scattered intensity.	45
1.12 The modeled scattered intensity for the ensemble of concentric shell of varying inner and outer radius.	46

1.13	The modeled scattered intensity from an ensemble of polydisperse spheres of median size 10 nm with varying polydispersity index $\sigma$ . Inset show radius distribution.	49
	Schematic of systems of hard spheres (a) dilute (b) concentrated. (c) $g(r)$ function for the hard sphere model (d) Scattering intensity determined using eq. 1.53 with $S(q)$ defined by eq.1.55, for different volume fractions $\Phi_v$ starting from 0 (top) up to 0.6 (bottom).	51
1.14		
1.15	(a) Schematic log-log plot of the mass $M(r)$ of a homogeneous object (b) the same for a fractal object (c) scattering intensity corresponding to a fractal object with $r_0=2$ nm, $\xi=50$ nm and $D=2.2$ .	52
1.16	A schematic of typical SAXS instrument is shown.	55
1.17	Schematic of the proposed SAXS beamline, at INDUS-2 synchrotron at RRCAT Indore, India, is presented.	56
1.18	Schematic of a typical SANS instrument is shown.	58
1.19	Schematic of MSANS instrument at Guide Tube laboratory of Dhruva reactor, India.	59
2.1	(a) The experimental SANS profiles are depicted. The solid line depicts the fit of the model to the data at three different heat treatment temperatures. (b) The model fitting of the experimental data with two length scale structure. It is clear from this figure that one length scale structure can not fit the experimental data completely.	63
2.2	Larger length scale pore size distribution of NiO powder samples. Inset shows the smaller length scale pore size distribution of the NiO powder sample.	64
2.3	SANS profiles for 1600°C sintered pellets for two thicknesses are shown.	68

	The corresponding extracted single scattering profile is compared with the experimental profiles for two thicknesses.	
2.4	Multiple scattering corrected SANS profiles with fitted model for different sintering temperatures in double logarithmic scale.	69
2.5	Smaller pore size distribution, at different sintering temperature, is depicted. Inset shows the size distributions of bigger pores.	71
2.6	(a) Real part ( $\epsilon'$ ) of the dielectric response as a function of frequency for different sintering temperatures (b) Imaginary part ( $\epsilon''$ ) of the dielectric response as a function of frequency for different sintering temperature.	72
2.7	Schematic of the spray hydrolysis method used for synthesizing $\text{TiO}_2$ submicrospheres.	77
2.8	SEM micrograph of (a) $2\text{Ni\_TiO}_2$ (b) $5\text{Ni\_TiO}_2$ (c) $10\text{Ni\_TiO}_2$ and (d) $15\text{Ni\_TiO}_2$ composite submicrospheres.	78
2.9	The SAXS profiles of the $\text{TiO}_2$ , doped $\text{TiO}_2$ and heat treated specimens.	79
2.10	(a) The primary $\text{TiO}_2$ NPs radius distribution, estimated by SAXS analysis. The inset shows the higher size contribution which may arise due to aggregation of primary NPs (b) $\text{TiO}_2$ NPs size distribution for the specimens heated at $600^\circ\text{C}$ . $r$ indicates the radius of the NPs.	79
2.11	High temperature XRD patterns of the Ni- $\text{TiO}_2$ microspheres.* marked peaks corresponds to Pt peaks. Anatase to rutile phase transition is observed beyond $600^\circ\text{C}$ . A and R denotes the anatase and rutile phase.	80
2.12	The schematic of the mechanism for the formation $\text{TiO}_2$ submicrospheres in the spray hydrolysis technique.	82
2.13	The SEM micrographs of the CNTs on (a) $5\text{Ni\_TiO}_2$ (b) $15\text{Ni\_TiO}_2$ substrate.	83

2.14	(a) The XRD patterns of the CNTs grown on TiO <sub>2</sub> microspheres. The TiO <sub>2</sub> is in the rutile phase corresponding to the JCPDS no. 21-1276. The * marked peak corresponds to the CNT. (b) Yield of CNTs, as estimated from the peak intensity corresponding graphite peak, is shown with different Ni concentration.	84
3.1	(a) SANS profiles in log-log scale for specimens sintered at different temperatures. Solid line represents the fit of the model to the scattering data. The profiles are shifted vertically for clarity. (b) Size distribution of the primary particles with increasing sintering temperature.	88
3.2	Evolution of the DLA clusters with different $\Delta_s$ . (a) Initial 2D DLA (b) modified DLA for $\Delta_s = 10$ (c) modified DLA for $\Delta_s = 30$ (d) modified DLA for $\Delta_s = 150$ .	93
3.3	Evolution of the size distribution of the primary particles as function of $\Delta_s$ (T).	93
3.4	Computed lower cutoff from simulation and observed lower cutoff from SANS at different temperatures are depicted. Inset shows computed upper cutoff from simulation and observed upper cutoff from SANS.	94
3.5	(a) USAXS profiles in double logarithmic scale. The solid lines are fit to the data. (b) USAXS profiles in Porod plot ( $I(q) q^4$ vs. $q$ ).	97
3.6	(a) The initial self-affined fractal surface simulated using spectral synthesis method for a fractal dimension 2.6 (b) $\log(S(k))$ vs. $\log(k)$ for the initial fractal surface with fractal dimension 2.6.	100
3.7	The surfaces for increasing $T_1$ values are depicted. It is evident that the surface becomes smoother with increase in $T_1$ .	102
3.8	The reduction of the surface width and the decrease of the fractal	102

	dimension with increase in $T_1$ are depicted.	
3.9	(a) Evolution of fractal dimension and square of the characteristic length with hydration time as observed from the USANS experiments. (b) Evolution of USANS intensity at $q \sim 0$ with hydration time.	106
3.10	The initial fractal object generated using DLA model, just at the onset of the hydration.	107
3.11	(a) The evolution of fractal dimension with Monte Carlo steps (b) The evolution of characteristic length with Monte Carlo steps.	108
3.12	Evolution of the fractal dimension and square of the characteristic length with Monte Carlo steps.	109
3.13	The morphology of the evolving cluster at different Monte Carlo steps for $p=1$ .	109
4.1	The schematic of the spray dryer utilized for slow drying experiment.	113
4.2	SEM micrographs of (a) sp-2.5 and (b) 5sp-5 (c) sp-10 and (d) sp-20 specimens.	114
4.3	(a) SANS profiles in Porod plot ( $I(q)q^4$ vs. $q$ ) indicating two level structures (b) SANS profiles in log-log plot and corresponding fit of profiles in line. The profiles are shifted vertically for clarity.	115
4.4	Estimated size distribution of the grains from analysis of DLS data.	115
4.5	The effect of the colloidal silica concentration on the relative density and relative viscosity of the dispersion. The solid lines represent guides to the eye in both the curves.	119
4.6	(a) Average grain size for various concentrations of silica colloid as estimated by DLS. (b) The specific surface area of the mesopores from SANS measurements.	121

4.7	Schematic of the proposed mechanism of the drying process of silica colloid (a) for small concentration (b) for large concentration.	124
4.8	SEM micrographs of the self-assembled grains are shown. It is seen that the powder grains are mainly spherical in shape for all cases.	126
4.9	SANS profile from diluted virgin silica colloidal dispersion. The size distribution of the NPs is shown in the inset.	127
4.10	SANS profiles of the self-assembled grains are shown in Porod representation. (b) Fit of the scattering model to the combined scattering data. Solid lines show the fit. The profiles are shifted vertically in order to show the fits clearly.	127
4.11	Schematic representation of the drying process of colloidal droplets, without and with presence of electrolyte, is shown.	132
5.1	Schematic of the LU 228 advance spray dryer.	135
5.2	Morphology of the spray dried grains obtained by varying atomization pressure (a) 0.5 kg/cm <sup>2</sup> (b) 1.0 kg/cm <sup>2</sup> (c) 2.0 kg/cm <sup>2</sup> (d) 4.0 kg/cm <sup>2</sup>	135
5.3	(a) SANS data for the specimens in double logarithmic scale. Solid lines represent fit to the data. Profiles have been shifted vertically for clarity. (b) SANS profiles for the specimens obtained at different specimens in Porod representation.	136
5.4	Histogram for size distribution of the spray dried grains at different atomization pressures by SEM micrograph analysis.	137
5.5	(a) Average size of the grains at different atomization pressures. The inset shows polydispersity in the size of the grains. (b) Variation of the size of central hole of doughnuts is depicted.	137

5.6	(a) The ratio of the size of doughnut hole to the overall size of grain with atomization pressure is shown. (b) The ratio of Porod levels at high and low $q$ as a function of atomization pressure.	138
5.7	The mechanism for formation of doughnuts and spherical grains from spherical droplet in different drying regimes.	143
5.8	SEM micrograph of the self-assembled grains obtained for drying of only 2 wt% silica dispersion.	146
5.9	SEM micrographs of calcined specimens of (a) S1pt5 (b) S1p1 (c) S1p2 (d) S1p3.	147
5.10	SEM micrographs of calcined specimens of (a) S2pt5 (b) S2p1 (c) S2p2.	147
5.11	(a) Heat flow and weight loss curves for spray dried grains for varying PEG 400 concentrations. (b) Heat flow and weight loss curve for the spray dried grains for varying PEG1450 concentrations.	148
5.12	Normalized SANS profiles of calcined assembled silica grains obtained for different concentrations of (a) PEG400 (b) PEG1450. The solid lines are fit of model to the data.	149
5.13	Pore size distribution for S1p2 and S1p3 calcined specimens is depicted. Inset shows the pore size distribution for S2p1 and S2p2 specimens. It is to be noted that these pores are templated by the free PEG aggregates.	152
5.14	Pore size distribution for S1p2 and S1p3 calcined specimens, as obtained from the SANS analysis. Inset shows the pore size distribution for S2p1 and S2p2 specimens. It is to be noted that these pores are templated by the free PEG aggregates.	152
5.15	The schematic shows drying of droplets containing (a) silica colloids coated with polymer, no PEG aggregate (b) silica colloids coated with	156

- polymer, PEG aggregates are small in number (c) silica colloids coated with polymer, PEG aggregates are larger in number.
- 5.16 The micrographs of assembled grains consist of (a) only SiO<sub>2</sub> NPs, inset show the cross sectional view of the hollow grains (b) only TiO<sub>2</sub> NPs, inset of shows the doughnut type of grains. 159
- 5.17 The micrographs of assembled grains consist of mixed colloids in weight ratio of (a) TiO<sub>2</sub>/SiO<sub>2</sub>=2.0., Inset shows a magnified grains, the rough surface of grains indicate that the presence of bigger NPs on the surface (b) TiO<sub>2</sub>/SiO<sub>2</sub>=1.0 (c) TiO<sub>2</sub>/SiO<sub>2</sub>=0.5. 160
- 5.18 (a) SAXS profiles of the SiO<sub>2</sub> and TiO<sub>2</sub> dispersion. SAXS profiles of the mixed dispersion having SiO<sub>2</sub> and TiO<sub>2</sub> in equal proportion. The lines represent the model fit to the data. (b) Bimodal size distribution of the TiO<sub>2</sub> NPs is shown. Inset shows the SiO<sub>2</sub> radius distribution. 160
- 5.19 (a) SANS profiles of the assembled composite grains. Inset shows the profiles in Porod representation (b) SANS profiles of the assembled composite grains in a magnified view. 161
- 5.20 SAXS profiles of the assembled grains in Porod representation. Inset shows the magnified view of correlation peak. 163
- 5.21 SANS/SAXS profiles of the self-assembled grains of TiO<sub>2</sub> and SiO<sub>2</sub>. The scattering profiles of assembled grains at two different times to compare the effect of aging on the grains. 164
- 5.22 The heat flow and weight loss curves for composite grains with different TiO<sub>2</sub>/SiO<sub>2</sub> ratio. 165
- 5.23 (a) The X-ray diffraction pattern of the TI specimens for different temperatures. (b) The X-ray diffraction pattern of the TiSipt5 specimens 166

for different temperatures. The \* marked peaks originate from Pt sample holder and should not be considered in the present perspective.

- 5.24 The schematic of the formation of assembled grains of TiO<sub>2</sub> NPs and composite grains. 170
- 6.1 SEM micrograph of (a) Sample E0 (b) Sample E2 (c) sample E4 (d) sample E6 173
- 6.2 SANS data from self assembled macro/mesoporous silica grains plotted in double logarithmic scale. The inset shows the Zone-III of the profiles plotted in Porod representation. 174
- 6.3 A schematic representation of possible evolutions of structures during drying of a droplet in presence of E. coli is depicted. 176
- 6.4 SEM micrograph of the composite grains (a) E. coli is not covered with poly-cationic PEI (b) E. coli coated with 0.2 % PEI (c) E. coli coated with 1.0 % PEI (d) E. coli coated with 2.0 % PEI. 178
- 6.5 SANS data from the hierarchically structured assembled grains. Three different length scales in the assembled grains are obvious from the scattering data. It is observed from the data that the correlation of the particles inside the grains gets modified with change in the surface charge of E-coli. 180
- 6.6 Schematic representation of the assembly process of silica and E. coli. (a) Both silica and E. coli have negative surface charges. (b) Silica is negative as earlier case but E. coli surface is coated with PEI to impart positive charge on E. coli surface. 183
- 6.7 SEM micrographs of the assembled grains. (a,b) Doughnut like capsules 186

prepared from only silica colloids. (c) Spherical capsules synthesized with silica colloids and SDS in absence of AHC. (d) Same as (c) but after removal of organic moieties. (e) Deformed doughnut like capsules synthesized with silica, SDS and 20 mM AHC. (f) Same as (e) but after removal of organic moieties. (g) Mushroom like grains synthesized with silica, SDS and 50 mM AHC. (h) Same as (g) but after removal of organic moieties.

- 6.8 Rheological response of the dispersions prior to the drying is shown. The inset shows the variation of the  $\zeta$  potential with AHC concentration. 187
- 6.9 SANS data for the non-calcined assembled silica-SDS microcapsules are depicted. Inset shows zoomed view of the zone-III which reflects the correlation between the jammed micelles. 189
- 6.10 SAXS pattern from the non-calcined assembled microcapsules. Peak at around  $q \sim 0.15 \text{ \AA}^{-1}$  is observed when SDS is present. A double peak manifests at highest AHC concentration (50 mM). 190
- 6.11 Schematic diagram shows two different mechanisms with no AHC and with large amount of AHC. At large AHC concentration, the ordering of cylindrical micelles during self-assembly occurs through an intermediate cubic phase between hexagonal and lamellar. 193

# LIST OF TABLES

	<b>Page</b>
1.1 Comparison of the various scattering parameters for Neutrons and X-rays.	32
1.2 Brightness & Fluxes for Neutron & X-ray Sources	54
1.3 Parameters for SAXS beamline at X-ray energy $E= 8$ keV (SHADOWVUI)	57
2.1 Important parameters from SANS and dielectric measurements.	71
2.2 The parameters obtained from analysis of XRD patterns for NiO-TiO <sub>2</sub> specimens.	81
4.1 Parameters obtained from SANS and DLS	118
4.2 Parameters, obtained from SANS analysis, are tabulated.	131
5.1 The fitting parameters obtained from SANS data analysis for calcined S1 specimens.	153
5.2 The fitting parameters obtained from SANS data analysis for calcined S2 specimens.	154
5.3 The parameters obtained from SANS/SAXS analysis.	163
5.4 The parameters obtained from analysis of XRD patterns for TI specimens.	167
5.5 The parameters obtained from analysis of XRD patterns for TIS1pt5 specimens.	167
6.1 Structural parameters obtained from SANS analysis	182

## Introduction

### 1.0. General Introduction

Nano-materials are at the leading edge of the rapidly developing field of nanotechnology. Since last decade, nano-materials in general and nano-ceramics in particular have gained tremendous importance owing to their potential technological applications. A reduction in particle size to nanometer scale results in various special and interesting properties vis-à-vis bulk properties<sup>1</sup>. The size dependent properties make these materials superior and indispensable in diverse area of human activities. Effects due to quantum size and high specific surface area are the driving force to obtain fine size particles with advanced physico-chemical properties<sup>2</sup>. Applications of nano-materials in technology have increased enormously and also have been commercialized for diverse applications<sup>3,4</sup>. In various functional applications, like drug delivery, optical, magnetic, sensors, solid oxide fuel cell, catalysis, nano-ceramics have been playing an important role. Schematic Fig. 1.1 shows the important areas of the nano-technology applications<sup>5</sup>.

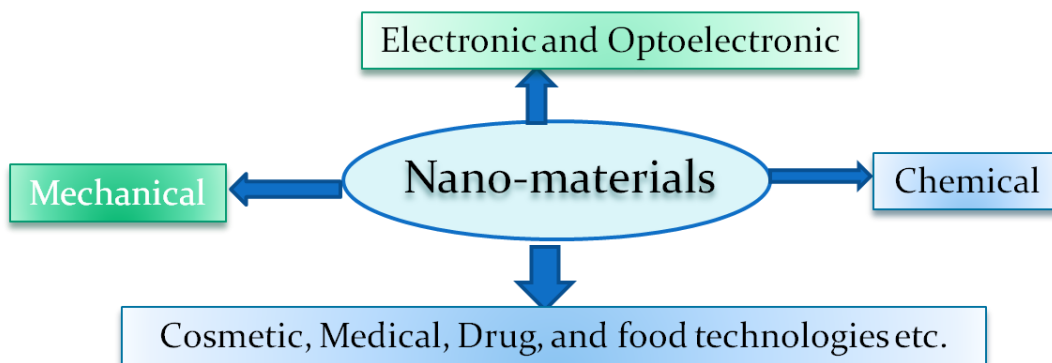


**Fig. 1.1** The schematic shows the application of the nano-materials in various areas of industry.

Two major methods for synthesizing nano-materials are sol-gel and precipitation techniques<sup>6</sup>. It is often observed that these synthesis techniques give rise to aggregates of nanoparticles (NPs). These aggregates consist of loosely bound structure of NPs. Because of negligible strength, the loosely bound structure of NPs has limited application. Sintering is a process which binds the NPs into a coherent structure imparting enough strength for its pertinent application. It has been found that ceramics with ultra fine microstructure are more ductile and have lower sintering temperature than their coarse-grained counterparts<sup>7,8</sup>. The restructuring of the mesoscopic morphology during sintering depends on various parameters<sup>9</sup> such as temperature, sintering time, initial morphology and intermediate phases etc. Sintering behavior of the nano-ceramics aggregates prepared by sol-gel or precipitation route have been investigated using small-angle scattering. Mesoscopic structural modifications during sintering of various important nano-ceramics systems such as NiO, YCrO<sub>3</sub>, Yttrium Aluminum Garnet (YAG) and TiO<sub>2</sub> etc. have been investigated. Monte-Carlo simulations have also been performed in some systems to understand the sintering behavior.

As discussed above, often the ceramics synthesized by sol-gel and precipitation technique results in agglomerated NPs. In this kind of the uncontrolled aggregates, some properties arising from nanophase may get suppressed. In order to overcome the uncontrolled aggregation of NPs, a relatively new self assembly technique has been utilized recently. Assembly of the NPs in a well controlled morphology may have potential applications in nanotechnology in wide domains, such as, photonics, electronics, sensors, energy storage and catalysis etc. Self assembly<sup>10,11</sup> is generally considered as the most promising means for designing and controlling the bottom up approach to synthesize structures with varied geometries like spheres, doughnuts, sheets, tubes, wires etc. In recent years, spray drying<sup>11-15</sup> has been found a special place in synthesizing hierarchically structured grains by atomizing a colloidal suspension into droplets and then converting these droplets into nanostructured

grains. The effect of various physico-chemical parameters on the assembly of NPs during drying has also been studied.

At this juncture, it is important to note that the pertinent length scales, which are present in the nano-ceramic and nano-composite systems discussed above, manifest in 1-1000 nm range. Small angle scattering<sup>16,17</sup> is an ideal technique to study the nano-ceramics and self-assembled materials. The theoretical and experimental background of small angle scattering will be discussed in the following section.

### 1.1. Small angle scattering

Small angle scattering (SAS) is one of the principal techniques to characterize the nano-metric entities as shown in Fig. 1.2.

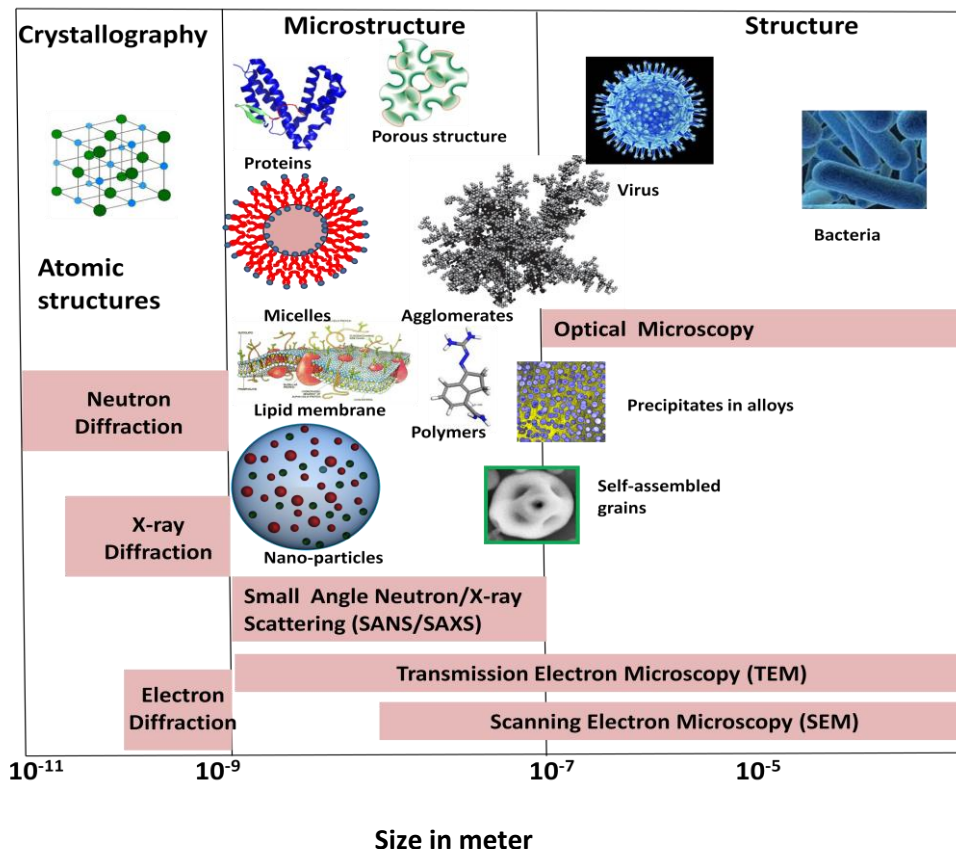


**Fig. 1.2** The length scales and various techniques to probe the different length scales.

The application of SAS in materials science varies from soft matter (surfactant, micelles and polymers), biology (proteins, lipid membrane) and colloidal systems to hierarchical structures

(aggregates of NPs, self-assembled grains). It is evident from Fig. 1.2 that the electron microscopy has a similar probing capacity as compared to scattering technique as far as probing length scale is concerned. However, the microscopy is a local probe of the matter and gives surface information only. The scattering techniques using neutron/X-ray is bulk sensitive techniques and gives statistically averaged information from the specimens. However, microscopy has the advantage that data are acquired in direct (real) space whereas scattering methods measure in reciprocal space. Electron microscopy and SAS can be used as complementary methods to probe the mesoscopic length scale. Fig. 1.3 shows the working principle of the microscopy and scattering techniques.

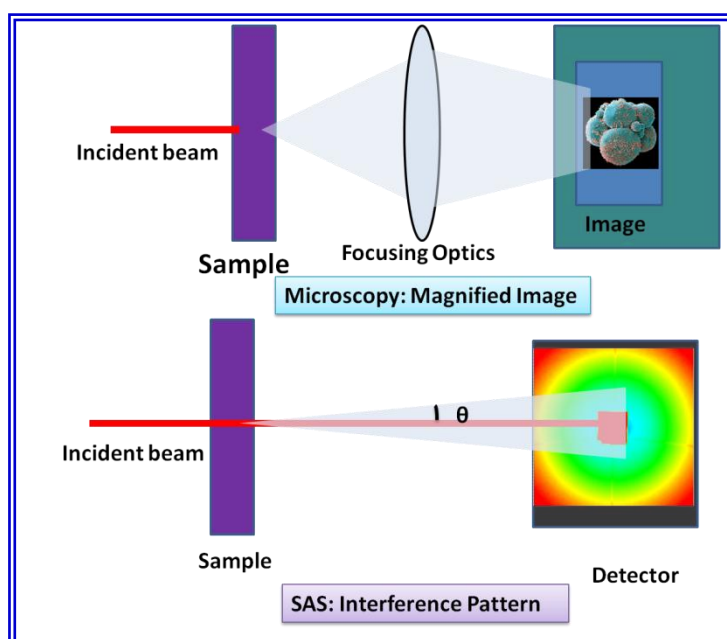


**Fig. 1.3** *The working principle of the microscopy and scattering experiments.*

Further, scattering data, in Fourier (also called reciprocal) space, has to be either inverted to extract real space information or has to be fitted to models describing structures in reciprocal space. Scattering methods measure density-density correlation functions. Because of this fact, the phase information is completely lost. It is not possible to reconstruct a complete image of the sample structure by scattering from one sample.

## 1.2. Interaction of radiation with matter

Different types of radiation interact with matter in different way which depends on the properties of the radiation.

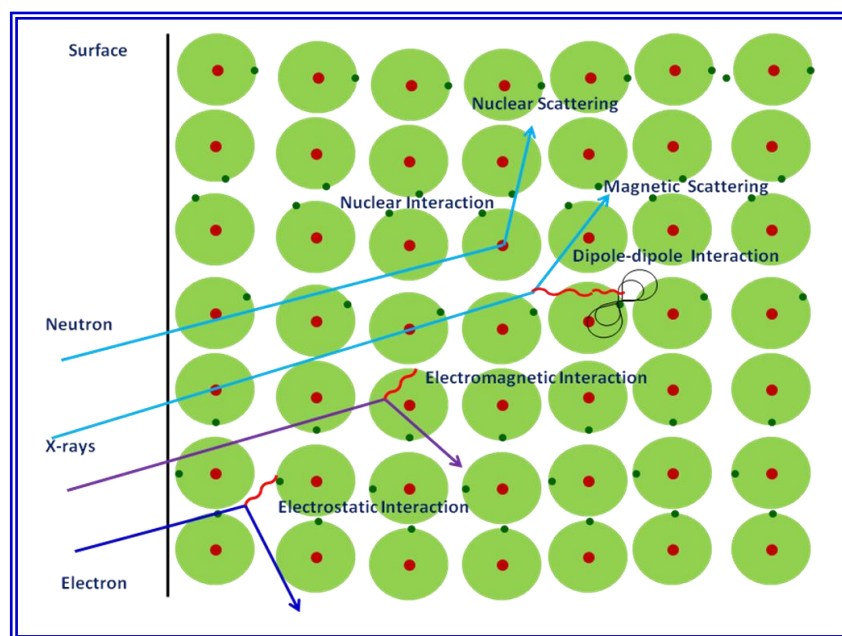


**Fig. 1.4** Interaction of different radiation with matter.

It is evident from Fig. 1.4 that neutron being a neutral particle, penetrates deep into the matter. It interacts with matter via nucleus scattering. Neutron possesses nuclear magnetic moment and hence it can interact with matter via dipole-dipole interaction. The X-rays being an electromagnetic radiation, interacts with matter via electromagnetic interactions. It interacts with the electron cloud of the atoms. The penetration depth for X-ray is lower as compared to that for the neutron. The electron, being charged particles, interacts with matters via electrostatic interaction. The electrostatic interactions are quite strong in nature. Due to strong interaction, the penetration depth is quite low, and electron as probe give only local information of the matter.

### 1.3. Comparing neutron and X-ray as a probe

Let us assume that a perfectly well collimated beam of radiation, i.e., plane wave is advancing through a scattering potential which is located at  $\mathbf{r}=0$ .

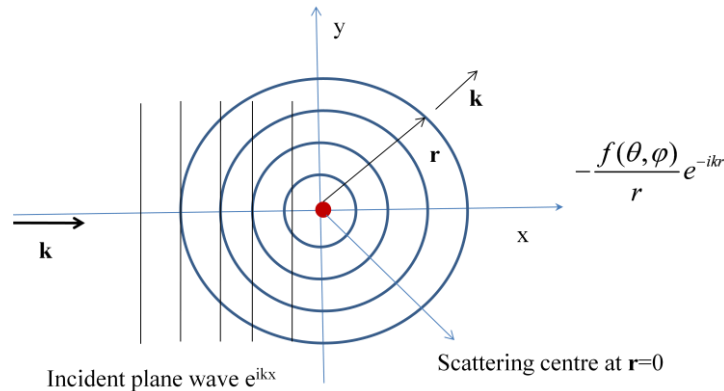


**Fig. 1.5** Scattering of a perfect collimated radiation under a scattering potential.

The scattered wave can be written as  $-\frac{f(\theta, \varphi)}{r} e^{-ikr}$  where  $f(\theta, \varphi)$  is called scattering amplitude or scattering length.  $f(\theta, \varphi)$  is related to Fourier transform of the scattering potential under the first-order Born approximation. For spherical symmetric potential the  $f(\theta, \varphi)$  is only a function of  $\theta$ , where  $2\theta$  is the scattering angle. It is important to note that the first-order Born approximation is valid for single scattering of the probing radiation. The microscopic scattering cross section can be written as,  $\frac{d\sigma}{d\Omega} = |f(\theta)|^2$ . In following section, we will see the nature of interaction of neutron and X-rays as a probe of matter.

The neutron interacts with nucleus, it is noted that nuclear interactions are very short range as compared to the typical wavelength of the thermal neutron. Hence, the thermal neutron sees, a delta potential at  $\mathbf{r}=0$ . Hence, the scattering amplitude or scattering length, in case of neutron, becomes constant. It is important to note that the scattering length may be negative and is related to phase change of the neutron after scattering. For neutrons, the scattering length is a nuclear property and it varies irregularly with atomic number. The

scattering lengths of elements, for neutron, are isotope and spin sensitive (Fig. 1.6). We see that hydrogen and deuterium have very different scattering lengths. This has advantage in deuterium labeling using the fact that the scattering lengths for hydrogen and deuterium are widely different ( scattering length for hydrogen  $b_H = -3.739 \times 10^{-13}$  cm and scattering length for deuterium  $b_D = 6.671 \times 10^{-13}$  cm, respectively). The random distribution of the different istopes and spins give rise to incoherent scattarering of the neutrons.

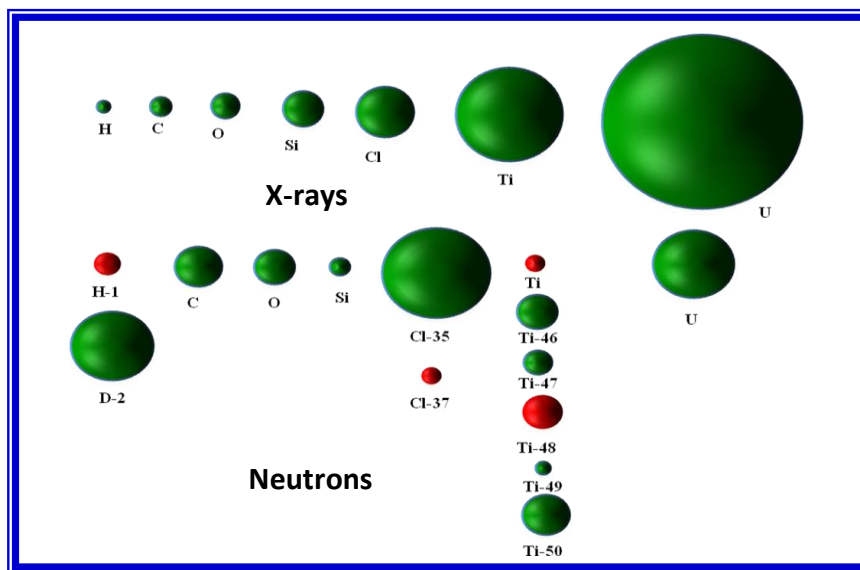


**Fig. 1.6** Variation of scattering lengths of different elements with respect to X-rays and neutrons.

In case of X-rays, the basic process of the scattering by materials is the photon-electron interaction. The elastic scattering produced by an isolated electron was derived by Thompson. The amplitude of the wave scattered by each electron has a well-defined phase relation with the amplitude of the incident wave, thus making interference effects possible. In the particular case of a non-polarized X-ray beam, such as those produced by a classical X-ray tube, the scattering power of one electron per solid angle,  $I_e$ , is a function of the angle

between the incident and the scattered beam,  $2\theta$ :  $I_e(2\theta) = I_0 r_e^2 \left( \frac{1 + \cos^2 2\theta}{2} \right)$  where  $I_0$  is the intensity of the incident beam and  $r_e$  is the classical radius of the electron,  $r_e^2 = 7.90 \times 10^{-26} \text{ cm}^2$ . For small scattering angles,  $\cos^2(2\theta) \sim 1$ , so as the scattering intensity per electron is simply given by  $I_e(2\theta) \sim I_0 r_e^2$ . In addition to the coherent or elastic X-ray scattering, the electrons also produce inelastic Compton scattering. Compton scattering being incoherent (i.e., no phase relationship exists between incident and scattered waves), the scattered waves do not interfere and thus the scattering intensity is not modulated by structure correlation effects. On the other hand, since the intensity of Compton scattering within the small-angle range is weak, its contribution can in practice be neglected<sup>16</sup>. The scattering of the X-rays with an atom can be treated as the scattering from different scattering centers with appropriate phase. The scattering amplitude for an atom is proportional to atomic number  $Z$ . It is to be noted that for X-rays, scattering amplitude of atom is a function of scattering angle unlike the case of neutrons. But for small angle scattering, it may be treated as constant. Hence, scattering length  $b$  of an atom in case of X-rays is  $r_e Z$ . Fig. 1.6 shows the variation of scattering length of the different elements for X-rays and neutron. It is evident from figure that the scattering length of an atom is proportional to the atomic number for X-rays. However, in case of neutrons, the scattering lengths of elements do not follow any trend with the atomic number of the element.

The scattering length, for an ensemble of  $N$  atoms can be written  $b = \sum_i N_i b_i$  where  $b_i$  is the scattering length of the  $i^{\text{th}}$  elements. For SAS, the observed length scale is much larger as compared to inter-atomic distances. Hence, we can define scattering length density (SLD) of a molecule as the ratio of the scattering length  $b$  and molecular volume  $v$ ,  $\rho(r) = \frac{b}{v}$ . The  $\rho(r)$  of a material is calculated from the products of the number density of  $j$ -type atom,  $N_j$ ,

and its scattering length  $b_j$ . For neutrons,  $\rho_N = \sum_j N_j \rho_j$  where  $b_j$  is the scattering length of an atom for neutrons. For X-rays,  $\rho_x = r_e \sum_j N_j \rho_j$  where  $r_e$  is the classical electron radius and  $\rho_j$  is electron density of  $j^{\text{th}}$  atom.

For the molecular length scale, SLD of material oscillates<sup>18</sup> (Fig. 1.7). In SAS experiments, the distances probed are generally much greater than the inter-atomic spacing, so the technique is sensitive to changes in scattering length density over distances up to ~1000 nm rather than the scattering length of individual atoms.

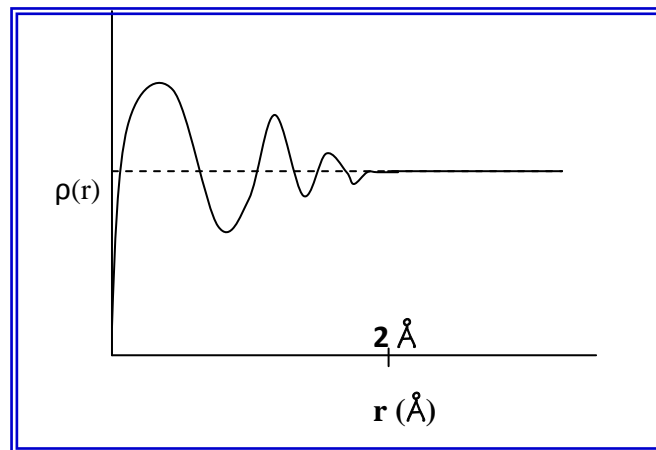


**Fig. 1.7** *The oscillations of scattering length density at molecular length scale.*

SLD is therefore a very useful concept because it can be used to describe the scattering from a large volume (such as particle) without having to specify the position of every atom.

The advantage and disadvantage of the neutrons and X-rays, as a probe for scattering experiments, has been outlined in Table 1.1. From these comparisons, it is evident that both neutron and X-rays are potential probes for different types of systems and may complement each other in some cases. The possibility of isotopic labeling is the advantage of small angle neutron scattering (SANS) over other SAS methods (such as small-angle X-ray scattering (SAXS) or light scattering). Labeling is difficult to achieve with X-rays, since this involves

substitution of heavy atom that changes the sample drastically. SANS has disadvantaged over SAXS by the intrinsically low flux of neutron sources (nuclear reactors or spallation sources using cold source moderators) compared to the orders of magnitude higher flux for X-ray sources (rotating anode or synchrotrons).

**Table 1.1** Comparison of the various scattering parameters for Neutron and X-ray.

	<b>Neutron</b>	<b>X-ray</b>
<b>Intensity</b>	Low	High
<b>H-sensitivity</b>	High	None
<b>Isotope-sensitivity</b>	Strong	None
<b>Heavy elements</b>	Low	High
<b>Spin-sensitivity</b>	Strong	Average
<b>Penetration depth</b>	High	Low
<b>Sample size/amount</b>	Large	Small
<b>Measurement time</b>	Long	Short
<b>Interaction with</b>	Nuclei Magnetic Moment Unsystematic variation with Z	Electron shell  Varies as $Z^2$
<b>Radiation damage</b>	Negligible	High

#### 1.4. Small-angle scattering theory

Let us assume an elastic scattering of the monochromatic radiation with matter. The scattering amplitude and intensity are functions of the scattering vector  $\mathbf{q}$ , which is defined as the difference between the wave-vectors  $\mathbf{K}_f$  and  $\mathbf{K}_i$  with modulus  $2\pi/\lambda$  having the directions of the scattered and incident beam, respectively (Fig. 1.8). Since  $\mathbf{K}_f$  and  $\mathbf{K}_i$  are proportional to the linear momentum of the scattered and incident radiation ( $\mathbf{p}=\hbar\mathbf{K}$ ,  $\hbar$  being the Plank

constant), respectively. The difference  $\mathbf{q}=\mathbf{K}_f - \mathbf{K}_i$  is the momentum transfer vector. As illustrated in Fig. 1.8, the modulus of  $\mathbf{q}$  is  $q = |\mathbf{q}| = 4\pi \sin(\theta)/\lambda$ ,  $2\theta$  being the scattering angle.

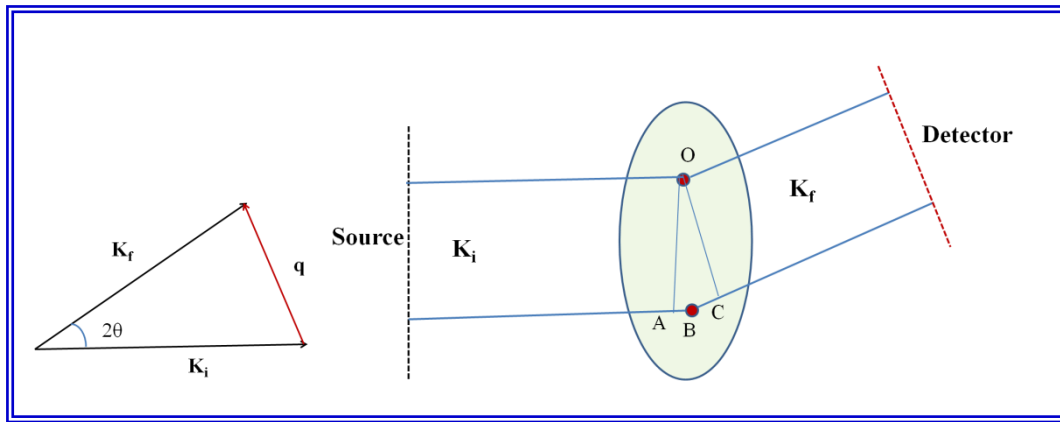


**Fig. 1.8** X-ray/neutron beam paths from the source to the detector, both elements located far away from the sample. The segment  $AB+BC$  is the optical path difference from which the phase shift is determined.

Now, the basic theory<sup>16-18</sup> of SAS by a three dimensional material whose structure is defined by a SLD  $\rho(\mathbf{r})$  will be presented. The scattering length density represents the low resolution structure – solely accounting for the mesoscopic structural features of the material. A low resolution SLD  $\rho(\mathbf{r})$  function describes, for example, the shape and size of nano-objects embedded in a solid or liquid matrix but not their detailed crystallographic structure.

The amplitude of the X-ray/neutron wavelet produced by the scattering from the scattering centers (for neutron, scattering centers are nucleus and for X-rays, scattering centers are electrons) located inside a particular volume element  $dv$  is  $dA(q) = \rho(\vec{r})dv e^{i\Delta\phi}$  where  $\rho(\mathbf{r}) dv$  is the number of scattering centers in the volume element  $dv$ .  $\rho(\vec{r})dv$  is the modulus of the amplitude of the scattered wavelet and  $e^{i\Delta\phi}$  is a phase factor that accounts for the phase difference,  $\Delta\phi$ , between the wavelets associated to the scattering by scattering centers in a volume element located at  $\mathbf{r}=0$  and in another arbitrary volume element  $dv$ . The optical path difference,  $\Delta s$ , associated with two wavelets corresponding to the scattering by

scattering centre inside a volume element at  $\mathbf{r}=0$  and another at  $\mathbf{r}$  (Fig. 1.8) is  $\Delta_s=AB+BC = -(\mathbf{K}_i \cdot \mathbf{r} - \mathbf{K}_f \cdot \mathbf{r})$  where  $\hat{K}_i$  and  $\hat{K}_f$  are unit vectors in the directions defined by  $\mathbf{K}_i$  and  $\mathbf{K}_f$ , respectively. Thus the phase shift defined as  $\Delta\Phi = 2\pi\Delta_s/\lambda$  becomes

$$\Delta\phi = -2\pi \frac{\hat{K}_f - \hat{K}_i \cdot \vec{r}}{\lambda} = -(\vec{K}_f - \vec{K}_i) \cdot \vec{r} = -\vec{q} \cdot \vec{r} \quad (1.1)$$

Substituting  $\Delta\Phi$  in eq. 1.1 and integrating over the whole volume  $V$ , the total scattering amplitude is given by

$$A(\vec{q}) = \int_V \rho(\vec{r}) e^{-i\vec{q} \cdot \vec{r}} dv \quad (1.2)$$

This is the amplitude of the scattered waves under the assumption of the kinematical theory of scattering disregarding multiple scattering and absorption effects. Eq. 1.2 indicates that  $A(\vec{q})$  is simply the Fourier transform of  $\rho(\mathbf{r})$ . Inversely, the  $\rho(\mathbf{r})$  can mathematically be obtained by a Fourier transformation of the amplitude function  $A(\vec{q})$ <sup>16-18</sup>:

$$\rho(\vec{r}) = \frac{1}{(2\pi)^3} \int A(\vec{q}) e^{i\vec{q} \cdot \vec{r}} dv_q \quad (1.3)$$

Since,  $I(\vec{q}) = A(\vec{q}) \times A(\vec{q})^* = |A(\vec{q})|^2$ , the square root of the measured  $I(q)$  function provides only the modulus of the scattering amplitude:

$$A(\vec{q}) = |I(\vec{q})|^{1/2} \quad (1.4)$$

Thus, eq. 1.3 cannot be directly applied to derive neither the  $\rho(\mathbf{r})$  and, consequently, nor the material structure. This is known as the *phase problem* in scattering experiments<sup>16-18</sup>. A procedure that can be applied to determine simple low resolution structures, without attention to the phase problem, is to begin with a proposed structure model providing an initial, guessed, SLD function  $\rho(\mathbf{r})$ . The scattering amplitude is determined using eq. 1.2 and then the trial intensity  $I(\vec{q}) = |A(\vec{q})|^2$  is compared to the experimental intensity. Since the amplitude of the scattered wave,  $A(\vec{q})$ , cannot be experimentally determined, it seems that it

would be useful to derive a relationship connecting the scattered intensity defined in reciprocal space,  $I(\mathbf{q})$ , to a function related to the structure in real space, both functions related by a Fourier transformation.

The SLD  $\rho(\mathbf{r})$  can be written as the sum of an average density  $\rho_a$  and its local deviations defined by  $\Delta\rho(\mathbf{r})$ :  $\rho(\vec{r}) = \rho_a + \Delta\rho(\vec{r})$  Substituting this form for  $\rho(\mathbf{r})$  in eq. 1.2 the scattering amplitude becomes<sup>16-18</sup>

$$A(\vec{q}) = \int_v \rho_a e^{-i\vec{q}\cdot\vec{r}} dv + \int_v \Delta\rho e^{-i\vec{q}\cdot\vec{r}} dv \quad (1.5)$$

For a macroscopic sample (with a very large volume compared to the X-ray/neutron wavelength), the first integral yields non-zero values only over an extremely small  $q$  range, close to  $q=0$ , that is not reached in typical SAS experiments.

$$A(\vec{q}) = \int_v \Delta\rho e^{-i\vec{q}\cdot\vec{r}} dv \quad (1.6)$$

Thus, the scattering intensity  $I(\mathbf{q})$  becomes

$$I(\vec{q}) = \int_v \int_v \Delta\rho(\vec{r}_1) \Delta\rho(\vec{r}_2) e^{-i\vec{q}\cdot(\vec{r}_1 - \vec{r}_2)} dv_1 dv_2 \quad (1.7)$$

Making  $\vec{r}_1 - \vec{r}_2 = \vec{r}$  eq. 1.7 can be written as

$$I(\vec{q}) = \int_v \int_v \Delta\rho(\vec{r}_2 + \vec{r}) \Delta\rho(\vec{r}_2) e^{-i\vec{q}\cdot\vec{r}} dv_2 dv \quad (1.8)$$

$$\text{Or } I(\vec{q}) = \int_v \gamma(\vec{r}) e^{-i\vec{q}\cdot\vec{r}} dv \quad (1.9)$$

Where

$$\gamma(\vec{r}) = \frac{1}{V} \int_v \Delta\rho(\vec{r}') \cdot \Delta\rho(\vec{r}' + \vec{r}) dv' = \overline{\Delta\rho(\vec{r}) \cdot \Delta\rho(\vec{r}' + \vec{r})} \quad (1.10)$$

The bar indicates the spatial average over the analyzed sample volume. The function  $\gamma(\mathbf{r})$  – is called correlation function<sup>16-18</sup> and is defined as the volume average of the product of  $\Delta\rho(\mathbf{r})$  in two volume elements  $dv$  located at  $\mathbf{r}_1$  and  $\mathbf{r}_2$  connected by a vector  $\mathbf{r}$ . The function  $\gamma(\mathbf{r})$  can be determined from an experimental scattering function  $I(\mathbf{q})$  by a Fourier transformation:

$$\gamma(\vec{r}) = \frac{1}{(2\pi)^3 V} \int I(\vec{q}) e^{i\vec{q}\cdot\vec{r}} dv_q \quad (1.11)$$

The correlation function  $\gamma(\mathbf{r})$  is related to the structure and can easily be determined, provided  $\rho(\mathbf{r})$  is known, by applying eq. 1.10. But, inversely, from a known  $\gamma(\mathbf{r})$  function,  $\rho(\mathbf{r})$  cannot generally be unambiguously inferred.

#### 1.4.1. Small-angle scattering by a macroscopically isotropic system

In the particular case of an isotropic system, the correlation function is independent of the direction of the vector  $\mathbf{r}$ , i.e.,  $\gamma(\mathbf{r})$  can be written as  $\gamma(r)$ . Consequently, the scattering intensity is also isotropic<sup>16-18</sup>. In this case the function  $e^{-i\mathbf{q}\cdot\mathbf{r}}$  is replaced in eq. 1.8 by its angular average for all orientations  $\langle \rangle$

$$\langle e^{-i\vec{q}\cdot\vec{r}} \rangle = \frac{\sin qr}{qr} \quad (1.12)$$

Thus, for an isotropic system, eq. 1.8 becomes

$$I(q) = V \int_0^\infty 4\pi r^2 \gamma(r) \frac{\sin qr}{qr} dr \quad (1.13)$$

And eq. 1.10 is given by

$$\gamma(r) = \frac{1}{(2\pi)^3 V} \int_0^\infty 4\pi q^2 I(q) \frac{\sin qr}{qr} dq \quad (1.14)$$

From eq. 1.10 the correlation function for  $r=0$  is

$$\gamma(0) = \frac{1}{V} \int_v \Delta\rho(\vec{r}) \cdot \Delta\rho(\vec{r}) dv = \overline{\Delta\rho(\vec{r})^2} \quad (1.15)$$

From eq. 1.15, it is evident that  $\gamma(0)$  is equal to the spatial average of the square SLD fluctuations over the whole volume. Taking the limit  $r \rightarrow 0$  in eq. 1.14, we have  $\sin(qr)/qr \rightarrow 1$

and thus the integral of the scattering intensity in reciprocal space  $Q = \int_0^\infty 4\pi q^2 I(q) dq$  becomes

equal to  $(2\pi)^3 V \gamma(0)$ . From eqs. 1.14 and 1.15, one finds that  $\gamma(0)$ ,  $Q$  and  $\overline{\Delta\rho(\vec{r})^2}$  are related

by

$$\gamma(0) = \frac{1}{(2\pi)^3 V} Q = \overline{\Delta\rho(\vec{r})^2} \quad (1.16)$$

Thus, the integral of the scattering intensity in reciprocal space,  $Q$ , is proportional to the spatial average of the square SLD fluctuations over the whole sample volume  $\overline{\Delta\rho(\vec{r})^2}$ .

#### 1.4.2. Small-angle scattering by an isotropic two-phase structure

The X-ray/neutron scattering by isotropic nanostructured systems composed of two well-defined homogeneous phases will now be described<sup>16-18</sup>. The volume fractions of the two phases are defined by  $\varphi_1$  and  $\varphi_2$  and the constant SLD within each of them are defined by  $\rho_1$  and  $\rho_2$ , respectively (Fig. 1.9a and 1.9b).

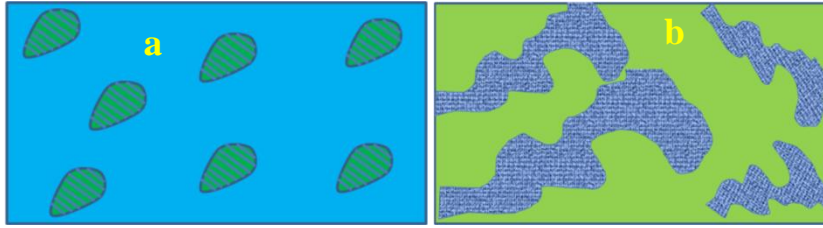


**Fig. 1.9** Schematic examples of two-phase systems (a) a set of isolated objects with a constant SLD embedded in a homogeneous matrix (b) continuous and interconnected phases, both with a constant SLD.

The correlation function  $\gamma(r)$  for an isotropic two-phase structure model can be expressed as<sup>19,20</sup>.

$$\gamma(r) = \varphi_1 \varphi_2 \rho_1 - \rho_2^2 \gamma_0(r) \quad (1.17)$$

where,  $\gamma_0(r)$  is the isotropic function named as characteristic function and only depends on the geometrical configuration of the two-phases.

If the system is composed of many isolated nano-objects with random orientations, the isotropic characteristic function is given by  $\gamma_0(r) = \langle \gamma_0(\vec{r}) \rangle$ .

Using eqs. 1.13, 1.14 and 1.17, the expressions for scattering intensity and  $\gamma_0(r)$  can be written as follows:

$$I(q) = V\varphi_1\varphi_2(\rho_1 - \rho_2)^2 \int_0^\infty 4\pi r^2 \gamma_0(r) \frac{\sin qr}{qr} dr \quad (1.19)$$

$$\gamma_0(r) = \frac{1}{(2\pi)^3 V\varphi_1\varphi_2(\rho_1 - \rho_2)^2} \int_0^\infty 4\pi q^2 I(q) \frac{\sin qr}{qr} dq \quad (1.20)$$

The characteristic function  $\gamma_0(r)$  can be defined for any type of two-density systems including those with bi-continuous geometries. It can be shown that  $\gamma_0(r)$  exhibits an asymptotic behavior within the small  $r$  range and is independent of the detailed configuration of the interfaces<sup>17</sup>

$$\gamma_0(r) = 1 - \frac{S/V}{4\varphi_1\varphi_2} r + \dots \quad r \rightarrow 0 \quad (1.21)$$

where  $S$  is total interface area of the two-density system within the sample volume  $V$ .

### 1.4.3. The integral of the scattering intensity in reciprocal space

From the expression for  $\gamma_0(r)$  (eq. 1.20) for  $r=0$  and taking into account that  $\gamma_0(0) = 1$  (eq. 1.21), the integral of the scattering intensity in reciprocal space,  $Q$ , can be written as

$$Q = \int_0^\infty 4\pi q^2 I(q) dq = (2\pi)^3 V\varphi_1\varphi_2(\rho_1 - \rho_2)^2 \quad (1.22)$$

Thus,  $Q$  only depends on the scattering length density contrast factor  $(\rho_1 - \rho_2)^2$  and on the volume fractions occupied by both phases, but not on their elaborate geometrical configuration. For example, in morphological transformations that maintain constant scattering length density and the volume fractions of both phases, even though the structure and, consequently, the shape of the scattering intensity curves vary,  $Q$  remains constant.  $Q$  (or  $Q/4\pi$ ) is often named as Porod invariant

### 1.4.4. Asymptotic behavior of scattering curves at high $q$ : Porod law

The general properties of Fourier analysis tell us that the asymptotic trend, at high  $q$ , of the scattering intensity  $I(q)$  is connected<sup>16-18</sup> to the behavior of the  $\gamma(r)$  function at small  $r$ . By taking into account eq. 1.21, the correlation function  $\gamma(r)$  can be approximated at small  $r$  by

$$\gamma(r) = \varphi_1 \varphi_2 (\rho_1 - \rho_2)^2 \left( 1 - \frac{S}{4V \varphi_1 \varphi_2} r \right) \quad (1.23)$$

This relation implies that the value of the first derivative of  $\gamma(r)$  at  $r=0$  is

$$\gamma'(0) = -(\rho_1 - \rho_2)^2 \frac{S}{4V} \quad (1.24)$$

Moreover, eq. 1.13 can be rewritten as

$$I(q) = -\frac{4\pi V}{q} \frac{d}{dq} \int_0^\infty \gamma(r) \cos(qr) dr \quad (1.25)$$

A first integration by parts of the integral in eq. 1.25 yields

$$\int_0^\infty \gamma(r) \cos(qr) dr = \frac{\gamma(r) \sin(qr)}{q} \Big|_{r=0}^\infty - \frac{1}{q} \int_0^\infty \gamma'(r) \sin(qr) dr \quad (1.26)$$

Since  $\gamma(r) \rightarrow 0$  as  $r \rightarrow \infty$  and  $\sin(qr) \rightarrow 0$  as  $r \rightarrow 0$ , the first term is equal to zero. The remaining one can be written as

$$-\frac{1}{q} \int_0^\infty \gamma'(r) \sin(qr) dr = \frac{\gamma'(r) \cos(qr)}{q^2} \Big|_{r=0}^\infty - \frac{1}{q^2} \int_0^\infty \gamma''(r) \cos(qr) dr = -\frac{\gamma'(0)}{q^2} - \frac{1}{q^2} \int_0^\infty \gamma''(r) \cos(qr) dr \quad (1.27)$$

In eq. 1.27, if  $\gamma''(r)$  is a continuous function, the second term decreases for  $q \rightarrow \infty$  faster than the first one. It has been shown that this condition is always fulfilled unless the interface surface contains portions that are parallel to each other, as it happens in the case of spheres and cylinders<sup>18-21</sup>. Assuming this condition is satisfied, Eq. 1.25 becomes

$$I(q) = -\frac{4\pi}{q} \frac{d}{dq} \left[ -\frac{\gamma'(0)}{q^2} \right] = -\frac{8\pi \gamma'(0)}{q^4} \quad (1.28)$$

and, reminding that  $\gamma'(0)$  is given by eq. 1.24, the asymptotic behavior of  $I(q)$  is given by

$$I(q) = \frac{2\pi(\rho_1 - \rho_2)^2 S}{q^4} \quad q \rightarrow \infty \quad (1.29)$$

Eq. 1.29, named as Porod law and it holds for most types of isotropic two phase systems with sharp interfaces. This equation is often applied to the study of disordered porous materials and to other two-phase systems whose relevant structure feature is the surface area.

The behavior of  $I(q)$  at high  $q$  is analyzed using a Porod plot ( $I(q)q^4$  versus  $q^4$ ) that is expected to be asymptotically constant. This plot allows one to determine (i) the asymptotic value of  $I(q)q^4$  and subsequently the interface surface area (ii) eventual positive or negative deviations from Porod law<sup>22</sup>.

The determination of the interface surface area using eq. 1.29 requires the measurement of the scattering intensity in absolute units. If the scattering intensity is only known in relative scale, it is still possible to obtain the surface area using together Porod's law (eq. 1.29) and the Porod invariant (eq. 1.22). The surface area per unit volume is then determined from

$$\frac{S}{V} = 4\pi^2 \varphi_1 \varphi_2 \frac{[I(q)q^4]_{q \rightarrow \infty}}{Q} \quad (1.30)$$

For the very particular case of identical spherical or cylindrical nano-objects, the oscillations remain, even for very high  $q$  values. In these cases, the Porod plot asymptotically show undamped oscillations superposed to a constant plateau<sup>21-24</sup>.

#### 1.4.5. Small-angle scattering of a dilute system of isolated nano-objects.

In the particular case of a dilute and isotropic system composed of a large number,  $N$ , of randomly oriented and isolated nano-objects, all having the same shape and size, the total

intensity is represented<sup>16-18</sup> as  $I(q) = \sum_{i=1}^N I_1(\vec{q})_i = N \left[ \frac{1}{N} \sum_{i=1}^N I_1(\vec{q})_i \right]$  (1.31)

The intensity  $I(q)$  is  $N$  times the individual intensity  $I_1(q)$  produced by one nano-object of volume  $V_1$  averaged for all orientations:  $I(q) = N \langle I_1(\vec{q}) \rangle$ . Thus, one can derive the scattering intensity,  $\langle I_1(q) \rangle$ , from the characteristic function for a single object averaged for all orientations,  $\gamma_0(r) = \langle \gamma_0(\vec{r}) \rangle$ , both functions being connected through a Fourier transformation (eq. 1.14). The spherically averaged characteristic function,  $\gamma_0(r)$ , for a single isolated and

homogeneous object with an SLD  $\rho_1$  embedded in an also homogeneous matrix with a density  $\rho_0$ , has the following properties<sup>17</sup>:

i) It can be expressed as

$$\gamma_0(r) = \frac{\gamma(r)}{N(V_1/V)(\rho_1 - \rho_0)^2} \quad (1.32)$$

ii) It is a positive and decreasing function.

iii) The asymptotic behavior, at low  $r$ , can be approximated by

$$\gamma_0(r) = 1 - \left( \frac{S_1}{4V_1} \right) r \quad \text{where } S_1 \text{ and } V_1 \text{ are the object surface area and volume, respectively.}$$

iv)  $\gamma_0(r) = 0$  for  $r > D_{\max}$ ,  $D_{\max}$  being the maximum diameter of the scattering object.

(v) The volume integral of  $\gamma_0(r)$  is  $\int_0^{D_{\max}} 4\pi r^2 \gamma_0(r) dr = V_1$

(vi) The scattering intensity is given by

$$I_1(q) = \langle I_1(\vec{q}) \rangle = (\rho_1 - \rho_0)^2 V_1 \int_0^{D_{\max}} 4\pi r^2 \gamma_0(r) \frac{\sin qr}{qr} dr \quad (1.33)$$

The properties of  $\gamma_0(r)$  for a spherically averaged single object, listed above, were derived from the general characteristics of the  $\gamma_0(r)$  function for arbitrary isotropic two phase systems, assuming the basic conditions underlying to an isolated nano-object immersed in a macroscopic volume, namely  $\phi_1 = NV_1/V$  and  $\phi_2 \approx 1$ .

### (a) Scattering intensity at $q=0$

From eq. 1.33 and taking into account the property mentioned in the previous section, the extrapolated value to  $q=0$  of the scattering intensity produced by a single nano-object and by a dilute set of  $N$  identical objects are, respectively, given by<sup>16-17</sup>

$$I_1(0) = (\rho_1 - \rho_0)^2 V_1^2 \quad \text{and} \quad I(0) = NI_1(0) = N(\rho_1 - \rho_0)^2 V_1^2 \quad (1.34)$$

The differences in the X-ray/neutron path length in the forward scattering direction ( $q=0$ ), associated to the wavelets scattered by each scatterers inside a nano-object, is zero. Consequently, all of them scatter in phase so that the amplitude is  $A_1(0) = \Delta n$ ,  $\Delta n$  being the excess in number of scatterer inside the objects with respect to the matrix. Thus, the scattering intensity results  $I_1(0) = [A_1(0)]^2 = \Delta n^2$  which is equivalent to eq. 1.34.

The invariant  $Q$ , for a dilute set of nano-objects of same size and shape, becomes  $Q = 8\pi^3 N (\rho_1 - \rho_2)^2 V_1$ . Thus, the volume  $V_1$  can be derived, regardless the object shape, from the quotient  $I(0)/Q$  as follows  $V_1 = 8\pi^3 \frac{I(0)}{Q}$

### (b) Asymptotic trend of the scattering intensity at small $q$ : Guinier law

The scattering intensity produced by a dilute set of  $N$  identical and randomly oriented nano-objects is  $N$  times the intensity scattered by one object with maximum size  $D_{\max}$  averaged for all orientations,  $I_1(q)$ , (eq. 1.33) so that

$$I(q) = N(\rho_1 - \rho_0)^2 V_1 \int_0^{D_{\max}} 4\pi r^2 \gamma_0(r) \frac{\sin qr}{qr} dr \quad (1.35)$$

$\sin(qr)/qr$  factor in eq. 1.35 can be substituted, for small  $q$ , by its approximated form  $(\sin qr)/qr = 1 - (q^2 r^2/6) + \dots$  keeping only two first term of the series, eq. 1.35 becomes

$$I(q) = N(\rho_1 - \rho_0)^2 V_1 \int_0^{D_{\max}} 4\pi r^2 \gamma_0(r) \left(1 - \frac{q^2 r^2}{6}\right) dr \quad (1.36)$$

eq. 1.36 can be rewritten as

$$I(q) = N(\rho_1 - \rho_0)^2 V_1^2 \left[ 1 - \frac{q^2}{6} \frac{1}{V_1} \int_0^{D_{\max}} 4\pi r^4 \gamma_0(r) dr \right] = N(\rho_1 - \rho_0)^2 V_1^2 \left[ 1 - \frac{q^2}{3} R_g^2 \right] \quad (1.37)$$

$$\text{Where } R_g = \left[ \frac{1}{2V_1} \int_0^{D_{\max}} 4\pi r^4 \gamma_0(r) dr \right]^{1/2} \quad (1.38)$$

$R_g$  being the radius of gyration with respect to the “centre of mass” of the scattering length density function that is defined for homogenous object as<sup>16-17</sup>

$$R_g = \left[ \frac{1}{V_1} \int_{V_1} r^2 dv \right]^{1/2} \quad (1.39)$$

Since the parabolic shape of  $I(q)$  within the small  $q$  range (eq. 1.37) is also described by the first two terms of the series representing a Gaussian function, the scattering intensity in the limit of small  $q$  can be written as

$$I(q) = N(\rho_1 - \rho_0)^2 V_1^2 e^{-\frac{R_g^2 q^2}{3}} \quad (1.40)$$

This is the well known Guinier law<sup>16</sup>. Guinier plots of the scattering intensity ( $\log I$  versus  $q^2$ ) are commonly used in order to derive the radius of gyration  $R_g$  from the slope of the straight line that is experimentally observed within a more or less wide  $q$  range at small  $q$ . This linear plot is also used to determine extrapolated scattering intensity  $I(0)$ . Guinier law also holds for dilute sets of objects with arbitrary and variable SLD  $\rho(r)$  embedded in a homogeneous matrix with density  $\rho_0$ . In this case the radius of gyration  $R_g$  is defined as<sup>16-17</sup>

$$R_g = \left[ \frac{\int_{V_1} \rho(\vec{r}) r^2 dv}{\int_{V_1} \rho(\vec{r}) dv} \right]^{1/2} \quad (1.41)$$

The radius of gyration of a homogeneous and spherical object is related to its radius  $R$  by

$$R_g = \sqrt{3/5} R.$$

### (c) Small-angle scattering by a dilute system of nano-objects of simple geometry

The scattering intensity produced by two types of nanostructured materials consisting of a dilute set of colloidal particles embedded in a homogeneous matrix<sup>16-17</sup> will be discussed in this section. These systems are (i) nano-objects of constant SLD  $\rho_1$  embedded in a matrix

with a constant SLD  $\rho_0$  and (ii) nano-objects with a centro-symmetrical SLD, defined by its density function  $\rho(r)$  and embedded in a homogeneous matrix of SLD  $\rho_0$ .

### Homogeneous spherical nano-objects embedded in a homogeneous matrix

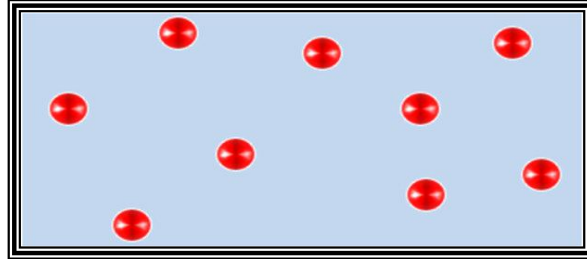


**Fig. 1.10** Ensemble of spherical nano-objects embedded into homogenous matrix in dilute limit.

The total scattering intensity produced by a dilute set of  $N$  identical homogeneous objects with SLD  $\rho_1$  embedded in a homogeneous matrix with density  $\rho_0$  is  $N$  times the scattering intensity produced by each nano-object. The scattering intensity produced by a single sphere can be derived<sup>25</sup> from the amplitude  $A_1(q)$  as follows

$$I_1(q) = |A_1(q)|^2 = \left| (\rho_1 - \rho_0) \int_0^R 4\pi r^2 \frac{\sin qr}{qr} dr \right|^2 \quad (1.42)$$

The eq. 1.42 becomes

$$I_1(q) = (\rho_1 - \rho_0)^2 \left( \frac{4\pi R^3}{3} \right)^2 F_s(qR)^2 \quad (1.43)$$

$$\text{Where } F_s(qR) = 3 \left( \frac{\sin qR - qR \cos qR}{(qR)^3} \right) \quad (1.44)$$

For  $N$  identical spheres:

$$I(q) = N I_1(q) = N (\rho_1 - \rho_0)^2 V_p^2 F_s(q, R)^2 \quad (1.45)$$

The  $F_s^2(q, R)$  is said to be form factor  $P(q, R)$ .

It is to be noted that  $I(q)$  in the above equation is microscopic cross section  $d\sigma/d\Omega$ .

The Macroscopic cross section  $d\Sigma/d\Omega$  can be defined as microscopic cross section per unit

$$\text{sample volume } \frac{1}{V} \frac{d\sigma}{d\Omega}$$

The eq. 1.45 transforms into

$$I(q) = \frac{N}{V} (\rho_1 - \rho_0)^2 V_p^2 P(q, R) \quad (1.46)$$

Where  $I(q)$  is the scattering intensity from per unit sample volume and  $V_p$  is the volume of the nano-object. Intensity functions predicted by eq. 1.46 are plotted in Fig. 1.11 for two sphere radii, namely  $R_1=10$  nm and  $R_2=20$  nm. As expected, the intensity  $I(0)$  (being proportional to  $R^6$ ) is higher for the larger sphere. At high  $q$  the intensity functions exhibit several maxima and zeros, the zeros being located at  $qR=4.52, 7.54, 10.87, \dots$ . These oscillations were actually observed in a number of experimental SAS studies of monodisperse or nearly monodisperse systems.

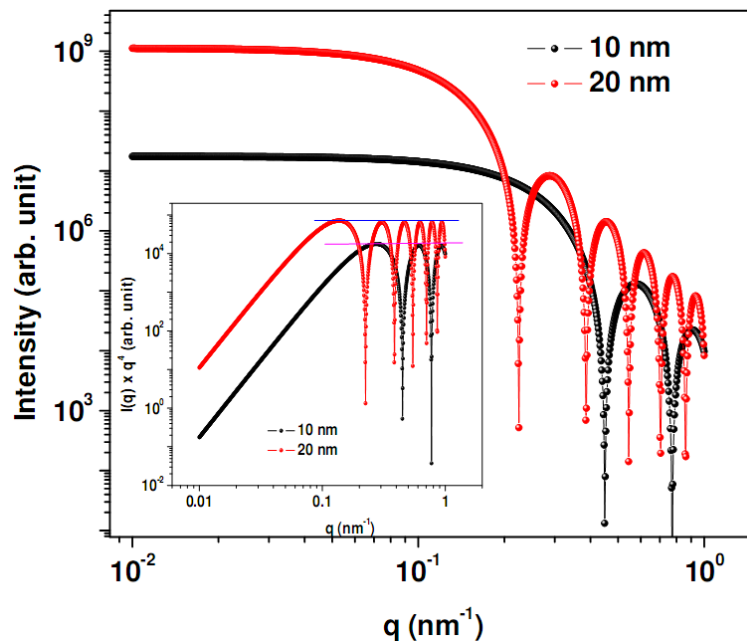


**Fig. 1.11** *The modeled scattered intensity from a monodisperse spheres of 10 and 20 nm. Inset shows the Porod plot of the scattered intensity.*

### Form factor of a spherical shell

Form factor for a spherical shell is obtained by subtracting the empty core with a proper weighting by the volumes:

$$P_{ss}(q) = F_{SS}(q)^2 = \left[ \frac{V(R_1)F_s(q, R_1) - V(R_2)F_s(q, R_2)}{V(R_1) - V(R_2)} \right]^2 \quad (1.47)$$

where  $V(R) = 4\pi R^3/3$  and  $R_1$  and  $R_2$  are the outer and inner radius of the shell, respectively.

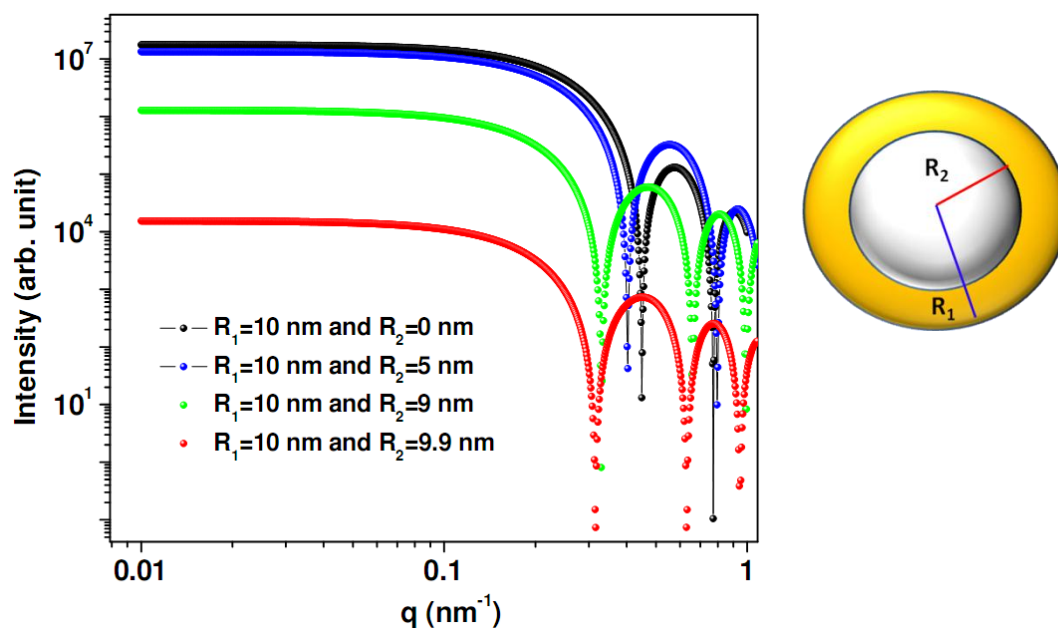
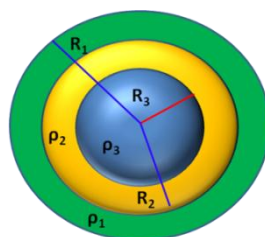


**Fig. 1.12** The modeled scattered intensity for the ensemble of concentric shell of varying inner and outer radius.

### Form factor of a concentric spherical shell

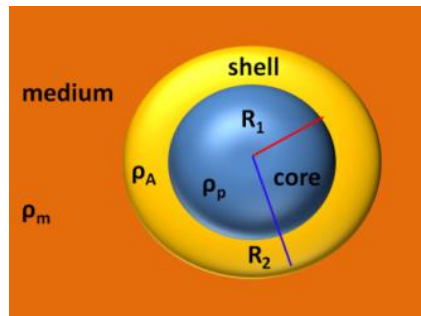


This form factor is a generalization of the shell form factor. Let  $R_i$ ,  $i=1, N$  be the radii of the shells and  $\rho_i$  be their scattering densities. With this:

$$P_{cs}(q) = F_{cs}(q)^2 = \left[ \frac{1}{M} \left\{ \rho_1 V(R_1) F_s(q, R_1) + \sum_{i=2}^N (\rho_i - \rho_{i-1}) V(R_i) F_s(q, R_i) \right\} \right]^2 \quad (1.48b)$$

where  $M$  is the scattering mass or scattering volume of the particle, given by:

$$M = \rho_1 V(R_1) + \sum_{i=2}^N V(R_i) (\rho_i - \rho_{i-1})$$



Similarly, the form factor for a core-shell particle in medium can be estimated as follows:

$$P_{csm}(q) = F_{csm}(q)^2 = \left[ \frac{(\rho_A - \rho_m) V(R_2) F_s(q, R_2) - V(R_1) F(q, R_1) + (\rho_p - \rho_m) V(R_1) F(q, R_1)}{(\rho_A - \rho_m) V(R_2) - V(R_1) - (\rho_p - \rho_m) V(R_1)} \right]^2 \quad (1.48b)$$

where,  $\rho_p$ ,  $\rho_A$ ,  $\rho_m$  are the SLD of the core, shell and medium respectively.  $R_1$  and  $R_2$  is inner and outer radius of the core-shell particle.  $V(R_1)$  and  $V(R_2)$  are the volumes of spheres having radius  $R_1$  and  $R_2$ .

### Form factor of ellipsoid of revolution

This expression was determined by Guinier<sup>26</sup>. The averaging over orientations has to be done numerically. For the semi axes  $R$ ,  $R$ ,  $\epsilon R$ :

$$P_{er}(q, R, \epsilon) = \int_0^{\pi/2} F_s^2[q, r(R, \epsilon, \alpha)] \sin(\alpha) d\alpha \quad (1.49)$$

Where  $r(R, \epsilon, \alpha) = R(\sin^2\alpha + \epsilon^2 \cos^2\alpha)^{1/2}$ . It is straight forward to generalize for concentric

elliptical shells.  $F_S(q, r)$  has to be replaced by  $F_{cs}(q)$  in which the volumes are  $V(R) = 4\pi\epsilon R^3/3$ .

Note, that the different shells can have different values of  $\epsilon$ .

### Form factor of a cylinder



The expression for a cylinder with radius  $R$  and length  $L$  was given by Fournet<sup>27</sup>.

$$P_{cyl}(q) = \int_0^{\pi/2} \left[ \frac{2B_1(qR \sin \alpha)}{qR \sin \alpha} \frac{\sin((qL \cos \alpha)/2)}{(qL \cos \alpha)/2} \right] \sin \alpha d\alpha \quad (1.50)$$

where  $B_1(x)$  is the first order Bessel functions. An expression for form factor of the cylinders consisting of concentric shells can be constructed by an approach similar to the one used for spherical particles.

### Isotropic system of polydisperse nano-objects with simple shapes

The scattering intensity function related to a dilute set of  $N$  spherical nano-objects with a radius distribution defined by  $N(R)$  is calculated by solving the following equation:

$$I(q) = \int N(R) I_1(q, R) dR \quad (1.51)$$

where  $N(R)dR$  is the number of spheres with a radius between  $R$  and  $R+dR$

with normalisation  $\int N(R) dR = N$  and  $I_1(q, R)$  is the scattering intensity produced by an isolated sphere. Thus the total scattering intensity is

$$I(q) = (\rho_1 - \rho_2)^2 \left( \frac{4\pi}{3} \right)^2 \int N(R) R^6 \left[ 3 \frac{\sin qR - qR \cos qR}{q^3 R^3} \right]^2 dR \quad (1.52)$$

The calculated intensity from eq. 1.52 for different size distributions is depicted in Fig. 1.13.

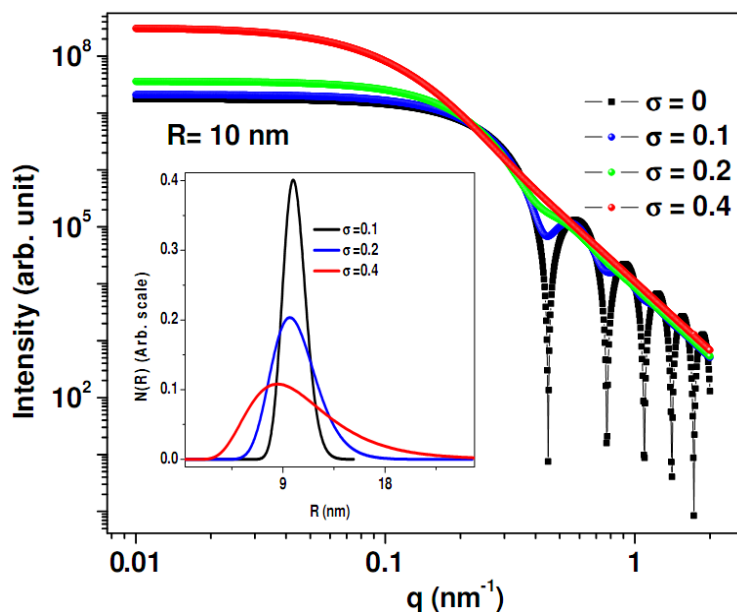


**Fig. 1.13** The models scattered intensity from an ensemble of polydisperse spheres of median size 10 nm with varying polydispersity index  $\sigma$ . Inset shows radius distribution.

#### 1.4.6. Small-angle scattering of a concentrated set of nano-objects

Many nano-materials consist of a concentrated set of isolated nano-objects embedded in a homogeneous matrix, e.g., colloidal sols (solid nano-clusters embedded in a liquid matrix) and nano hybrid materials (solid inorganic clusters embedded in a solid polymeric matrix). Often these systems cannot be considered as dilute in the sense that the scattering intensity is not simply given by  $I(q)=N \times I_1(q)$  over the whole  $q$  range. It will be described in this section that how to analyze SAS results corresponding to materials whose structure can be described by simple models, namely (i) concentrated systems composed of isolated nano-objects with spherical shape and (ii) fractal structures built up by the aggregation of primary nano-objects in solid or liquid solutions.

##### (a) The hard sphere model

For a concentrated system of  $N$  of nano-objects,  $I(q)=N \langle I_1(\mathbf{q}) \rangle$  does no longer apply over the whole  $q$  range. In the case of simple isotropic systems consisting of centro-symmetrical and

spatially correlated objects, it is possible to decouple the function defining the  $q$  dependence of the total scattered intensity  $I(q)$  in two terms: the intensity produced by an isolated object,  $I_1(q)$  and the structure function,  $S(q)$ , which accounts for interference effects between the elementary scattered wavelets from different objects. Thus, the scattering intensity expected from this model can be written as

$$I(q) = N I_1(q) S(q) \quad (1.53)$$

Eq. 1.53 is rigorously obeyed only when the scattering system is composed of identical spheres (more generally centro-symmetrical objects). For dilute systems,  $S(q) = 1$  holds over the whole  $q$  range. The structure factor corresponding to an isotropic set of spherical objects is given by<sup>16</sup>

$$S(q) = 1 + \frac{1}{V_p} \int_0^\infty g(r) - 1 \ 4\pi r^2 \frac{\sin qr}{qr} dr \quad (1.54)$$

where  $V_p = V/N$  is the volume available per object and  $g(r)$  is a function defined in such a way that  $4\pi r^2 g(r) dr / V_p$  yields the average number of nano-objects,  $N(r)$ , at a distance between  $r$  and  $r+dr$  from an object located at the origin. From this definition, we find that  $g(r)$  is equal to 1 corresponds to a random spatial distribution. For a set of completely disordered objects  $g(r) = 1$  for all  $r$ . For any type of system with short-range correlation,  $g(r)$  tends to 1 in the high  $r$  limit.

The particles interact with the hard-sphere radius ( $R_{HS}$ ) and have a hard-sphere volume fraction  $\Phi_v$ . The expression for  $S(q)$  has been estimated with the Percus-Yevick approximation<sup>29-32</sup>:

$$S_{HS}(q) = \frac{1}{1 + 24\Phi_v G(R_{HS}q) / (R_{HS}q)} \quad (1.55)$$

The function  $G(R_{HS}q)$  is available in the literature.

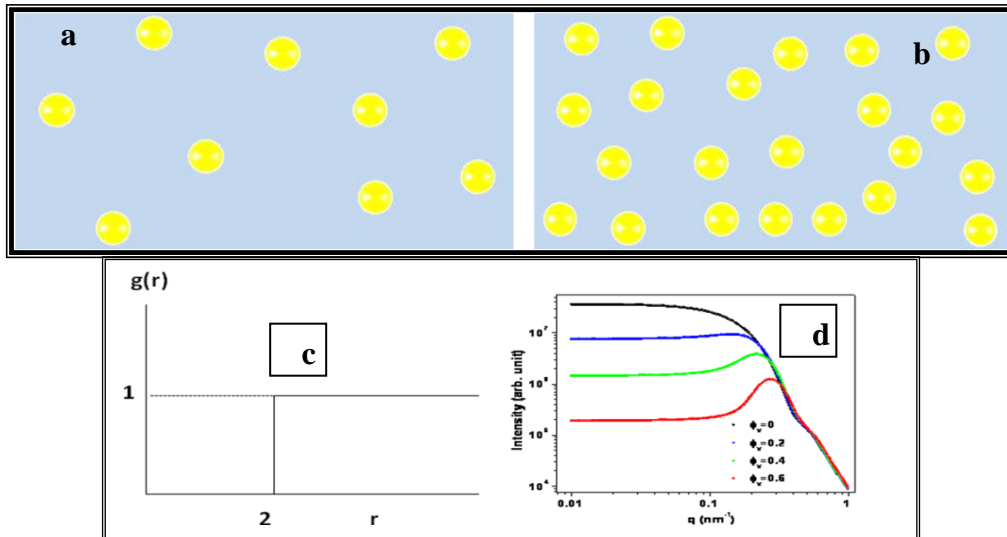


**Fig. 1.14** Schematic of systems of hard spheres (a) dilute (b) concentrated (c)  $g(r)$  function for the hard sphere model (d) Scattering intensity determined using eq. 1.53 with  $S(q)$  defined by eq.1.55, for different volume fractions  $\Phi_v$  starting from 0 (top) up to 0.6 (bottom).

### (b) Sticky hard-sphere potential

The model was introduced by Baxter<sup>33</sup>. The particles have a hard-sphere radius  $R_{HS}$  and a delta function attractive potential at the surface. The stickiness of the particles is given by a parameter. The expressions for the structure factor can be calculated with the Percus-Yevick approximation<sup>33</sup>.

### (c) Fractal structures

The fractal model has been applied to describe the structure of many materials generated by aggregation processes in a liquid or solid medium. Many sols that have been investigated by small-angle scattering in situ exhibit this type of structure<sup>18</sup>. Fractal objects can be characterized by three relevant structural parameters<sup>18</sup>: (i) a radius  $r_0$ , which corresponds to the size of the individual primary particles (basic nano-objects that build up the fractal structure) (ii) a fractal dimension  $D$  that depends on the mechanism of clustering or aggregation and (iii) a correlation length  $\xi$  that defines the whole aggregate size if the fractal

objects are isolated or a cut-off distance of the fractal structure for percolated systems such as fractal gels.

For a homogenous object or for a fractal aggregate, such as those schematically illustrated in Fig. 1.15a and 1.15b, respectively, the total number of primary objects or building blocks  $N$  located inside a sphere of radius  $r$ , measured from the center of mass, is given by

$$N(r) = \left( \frac{r}{r_0} \right)^D \quad (1.56)$$

This equation implies that the mass function  $M(r)$  is also proportional to  $r^D$ .

The exponent in eq. 1.56 for homogeneous objects is  $D=3$ , while  $D<3$  for fractal structures. The value of  $D$  depends on the particular mechanism of aggregation. Many mechanisms were theoretically analyzed and the respective fractal dimensions of the resulting structures were determined. This implies that the experimental evaluation of the dimension  $D$  may yield a useful insight about the predominant mechanism that governs the aggregation process<sup>18</sup>.

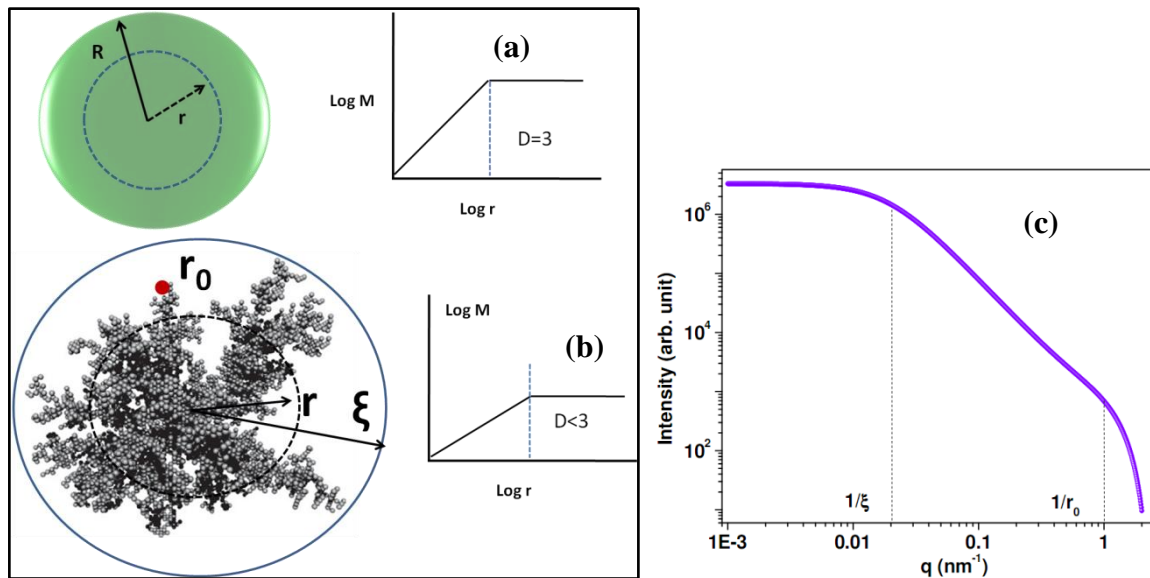


**Fig. 1.15** (a) Schematic log-log plot of the mass  $M(r)$  of a homogeneous object (b) the same for a fractal object (c) scattering intensity corresponding to a fractal object with  $r_0=2$  nm,  $\xi=50$  nm and  $D=2.2$ .

In order to define the radial distribution function  $g(r)$  associated to a fractal structure, Sinha *et al.*<sup>34</sup> included a cut-off function that makes the number density of primary objects at high  $r$  to be equal to the average number density. Later on, Chen and Teixeira<sup>35</sup> have used the general theory of liquids in order to define the function  $g(r)$  as follows

$$\frac{N}{V} g(r) = \frac{N}{V} + \left( \frac{D}{4\pi r_0^D} r^{D-3} \right) e^{-\frac{r}{\xi}} \quad (1.57)$$

Thus, substituting eq. 1.57 in the eq. 1.54, the structure function  $S(q)$  becomes

$$S(q) = 1 + \frac{1}{(qr_0)^D} \frac{D\Gamma(D-1)}{\left[1 + 1/(q^2\xi^2)\right]^{(D-1)/2}} \sin\left[(D-1)\tan^{-1}(q\xi)\right] \quad (1.58)$$

Since the primary particles are much smaller than the fractal aggregates,  $I_1(q)$  is a constant within a wide  $q$  range, so as the variation of the scattering intensity at small and intermediate  $q$  is dominated by the structure function. At high  $q$ ,  $S(q)$  becomes a constant and so, over this  $q$  range, the variation in the scattering intensity is governed by  $I_1(q)$ .

If the condition  $r_0 \gg \xi$  is obeyed, the scattering intensity exhibits three distinct  $q$  dependences over different  $q$  ranges (Fig. 1.15c). The main features of the scattering curves are directly and simply connected to the relevant structure parameters of the fractal nano-objects as shown in Fig. 1.15b. It is a general consensus that, in order to safely establish the fractal nature of the aggregates, the ratio  $\xi/r_0$  should be larger than about 10.

### 1.5. Small angle scattering: Instrumental considerations

The small angle scattering instruments are primarily based on either neutron or X-rays as a probe. Table 1.2 shows the typical parameters of the neutron and X-ray sources. The instruments for SAS are designed in view of the above parameters. The SANS instruments are basically low flux and low resolution instruments and ideal for hydrogen containing specimens due to isotope labeling. However, the instruments based on X-rays are high flux and high resolution especially synchrotron based instrument. The various *in-situ* experiments

can be performed on X-rays based SAS instrument which is not otherwise possible in neutron based instruments.

**Table 1.2** Typical values of brightness & fluxes for neutron & X-ray sources

	<b>Brightness</b> ( $\text{s}^{-1} \text{m}^{-2} \text{mrad}^{-2}$ )	<b>Energy resolution</b>  den/E  (%)	<b>Divergence</b>  ( $\text{mrad}^2$ )	<b>Flux</b>  ( $\text{s}^{-1} \text{m}^{-2}$ )
<b>Neutrons</b>	$10^9$	2	10 x 10	$10^{11}$
<b>Rotating Anode</b>	$10^{10}$	3	0.5 x 10	$5 \times 10^{10}$
<b>Bending Magnet</b>	$10^{18}$	0.01	0.1 x 5	$5 \times 10^{17}$
<b>Undulate</b>	$10^{27}$	0.01	0.01 x 0.1	$10^{24}$
Flux=brightness*divergence; brilliance=brightness/energy bandwidth				

### 1.5.1. Laboratory based SAXS instrument

In a SAXS instrument a monochromatic beam of X-ray is incident on a sample from which some of the X-rays get scattered, while most simply go through the sample without interacting with it. The scattered X-rays form a scattering pattern which is then detected at a detector (typically a 2-dimensional X-ray detector situated behind the sample perpendicular to the direction of the primary beam) that initially hit the sample. The scattering pattern contains the information on the structure of the sample. In SAXS, the non-scattered beam that merely travels through the sample must be blocked without blocking the closely adjacent scattered radiation. Most available X-ray sources produce divergent beams and this compounds the problem. In principle, the problem could be overcome by making beam parallel by a multilayer parabolic mirror (Gobble mirror) in conjunction with slit collimation.

A schematic of typical laboratory based SAXS instrument is shown in Fig. 1.16. Laboratory SAXS instruments can be divided into two main groups:

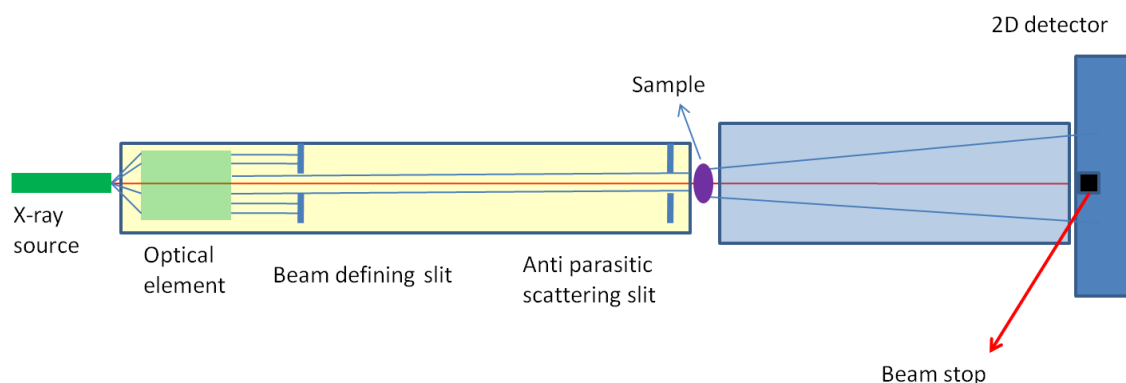


**Fig. 1.16** A schematic of typical SAXS instrument is shown.

Point-collimation instruments have pinholes that shape the X-ray beam to a small circular or elliptical spot that illuminates the sample. Thus, the scattering is centro-symmetric about the primary X-ray beam and the scattering pattern in the detection plane consists of circles around the primary beam. Owing to the small illuminated sample volume and the wastefulness of the collimation process — only those photons are allowed to pass that happen to fly in the right direction — the scattered intensity is small and therefore the measurement time is in the order of hours or days in case of very weak scatterers. If focusing optics like bent mirrors or bent monochromatic crystals or collimating and monochromating optics like multilayers are used, measurement time can be greatly reduced. Point collimation geometry allows one to investigate non-isotropic systems such as fibers, sheared liquids.

Line-collimation instruments confine the beam only in one dimension so that the beam profile is a long but narrow line. The illuminated sample volume is much larger compared to that in point-collimation and the scattered intensity at the same flux density is proportionally larger. Thus measuring times with line-collimation SAXS instruments are much shorter compared to point-collimation and are in the range of minutes. A disadvantage is that the recorded pattern is essentially an integrated superposition (a self-convolution) of

many pinhole patterns. The resulting smearing can be easily removed using model-free algorithms or deconvolution methods based on Fourier transformation, but only if the system is isotropic. Line collimation is of great benefit for any isotropic nanostructured materials, e.g., proteins, surfactants, particle dispersion and emulsions.

### 1.5.2. Synchrotron based SAXS instrument

A layout of the synchrotron based SAXS beam line<sup>36a</sup> that is proposed at INDUS-2 synchrotron source at RRCAT, Indore, India is shown in Fig. 1.17.

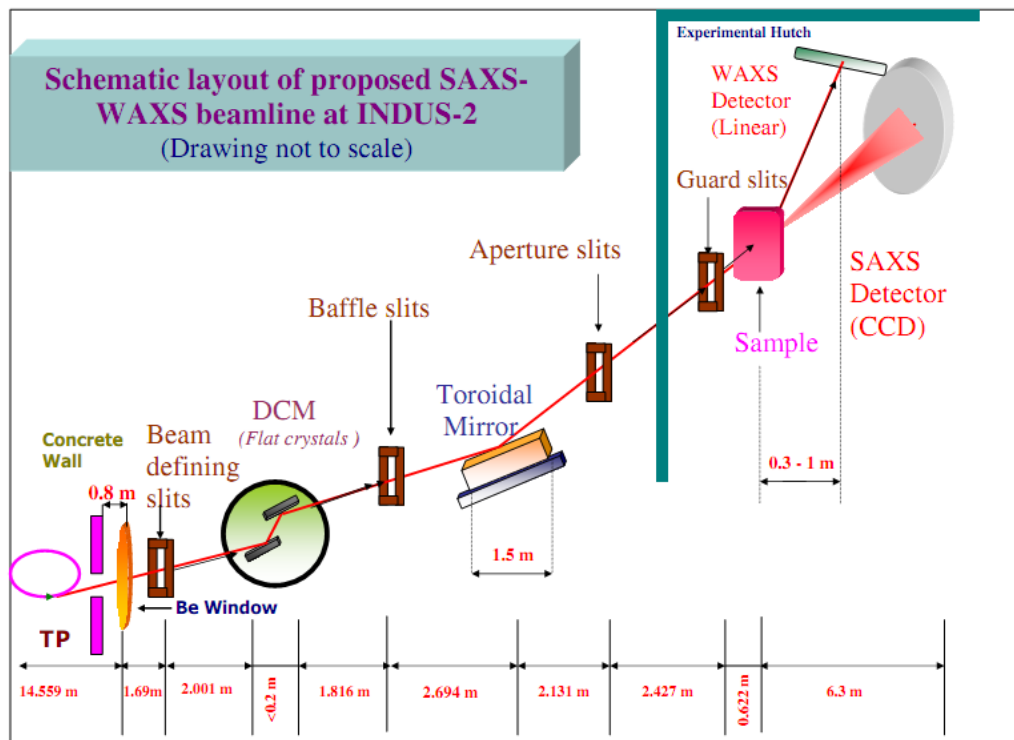


**Fig. 1.17** Schematic of the proposed SAXS beamline, at INDUS-2 synchrotron at RRCAT Indore, India, is presented.

The white synchrotrons beam emerging from electron storage ring hits the first optical element, i.e., double crystal monochromator, selects the X-ray wavelength keeping the exit height of the beam fixed. The monochromatic beam falls on the toroidal mirror which focuses the 2 dimensional X-ray beam on the detector. The useful energy range is from 5 KeV to 20

KeV. The sample to detector distance will be varied to modify the experimental q-range. The important parameters are shown in Table 1.3 as estimated by SHADOWVUI calculations.

**Table 1.3** Parameters for SAXS beamline at 8 keV X-ray energy (SHADOWVUI)

	Flux density (photon/sec/mm <sup>2</sup> )	Beam size		Beam divergence	
		FWHM (x) (mm)	FWHM (y) (mm)	FWHM (x <sub>p</sub> ) (mrad)	FWHM (y <sub>p</sub> ) (mrad)
Source	8.03 x 10 <sup>17</sup>	0.96	0.47	1.97	0.13
1 <sup>st</sup> Crystal	3.16 x 10 <sup>15</sup>	35.22	2.25	1.97	0.17
2 <sup>nd</sup> crystal	3.29 x 10 <sup>10</sup>	35.36	2.25	1.97	0.13
Mirror	1.55 x 10 <sup>10</sup>	43.84	2.76	1.97	0.13
Sample	3.30 x 10 <sup>10</sup>	18.64	2.91	2.94	0.36
Farthest position of detector	7.48 x 10 <sup>12</sup>	0.52	0.46	2.94	0.36

### 1.5.3. SANS instruments

#### Typical pin-hole based instrument

Four steps used in all SANS techniques (as shown in Fig. 1.18<sup>36b</sup>) are following: (1) Monochromatisation is performed mostly using a velocity selector/crystal. (2) Collimation is performed through the use of two apertures (a source aperture and a sample aperture) placed far (meters) apart. (3) Scattering of the monochromatic collimated beam is from sample

liquid or solid. (4) Detection is performed using a neutron area detector inside an evacuated scattering vessel.

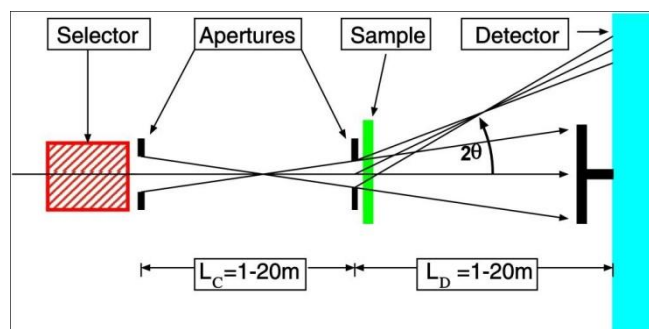


**Fig. 1.18** Schematic of a typical SANS instrument is shown.

The large collimation and scattering lengths make SANS instruments very long (typically 30 m long) compared to other scattering instruments. The collimation usually consists of a set of circular (source and sample) apertures that converges the neutron beam onto the detector. Typical adjustable flight path distances are from 1 m to 20 m depending on resolution and intensity considerations. The post sample flight path is usually an evacuated cylindrical tube (to avoid scattering from nitrogen in air) that permits the translation of an area detector along rails in order to change the sample-to-detector distance. The area detector is often a gas detector with 0.5 cm to 1 cm resolution.

### **Double crystal based instrument**

The typical maximum accessible length scale for a pinhole collimation instrument is  $\sim 10^2$  nm. But large inhomogeneities as commonly encountered in cements, ceramics, macromolecules, magnetic domains are beyond the resolution limit of the conventional pinhole collimation instrument. To access larger length scales, non-dispersive (1, -1) double crystal based instrument is used. The sample is placed between the two crystals, and the scattering profiles of the specimens are recorded by rotating one crystal against other. The instrument consists

of a non-dispersive (1, -1) setting of (111) reflections of silicon single crystals with sample between the two crystals. The schematic of a double crystal based instrument installed at Guide Tube Laboratory of Dhruva reactor, India<sup>36,37</sup> is shown in Fig. 1.19.

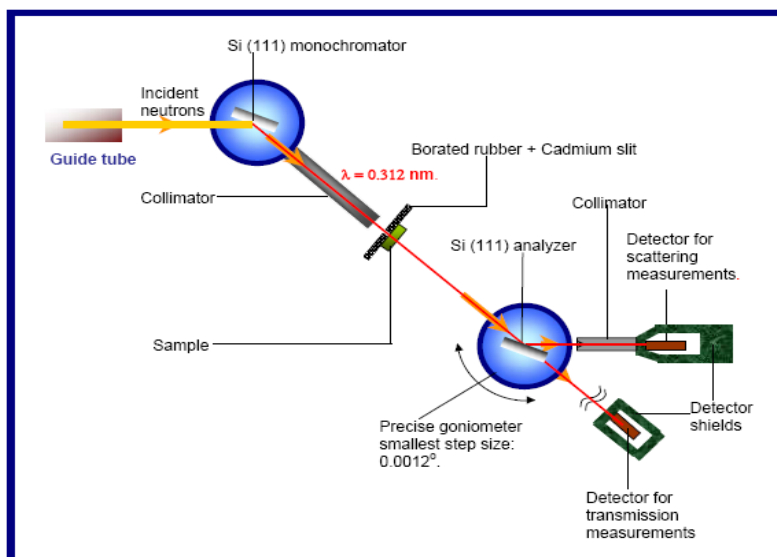


**Fig. 1.19** Schematic of MSANS instrument at Guide Tube laboratory of Dhruva reactor, India.

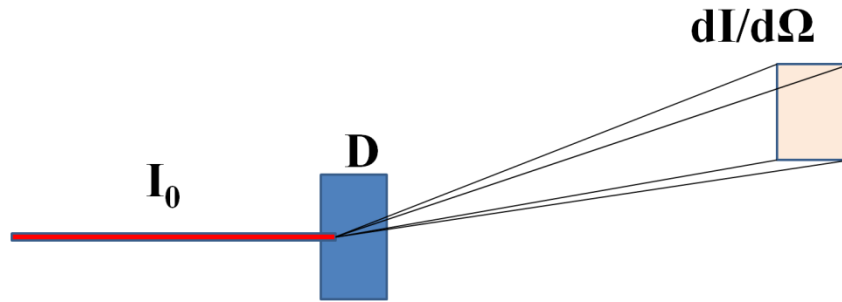
In this kind of double crystal based instruments, unlike pinhole collimation instruments, the collimation is performed in the reciprocal space only and the resolution in  $q$  is independent of the beam cross section. Because of the non-dispersive setting of both the crystals, the width of the rocking curve is independent of the divergence of the incoming beam.

#### 1.5.4. Smearing effects in SAS measurements

Experimentally measured scattering data differ from theoretical curves because of departures from point geometry in a real instrument. In a small-angle scattering instrument, there are three contributions to the smearing of an ideal curve: (1) the angular divergence of the beam; (2) the finite resolution of the detector; and (3) the polychromatic nature of the beam<sup>38</sup>. Various methods which are available in literature can be used to correct the smearing effects<sup>39-42</sup>.

### 1.5.7. Absolute intensity/scattering cross section

The SAS data normalized for scattering cross-section per unit sample volume is termed as "absolute intensity  $\frac{d\Sigma}{d\Omega}(q)$ ". The absolute intensity scale for the SAS data is sample characteristic dependent only and is independent of probing flux, sample volume etc.



SAS data in the absolute scattering scale requires many details during the measurement. In experimental measurements, the neutrons/photons collected by the detector per second, namely, the measured scattering intensity  $I_m(q)$  from a sample is proportional to factors like (i) the incident beam intensity  $I_0$ ; (ii) the scattering differential cross-section per unit volume of the sample  $\frac{d\Sigma}{d\Omega}(q) = \frac{1}{V} \frac{d\sigma}{d\Omega}(q)$  ( $\text{cm}^{-1}$ ); (iii) the sample exposure area  $A$  (usually the beam size); (iv) sample thickness  $t$ ; (v) sample transmission  $\tau$ ; (vi) the solid angle  $\Delta\Omega$  subtended by the detector pixel at the sample; (vii) the detector efficiency  $e$  and can be expressed as

$$I_m(q) = I_0 e A t \tau \frac{d\Sigma}{d\Omega} d\Omega \longrightarrow \frac{d\Sigma}{d\Omega} = \frac{1}{I_0 e A t \tau} \frac{I_m(q)}{d\Omega} \left[ \text{cm}^{-1} \text{sterad}^{-1} \right] \quad (1.59)$$

During the data reduction, one often use a standard sample of known  $\frac{d\Sigma}{d\Omega}$  to deduce the common instrument factor  $f$  ( $= I_0 A \Delta\Omega e$ ), using the  $I_m(q)$  measured under a specific instrumental setting. Sample thickness and transmission can be measured. Water is well suited as a calibration standard because of the angle-independent scattering<sup>43</sup>.

# Probing Mesoscopic Morphology of Euclidean Nano-ceramics Aggregates

Present chapter deals with the SAS investigations of non-fractal, i.e., Euclidian aggregates of various important nano-ceramics. The nano-ceramics which are covered in this chapter are NiO, YCrO<sub>3</sub>, TiO<sub>2</sub> and TiO<sub>2</sub>-carbon nanotube composites.

### 2.1. Evolution of Pore Morphology in the NiO Aggregates

#### 2.1.1. Introduction

The Ultra-fine NiO nano-ceramic particles with a uniform size are strongly desirable for many applications, e.g., synthesis of composite materials, magnetic, electro chromic, heterogeneous catalytic materials etc. However, the functional properties of NiO and its applicability significantly depend on factors like pore morphology, pore matrix-interface and also porosity.

Sintering is a process that controls porosity and pore morphology in ceramics. Sintering is a process that bonds particles together into a solid coherent structure by means of mass transport mechanism. Initial virgin powder possesses large surface area relative to its volume. This surface area/surface energy provides the driving force for sintering, i.e., reduction of free surface energy occurs due to high surface area of particles<sup>9</sup>. Pore-size distribution and pores connectivity of particles evolve with heat treatment temperature and time. In the case of sintering, the porosity shrinkage is mainly governed by the path in which the surface energy gets minimized. The spatial evolution in the sintering involves different

length scales: atomic, microscopic and macroscopic. Microscopically the sintering of crystalline solids is a result of both surface motion and grain boundary motion to minimize the total sum of surface energy and grain boundary energy. The sintering mechanisms of the crystalline particles are divided into densifying mechanisms (grain boundary diffusion) and non-densifying mechanisms (surface diffusion). The rigid body motion of the particles takes place in densifying mechanisms. On the other hand, the non-densifying mechanism gives the shift of center of the mass of particles but no relative motion.

SAS has been found to be a fruitful nondestructive technique to study the mesoscopic structures in porous materials<sup>44-46,47</sup>. Compared to other complementary techniques like mercury porosimetry, BET etc., to study the pore structure in a porous material, SANS possesses some special advantages, in particular probing closed pores in addition to the open pores.

### **2.1.2. Experiments**

Chemical preparation of NiO nanoparticles (NPs) is composed of two stages: the formation of nickel hydroxide precursor precipitate and subsequent transformation to NiO by thermal treatment<sup>48</sup>. The virgin powder obtained is also heat treated at 600°C and 900°C. SANS experiments on powder samples have been performed using MSANS instrument at Guide Tube Laboratory of the Dhruva reactor at Trombay, India<sup>36,37</sup>. SANS profiles of the specimens recorded by the instrument were corrected for smearing effect using established methods<sup>41,42,49</sup> prior to data analysis.

### **2.1.3. Results and discussion**

It is discernible from Fig. 2.1a that the SANS profiles within the experimental  $q$  range can be subdivided into two zones. The first zone is approximately below  $q \sim 0.045 \text{ nm}^{-1}$  and the

other is above  $q \sim 0.045 \text{ nm}^{-1}$  and the nature of the two regions gets modified with heat treatment. This feature of the SANS data indicates the presence of at least two length scale in the system. In fact it will be seen later that the present SANS data is within the experimentally accessible  $q$  range indicating the presence of pore structures with two widely separated lengths.

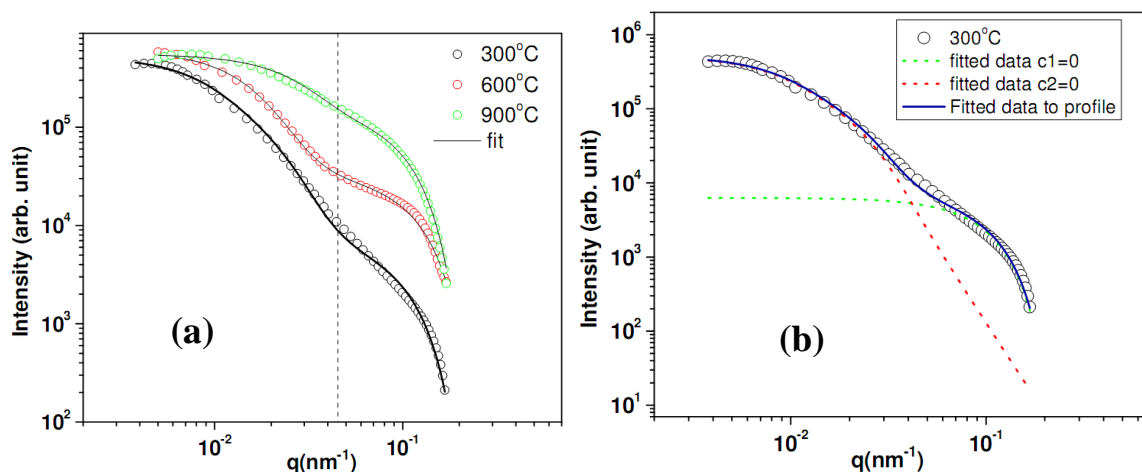


**Fig. 2.1** (a) The experimental SANS profiles are depicted. The solid line depicts the fit of the model to the data at three different heat treatment temperatures. (b) The model fitting of the experimental data with two length scale structure. It is clear from this figure that one length scale structure can not fit the experimental data completely.

The scattering intensity from an ensemble of polydisperse spherical pores is given by,

$$I(q) = C \int D(R) V^2 \overline{P}(q, R) dR \quad (2.1)$$

where  $P(q)$  is form factor for spherical pores and  $D(R)$  is pore size distribution, i.e.,  $D(R) dR$  represents the probability of having pores with radius between  $R$  to  $R+dR$ .  $V(R)$  is the volume ( $4\pi R^3/3$ ) of a pore of radius  $R$ .  $C$  is a scale factor which is independent of  $q$ . It depends on the number density of pores and scattering contrast between the matrix and the pores. For the present data,  $D(R)$  has been assumed as Weibull distribution<sup>51</sup>,

$$D(r, a, b) = \left(\frac{b}{a}\right) \left(\frac{r}{a}\right)^{b-1} \exp\left[-\left(\frac{r}{a}\right)^b\right] \quad (2.2)$$

where  $a$  and  $b$  are the parameters of the distribution,  $a$  is the scale of the distribution and  $b$  is the shape of the distribution. This distribution has a special feature that it can be skewed in both side depending on the values of  $a$  and  $b$ .

The experimental SANS profiles has been tried to fit with the model in eq. 2.1. However, it has been found that only one distribution could not explain the whole SANS profile but it needs at least two distributions to describe the SANS profiles in the whole  $q$  range. It is clear from Fig. 2.1b that combination of the two dotted curves which originates from two distribution of pores, can give a reasonable good fit to the experimental SANS data (as shown by the solid line in Fig. 2.1b). Hence, to incorporate the effect of two types of pore structures (type-1 for the larger pores and type-2 for the smaller pores), the SANS data have been analyzed in the light of the following extended model<sup>48</sup>:

$$I(q) = C_1 \int P(q, R_1) V_p^2 D_{\text{larger}}(R_1) dR_1 + C_2 \int P(q, R_2) V_p^2 D_{\text{smaller}}(R_2) dR_2 \quad (2.3)$$

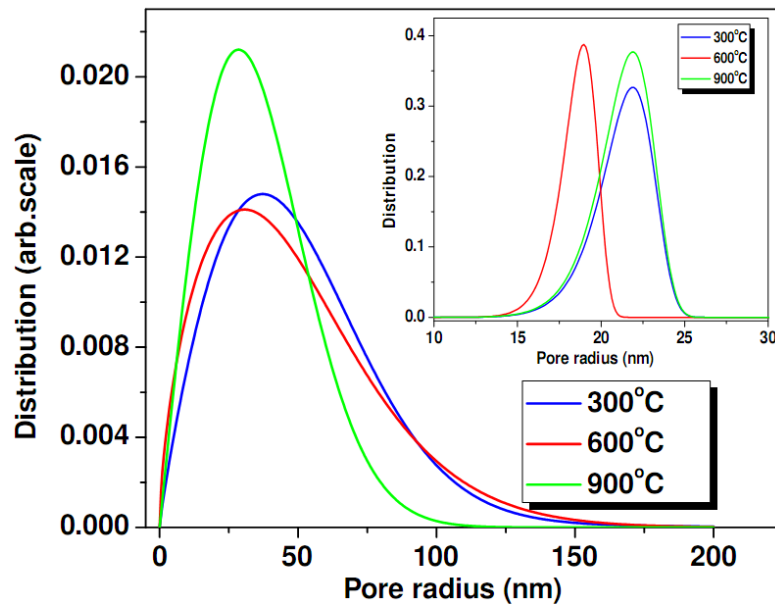


**Fig. 2.2** Larger length scale pore size distribution of NiO powder samples. Inset shows the smaller length scale pore size distribution of the NiO powder sample.

The values of  $C_1$  and  $C_2$  in eq. 2.3 depend on the number density of pores and the scattering length density of the porous materials. However, in order to estimate  $C_1$  and  $C_2$ , the scattering profiles should be represented in absolute scale. However, sample thickness is required to convert the scattering data into absolute scale as shown in chapter-1 (eq. 1.59). In present case, scattering experiments have been carried out on powder specimens where sample thickness is not defined. One can estimate only the ratio of  $C_1/C_2$ , indicative of the relative contribution of two types of pores, when scattering data is available in arbitrary unit only. The typical value of the  $C_1/C_2$  for 300°C are found to be ~0.03 whereas at 600°C; this ratio becomes ~0.0007. It indicates that number density of bigger pores decreases at higher temperature. Estimated larger pore size distribution (type-1 pores), for samples heated at 300, 600 and 900°C, respectively, estimated from the analysis are depicted in Fig. 2.2. It is evident from Fig. 2.2 that the distribution becomes somewhat less polydisperse with increase in heat treatment temperature. Further, average value of the pore distribution shifts towards lower radius side. The high-end tail part of the distribution is significantly modified after heat treatment.

These observations can be explained on the basis of the morphological modification during heat treatment. During the initial stage of heat treatment, neck begins to form between the two agglomerated particles. Neck formation is driven by the energy gradient resulting from the difference in curvatures of the particle and the neck. In this process, surface diffusion is the primary transport mechanism and subsequently the adjacent necks begin to impinge upon each other. Densification and grain growth starts in this process. Bulk transport mechanisms, such as grain boundary diffusion and volume diffusion, dominate the heat treatment process during the later stage. This leads to the shrinkage of the intra-agglomerate pores and also this process involves the reduction in the polydispersity of the pore size. The type-2 (smaller length scale) pore size distributions for the samples heat treated at 300, 600,

and 900°C are depicted in the inset of Fig. 2.2. From the figure, it is discernible that the distribution for the type-2 pores lies in the significantly lower length scale than that for the type-1 pores and is much less polydisperse in nature compared to the type-1 pores. It is observed from the inset that on an average there has not been significant modifications of the type-2 pores due to heat treatment.

#### **2.1.4. Conclusions**

Existence of pore structures at two wide separated lengths in the agglomerates was elucidated from SANS. It has been shown that the number density and size of larger pores get significantly modified under heat treatment. Shrinkage of the pores occurs with increasing heat treatment temperature and is attributed to mass transport by grain boundary diffusion.

## **2.2. Evolution of Pore Morphology in YCrO<sub>3</sub> Aggregates**

### **2.2.1. Introduction**

Recently, YCrO<sub>3</sub>, a rare-earth chromate, has been observed as biferroic in nature<sup>52</sup>. Biferroic materials which possess both ferromagnetic and ferroelectric properties are of special interest because of their potential technological applications<sup>53</sup>. Dielectric properties of porous materials have been the subject of an immense interest for quite some time<sup>54</sup>.

Factors which affect the dielectric constant and loss are broadly classified into two categories: intrinsic and extrinsic. Intrinsic losses are dependent on the crystal structure and can be described in terms of the interaction of the phonon system with the alternating electric field. Whereas, extrinsic losses depend on the heterogeneity of the medium such as porosity, impurities, grain boundaries, micro-cracks, random crystal orientation etc<sup>55-57</sup>.

In an inhomogeneous material, motion of charge carriers may occur easily through one phase and therefore motion of charge carriers is constricted at phase boundaries. For

example, in porous materials, pores can be considered as inhomogeneities in a solid matrix. Charge carriers movement through solid matrix is relatively easier as compared to movements through pores. As a result, charge builds up at interfaces and forms dipole. These dipoles can be polarized in the external applied electric field. Such effects are known as Maxwell-Wagner effects<sup>58,59</sup>. Thus, Maxwell-Wagner effects or interfacial polarization plays a significant role in porous materials as far as its dielectric response is concerned.

In general, dielectric properties of materials may be represented by a complex electrical permittivity,  $\epsilon^* = \epsilon' + i\epsilon''$ . Complex part of permittivity ( $\epsilon''$ ) is a measure of energy dissipation in the material. Dielectric loss is generally described in terms of the loss tangent,  $\tan(\delta) = \frac{\epsilon''}{\epsilon'}$ . The effect of the pore morphology on dielectric response have been investigated by SANS and dielectric measurements.

### **2.2.2. Experimental details**

Nano-crystalline  $\text{YCrO}_3$  has been prepared by a gel-combustion technique<sup>60</sup>. For the present study, the powder has been calcined at  $600^\circ\text{C}$  to obtain chemically pure and crystalline product. The resulting nano crystalline powder was cold pressed into pellets at a compaction pressure of 200 MPa using hydraulic press. The pellets were sintered at temperatures of 1300, 1400, 1500 and  $1600^\circ\text{C}$ . The porosity measurements have been carried out by gravimetric method. The estimated porosity in percentage  $(1 - (\text{actual density} / \text{theoretical density})) \times 100$  has been tabulated in Table 2.1.

SANS experiments have been performed on pellets using MSANS instrument at Guide Tube Laboratory of the Dhruva reactor at Trombay, India. To access higher q-range, experiments have also been performed using a 5 meter long slit-geometry SANS diffractometer at Guide tube Lab at Dhruva, India<sup>61</sup>.

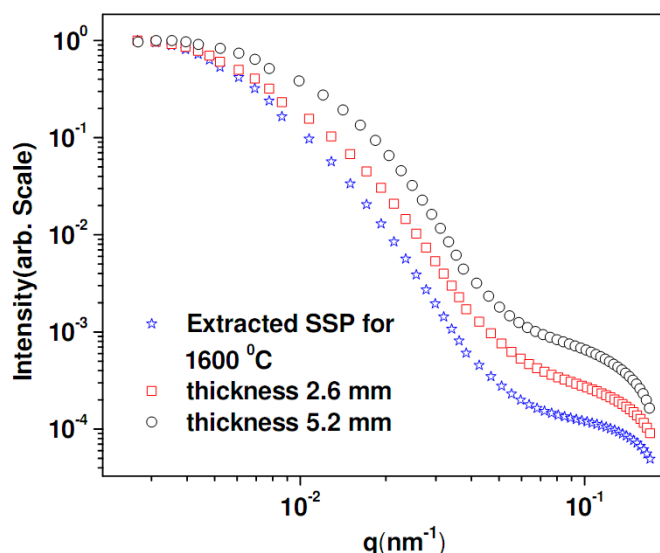


**Fig. 2.3** SANS profiles for 1600°C sintered pellets for two thicknesses are shown. The corresponding extracted single scattering profile is compared with the experimental profiles for two thicknesses.

In order to correct the multiple scattering effects<sup>62-65</sup> for the above specimens, SANS experiments were performed for two different thickness of each specimen. SANS profiles for two different thicknesses corresponding to specimen sintered at 1600°C are depicted in Fig. 2.3. The profiles are normalized at the lowest accessible  $q$  value in order to compare the functionality of two profiles. It is evident from the figure that the profiles are significantly modified with variation in the sample thickness and hence the effect of multiple scattering in the present case cannot be neglected. Using the methodology as described above, the corresponding single scattering profile (SSP), extracted from the multiple scattered profiles (for two different thicknesses) is depicted in Fig. 2.3. It is evident that the extracted SSP is sharper as compared to the recorded profiles which are affected by multiple scattering. Similarly, for other recorded profiles, the SSP was extracted with the above mentioned algorithm. The corrected SANS profiles are plotted in Fig. 2.4 for different sintering temperatures.

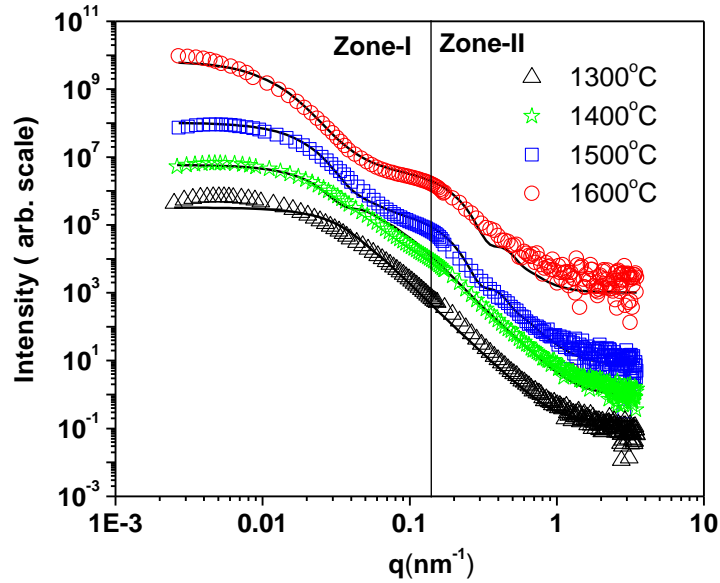


**Fig. 2.4** Multiple scattering corrected SANS profiles with fitted model for different sintering temperatures in double logarithmic scale.

Capacitance and  $\tan(\delta)$  values have been measured using a RLC bridge in frequency range 0.02-1000 kHz. Values of the relative permittivity ( $\epsilon'_r$ ) at various frequencies have been calculated from the measured capacitance values by using the appropriate geometric factor. Imaginary part ( $\epsilon''_r$ ) has been calculated by multiplying  $\epsilon'_r$  with  $\tan(\delta)$ .

### 2.2.3. Data analysis and discussions

It is observed from Fig. 2.4 that SANS profiles get significantly modified as sintering temperature is increased. A shoulder like feature (at  $q \sim 0.15 \text{ nm}^{-1}$ ) starts appearing at 1400°C and becomes more pronounced at higher sintering temperatures also the shoulder position does not shift appreciably with sintering temperature. In other words, the shoulder like feature is pronounced as porosity decreases. It is observed from Fig. 2.4, that the whole profile may be segmented in two zones, namely zone-I (below  $0.15 \text{ nm}^{-1}$ ) and zone-II (above  $0.15 \text{ nm}^{-1}$ ). The appearance of shoulder in the scattering profile may originate from one of the following possibilities. Firstly, it may appear due to the correlation in the pore structure

and manifests in the scattering profile. Secondly, the shouldering effect may be due to the modification in the pore-size distribution during sintering. Emergence of bi-modal pore size distribution with well separated modes during sintering is also a possibility. The first possibility, in the present case, can be disregarded on the basis of the fact that the prominence of the shoulder like feature increases with decreasing porosity. For the validity of the first possibility it should be other way, i.e., the shoulder like feature should be more pronounced when porosity is more. So, the second possibility appears to be a more plausible reason in the present case.

For the specimen sintered at the 1300°C temperature, the shoulder does not exist and has been explained by a single pore-size distribution. SANS profiles for specimens sintered beyond 1300°C were analyzed by introducing a distribution function  $D(r)$  which is the linear combination of the two distributions (eq. 2.3) in order to explain the whole profile. The distribution of size of the pores has been assumed to be lognormal in nature and the basis for this assumption is explained in literature<sup>66,67</sup>.

$$D(r, r_0, \sigma) = \frac{1}{\sqrt{2\pi r^2 \sigma^2}} \exp\left[-\frac{\ln(r/r_0)^2}{2\sigma^2}\right] \quad (2.4)$$

where,  $r_0$  is the median radius of the distribution;  $\sigma$  is the polydispersity index of the distribution which lies between 0 and 1. Higher the polydispersity index, higher is the polydispersity in size. The average size is can be estimated as  $r_0 \exp(\sigma^2 / 2)$ . Polydispersity can be calculated as  $\sqrt{\langle r^2 \rangle - \langle r \rangle^2}$ , where  $\langle r^2 \rangle$  is the second moment of the size distribution and  $\langle r \rangle$  is the average radius. The estimated polydispersity is shown in Table 2.1 Estimated pore-size distributions are depicted in Fig. 2.5. The extracted parameters from the above model have been tabulated in Table 2.1.

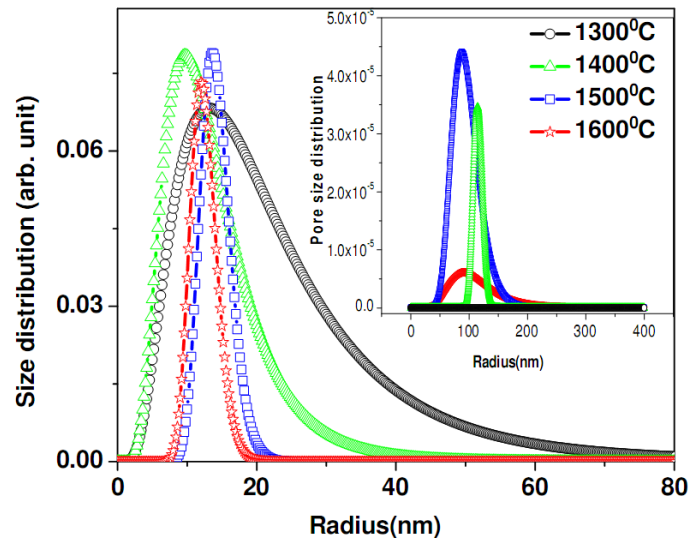


**Fig. 2.5** Smaller pore size distribution, at different sintering temperature, is depicted. Inset shows the size distributions of bigger pores.

**Table 2.1** Important parameters from SANS and dielectric measurements.

Sintering temperature (°C)	Porosity (%)	Average pore size (nm)	Polydispersity (nm)	$f_p$ (Hz)	m	n	(1-n)
1300	61	14.3	16.9	$1.6 \times 10^3$	0.42	0.25	-0.75
1400	59	8.5	9.1	$0.8 \times 10^3$	0.39	0.28	-0.72
1500	42	8.8	7.9	$5.6 \times 10^4$	1.0	0.005	-2
1600	22	7.6	6.5	$4.0 \times 10^4$	0.99	0	-2

The number density of the higher size pores was found significantly smaller than that of the lower size pores. The higher pore-size distribution is plotted separately in the inset of the figure for clarity. It is interesting to note that the number density of the bigger pores is significantly small as compared to that of the smaller pores (typical ratio  $\sim 10^{-4}$ ). However, due to the fact that the scattering intensity depends on the sixth power of the radius of the particles, it contributes significantly to the scattering intensity.

From Fig. 2.5 and Table 2.1, it is observed that average pore-size is reduced and overall polydispersity of the pore-size distribution also decreased with increasing sintering temperature. It has also been observed from Table 2.1 that, as expected, porosity decreases significantly as sintering temperature is increased. These observed variations in pore structure and porosity can be explained on the basis of the sintering theory. At higher sintering temperature grain size increases, the pores tend to break away from the grain boundaries and become spherical. Smaller pores are eliminated, while larger pores can grow.

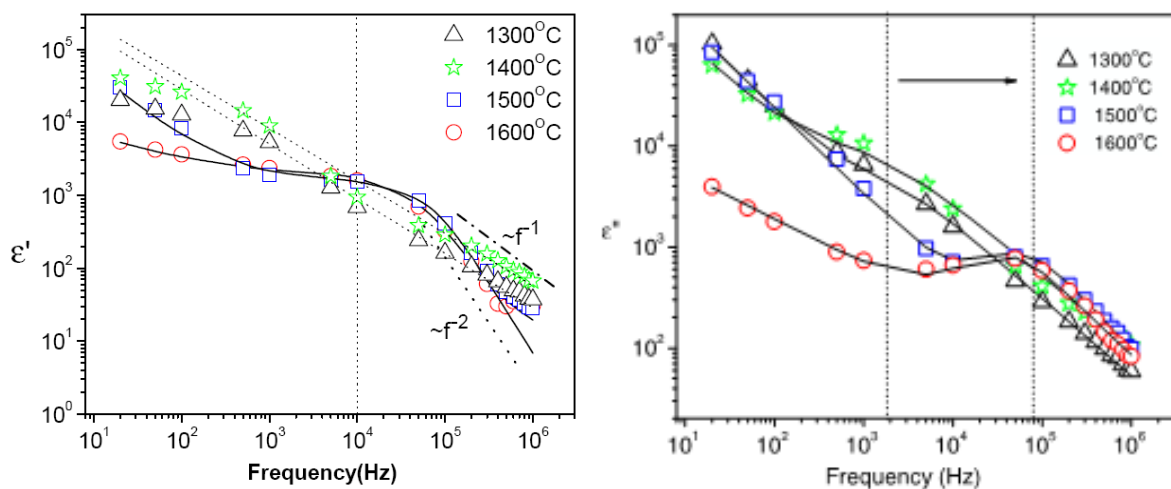


**Fig. 2.6** (a) Real part ( $\epsilon'$ ) of the dielectric response as a function of frequency for different sintering temperatures (b) Imaginary part ( $\epsilon''$ ) of the dielectric response as a function of frequency for different sintering temperature.

From Fig. 2.6a, it is discernible that the frequency dependence of  $\epsilon'$  shows a significant change above  $10^4$  Hz. For samples sintered up to  $1400^\circ\text{C}$ , the high frequency variation of  $\epsilon'$  shows  $f^{-1}$  dependence, i.e., the slope of the straight line in double logarithmic plot is -1. However, the situation is significantly different for the samples sintered at higher temperatures. In this case the dependence of  $\epsilon'$  at higher frequency regime is  $\sim f^{-2}$  yielding a slope of the straight line of the log-log plot of -2. So, there is a change of slope from -1 to -2 as the sintering temperature is increased. Like the variation in the real part of the

permittivity, the imaginary part is also significantly altered by sintering vis-à-vis the pore structure modification.

From Fig. 2.6b, it is evident that the imaginary part of dielectric response shows some kind of peak like feature (at  $f \sim 8 \times 10^4$  Hz) for the specimen sintered at 1500 and 1600° C. A closer look to Fig. 2.6b shows a broadened peak/hump like feature at around frequency  $\sim 2 \times 10^3$  Hz. However, it is seen that the anomalous increase near low frequency region shadows the exact peak position. It means, peak like structures exist even in this case but it is not very pronounced as compared to the profiles for pellets sintered at 1500 and 1600°C. It is also interesting to observe that the dielectric loss increases as frequency decreases in low frequency regime.

The dielectric loss peak is represented empirically by Jonscher model<sup>68</sup>, which is also known as universal dielectric response (UDR) and can be expressed as

$$\varepsilon''(f) = \frac{c_3}{\left(\frac{f}{f_p}\right)^{-m} + \left(\frac{f}{f_p}\right)^{1-n}} \quad (2.5)$$

where  $f_p$  characterizes the peak frequency. Here exponents,  $m$  and  $1-n$  are both vary in the range 0-1. A Debye type response corresponds to both these exponents being equal to unity, i.e., the situation with  $m=1$  and  $n=0$ . When the exponent  $m$  and  $(1-n)$  are both close to unity then the response is called a near-Debye type. And when exponent the  $m$  and  $(1-n)$  are far from unity then the response is called non-Debye response. It is noteworthy that a classical Debye type response corresponds to a non-interacting dipolar system. A non-Debye type response corresponds to an interacting dipole systems and the parameters  $m$  and  $(1-n)$  represents the degree of correlation between dipoles.

However, the eq. 2.5 does not take into account the anomalous increase in low frequency regime. This can be accounted by a modification of eq. 2.5 by adding a power law term in the

same<sup>69</sup>. Thus, to fit the whole spectrum including the low frequency anomalous increase, the following expression was used

$$\varepsilon''(f) = \frac{c_3}{\left(\frac{f}{f_p}\right)^{-m} + \left(\frac{f}{f_p}\right)^{1-n}} + c_4 f^{m_1} \quad (2.6)$$

Thus, in eq. 2.6 the first term corresponds to dielectric response which involves a relaxation process, which occurs primarily in dipolar systems. The second term corresponds to the response from the charge carrier's movement such as conduction, hoping, jump, diffusion etc, which is mainly responsible for the loss in the dielectric materials at lower frequencies. If the contribution from second term is not considered, one gets a frequency independent response at low frequencies ( $f \ll f_p$ ). Frequency independent response (for  $f \ll f_p$ ) corresponds to the pure dc conductivity which is due to motion of ions and electrons. However, Jonscher et al<sup>69</sup> has shown that the motion of a bound charge has a different frequency response in comparison to that of the motion of free charge. The motion of bound charge carriers, such as ionic diffusion, hoping etc in medium results into frequency dependant loss term of dielectric response at low frequencies. So the dielectric response of the samples can be broadly divided into two parts, low frequency contribution due to charge carrier transport and high frequency contribution due to dipolar relaxation process.

It is clear from Table 2.1 that for the pellets sintered at 1300 and 1400°C, the imaginary part of the dielectric response are best fitted for  $m=0.42, 0.39$  and  $n=0.25, 0.28$ , respectively. As described earlier that this situation, i.e., the strong deviation of  $m$  and  $(1-n)$  from unity correspond to a non-Debye type response. In contrast, for the case of pellets sintered at 1500 and 1600°C the imaginary part of the response is best fitted with  $m=1.0, 0.99$  and  $n=0.005, 0$ , respectively. This situation corresponds to the near-Debye type dielectric response. This indicates a transition of dielectric response from non-Debye type to near-Debye type. This occurs with increase in sintering temperature vis-à-vis with modification of pore structure and

pore connectivity. The analysis for real part of the permittivity also confirms the transition from a non-Debye type to near-Debye dielectric response<sup>66</sup>.

As mentioned earlier interfacial polarization across pore boundary results into a dipolar system. Pore network at relatively lower sintering temperature (below 1400° C) is expected to be somewhat random and polydisperse in nature. At this temperature pores are connected to some extent and porosity is larger and results to an interacting dipolar system. With increase in the sintering temperature, the pores become more isolated and less polydisperse. So when the sintering temperature is below 1500 °C a non-Debye type of response appears and is primarily attributed to the interconnected polydisperse pores with rough pore-matrix interface. When the sintering temperature is enhanced beyond 1400°C, the overall polydispersity of the size distribution and also porosity decreases significantly. Further, the connectivity of pores breaks as sintering temperature is increased. Sintering at higher temperature gives rise to a smoothening of the pore-matrix interface<sup>70-75</sup>. Thus, geometrical modifications in the pore structure upon sintering at higher temperature results to a non-interacting dipole system leading to a near-Debye type response.

### **2.2.5. Conclusions**

Reduction in polydispersity of the pore-size distribution, in nano-crystalline YCrO<sub>3</sub>, occurs as sintering temperature is enhanced. A shoulder like feature in SANS data beyond sintering temperature of 1400°C is attributed to the significant modifications in the pore structure and emergence of bi-modal pore-size distributions with well separated modes upon sintering.

Dielectric response in frequency range 0.02 kHz-1000 kHz showed a strong dependence on the pore characteristics. A transition from non-Debye response to near Debye response was observed as sintering temperature is increased beyond 1400°C and is corroborated by the results obtained from the SANS analysis. This is attributed to the combined effect of pore-matrix interface smoothening, reduction of polydispersity of the pore

size distribution and breaking of connectivity of the pores with increasing sintering temperature.

## **2.3. Investigation on TiO<sub>2</sub> and TiO<sub>2</sub>-CNT Composite Submicrospheres**

### **2.3.1. Introduction**

In recent years, Titania (TiO<sub>2</sub>) has been in the forefront of materials research due to its crucial applications<sup>76,77</sup> in solar cells, portable lithium ion batteries, hydrogen storage etc. Further, it has drawn a lot of interest in photocatalytic degradation of toxic and non-biodegradable organic effluents for decontamination of waste water and environment purification<sup>78</sup>. It has been found that surface area and nature of crystalline phase plays an important role in deciding the efficiency of photo catalysis. Titania exists in three crystalline forms anatase (tetragonal, space group I41/amd), rutile (tetragonal, space group P42/mmm) and brookite (orthorhombic, space Pcab). Anatase and brookite are metastable states which irreversibly transform into a stable rutile phase. At very small particle dimensions, the surface energy is an important part of the total energy and it has been found that the surface energy of anatase is lower than those of rutile and brookite. Surface energy considerations accurately describe the observation of a crossover size of about 30 nm where anatase nanoparticles transform to rutile<sup>79</sup>. Photocatalytic activity of amorphous phase is reported to be rather poor than that of crystalline phase<sup>79</sup>. Among crystalline phase anatase phase is found to be most effective.

Doping of various transition metals has been investigated for improvement towards photo catalytic applications. NiO is a p-type semiconductor that with excess oxygen in NiO produces a Ni<sup>2+</sup> vacancy, which leads to the creation of a hole on two adjacent Ni<sup>2+</sup> ions, thus producing Ni<sup>3+</sup> ions<sup>80</sup>. It acts as a co-catalyst in TiO<sub>2</sub> for UV induced water splitting<sup>81</sup>. Recently, Nagamine et al. reported a simple method for preparing a TiO<sub>2</sub> microsphere. Water is sprayed, by using a commercial nozzle with N<sub>2</sub> as the carrier gas, into an organic solution

of titanium tetraisopropoxide (TTIP)<sup>82</sup>. Nagaoka et al. prepared the carbon/TiO<sub>2</sub> microsphere composite from the cellulose/TiO<sub>2</sub> micro-sphere composite<sup>83</sup>.

In present work, we report synthesis of sub-micrometric TiO<sub>2</sub> powders using a facile one step synthesis method of spray hydrolysis<sup>82-84</sup>. Further, it will be shown in this section that NiO doped TiO<sub>2</sub> can be successfully used as a substrate for growing carbon nanotubes.

### 2.3.2. Experiments

Different concentration of Ni(NO<sub>3</sub>)<sub>2</sub> has been mixed with 5 ml of deionized water. The concentration of nitrate has been chosen in such a way that the weight of Ni varies as 2, 5, 10 and 15 wt% of TiO<sub>2</sub> in composites.

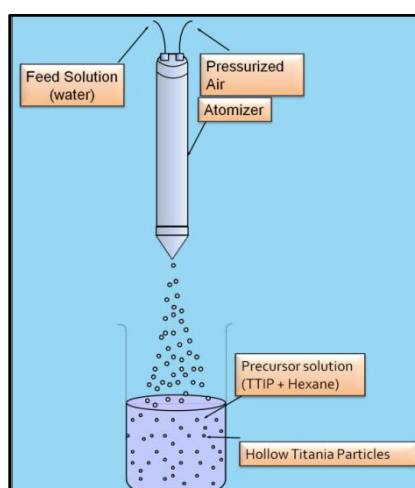


**Fig. 2.7** Schematic of the spray hydrolysis method used for synthesizing TiO<sub>2</sub> submicrospheres.

The nitrate mixed water is sprayed by a two fluid nozzle into mixture of 10 ml of titanium isopropoxide (TTIP) and 90 ml Hexane under stirring as shown in Fig. 2.7.

A greenish color precipitates obtained within a few seconds. Resulting precipitates was filtered, washed and dried. The specimens were named as 2Ni\_TiO<sub>2</sub>, 5Ni\_TiO<sub>2</sub>, 10Ni\_TiO<sub>2</sub> and 15Ni\_TiO<sub>2</sub> according to Ni weight percent<sup>85</sup>. Electron micrographs were obtained using

CAM Scan (UK) instrument (Model 2300CT/100). To probe the internal morphology of the submicrospheres, SAXS experiments have been performed on  $\text{TiO}_2$ ,  $5\text{Ni}_2\text{TiO}_2$  and  $10\text{Ni}_2\text{TiO}_2$  specimens. SAXS experiments have also been performed on the heat treated specimens at  $600^\circ\text{C}$  for 4 hrs. To probe the microscopic stability of the submicrospheres high temperature XRD experiments have been performed using a diffractometer ( $\text{CuK}_\alpha$  source) in  $\theta$ - $\theta$  geometry with 2 deg/min scanning speed.

### 2.3.3. Results and discussion

The SEM micrographs of the doped- $\text{TiO}_2$  specimens are shown in Fig. 2.8. The grains are approximately spherical having size less than a micron. Similar morphology has also been observed for only  $\text{TiO}_2$  specimens<sup>86</sup>.

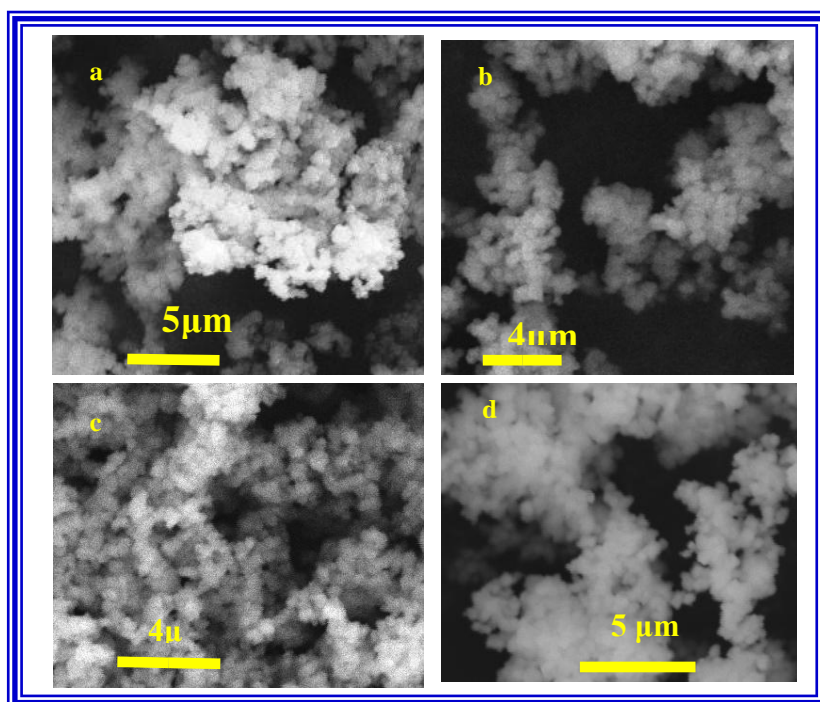


**Fig 2.8** SEM micrograph of (a)  $2\text{Ni}_2\text{TiO}_2$  (b)  $5\text{Ni}_2\text{TiO}_2$  (c)  $10\text{Ni}_2\text{TiO}_2$  and (d)  $15 \text{Ni}_2\text{TiO}_2$  composite submicrospheres.

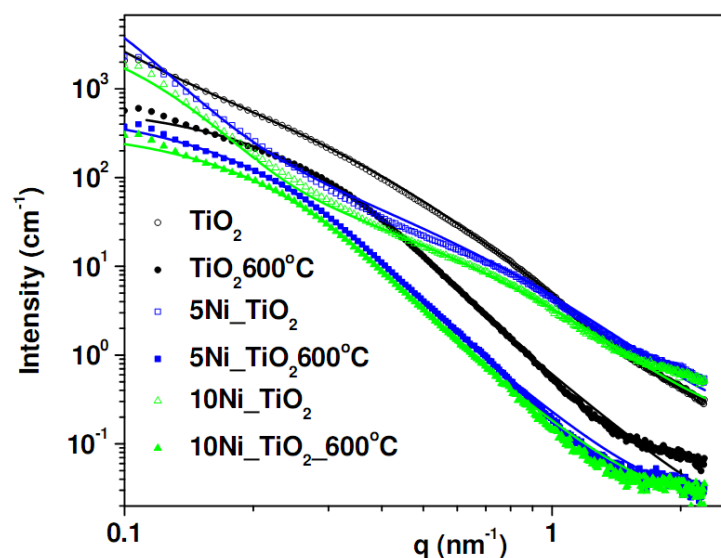


**Fig. 2.9** The SAXS profiles of the  $\text{TiO}_2$ , doped  $\text{TiO}_2$  and heat treated specimens.

The scattering profiles are shown in Fig. 2.9. It is evident from Fig. 2.9 that scattering profiles of  $\text{TiO}_2$  specimens is quite different as compared to that for doped specimens. Similarly, the SAXS profiles of the heat treated samples are sharper as compared to that of the un-treated samples.

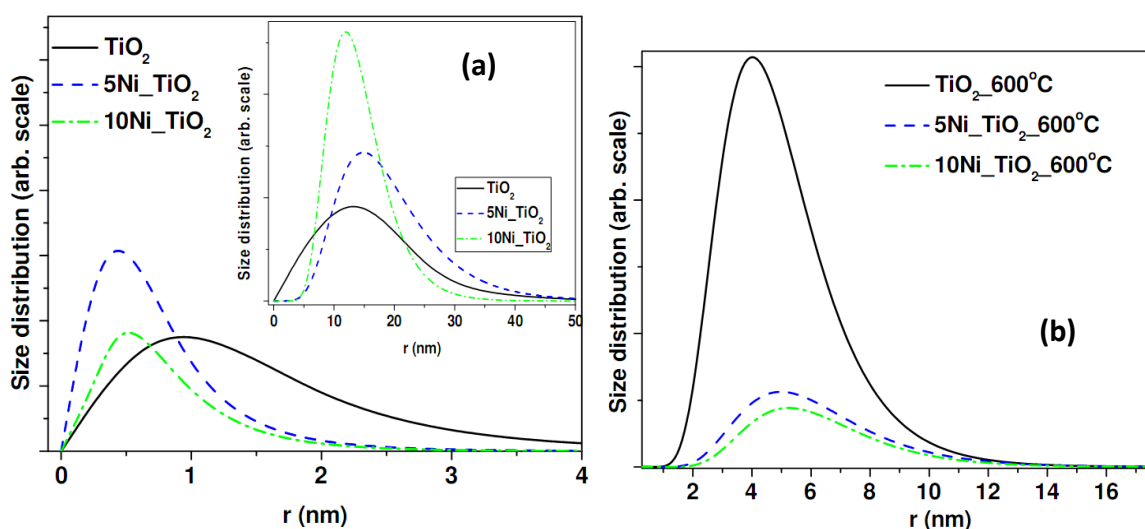


**Fig. 2.10** (a) The primary  $\text{TiO}_2$  NPs radius distribution, estimated by SAXS analysis. The inset shows the higher size contribution which may arise due to aggregation of primary NPs (b)  $\text{TiO}_2$  NPs size distribution for the specimens heated at  $600^\circ\text{C}$ .  $r$  indicates the radius of the NPs.

Ensemble of polydisperse spheres (eq. 2.1) has been taken as a model to fit the scattering data. It is seen that the contribution from two type of size distribution is required to fit the data (eq. 2.3). The estimated size distribution is shown in Fig. 2.10a.

From Fig. 2.10a, it is evident that size of TiO<sub>2</sub> NPs is quite polydisperse. The average radius is typically ~1.5 nm. However, size of TiO<sub>2</sub> NPs for doped specimens is relatively less polydisperse with average radius less than 1 nm. The average radius of bigger NPs is approximately 15 nm with varying polydispersity. The effect of heat treatment is quite significant and is manifested in scattering profiles as well. The scattering profiles become sharper for the heat treated specimens indicating growth of NPs. The estimated size of TiO<sub>2</sub> NPs for heat treated specimens is shown in Fig. 2.10b. It is evident that the radius of TiO<sub>2</sub> NPs grows to approximately 5 nm at 600°C for all the specimens.

The evolution of the microscopic structure has been depicted in Fig. 2.11.

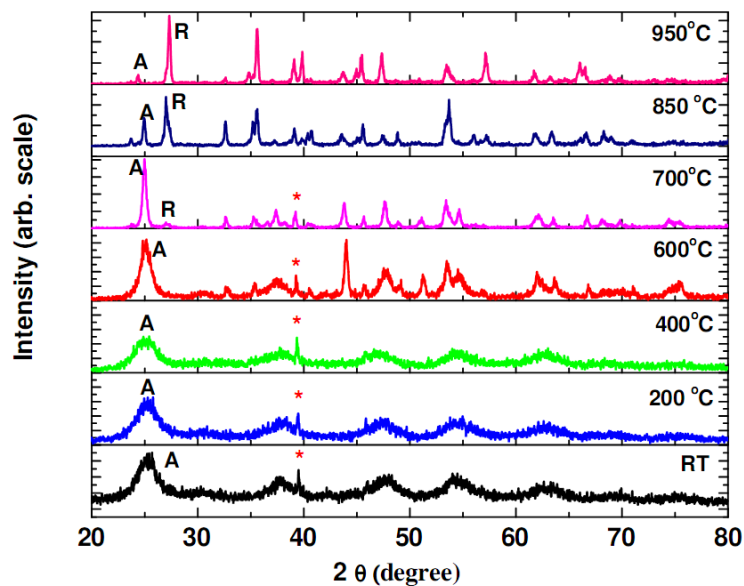


**Fig. 2.11** High temperature XRD patterns of the Ni-TiO<sub>2</sub> microspheres.\* marked peaks corresponds to Pt peaks. Anatase to rutile phase transition is observed beyond 600 °C. A and R denotes the anatase and rutile phase.

It is evident from Fig. 2.11 that TiO<sub>2</sub> NPs exists in anatase phase having substantial amorphous contribution at ambient temperature. The broadening of the peak is quite significant at lower temperatures. There is no clear phase transition of TiO<sub>2</sub> below 600°C. The weight fraction of anatase (W<sub>A</sub>) and rutile (W<sub>R</sub>) in both the specimens were estimated from the Spurr equations<sup>87</sup>

$$W_A = \frac{1}{1+1.26 I_R / I_A} \quad W_R = \frac{1}{1+0.8 I_A / I_R} \quad (2.7)$$

where I<sub>A</sub> and I<sub>R</sub> are the intensities of peaks corresponding to (101) plane of anatase and (110) plane of rutile phase, respectively. The fractions of anatase and rutile phases, at different temperatures, have been tabulated in Tables 2.2.

**Table 2.2** The parameters obtained from analysis of XRD patterns for NiO-TiO<sub>2</sub> specimens.

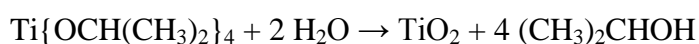
Temperature (°C)	Weight percent		Average anatase crystallite size (nm)	Average rutile crystallite size (nm)
	Anatase	Rutile		
27	100	-	4.1	-
200	100	-	3.8	-
400	100	-	3.8	-
600	100	-	7.2	-
700	93.3	6.7	19.3	14.6
850	35.5	64.3	30.1	19.2
950	8.9	91.1	34.5	30.4

Mean crystallite size for anatase and rutile phases was calculated from the broadening of the X-ray reflections (101) crystallographic plane for anatase and (110) for rutile, using the Scherrer's formula<sup>50</sup>. It is evident from Table 2.2 that average crystallite size for virgin

powder is typically 4.1 nm and it grows to 7.2 nm at 600°C. A rutile phase appears at 700°C with an average crystallite size of 14.6 nm. The anatase crystallite size is 19.3 nm at 700°C and it grows to 30 nm. The weight fraction of rutile phase increases with increasing temperature.

Let us understand the mechanism of formation of TiO<sub>2</sub> submicrospheres:

The hydrolysis reaction for TTIP can be written as:



We consider a spherical water droplet surrounded by a hexane phase containing TTIP (see Fig 2.12). The diffusion of TTIP into water droplet takes place only after it gets partially hydrolyzed at the water–hexane interface because of its low solubility in water. Titanium hydroxide, yielded by partial hydrolysis, is hydrophilic and diffuses toward the droplet center through the water–hexane interface. In the course of diffusion, titanium hydroxide undergoes to further hydrolysis and condensation reaction. This leads to the formation of TiO<sub>2</sub> NPs which subsequently form submicrosphere. The formation of submicrospheres is not possible without the presence of the oil-water interface.

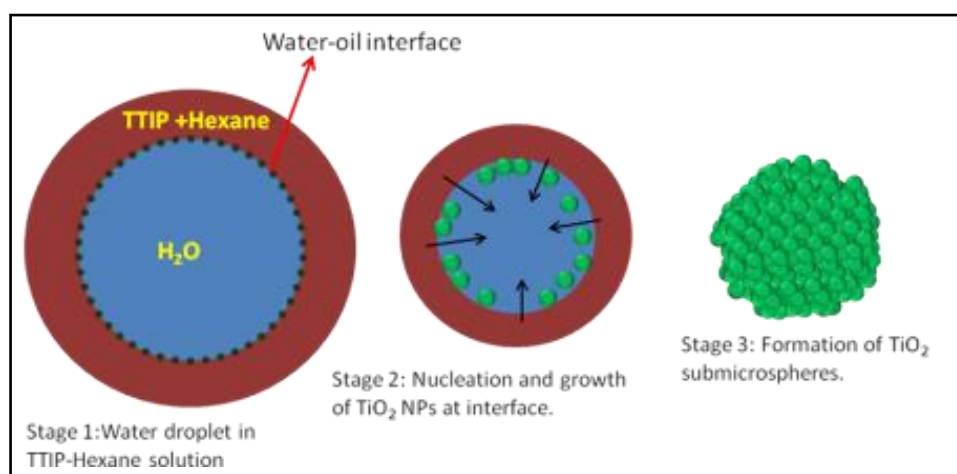


**Fig. 2.12** The schematic of the mechanism for the formation TiO<sub>2</sub> submicrospheres in the spray hydrolysis technique.

To synthesize the CNTs, catalytic Chemical Vapour Deposition (CVD) was used. NiO-TiO<sub>2</sub> (1gm) was taken in a ceramic boat and kept inside the horizontal quartz tube. Initially, the boat with the supported catalyst was allowed to pass at the flow rate of 1 liter/min in order to create the inert atmosphere inside the tube as soon as the desired temperature (750°C) is obtained, the boat is pushed into the effective heating zone and the acetylene (C<sub>2</sub>H<sub>2</sub>) gas was allowed to flow at the rate of 100cc/m for 15 min. After the growth of CNT the residue was purified by acid treatment process<sup>40,41</sup>. The SEM micrograph of the CNT grown TiO<sub>2</sub> is depicted in Fig. 2.13. It is to be noted that it is not possible to differentiate the nature of the carbon nanotubes from the SEM or SAS measurements. However, in future, one can perform the detailed studies on the correlation between the ceramic parameters and type of CNTs which is grown on it.

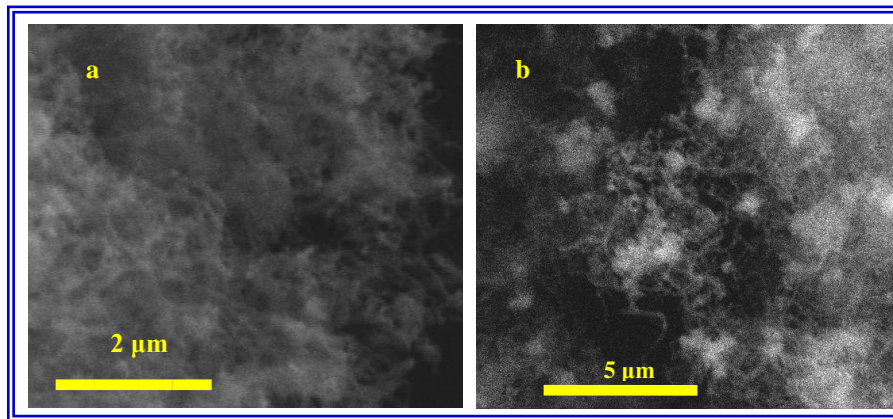


**Fig. 2.13** The SEM micrographs of the CNTs on (a) 5Ni-TiO<sub>2</sub> (b) 15Ni-TiO<sub>2</sub> substrate.

The CNTs grown TiO<sub>2</sub> were also characterized by XRD and are shown in Fig. 2.14a. The TiO<sub>2</sub> in the composite exists in the rutile phase. The contribution of the peak corresponding to graphite increases with increasing Ni weight percent. The yields of CNTs have been estimated by the XRD data and are shown in Fig. 2.14b. It is evident from figure that the yield of CNTs increases with increasing Ni weight percent.

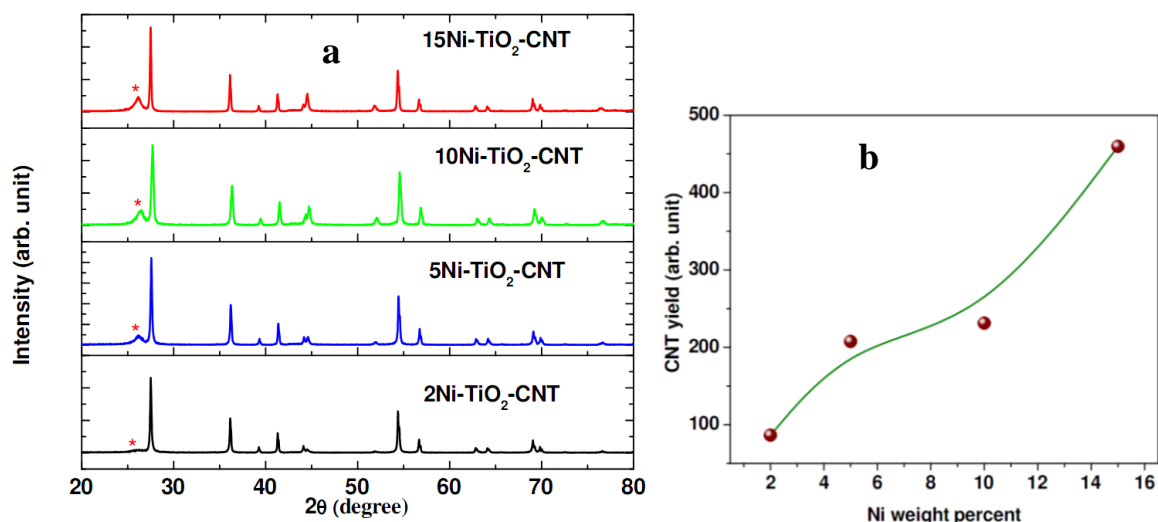


**Fig. 2.14** (a) The XRD patterns of the CNTs grown on  $\text{TiO}_2$  microspheres. The \* marked peak corresponds to the CNT. (b) Yield of CNTs, as estimated from the peak intensity corresponding graphite peak, is shown with different Ni concentration.

One can estimate the quantitative yield of CNTs by thermogravimetric analysis by measuring weight loss during burning of the CNTs at high temperature. It is also possible to estimate yield of CNTs by differentiating the weight of the powder before and after growth of the CNTs. We propose that Ni- $\text{TiO}_2$  doped CNTs composites can be utilized as a novel material for hydrogen generation and subsequently storage of produced hydrogen.

#### 2.3.4. Conclusions

The submicrospheres of NiO doped  $\text{TiO}_2$  have been synthesized by spray hydrolysis technique. Size of NPs increases with heat treatment. The initial phase of the  $\text{TiO}_2$  is anatase due its small size. Rutile phase appear beyond  $600^\circ\text{C}$  due to growth of NPs beyond 14 nm size. NiO- $\text{TiO}_2$  composite is good candidate as a substrate to synthesize the CNTs. The yield of CNTs increases with increasing Ni content in the composite.

# Probing Mesoscopic Morphology of the Non-Euclidean Nano-ceramics Aggregates

### 3.0. General Introduction

In many natural and synthetic objects, the structures manifest in such a way that introduction of a new outlook, different from those adopted for normal Euclidean objects, becomes imminent for mathematical description and quantification of its structures. Since Benoît Mandelbrot first brought the idea of fractals<sup>90</sup>, the self-similarity/self-affinity has wormed its way into various branches of sciences as well as in psychology and even in abstract arts. Many naturally occurring materials like rocks<sup>91,92</sup>, coals<sup>93,94</sup>, cauliflowers, some special coastlines etc. are some examples of such natural fractal objects. Synthesized objects like hydrated cement pastes<sup>95,96</sup>, surfaces prepared by molecular beam epitaxy etc. also are known to be fractal in nature and its fractal nature depends strongly on their synthesis route. The formal mathematical definition of fractal is defined by Benoit Mandelbrot. It says that a fractal is an object for which the Hausdorff dimension is less than the Euclidian object where it is embedded and may fall between the integers. Generally, we can define a fractal as a rough or fragmented geometric shape that can be subdivided in parts, each of which is a reduced-size copy of the whole. Consider the number  $N(r)$  of balls of radius  $r$  required to cover fractal object completely. Hausdorff dimension or fractal dimension is the unique number  $D$  such that  $N(r)$  grows as  $1/r^D$  as  $r$  approaches zero.

An object, which is fractal over a wide length-scale, can be either of mass fractal<sup>97</sup> or of surface fractal<sup>97</sup> in nature. For a mass fractal object, the mass or the volume is proportional to  $r^{D_m}$ , where  $D_m$  is known as mass fractal dimension, which is less than 3. For a surface fractal object, the self-similarity or the self-affinity exists only on the surface of the object. In this case the surface area scales with  $r^{D_s}$ , where  $D_s$  is known as surface fractal dimension. The value of  $D_s$  lies between 2 and 3. It is noteworthy that for a smooth surface, the surface area scales with  $r^2$ . A mass fractal object, by default, is also a surface fractal but a surface fractal object need not be a mass fractal object.

It is noteworthy that due to the power law correlation in the fractal systems in real space, SAXS profile also manifests a power law<sup>98,99</sup> in  $q$ . The exponent of that power law is a non-integer and depends on the nature of the fractal. For a mass fractal object, scattering intensity  $I(q)$  follows  $q^{-\alpha}$  behaviour. In this case the mass fractal dimension ( $D_m$ ) is equal to the value of  $\alpha$ . For a surface fractal object  $4 \geq \alpha \geq 3$  and in this case the surface fractal dimension ( $D_s$ ) is equal to  $6 - \alpha$  and lies between 2 and 3.

Present chapter of the thesis deals with the SAS investigations of fractal, i.e., non-Euclidian aggregates of various important nano-ceramics. The nano-ceramics which are covered in this chapter are  $Y_3Al_5O_{12}$  (YAG),  $Nd_2O_3$  doped  $CeO_2$  and hydration of calcium silicates.

### **3.1. Evolution of $Y_3Al_5O_{12}$ Fractal Aggregates under Thermal Annealing**

#### **3.1.1. Introduction**

The instabilities during growth, evolution and construction of systems with non-equilibrium morphologies that imitate the spontaneous pattern formation in nature, play an important role in Physics, Chemistry, Materials science and Biology<sup>100-107</sup>. In general, precipitation and sol-gel synthesis methods are widely used to prepare nano-ceramic powders. The growth of NPs

aggregates may result into unstable dendrite structures with a large surface to volume ratio depending on thermodynamical environments<sup>108</sup>. The concept of fractal geometry is widely used to describe such spatially inhomogeneous systems<sup>90,109,110</sup>. Although growth mechanisms for fractal structures have been studied extensively, subsequent structural relaxation after growth remains an important issue. It is worthy to mention that a fractal cluster is thermodynamically metastable<sup>111</sup> as the ratio of its surface to volume is significantly large. Therefore, it is of importance to analyze possible pathways of relaxation processes towards more stable configurations with respect to some thermodynamical variable. Excess surface energy of fractal objects gives rise to a number of evolutionary processes that leads to significant structural modifications during its relaxation. Pertinent physical examples include annealing of dendrite inclusions in solids, healing of cracks in ceramics during sintering, temperature-induced transformations in composites, relaxation of rough surfaces and aging of colloidal particles<sup>112-116</sup>. In all the above cases, the total amount of mass remains conserved during the evolution that is driven by the excess interfacial energy.

There are two broad types of restructuring of fractal clusters during sintering. In first case, fractal aggregates of weakly bonded primary particles tend to collapse and become more compact during annealing<sup>117,118</sup>. In second case, fractal aggregates of strongly bonded particles retain their general topology with a decrease in the radius of gyration and an increase of size of the subunits due to sintering<sup>119,120</sup>. In recent studies<sup>111,121,122</sup>, simulations for thermal annealing of 2D fractals have been carried out<sup>123-130</sup>.

In a structural relaxation of fractals during sintering, two major parameters that govern the evolution are temperature and time. Considering a linear sintering law for two spherical particles in terms of the total surface area reduction can be written as,

$da/dt = -(a - a_s)/\tau_f$  where  $a_s$  is the final surface area of coalesced particle with conserved volume and  $\tau_f$  is the characteristic sintering time<sup>124,131,132</sup>. It is evident from above equation that the evolution under sintering depends<sup>133</sup> on the characteristic sintering time  $\tau_f$  which is given by  $\tau_f = Ad_p^4 \exp\left(\frac{E_a}{kT}\right)$ , where  $A$  is the pre-exponent factor,  $E_a$  is the activation energy of the diffusion process,  $k$  is the Boltzmann constant,  $T$  represents the temperature and  $d_p$  is the diameter of individual particle.

### 3.1.2. Experiments

YAG has been synthesized by homogeneous precipitation technique using aqueous solution of aluminum nitrate, yttrium nitrate and urea<sup>134</sup>. As formed powder were sintered at 800, 900, 1000, 1100, 1200 and 1300 °C, respectively. SANS experiments have been carried out using a MSANS instrument at the Guide Tube Laboratory of the Dhruva reactor at Trombay, India. SANS profiles have been shown in Fig. 3.1a.

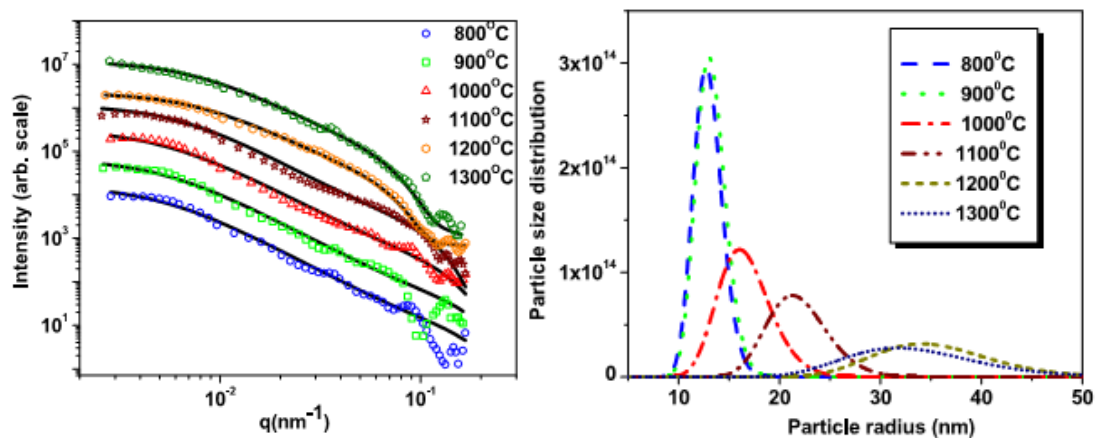


**Fig. 3.1** (a) SANS profiles in log-log scale for specimens sintered at different temperatures. Solid line represents the fit of the model to the scattering data. The profiles are shifted vertically for clarity. (b) Size distribution of the primary particles with increasing sintering temperature.

### 3.1.3. SANS data analysis

From Fig. 3.1, it is evident that scattering profiles show a linear domain over a wide  $q$ -range when plotted in double logarithmic scale. The extent of linear domain varies with sintering temperature while slope of linear region remains invariant for all profiles. In view of the above fact, scattering profiles of the specimens have been analyzed by assuming fractal type correlation of the primary NPs. In such a case, the scattered intensity may be represented as,

$$I(q) = C \left[ \int D(r) V^2(r) P(q, r) dr \right] S(q, r_{av}) \quad (3.1)$$

where  $P(q, r)$  is the spherical form factor for primary NPs,  $V(r)$  is volume of particle having radius  $r$  and  $C$  is  $q$  independent scale factor. In present case, a normalized lognormal distribution is assumed as size distribution of the primary particles of aggregates<sup>134,135</sup>. In eq. 3.1,  $S(q, r_{av})$  represents the structure factor (eq. 1.58), due to fractal correlation<sup>98,99</sup> (eq. 1.57) of the particles in the aggregate with fractal dimension  $D_f$  and average size  $r_{av}$  of primary particles which is assumed as the lower cutoff of fractal aggregate,  $\xi$  is the upper cutoff. Estimated size distributions of the primary particles at different sintering temperatures have been depicted in Fig.3.1b.

### 3.1.4. Computer simulation

To interpret the experimental observations, a computer simulation has been carried out. In last two decades, various computer models have been developed to simulate random fractal objects originated from the agglomeration of the smaller particles. Some of these models are diffusion limited aggregation (DLA)<sup>136</sup>, cluster-cluster aggregation (CCA)<sup>137</sup>, tunable dimension cluster-cluster aggregation (tCCA)<sup>138,139</sup> and reaction limited cluster-cluster aggregation (RLCCA)<sup>140</sup>.

It is observed from scattering experiments that YAG nanoceramic possesses a fractal type of aggregates. The fractal dimension  $D_f$  has been found to be approximately  $2.3 \pm 0.2$  indicating a diffusion limited aggregate type of fractal morphology of the aggregates embedded in 3 dimension. It is important to mention here that fractal dimension for 2D DLA is 1.7 whereas fractal dimension for DLA in 3D is 2.5. Fractal dimension in case of CCA process varies from 1.7 to 2.4. Thus, CCA process may give fractal dimension very close to experimentally observed value. However, our aim was to validate the sintering mechanism for the coarsening of the aggregate. The choice of the DLA aggregate was based on its simplistic aggregation model as well as modest requirement of computation. Fractal dimension of 3D DLA is not very different from experimentally observed value. DLA model is one of the simplest models of these kinds. Such fractal cluster can develop during the diffusion control growth and choice of DLA like fractal cluster is physically motivated. It is important to note that, simulation on 3D DLA can facilitate the estimation of scattering profiles directly. Due to computational complexity, present simulation has been restricted to two dimensional DLA cluster as a starting aggregate model. In present simulation, a DLA cluster consisting of 10000 particles is generated on a square lattice. At the beginning of the simulation, the mass and radius of particle have been taken to be 1.0 unit and 0.5 units, respectively.

We know that the particles in fractal aggregates are connected by attractive forces such as van der Waals or other molecular forces resulting covalent bonding. The bonds between the particles represent an energy-barrier that prevents rearrangement. A minimum energy is required to overcome such energy barrier. It is important to note that for restructuring of aggregate, it is not necessary to break the bonds completely. Therefore, it is expected that the activation energy  $E_a$  for rearrangement of the aggregate is lower than the bond energy  $E_b$ <sup>141</sup>. It is interesting to mention that driving force for the mass transport during

sintering is high surface energy of the aggregate of fine particles. Diffusion transports matter along free surfaces and volumes of particles along grain boundaries between them and also transportation of matter are mediated through a vapor phase around them. The diffusion coefficients, for different processes involved, are different from each other. A numerical simulation of sintering process is engrossed as various diffusion processes are relevant at different stages of sintering, albeit, we attempted a model for simulation to explain the experimental observations. In present simulation, an effective diffusion coefficient has been defined to account all diffusion transport mechanisms.

A localized sintering model<sup>131</sup> has been adopted to simulate the structural evolution of fractal clusters as a function of sintering temperature. This model is based on the experimentally observed phenomenon that sintering starts with the merging of neighboring particles that are in contact in aggregate<sup>124</sup>. It is interesting to note that model of local group merge sintering involves the diffusion of matter locally and detailed kinetics of the sintering is ignored.

Diffusion length in a sintering process is defined as,

$$\sqrt{\langle r^2(t) \rangle} = \sqrt{D_{\text{eff}} t} \quad (3.2)$$

where  $D_{\text{eff}}$  is the effective diffusion coefficient and  $t$  is time. In present model, diffusion of particles occurs locally. Thus, sintering distance  $\Delta_s$  is assumed to be equal to diffusion length.

From Arrhenius equation, diffusion coefficient  $D_{\text{eff}}$  is related to temperature  $T$ ,

$$D_{\text{eff}} = D_0 \exp(-E_a / kT) \quad (3.3)$$

where  $D_0$  is constant. Here, activation energy has been assumed to be independent of temperature for small temperature variation. From eq. 3.2 and 3.3, a relation between  $\Delta_s$  and sintering temperature at a fixed time may be derived as,

$$T = \frac{E_a / k}{\log(D_0 t / \Delta_s^2)} = \frac{E_a / k}{\log D_0 t + \log(1 / \Delta_s^2)} = \frac{C_1}{C_2 + \log(1 / \Delta_s^2)} \quad (3.4)$$

From eq. 3.4, it is evident that  $\Delta_s$  increases with increasing sintering temperature. It is interesting to note that sintering distance  $\Delta_s$  is not only the function of the temperature but also depends on the size of the particle formed by merging of smaller particles. In present model, Ostwald-ripening type of evolution of fractal aggregates under conservative conditions is adopted. It means that larger the particle size in the cluster, larger is  $\Delta_s$ . A bigger particle would grow at the expense of the smaller ones keeping mass conserved.

The local group merge restructuring is carried out according to following algorithm. At first, any particle in cluster is chosen randomly. The neighboring particles have been calculated according to some fixed sintering distance  $\Delta_s$ . They were grouped and merged to form a new particle. The mass of this bigger particle will be sum of masses of all merging particles and radius is calculated in accordance with the mass conservation of the system. The centre of the new primary particle will be situated at the centre of mass of the merged particles. An off-lattice model is used to displace the new primary particles, formed by merging of the smaller particles, towards centre of mass of the DLA aggregate with condition that all neighboring particles remain in contact. Then another random particle is chosen for same  $\Delta_s$  and the above mentioned process is reiterated. This process is carried out repeatedly until we could find some neighbours for same  $\Delta_s$ . Simulation steps are performed for increasing  $\Delta_s$  by using above algorithm as sintering temperature increases. The evolution of fractal cluster with  $\Delta_s$  is shown in Fig. 3.2.

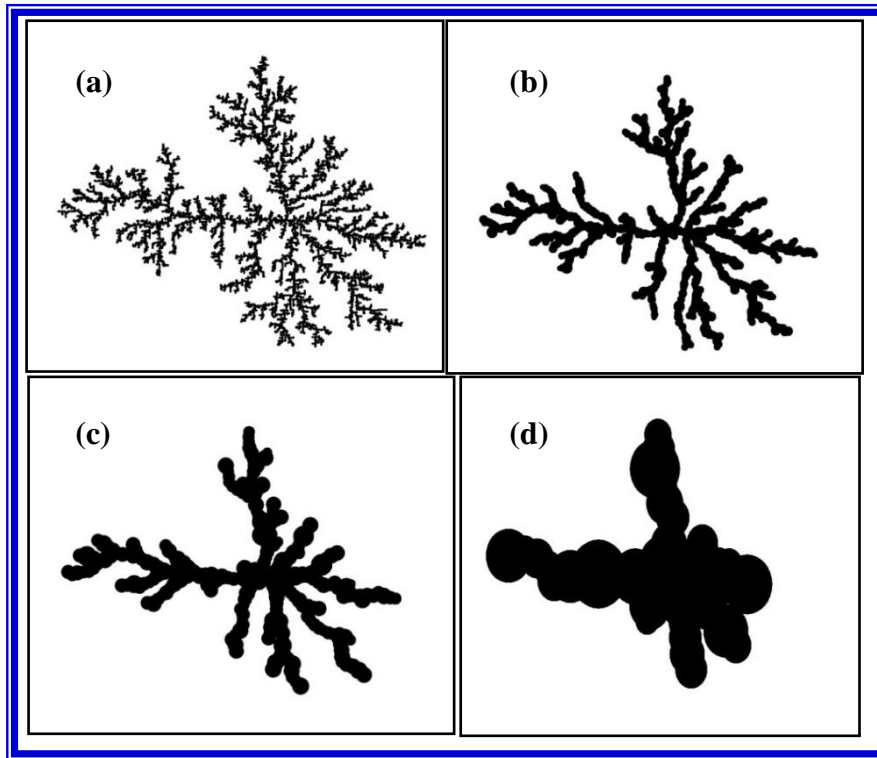


**Fig. 3.2** Evolution of the DLA clusters with different  $\Delta_s$ . (a) Initial 2D DLA (b) modified DLA for  $\Delta_s = 10$  (c) modified DLA for  $\Delta_s = 30$  (d) modified DLA for  $\Delta_s = 150$ .

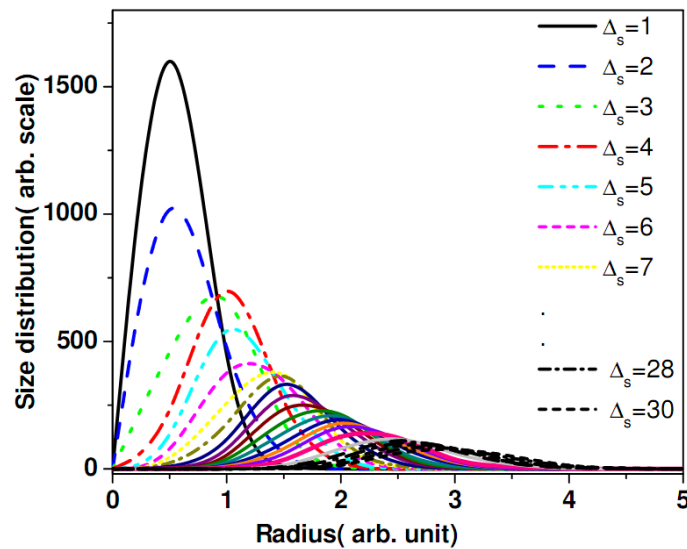


**Fig. 3.3** Evolution of the size distribution of the primary particles as function of  $\Delta_s (T)$ .

Fractal dimension of the cluster before and after the sintering restructuring can be calculated by the power law relationship between mass and radius,  $M \propto R_f^D$ , where  $R$  is radius of searching circle assuming centre of mass of cluster as origin<sup>134</sup>. It is interesting to note that

for a fixed  $\Delta_s$ , the chosen random particle in DLA cluster may have different numbers of neighbours. Accordingly after first step of simulation, primary particle size will be polydisperse in nature. The evolution of size distribution of primary particles with  $\Delta_s$  is shown in Fig. 3.3.

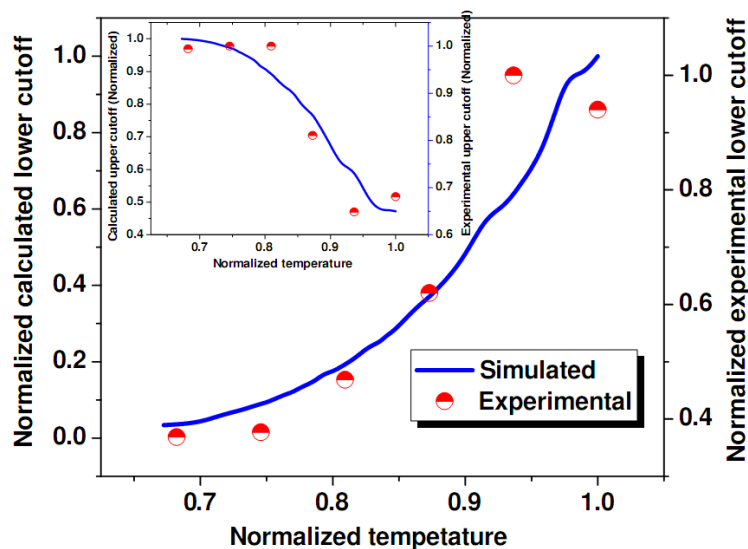


**Fig. 3.4** Computed lower cutoff from simulation and observed lower cutoff from SANS at different temperatures are depicted. Inset shows computed upper cutoff from simulation and observed upper cutoff from SANS.

Lower cutoff of fractal aggregate for each  $\Delta_s$  have been estimated by taking average of the size distribution. The upper cutoff is assumed as the radius of gyration  $R_g$  of fractal cluster,  $R_g^2 = \sum_i m_i r_i^2 / \sum_i m_i$  where  $m_i$  is mass of  $i^{\text{th}}$  particle in cluster,  $r_i$  is distance of  $i^{\text{th}}$  particle from centre of mass of cluster. Evolution of the cutoffs of fractal aggregate have been shown in Fig. 3.4.

### 3.1.5. Results and discussion

From Fig. 3.1a, scattering profiles of YAG nanoceramic indicate fractal morphology of aggregates at all sintering temperatures under study. But extent of linear region of profiles in

log-log plot decreases with increasing sintering temperature exhibiting modification in upper and lower cutoffs of the fractal aggregate. From Fig. 3.2, the evolution of the DLA cluster has been shown for different  $\Delta_s$  vis-à-vis different simulation sintering temperature. Initially, DLA aggregate is not very compact and many sites, in particular, edge sites of cluster have relatively fewer neighbours leading to higher surface area of the cluster. Sintering provides required activation energy to the atoms for diffusion. Diffusion of the atoms plays an important role to decide the morphological change during sintering. Two types of diffusion mechanisms are possible. In one case, diffusion occurs in small steps, i.e., the mobility of the cluster atoms is lower and in second case, diffusion occurs over an extended zone in large steps with higher mobility of the cluster atoms. Depending upon the type of diffusion process, the morphology of cluster gets modified accordingly. In case of present model, the small step diffusion dominates over extended zone diffusion. This process leads to smoothing of the aggregate branches locally by keeping overall cluster morphology unaltered. But at significantly high temperature, even the low resolution morphology gets modified as evident from Fig. 3.2.

The experimental and simulated fractal cutoffs at different sintering temperatures (normalized scale) have been depicted in Fig. 3.4. It is evident that the variation of experimental and calculated cutoff lengths corroborates each other within experimental error bars. In real situation, sintering process involves different mass transport mechanisms at different stages of sintering. It is to be noted that initial DLA cluster consists of monodisperse particles; polydispersity in size distribution of the particles creeps in as sintering proceeds.

### **3.1.6. Conclusions**

Scattering experiments reveal that YAG nano-ceramics are made of fractal aggregates. The cutoff lengths vary with sintering temperature while fractal dimension of cluster remains

same. A local group merge sintering model has been adopted to modify the 2D DLA cluster for explaining the experimental observations. Results of numerical simulations corroborate the experimental observations. Main effect of thermal relaxation under annealing of YAG fractal cluster is coarsening of fractal structure keeping the fractal dimension invariant. Coarsening of fractals aggregate indicate the nature of binding of the primary particle within aggregate. The particles are binding each other strongly, i.e., mobility of the atoms is less and at elevated temperature and they can move locally to the branches of the fractal clusters. In future, the restructuring of the 3D DLA aggregates under annealing will be tried and scattering profiles will be estimated directly, in order to compare the experimental results.

## **3.2. Smoothing of Non-Euclidean Surface of $\text{Nd}_2\text{O}_3$ Doped $\text{CeO}_2$ under Sintering**

### **3.2.1. Introduction**

Nano-crystalline materials, which have gained a tremendous attention in basic sciences as well as in technology since last decade, often form agglomerates because of their very small size. Often such agglomerates vis-à-vis the surface roughness of these nano-crystalline materials can be viewed as self-similar or self-affined fractal structures. Its fractal dimension defines the quantitative measure of such fractal agglomerates, which is different from its normal Euclidean dimension. Micro-structural evolution of such nano-crystalline ceramics under sintering is a crucial aspect as far as their various potential applications are concerned. In general, in sintering process, densification occurs via the path where surface energy is reduced by elimination of solid-pore interfaces. The reduction of free energy is facilitated by movement of materials from the region with higher radius of curvature to the lower radius of curvature causing densification. The surface microstructure as well as the agglomeration behaviour changes with the advancement of sintering process and mainly depends on sintering temperature/time.

Doped Ceria is an important material<sup>142,143</sup> in view of its potential applications<sup>144,145</sup> as a solid electrolyte for its use in oxygen concentration cells and in solid oxide fuel cells. In present section, evolution of mesoscopic surface of  $\text{Ce}_{0.50}\text{Nd}_{0.50}\text{O}_{1.75}$  have been investigated using ultra small angle X-ray scattering (USAXS) under sintering. An attempt has been made to understand the USAXS results by performing a Monte Carlo based simulation.

### 3.2.2 Experimental

AR grade cerium nitrate [ $\text{Ce}(\text{NO}_3)_3 \cdot 6\text{H}_2\text{O}$ ],  $\text{Nd}_2\text{O}_3$ , and glycine ( $\text{NH}_2\text{CH}_2\text{COOH}$ ) were used as the starting reagents<sup>144</sup>. The further heat treatment of the  $\text{Ce}_{0.50}\text{Nd}_{0.50}\text{O}_{1.75}$  powder has been carried out at three temperatures namely, 800, 1000 and 1200°C, respectively. USAXS experiments have been carried out using a triple bounce channel cut crystal based USAXS instrument mounted on a rotating anode source<sup>146</sup>. Fig. 3.5a shows the USAXS profiles in double logarithmic scales and Fig. 3.5b depicts the same profiles in Porod plot ( $I(q)q^4$  vs  $q$ ) in order to show the variation of the slope of the different profiles at higher  $q$ .

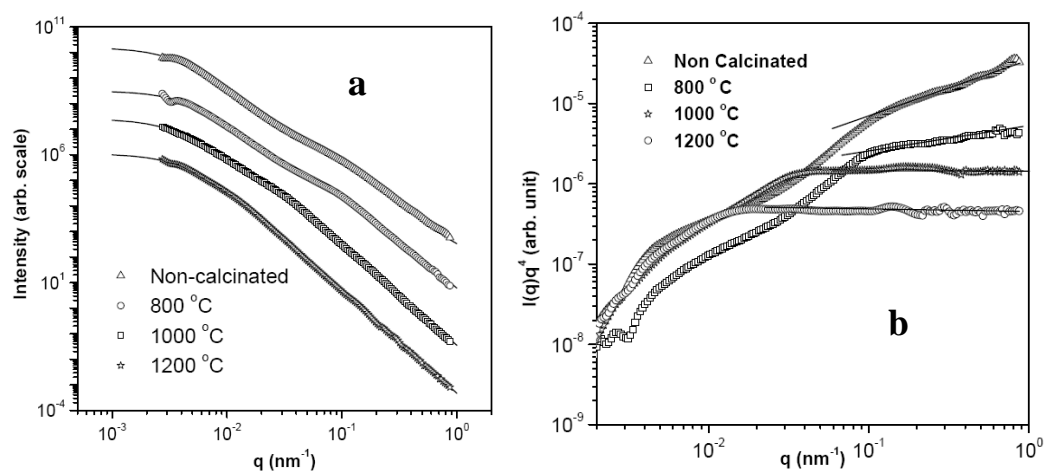


**Fig. 3.5** (a) USAXS profiles in double logarithmic scale. The solid lines are model fit to the data. (b) USAXS profiles in Porod plot ( $I(q)q^4$  vs.  $q$ ).

### 3.2.3. Data analysis

From Fig. 3.5a, it is discernible that scattering profile for non-sintered sample shows a straight-line behaviour in log-log plot (i.e., a power law relationship with  $q$ ). In addition, there is a slight change in slope at around  $q \sim 0.1 \text{ nm}^{-1}$  where appears a small hump. From Fig. 3.5b, it is evident that the slope of the profile is not equal to 4 at any part of the  $q$  range. The exponent of power law for  $q > 0.1 \text{ nm}^{-1}$  is  $\sim 3.4$  for non-sintered sample. It is also evident from Fig. 3.5b that high  $q$  part of the profile is significantly affected by sintering; particularly slope at high  $q$  region. With increase in temperature of sintering, value of slope at high  $q$  part tends to be  $\sim 4$  and hump at  $q \approx 0.1 \text{ nm}^{-1}$  disappears. The above observations, along with the nature of the high  $q$  region, guide us to analyze the data in terms of fractal model. For non-sintered sample, negative exponent of power law (for  $0.1 \text{ nm}^{-1} < q < 1 \text{ nm}^{-1}$ ) is estimated to be nearly 3.4. This hints that the surface of agglomerated particles may be viewed as a fractal surface. It is observed from Fig. 3.5b that negative exponent of power law gradually reaches to 4 with increasing temperature indicating a smoothing of surface. For non-sintered samples, intensity also increases below the hump at around  $q \approx 0.1 \text{ nm}^{-1}$ . The total intensity profile  $I(q)$  for the samples has been modeled as following.

$$I(q) = C_s q^{-1} (1 + q^2 \xi_s^2)^{\left(\frac{D_s - 5}{2}\right)} \sin((D_s - 1) \tan^{-1}(q \xi_s)) + \frac{C_a}{(1 + q^2 \xi_a^2)^n} \quad (3.5)$$

where first term corresponds to scattering from fractal surface<sup>147</sup> and second term is Debye-Büche term<sup>148,149</sup> to account for increase below the hump. Such increase is due to agglomerated volume at relatively larger length scale. Shah et al.<sup>149</sup> have used the Debye-Büche function to interpret their data on dense highly polydisperse fractal aggregates.  $C_s$  and  $C_a$  are scale factors and  $\xi_s$  is upper cut-off of surface fractal. For sample sintered at highest temperature ( $1200^\circ \text{ C}$ ), first term alone is able to describe the whole profile (which follows a

Porod behaviour ( $q^{-4}$  at high  $q$  region) and in this case surface becomes smooth in nature, i.e.,  $D_s$  becomes 2.

### 3.2.4. Monte Carlo based computer simulation and discussions

Monte Carlo method provides a platform to simulate various stochastic processes in materials science. The area of fractals has also been enriched, since last two decades, by applying this technique. Self-similarity and fractal nature of a rough interface has been studied using two-dimensional Monte Carlo technique<sup>150</sup> by Mon et al. Scaling of rough surfaces under surface diffusion has been investigated using a random deposition model in two dimensions<sup>151,152</sup>. Very recently, a stochastic simulation model has been applied to model the three-dimensional morphology of nano-scale aggregates formed by concurrent coagulation and sintering<sup>153</sup>.

To understand the USAXS results, i.e., the smoothening of the fractal surface under sintering, a Monte Carlo based simulation has been attempted. The basic steps of the simulations are the following. Initially, a fractal surface with a particular surface fractal dimension is generated using Fourier filtering based spectral synthesis method<sup>154</sup>.

Based on the Fourier filtering spectral analysis method<sup>154</sup>, an initial self-affined surface (200 X 200 system size) having a fractal dimension of 2.6 has been generated and is shown in Fig. 3.6a. The left part of Fig. 3.6a shows surface morphology and right part shows contour of the same surface. At this point, it should be mentioned that spectral density  $S(k)$  for a self-similar objects exactly follow a power law, i.e., a straight line behaviour in  $\log(S(k))$  vs.  $\log(k)$  plot. Verification of fractal nature (with fractal dimension 2.6) is done by calculating the linearity of  $\log(S(k))$  vs.  $\log(k)$  curve as shown in Fig. 3.6b.

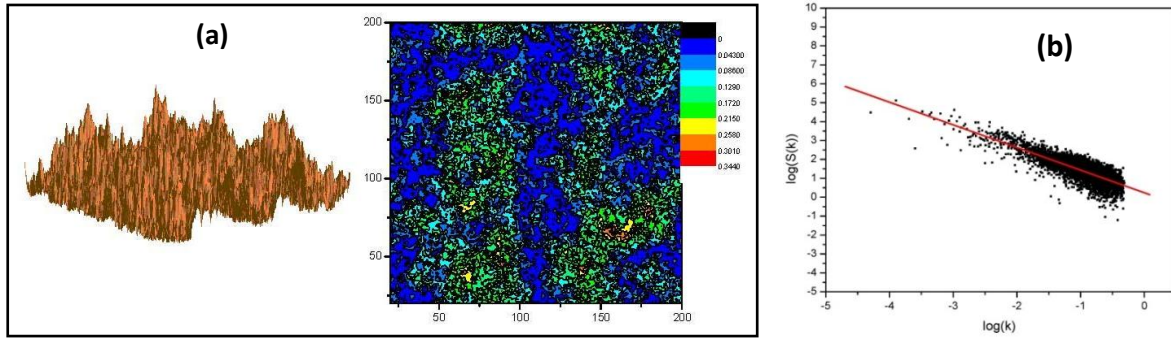


**Fig. 3.6** (a) The initial self-affine fractal surface simulated using spectral synthesis method for a fractal dimension 2.6 (b)  $\log(S(k))$  vs.  $\log(k)$  for the initial fractal surface with fractal dimension 2.6.

Once fractal surface is generated, effect of sintering under different temperature conditions has been studied by modifying the surface according to movement of materials via diffusion mechanism. The algorithm followed in the present case is as follows.

Let  $h(x, y)$  defines the height of any randomly chosen point  $P(x, y)$  on the fractal surface. First, it is checked whether the point  $P$  has a positive local roughness which is defined as the difference between the height of  $P$  and the average height of all the nearest neighbours. Then another point  $P'(x', y')$  on surface is chosen randomly. If the point  $P_1$  (at height  $(h'(x', y'))$ ) has a negative local roughness, then local roughness difference ( $\Delta\gamma$ ) and height difference ( $\Delta h$ ) is calculated. If the activation energy is  $\Delta E$  at temperature  $T$ , then diffusion coefficient is proportional to  $\text{Exp}(-\Delta E/K_B T)$ . The probability ( $\Omega$ ) of material movement from one site to another will depend on activation energy due to local roughness difference. Hence, probability of material movement can be written  $\text{Exp}(-\Delta\gamma/T_1)$ , where  $T_1$  is a factor which is proportional to temperature  $T$ . Depending on the above probability, mass transfer takes place during sintering, i.e., height of the point  $P(x, y)$  is modified to  $h(x, y) - \Omega \times (\Delta h/2)$  and that for the  $P'(x', y')$  is modified to  $h'(x', y') + \Omega \times (\Delta h/2)$ . The average width ( $W = \sqrt{\sum [h(x,y) - \bar{h}]^2 / N^2}$ , where  $\bar{h}$  is the average height and  $N \times N$  is the system size) of the surface

is calculated at each iteration. The average width  $W$  starts decreasing sharply initially and decreases slowly after a reasonably large time step when surface is nearly equilibrated at a particular temperature. Long time width ( $W$ ) of the surface is noted for various  $T_1$  values. Equilibrated surface has been registered. The spectral density  $S(k)$  of the surfaces at various  $T_1$  values is calculated. The modification in fractal nature of the initial surface is noted by plotting the  $\log(S(k))$  vs.  $\log(k)$  for different values of  $k$ . If the fractal correlation exists in the structure, the curve  $\log(S(k))$  vs.  $\log(k)$  can be fitted to a straight line and fractal dimension can be estimated<sup>154</sup> from slope of the straight line. Here it should be mentioned that in reality mass transfer from one site to the other distant site could occur via the nearest neighbours only. However, in the simulation process this corresponds to a very huge number of Monte Carlo steps vis-à-vis an enormously large computation time. However, as we are presently interested only in the effect of sintering temperature under large sintering time, mass transfer from one source site to another distant target site, other than the nearest-neighbours sites, was also allowed keeping the number of Monte Carlo steps constant for all temperatures. In fact, this corresponds to the sintering phenomenon at various temperatures for a fixed sintering time. It also important to mention at this juncture that in the activation driven process, particles can also move from a point having lower local roughness to a point having higher local roughness with a small probability. However, this process will take long time and is difficult to handle as far as computation time is concerned. However, this approximation may lead to different shape of the width vs. temperature curve.

The contour of the surface at various  $T_1$  ( $T_1 \propto$  Temperature) value are plotted in Fig. 3.7. It is evident from the figure that surface roughness is getting reduced gradually as  $T_1$  is increased. At high enough temperature the surface roughness almost remains absent.

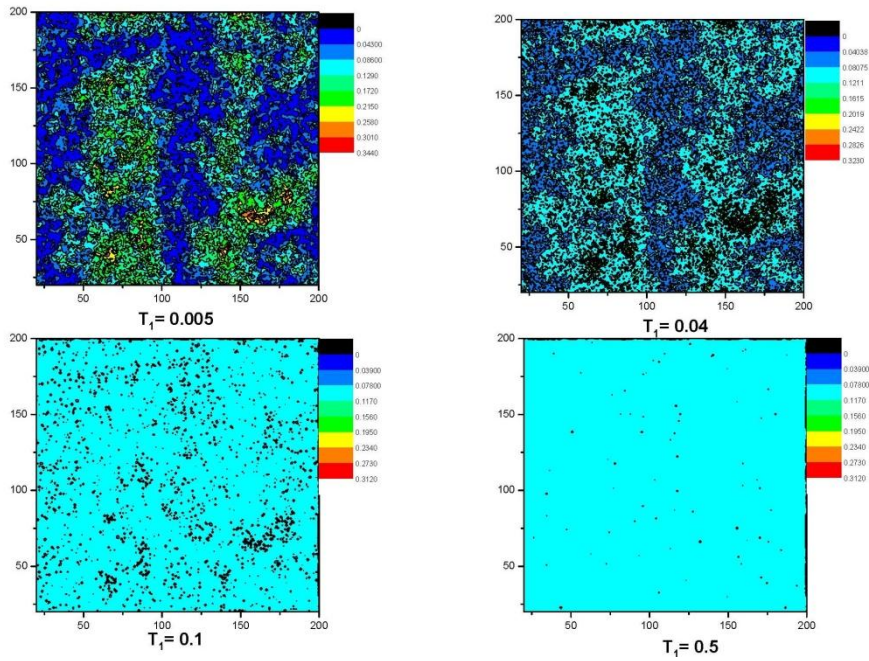


**Fig. 3.7** The surfaces for increasing  $T_1$  values are depicted. It is evident that the surface becomes smoother with increase in  $T_1$ .

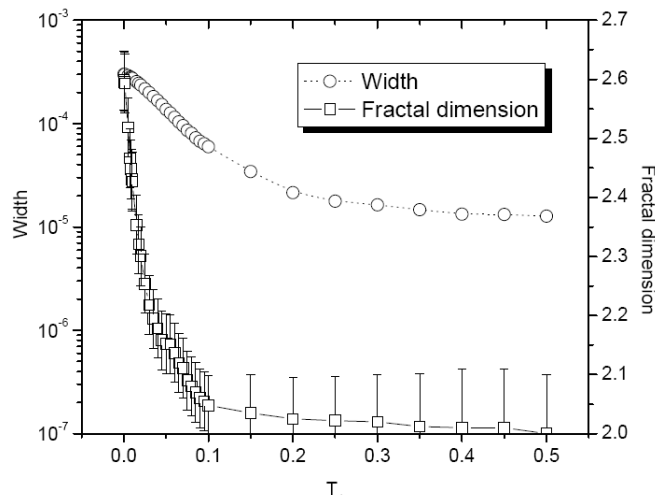


**Fig. 3.8** The reduction of the surface width and the decrease of the fractal dimension with increase in  $T_1$  are depicted.

The variation of the surface width ( $W$ ) and the calculated fractal dimension of the sintered surface with varying  $T_1$  values are plotted in Fig. 3.8. It is seen that the value of  $W$  decreases gradually with temperature. The fractal dimension decreases more sharply than the width.

At this juncture, it is to be noted that the present simulation aims to understand the effect of annealing on the fractal morphology. Since, in present case, the annealing time is sufficient to reach equilibrated surface morphology at each temperature, the time dependent simulation i.e. Brownian dynamics is not needed. However, at high temperature activation dependent diffusion will increase. Hence, it was important to take account the diffusion during MC simulation in present work.

### **3.2.5. Conclusions**

USAXS study revealed that a relatively high surface fractal dimension ( $\sim 2.6$ ) in the non-sintered ceramic gradually reduces to the normal Euclidean surface dimension of 2.0 at high sintering temperature. Monte Carlo based computer simulation establishes that such smoothening of fractally rough surface under sintering is possible due to diffusion transport of materials from regions of higher local roughness to lower one. Surface fractal, being in meta-stable state, tries to minimize its surface energy during sintering; a smooth surface gradually develops with increase in sintering temperature.

## **3.3. Temporal Evolution of Characteristic Length and Fractal Dimension for a Non-Euclidean System**

### **3.3.1. Introduction**

Temporal evolution of mesoscopic structures in condensed systems has received a considerable attention in recent years altogether from experimental, computational and theoretical points of view. This is due to the relevance of this phenomenon in a wide variety of materials including technologically important materials like cements<sup>95,96,129</sup>, alloys<sup>155-166</sup>, ceramics<sup>167-169</sup>, xerogels<sup>170</sup>, polymer<sup>171-176</sup>, glasses<sup>177-188</sup>, liquid mixture<sup>189-195</sup> etc. The new phase formation is an example of first order phenomenon and is a highly non-linear process

far from equilibrium. The second phase starts growing in size, after the formation, with time and is influenced by several thermodynamical parameters. The phenomenon indicates an emergence of morphological pattern of the domains at earlier times looking statistically similar to patterns at later times, apart from the global change of scale implied by the growth of a characteristic length  $L(t)$ -a measure of the time dependent domain size of the new phase.

The characteristic length  $L(t)$  is estimated from scattering profiles as follows,

$$L(t) = \left( \frac{\int q I(q, t) dq}{\int I(q, t) dq} \right)^{-1}. \text{ For a non-Euclidean system}^{90}, \text{ like hydrating cement paste,}$$

understanding the growth of second phase constitutes an important area of research because porosity, microstructure, interconnectivity etc., are important properties of final cement product.

Hydrated cement paste has been known to possess non-Euclidean geometry over a wide length scale. Hydration reaction on a fractal network of cement grains eventually gives rise to space filling effect and interlocking between the cement grains. During hydration reaction, calcium silicates, main constituent of cements, react with water and produce calcium silicate hydrate (C-S-H) gel and calcium hydroxide. The gel, formed by hydration reaction, starts filling space around and between cement particles by diffusion based mass transport, locking the mass together. By this dynamical process of hydration, fractal morphology of hydrated mass evolves with time and object with non- Euclidean geometry gradually gets modified towards a consolidated Euclidean mass. The hydration kinetics determines the rate of dynamical evolution of the fractal dimension and the overall characteristic length scale. The kinetics depends on cement ingredients, cement to water ratio, humidity etc.

To understand the new phase formation and the evolution of new phase in non-Euclidean systems, real time ultra small-angle neutron scattering (USANS) investigations<sup>95,96,129</sup> on hydrated paste of tri-calcium-silicate ( $3\text{CaO}\cdot\text{SiO}_2 \equiv \text{C}_3\text{S}$ ), di-calcium-silicate ( $2\text{CaO}\cdot\text{SiO}_2 \equiv \text{C}_2\text{S}$ ), ordinary Portland cement (OPC) and calcium sulphates were performed. It is worthy to mention that these studies indicated non-uniqueness in the trend of dynamical evolution in these systems. It is to be noted that  $\text{C}_3\text{S}$  and  $\text{C}_2\text{S}$  are the two major components of ordinary Portland cement which is actually a mixture of several silicate and calcium aluminate phases. The hydration kinetics of  $\text{C}_2\text{S}$  and OPC is same as that for  $\text{C}_3\text{S}$  at least in qualitative manner<sup>96</sup>. It was shown<sup>95,96</sup> that hydration reaction of calcium silicates ( $\text{C}_3\text{S}$  and  $\text{C}_2\text{S}$ ) and ordinary Portland cements (OPC) with light water, the fractal dimension starts increasing just after the onset of the hydration reaction and then it reaches a plateau. Further, temporal evolution of the square of the characteristic length ( $L$ ) of the system mimics the functional trend of evolution of the fractal dimension ( $D_f$ ) (Fig. 3.9a for  $\text{C}_3\text{S}$  with cement to water ratio 30 %).

It is interesting to note that these observations indicate that two physical quantities, characteristic length and fractal dimension, having different dimensionality (as fractal dimension is a dimension less quantity while characteristic length has a dimension of length) reaches to a plateau almost at the similar time and almost in a similar fashion (Fig. 3.9a). What remains to be understood is whether the similarity of temporal evolution patterns of altogether two different physical quantities an accidental one. But repeated measurements<sup>96</sup>, varying over wide range of composition, brought out this phenomenal accidental similarity.

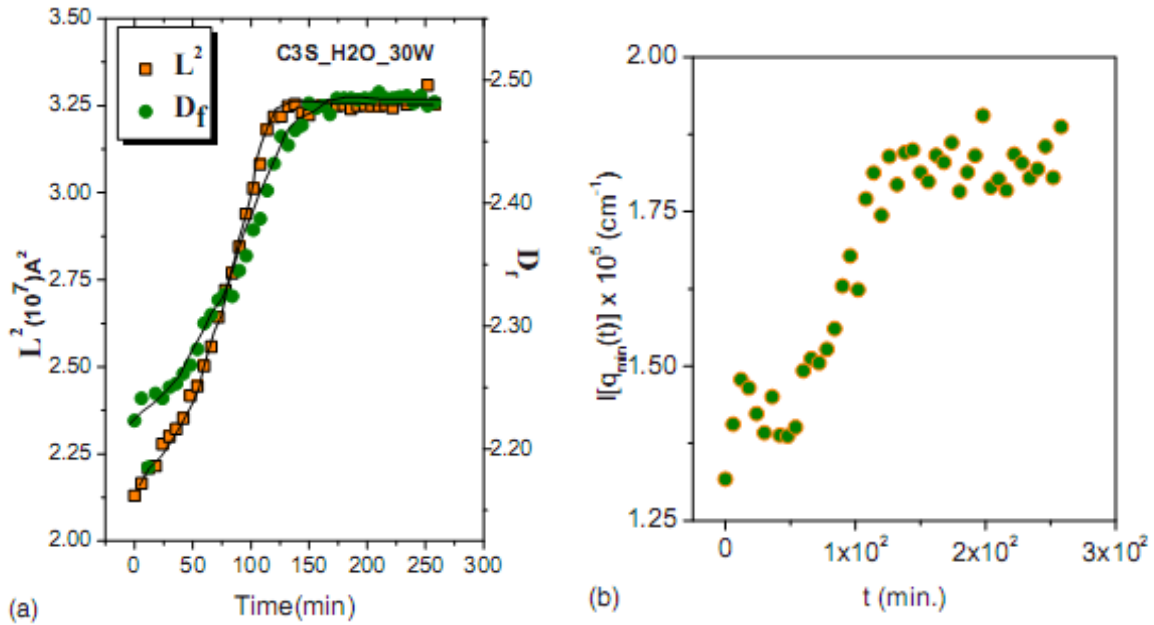


**Fig. 3.9** (a) Evolution of fractal dimension and square of the characteristic length with hydration time as observed from the USANS experiments (b) Evolution of USANS intensity at  $q \sim 0$  with hydration time.

In fact, such incomprehensible observation prompted us to understand the evolution in detail by performing a model simulation. Further, the scattering intensity at the minimum accessible  $q$  also showed a similar trend (Fig. 3.9b), i.e., it reaches a plateau after a transient time as shown by fractal dimension and characteristic length.

In the present section, a model simulation has been attempted in order to understand some of the above USANS experimental observations on dynamical evolution of mesoscopic structure during cement hydration.

### 3.3.2. Computer model and the results on structure evolution during cement hydration

It is well established that during hydration reaction cement particles and C-S-H gel system constitute non-Euclidean fractal morphology<sup>167-169,198</sup>. For simplicity, the initial structure (i.e., the structure just after onset of hydration reaction) of the cement-gel system, in the present

case, has been represented by a DLA kind of fractal structure. Further, to avoid the huge computation time while modeling for the evolution of this structure during hydration, the simulation has been restricted in two dimensions only.

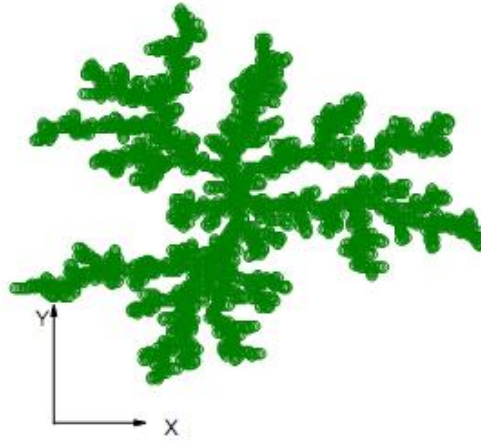


**Fig. 3.10** *The initial fractal object generated using DLA model, just at the onset of the hydration.*

Fig. 3.10 depicts the initial structure (consisting of 3000 lattice points) obtained from DLA approach. It is noteworthy to mention that the Fractal dimension for a 2D DLA cluster is  $\sim 1.67$  and the corresponding Euclidean dimension is two. Any lattice site with all nearest neighbor sites filled is denoted as a “*saturated site*” while a site with unfilled neighbours is denoted as an “*unsaturated site*”. In the next step, the evolution of this structure has been investigated in the light of cement hydration.

The initial DLA structure gets modified because of the onset of the hydration reaction at the available sites (Fig. 3.10). As the time proceeds, the gel fills the available space and gradually, the structure tends to be a consolidated one. However, the speed of the smoothening process depends on the rate of the reaction kinetics. The present simulation proceeds in the following way. A lattice site  $N(X, Y)$  on the cluster is chosen at random. Let us consider that the probability of onset of hydration reaction is  $p$ . If the site is an ‘*unsaturated*’ one, then one of the available sites is selected according to the given

probability  $p$ . In this simulation, the available sites were restricted within a zone of maximum linear extent of the initial cluster. This restriction arises because of the fact that another cluster adjacent to this present cluster will not allow the growth beyond the zone of maximum linear extent of the former cluster. Once, the site is chosen for the onset of hydration reaction, the site is filled and becomes a part of the cluster. The fractal dimension at various instance of the evolving cluster is calculated using box counting method. The evolution of the fractal dimension with Monte Carlo steps for different  $p$  values is plotted in Fig. 3.11a. The effective characteristic length was considered as the square root of the total area of the evolving cluster at any particular instant. The evolution of the characteristic length  $L$  with Monte Carlo simulation, as obtained from the present simulation, has been depicted in Fig. 3.11b.

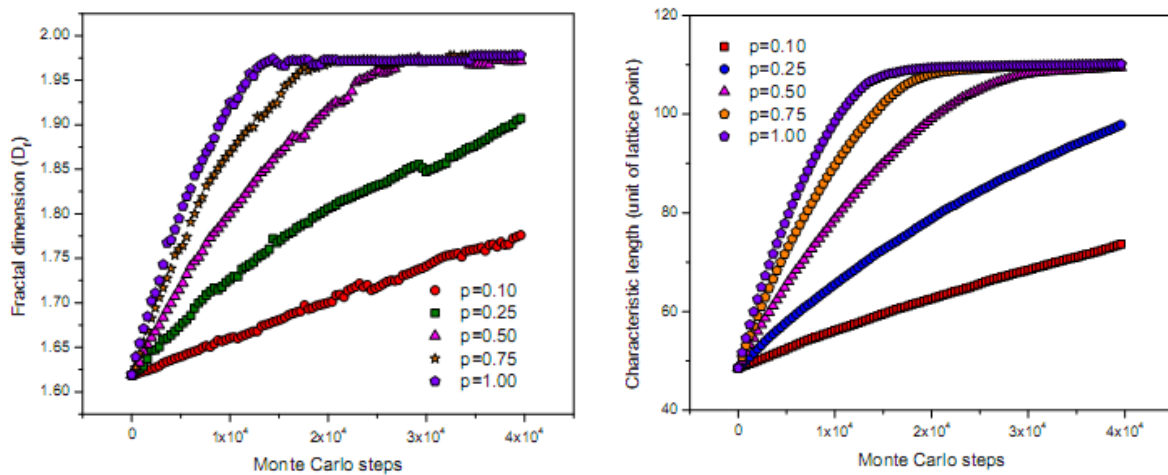


**Fig. 3.11** (a) The evolution of fractal dimension with Monte Carlo steps (b) The evolution of characteristic length with Monte Carlo steps.

The functionality of the evolution of the fractal dimension and the characteristic length are compared in Fig. 3.12 for  $p=1$ . The shapes of the evolving cluster for different Monte Carlo steps for  $p=1$  is depicted in Fig. 3.13.

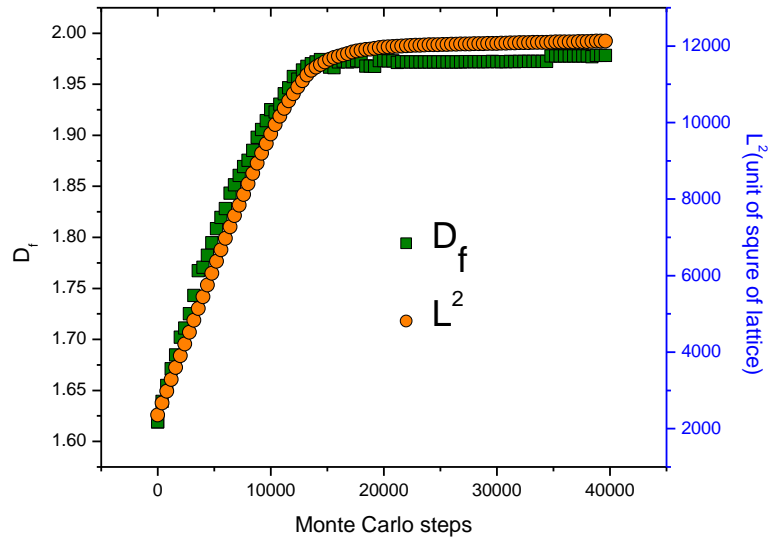


**Fig. 3.12** Evolution of the fractal dimension and square of the characteristic length with Monte Carlo steps.

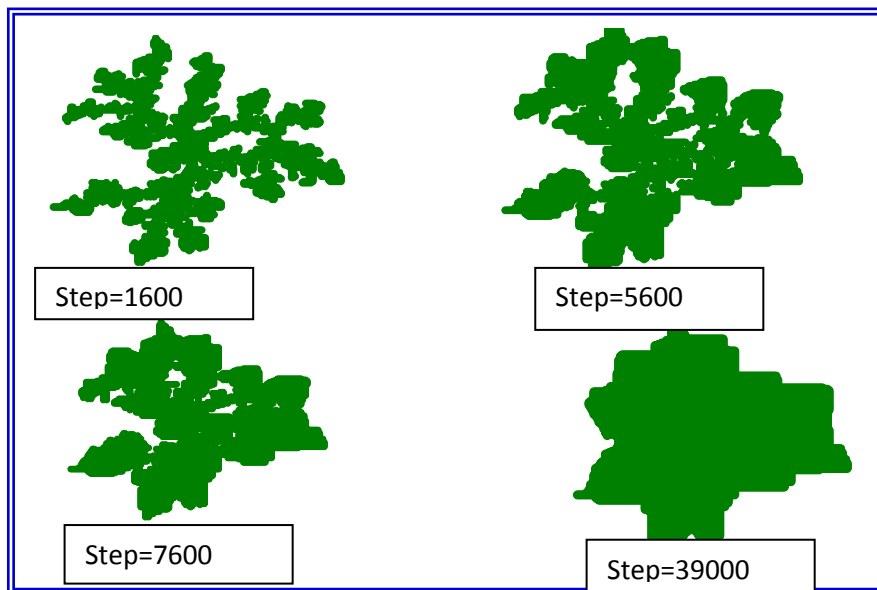


**Fig. 3.13** The morphology of the evolving cluster at different Monte Carlo steps for  $p=1$ .

From Figs. 3.11a and 3.11b, it is evident that the onset of hydration reaction leads to the attainment of more compact structure as both the fractal dimension ( $D_f$ ) and the square of characteristic length scale ( $L$ ) increases. From, Fig. 3.12, it is evident that the nature of the evolution for  $D_f$  and  $L^2$  are almost similar and both of them reaches a plateau at the same

value of the Monte Carlo steps. This corroborates with the trends as observed from the USANS experiments on normal light water hydration of  $C_3S$ ,  $C_2S$  and OPC. Instead of possessing different dimensionality, two physical quantities, fractal dimension (dimensionless quantity) and characteristic length (having a dimension of length) reaches a plateau almost at the same time and almost at same fashion. This may be explained by the fact that the increase in the fractal dimension by the space filling gel occurs within the zone of maximum linear extent of a cluster due to the spatial constraint of the adjacent cluster and hence the modification in the fractal dimension is associated with the similar modification in characteristic length scale. The exact functional variation of  $D_f$  and  $L^2$  obtained by the present model simulation differs slightly at initial time. This may be due to appearance of closed pore during hydration. The model will be refined in near future to account the effect of presence of closed pores during hydration.

### **3.3.3. Conclusions**

Monte Carlo based model simulation showed that the evolution of the fractal dimension of non-Euclidean cluster of hydrated cement paste proceeds by space filling effect of the C-S-H gel during hydration reaction. The model corroborates well with the trend of evolution of the fractal dimension and the characteristic length as observed by USANS measurements on calcium silicates ( $C_3S$  and  $C_2S$ ) and ordinary Portland cements (OPC). Further, it also supports the appearance of plateau for the above physical quantities nearly at the same time during hydration.

# Hierarchical nano-composites via evaporation induced assembly under non-buckling regime

## 4.0. General Introduction

Self assembly<sup>10,11</sup> is generally considered as the most promising means for designing and controlling the bottom up approach to synthesize structures with varied geometries like spheres, doughnuts, sheets, tubes, wires etc. A process of fabricating micrometric solid particles with internal nano structures is of potential interest for a variety of practical applications<sup>199,200</sup>, especially in fabricating nano devices.

In recent years, spray drying<sup>12</sup> has been found a special place in synthesizing hierarchically structured grains by atomizing a colloidal suspension into droplets and then converting these droplets into nanostructured grains. Micrometer-sized particles possessing mesoscopic pores may be synthesized by this technique. These porous materials are potential candidates for various applications, such as catalysis<sup>201-204</sup>, chromatography<sup>205-208</sup>, drug delivery<sup>209,210</sup>, hosts for optically active compounds<sup>211,212</sup> etc. Control of morphological properties of assembled grains is a crucial factor as far as the design of functional materials<sup>213-218,219-223</sup> is concerned. It is important to note that in this process, droplets do not remain in contact with any substrate. Due to absence of contact line with any substrate, surface tension does not play significant role.

During drying process, colloidal droplets undergo a variety of mechanical processes that are of both fundamental and practical interest<sup>224-227</sup>. The receding surface of drying droplet gives rise to a particle-dense region at surface of the droplet during drying. As drying

continues, particles on air-water interface eventually reach a limit of jamming such that inter-particle repulsions resist further packing. The solvent, however, continues to evaporate through the porous membrane formed by particles interstices. The decrease in solvent volume results the fluid menisci between the closely packed particles. This causes the formation of the menisci at air-water interface and the droplet pressure to decrease<sup>225-228</sup>. The decrease in droplet pressure exerts a compressive capillary stress on the particle shell. If stress due to capillary force on the drying droplet is less than the repulsive force between particles, the shell manifests viscoelastic behaviour<sup>229-231</sup> and droplets shrink isotropically resulting to a spherical grain. Drying in this case is said to occur in non-buckling regime. If the stress on the drying droplet is larger than the repulsive force between particles, shell behaves as elastic shell and responds to the stress leading to a buckling of the shell which may results into hollow or buckled grains. In such a case, the drying is said to occur in buckling regime.

The quantitative measure of the strength of drying is represented by Peclet number  $P_e$  and is defined as the ratio of  $R^2$  and  $D\tau$ , where  $R$  is radius of droplet,  $D$  is diffusion coefficient of colloidal particles in droplet and  $\tau$  is drying time. If Peclet number  $P_e \gg 1$ , drying is said to be fast or in buckling regime and there is a formation of hollow or crumpled grain during drying. However, if Peclet number  $P_e \ll 1$ , drying process is regarded as slow process or in non-buckling regime and the droplets shrink isotropically throughout the drying process resulting into spherical grain<sup>12,231-233</sup>.

#### **4.1. Evaporation-induced Self assembly of Nanoparticles in Non-buckling Regime: Effect of Initial Colloidal Concentration**

##### **4.1.1. Introduction**

In the slow drying condition, NPs get enough time such that they assembled in a uniform fashion in the grain. However, this should also depend on the diffusion coefficient of the

particles inside the drying droplet. Diffusion coefficient, in turn, depends on the viscosity of initial suspension. Thus, uniformity of packing may be modified by varying colloidal concentration vis-à-vis viscosity. In order to investigate the effect of colloidal concentration on packing of NPs inside grains in slow drying regime, spray drying experiments have been performed on silica colloids with different concentration of initial suspension.

#### 4.1.2. Experimental methods

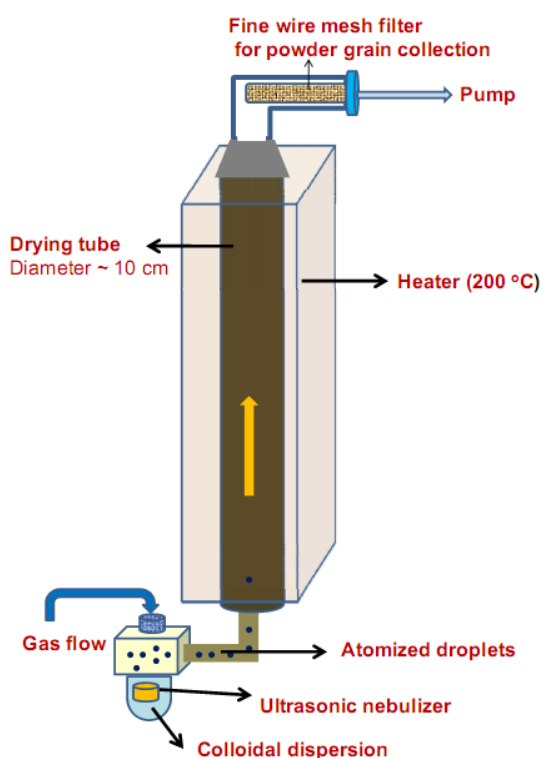


**Fig. 4.1** *The schematic of the spray dryer utilized for slow drying experiment.*

Initial 40 wt% silica colloidal dispersion was diluted to make 20%, 10%, 5% and 2.5% dispersions. Spray drying of the dispersions was carried out using an in-house spray dryer<sup>234</sup>. A schematic diagram of the spray dryer is depicted in Fig. 4.1. The instrument consists of a cylindrical drying chamber of ~10 cm in diameter and of 100 cm in length. The droplets were generated using an ultrasonic nebulizer at the bottom of the spray dryer. The feed rate was kept at ~ 60 ml/hr. The temperature of the oven was kept at 160 °C. The aspiration value was

kept at 40 liter/ min. The dried micrometric powder grains were collected at the end of the drying chamber using a wire mesh filter. Powders collected from wire mesh, for 2.5%, 5%, 10% and 20% colloid dispersions were denoted as sp-2.5, sp-5, sp-10 and sp-20, respectively.

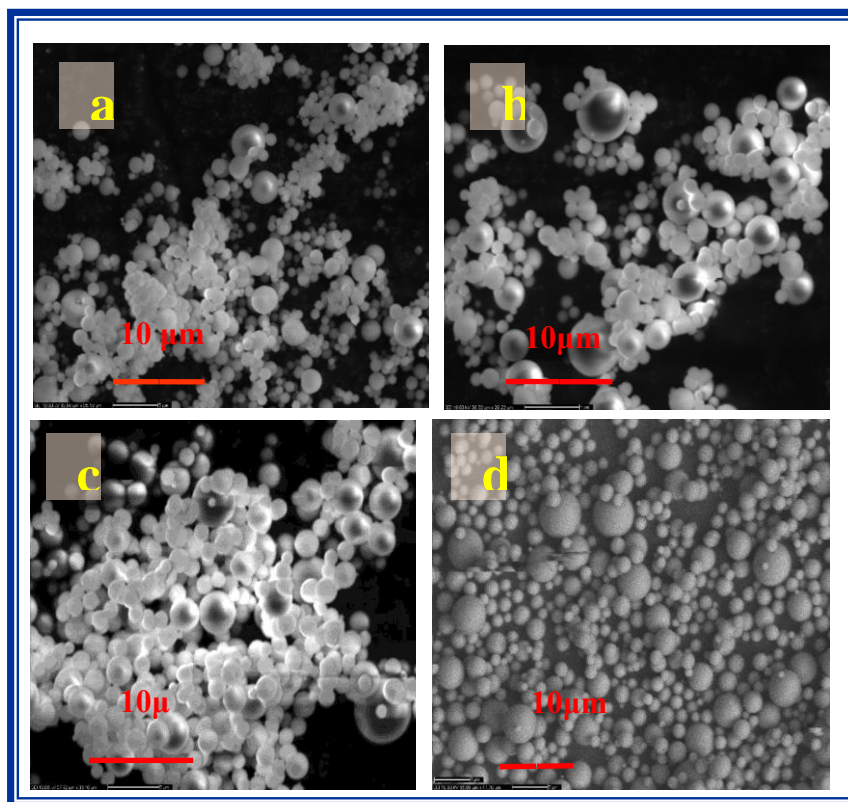


**Fig. 4.2** SEM micrographs of (a) sp-2.5 and (b) sp-5 (c) sp-10 and (d) sp-20 specimens.

The assembled dried grains were characterized using SEM, SANS and DLS. Micrographs of sp-2.5, sp-5, sp-10 and sp-20 samples have been depicted in Fig. 4.2.

In order to access a wide range of  $q$ , SANS experiments on spray dried samples were performed using two instruments: (i) a double crystal based SANS facility and (ii) a 5 meter long conventional slit geometry instrument at Guide Tube Laboratory of Dhruva reactor, Mumbai, India. Fig. 4.3a depicts the SANS profiles in Porod representation ( $I(q)q^4$  vs.  $q$ ) in absolute scale ( $\text{cm}^{-5}$ ) for different specimens.

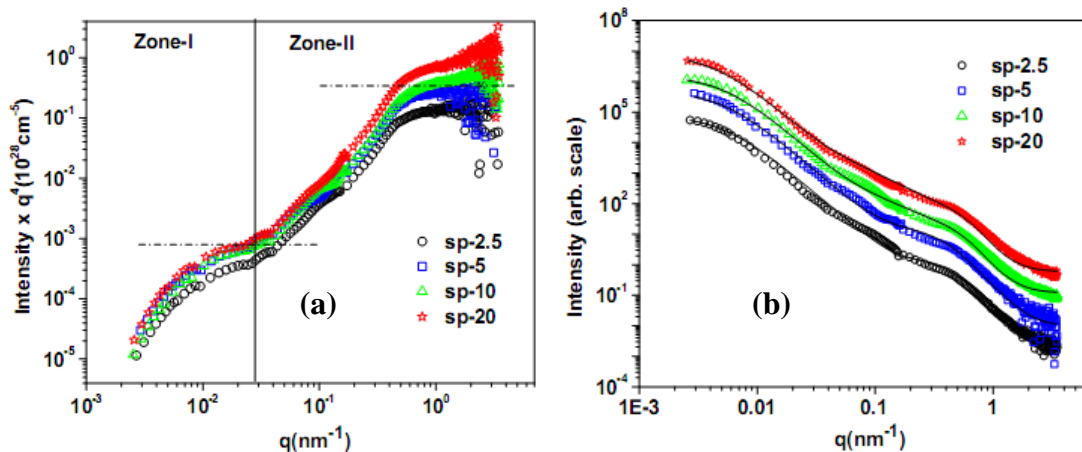


**Fig. 4.3** (a) SANS profiles in Porod plot ( $I(q)q^4$  vs.  $q$ ) indicating two level structures (b) SANS profiles in log-log plot and corresponding fit of profiles in line. The profiles are shifted vertically for clarity.

Size distributions of the dried grains as obtained from DLS measurements are depicted in Fig. 4.4. The average size of the grains has been estimated by DLS measurements. The polydispersity in the grains has been represented as percentage ratio of standard deviation to the average size of the grains. The estimated size of the grains and polydispersity has been tabulated in Table 4.1.

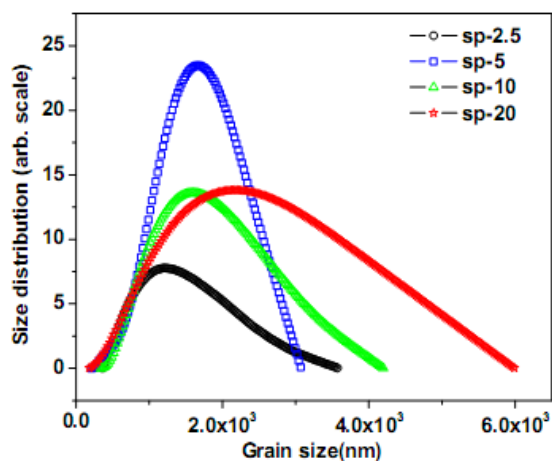


**Fig. 4.4** Estimated size distribution of the grains from analysis of DLS data.

### 4.1.3. Results and discussion

Peclet number  $P_e$  for present experimental conditions has been estimated<sup>240</sup> to be 0.05 which is much less than unity. Thus, it is evident that spray drying of colloidal silica has been carried out in a slow drying regime. The spherical shape of self assembled grains for all the samples is evident from Fig. 4.2. This in turn also indicates that present situation for drying complies with slow spray drying regime, i.e., a non-buckling regime. It is also evident from SEM micrographs that size of dried grains increases with increasing colloidal concentration. It is noteworthy that polydispersity in size of assembled grains has been observed because of fluctuations in atomization process.

Scattering profiles for sp-2.5, sp-5, sp-10 and sp-20 samples indicate two length scale structure of assembled grains as evident from two distinct zones in Fig. 4.3. It is evident from SEM micrographs that dried grains are of one to two micrometer in size. The maximum accessible length scale by MSANS facility is approximately 1000 nm. Thus, present SANS data could reveal the internal structure of grains well and only a part of size distribution of assembled grains. The total scattering intensity  $I(q)$  from dried grains may be represented by,

$$I(q) = C_0 I_s(q) + \frac{C_1}{1 + q^2 \xi^2} \quad (4.1)$$

where,  $C_0$  and  $C_1$  are  $q$  independent scale factors that depend on volume fraction, contrast etc.

$I_s(q)$  corresponds to the scattering contribution from jammed silica particles and is given by

$$I_s(q) = \frac{\int_0^{\infty} P_s(q, r) D(r) v^2(r) S(q, r) dr}{\int_0^{\infty} v(r) D(r) dr} \quad (4.2)$$

where,  $P_s(q,r)$  represents the normalized spherical form factor of colloids with radius  $r$ .  $S(q, r)$  is inter-particle structure factor. It depends on the type of interaction and also on volume fraction  $(\phi_v)_g$  of silica NPs in the grain.  $D(r)$  represents size distribution of NPs inside grains. It is important to discuss that SANS data for the internal structure of spray grains (eq. 4.2) has been analyzed by assuming local monodisperse approximation<sup>235</sup> to include the effect of polydispersity on the structure factor  $S(q, r)$ . This approach works better<sup>218,235</sup> than the decoupling approximation<sup>236</sup> for the systems with larger polydispersity and higher concentration. It is to be noted that the polydispersity in the initial silica colloids, taken for spray drying experiments, is significant hence local monodisperse approximation works better in present case<sup>240</sup>.

The second term is Debye–Bueche type term in order to take into account the scattering contribution from overall grains. The parameter  $\xi$  represents typical higher length scale of self assembled grain. Here, it is worthy to mention that this term validates Porod behaviour for  $\alpha=2$  at high  $q$  and also obeys Guinier behaviour at low  $q$ . The fit (Fig. 4.3b) of the model to the SANS profiles for the samples remain reasonable.

At this juncture, it is interesting to mention that self assembly of NPs during spray drying will also lead to some interstitial pores. The specific surface area  $\Sigma_{\text{meso}}$  of such mesopores has been estimated from scattering data as below,

$$\Sigma_{\text{meso}} = \frac{\lim_{q \rightarrow \infty} (Iq^4)}{2\pi\Delta\rho^2 d_s} \quad (4.3)$$

where,  $\Delta\rho^2$  represents scattering length density contrast between silica and air,  $d_s$  is density of silica NPs. It is important to note that calculation of specific surface area by the above equation require SANS profiles in absolute scale. SANS data analysis for powder samples is not quite simple as sample thickness is not known in such a case. In recent past, Spalla et

al.<sup>237</sup> presented a methodology for the analysis of SAS profile for granular media. The SANS data may be put in absolute scale ( $\text{cm}^{-1}$ ) by using the effective thickness of powder sample which is estimated by transmission measurements. The estimated specific surface area of the mesoscopic pore interface for different specimens has been tabulated in Table 4.1.

The parameters obtained from SANS and DLS analyses are also tabulated in Table 4.1. The grain size distributions obtained from DLS data were in agreement to that evidenced from SEM micrographs in a qualitative manner. It is seen from Fig. 4.4 that grain size distributions shift towards higher side of size with increasing initial colloidal concentration.

**Table 4.1** Parameters obtained from SANS and DLS

Colloidal concentration (wt%)	Silica volume fraction in dried grain $(\phi_v)_g$	$\xi(\text{nm})$	$\Sigma_{\text{meso}}$ ( $\text{m}^2/\text{gm}$ )	Average grain size ( $\mu\text{m}$ )	Polydispersity in the grain size (%)
2.5	$0.64 \pm 0.01$	189	10.4	1.59	40
5.0	$0.52 \pm 0.03$	189	20.0	1.73	36
10.0	$0.35 \pm 0.05$	189	30.0	1.97	39
20.0	$0.25 \pm 0.08$	223	48.0	2.73	41

The average atomized droplet size by an ultrasonic nebulizer may be written as,

$$R_d = k \sqrt[3]{\frac{\gamma}{\rho f^2}} \quad (4.4)$$

Where,  $\gamma$  is the surface tension of solution,  $\rho$  is the density of the solution,  $f$  is the ultrasonic frequency and  $k$  is proportionality constant.

Let us see the effect of silica volume fraction on density and viscosity of the dispersion prior to spray drying. Density of the dispersion with varying silica concentration has been

estimated by taking into account the proper weightage of silica and water in the dispersion. The effect of colloidal concentration on the relative density of the dispersion ( $\rho_r$ ) has been depicted in Fig. 4.5. It is evident from the figure that  $\rho_r$  varies only 10 % when concentration is increased from 2.5 % to 20%.

However, the effect of increase in silica volume fraction ( $\phi_v$ )<sub>d</sub> in the initial dispersion on viscosity of dispersion is much more significant as describe below (eq. 4.5)<sup>238,239</sup>. It is to be noted that the silica volume fraction ( $\phi_v$ )<sub>d</sub> in the dispersion is estimated by dividing the silica mass fraction ( $\phi_m$ )<sub>d</sub> by the density of the silica (2 g/cc). On expansion of  $\eta_r$  in terms of  $\phi_v$ , we obtain

$$\eta_r = 1 + 2.5\phi_v + 6.2\phi_v^2 + \text{higher order terms} \quad (4.5)$$

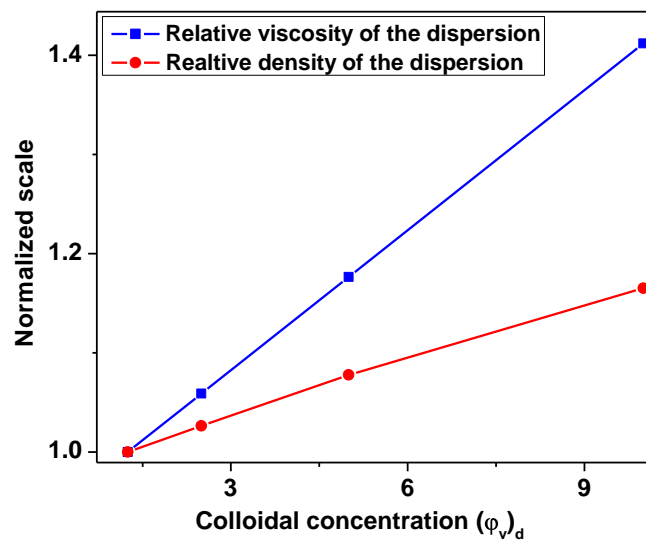


**Fig. 4.5** The effect of the colloidal silica concentration on the relative density and relative viscosity of the dispersion. X-axis represents the percentage silica volume fraction. The solid lines represent guides to the eye in both the curves.

Variation of relative viscosity of the dispersion with silica volume fraction is depicted in Fig. 4.5. Please note that in Fig. 4.5, the values of relative density and relative viscosity have been normalized at lowest concentration value for clarity. It is interesting to see that relative viscosity varies up to 40% when colloidal concentration is increased from 2.5 % to 20%. Thus, the effect of the silica volume fraction on relative viscosity of the dispersion is much more prominent as compared to the effect on relative density of the dispersion.

A relation between droplet size and grain size may be derived from mass conservation principle if coalescence of droplets during drying is neglected<sup>240,241</sup>. Suppose,  $(\phi_v)_d$  is silica volume fraction of colloid,  $V_{\text{droplet}} = \frac{4\pi}{3} R_d^3$  is volume of droplet with radius  $R_d$  and  $d_s$  is the silica density.  $(\phi_v)_g$  is volume fraction of the silica in dried grain,  $V_{\text{grain}} = \frac{4\pi}{3} R_g^3$  is volume of grain with radius  $R_g$ ,

$$(\phi_v)_d V_{\text{droplet}} d_s = (\phi_v)_g V_{\text{grain}} d_s \Rightarrow (\phi_v)_d \frac{4\pi}{3} R_d^3 = (\phi_v)_g \frac{4\pi}{3} R_g^3$$

$$\frac{R_g^3}{R_d^3} = \frac{(\phi_v)_d}{(\phi_v)_g} \Rightarrow R_g = R_d \left[ \frac{(\phi_v)_d}{2(\phi_v)_g} \right]^{\frac{1}{3}} \quad (4.6)$$

Where,  $(\phi_m)_d d_w = (\phi_v)_d d_s$  and  $(\phi_m)_d$  is the silica weight fraction in initial colloidal dispersion. Silica density  $d_s$  is assumed to be 2.0 gm/cc.

It is evident from the eq. 4.4 that size of the droplet depends on density of dispersion. It is shown in Fig. 4.5 that density of silica dispersion increases up to 10% when concentration of dispersion is increased to 20 wt%. Size of the initial droplet depends on cube root of the density, thus the effect of concentration of initial dispersion on droplet size may be approximately 3%, when concentration of dispersion is increased to 20%. Therefore, it is a

good approximation that initial droplet size obtained by ultrasonic nebulizer is approximately independent of initial concentration of silica dispersion.

From eq. 4.6, it is discernible that radius of grain  $R_g$  and  $(\phi_m)_d$  should follow a power law relationship with an exponent  $1/3$ , if volume fraction of silica NPs in the grain  $(\phi_v)_g$  is constant. In Fig. 4.6a, grain radius  $R_g$ , as estimated by DLS, is plotted as a function of colloidal concentration  $(\phi_m)_d$  in log-log plot. This shows a non-linear behaviour indicating that  $(\phi_v)_g$  is not constant but depends on the initial colloidal concentration. Specific surface area  $\Sigma_{meso}$  due to mesopores between silica NPs is plotted with colloidal concentration  $\phi_m$  (Fig. 4.6b). It is observed that the specific surface area  $\Sigma_{meso}$  increases with increasing  $\phi_m$ . In case of isotropic shrinkage of colloid droplets with constant packing fraction silica NPs specific surface area should remain invariant for all the samples because it is the ratio of the surface area and volume.

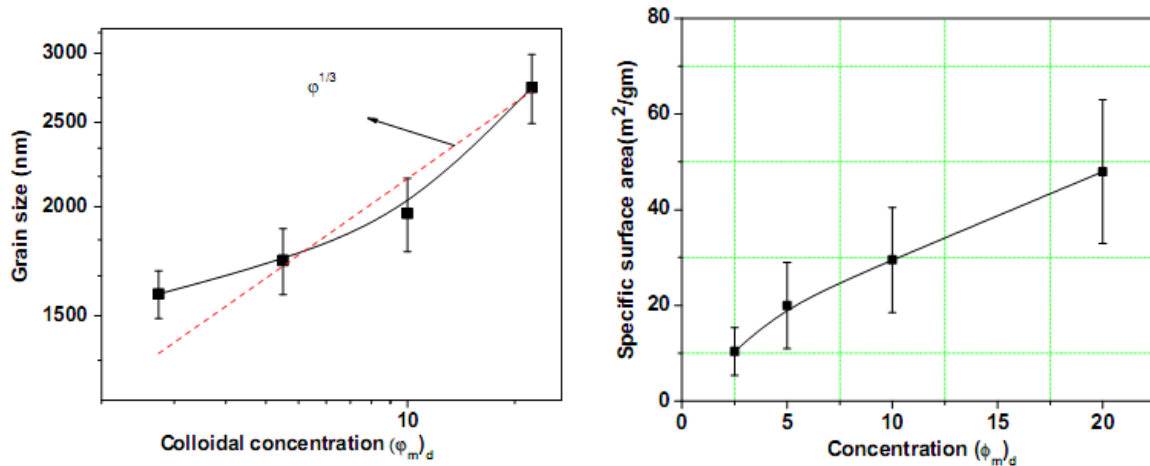


**Fig. 4.6** (a) Average grain size for various concentrations of silica colloid as estimated by DLS. (b) The specific surface area of the mesopores from SANS measurements.

From Fig. 4.6b, it has been inferred that packing of silica NPs is not same for all samples but indeed is a function of colloidal concentration. From eq. 4.6, ratio of packing fractions for different samples may be estimated by average size of dried grains <sup>240,241</sup>.

$$\frac{\phi_{2.5}}{\phi_5} = 1.30 \quad \frac{\phi_5}{\phi_{10}} = 1.45 \quad \frac{\phi_{10}}{\phi_{20}} = 1.37 \quad (4.7)$$

It is evident from the eq. 4.7 that the silica volume fraction in dried grains is decreasing with increasing colloidal concentration. Thus, silica volume fraction is highest in sp-2.5 sample and lowest in sp-20 sample. Assuming the silica volume fraction in dried grain for sp-2.5 sample is equal to that of random close packing (RCP) value ~0.64, silica volume fraction for other samples can be calculated. Silica volume fractions for sp-5, sp-10 and sp-20 have been estimated to be 0.49, 0.34 and 0.25, respectively. The silica volume fractions have also been estimated from SANS profiles and are tabulated in Table 4.1. It has been found that silica volume fractions in grains for different samples calculated from eq. 4.7 are supported by SANS results. It is interesting to note that although, spherical grains have been obtained for all the specimens, packing of NPs did not remain invariant when silica volume fraction is changed even in slow drying regime.

The above experimental observations during drying of droplets of colloidal suspensions may be understood as follows. Initially, atomized colloid droplets behave like pure liquids and shrink isotropically. As droplets get dried in the drying chamber, a viscoelastic shell of densely packed particles forms at its interface<sup>229</sup>. Initially, the shell yields and thickens as droplet shrinks. As water evaporates, tiny menisci form in the gaps between particles at the surface of the shell. This gives rise to a capillary force which is exerted on the shell. As volume of droplet decreases during drying, new particles join the shell. In addition, surface area of droplet shrinks as it dries, forcing the shell to thicken and its particles to

rearrange. The volume fraction of NPs in the shell is always greater than that in rest of the droplet. Thus, colloidal droplets have different volume fraction of particles at the shell and at the bulk. Although, packing fraction of NPs at the shell of the dried grain is constant and is closer to the random close packing value. But boundary between the shell and the bulk of droplet depends on time ( $\tau_{dry}$ ) for water to evaporate and time ( $\tau_{mix}$ ) required for homogenizing droplet. In other words, shell thickness is a function of drying parameters  $\tau_{dry}$  and  $\tau_{mix}$ . Mixing time is the time, that a suspended particle takes to diffuse across the radius of the droplet, i.e.,  $\tau_{mix} \sim R_d^2/D$ , D is diffusion coefficient of particle. It is to be noted that if  $\tau_{dry}$  decreases, NPs get less time to rearrange itself leading to a thinner shell. Further, the particles in the bulk of droplets do not get enough time to jam leading to a relatively lower volume fraction at the bulk of the grain as compared to that at the shell. Similarly, if  $\tau_{mix}$  increases, NPs take longer time to mix leading to thinning of the shell and loosely packing of NPs in the core of the dried grain. These ratio of  $\tau_{mix}$  and  $\tau_{dry}$  is nothing but Peclet number  $P_e$  ( $= \tau_{mix} / \tau_{dry}$ ). Larger the value of Peclet number  $P_e$  in non-buckling regime larger is the difference between jamming of NPs at shell and the bulk. Thus, ratio of packing fractions of NPs at the shell and in the bulk depends on Peclet number  $P_e$ . Since, packing fraction at the shell of dried grain is fixed to random close value; packing fraction in the bulk of grain depends on the Peclet number.

It is already discussed that viscosity of the dispersion increases with concentration of colloids. From Einstein diffusion theory, diffusion coefficient D of a particle with radius r in a medium can be written as,  $D = k_B T / 6\pi\eta r$ , where  $k_B$  is the Boltzmann constant, T is temperature in Kelvin,  $\eta$  is the viscosity of the medium. Diffusion coefficient D of a particle decreases with increasing viscosity of the medium. From Fig. 4.5, it is evident that the relative viscosity increases up to 40% when colloidal concentration is increased from 2.5% to

20%. Thus, Peclet number  $P_e$  increases with concentration due to reduction in  $D$  although it is less than unity. It indicates that shape of the assembled grains remains spherical in all the cases but the average packing of NPs in the grains is different. In sp-2.5 specimen, starting colloidal concentration was lowest; therefore, Peclet number  $P_e$  was smallest. This leads to least difference in packing of NPs at the shell and in the core. It is experimentally verified by SANS and DLS that average packing fraction in the grain of sp-2.5 is equal to that of random close packing (0.64) which implies that packing of the NPs is uniform throughout the grain. However, for sp-5, sp-10 and sp-20 specimens, initial colloidal concentration was higher and that leads to larger difference between the packing at shell and core of the grain. From SANS and DLS, average silica volume fractions for sp-5, sp-10 and sp-20 have been found 0.49, 0.34 and 0.25, respectively. The volume fraction at the shell will be same as that of RCP value (0.64) for all the specimens, which results to a somewhat smaller volume fraction in the core of dried grains. It is possible that hollow structure may exist at the core of the dried grains for sp-10 and sp-20 specimens. The packing mechanism for smaller and higher initial concentration of the NPs, during spray drying, has been depicted schematically in Fig. 4.7.

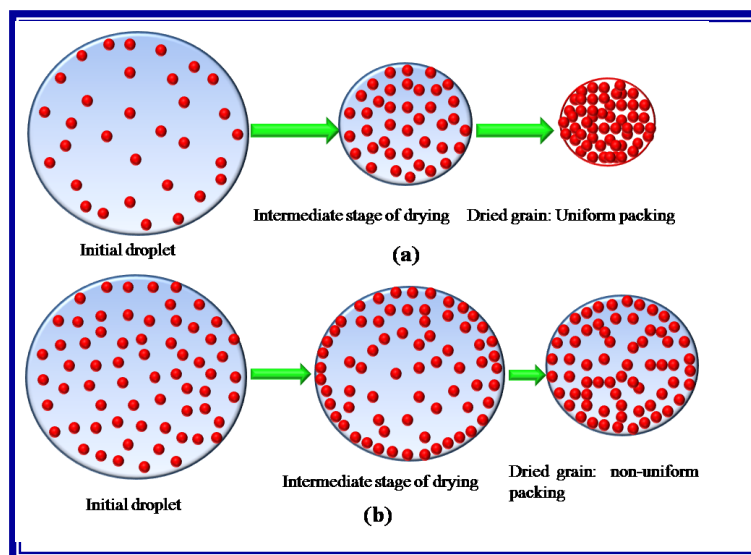


**Fig. 4.7** Schematic of the proposed mechanism of the drying process of silica colloid (a) for small concentration (b) for large concentration.

#### **4.1.4. Conclusions**

Spray drying experiments of silica colloids with varying initial colloidal concentration have been carried out under slow drying regime. The average size of the dried grain increases as the initial colloidal concentration was increased. Although overall morphology of the assembled grains remains spherical for all concentrations, packing of NPs in the grains depends on the concentration of initial colloidal dispersion as evidenced from scattering studies. It has been found that average packing fraction of NPs in the grains reduces with increasing concentration. Further, packing of NPs in the assembled grains is not uniform at higher colloidal concentration. These results were attributed to variation in Peclet number because of modification of viscosity of initial colloidal dispersion.

#### **4.2. Evaporation-induced Self Assembly of Nanoparticles in Non-buckling Regime: Effect of Charge Variation of the Colloid**

##### **4.2.1. Introduction**

In general, a droplet containing stable dispersion of colloidal NPs, shrinks in an isotropic manner and in such a situation the final arrangements of NPs inside an assembled grain, corresponds to a packing due to random jamming of the constituent particles<sup>232,233,240,241</sup>. For particles with spherical geometry, in an ideal random jamming situation, volume fraction corresponds to nearly 0.6 and the correlation may be considered as of hard sphere type. However, such packing of the constituent particles inside assembled grains may be modified by altering the physico-chemical parameters of the self-assembly process. By doing so, one can also alter the available interfacial area inside the assembled grains, which may be an important parameter in any catalytic application. The present study aimed at modification of internal structure in such assembled grains by addition of electrolyte in the initial colloidal dispersion and thus by altering the jamming mechanism.

In this section, modifications of internal structure in self-assembled grains of silica NPs, synthesized by spray drying, have been demonstrated. It will be shown that inter-particle correlation of colloidal particles and available specific surface area of silica void interfaces in grains get modified significantly by adding electrolyte in colloidal dispersion prior to spray drying.

#### 4.2.2. Experimental methods

Silica dispersions (5wt %) with varying NaCl concentration (0.0, 0.1, 0.2, 0.5 and 1.0 % in weight) has been prepared for further spray drying purpose. It was found that for NaCl concentration beyond 1.5 %, dispersion became unstable and got phase separated. Spray drying of the above silica colloidal dispersions was carried out using an in-house spray drier<sup>234</sup> in a slow drying regime<sup>233</sup>. The dried micrometric/sub-micrometric powders ( $P_{0.0}$ ,  $P_{0.1}$ ,  $P_{0.2}$ ,  $P_{0.5}$ ,  $P_{1.0}$  for 0.0, 0.1, 0.2, 0.5 and 1.0 wt % NaCl, respectively) were collected at the end of the drying chamber using a wire mesh (400 mesh) filter. The samples  $P_{0.1}$  -  $P_{1.0}$  were washed carefully and thoroughly with water and dried in order to remove electrolytes. SEM micrographs of  $P_{0.0}$ ,  $P_{0.5}$  and  $P_{1.0}$  powder samples are depicted in Fig. 4.8.

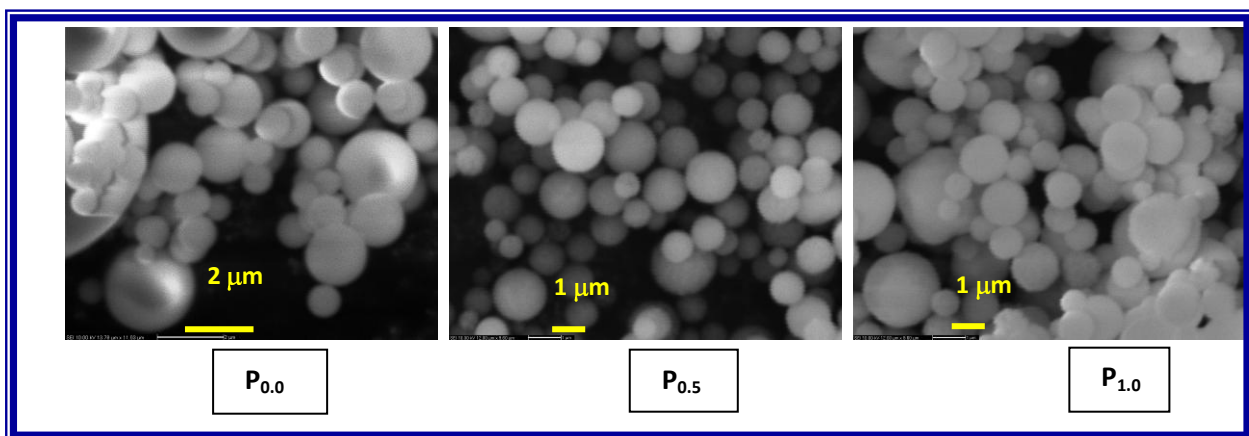


**Fig 4.8** SEM micrographs of the self-assembled grains are shown. It is seen that the powder grains are mainly spherical in shape for all cases.

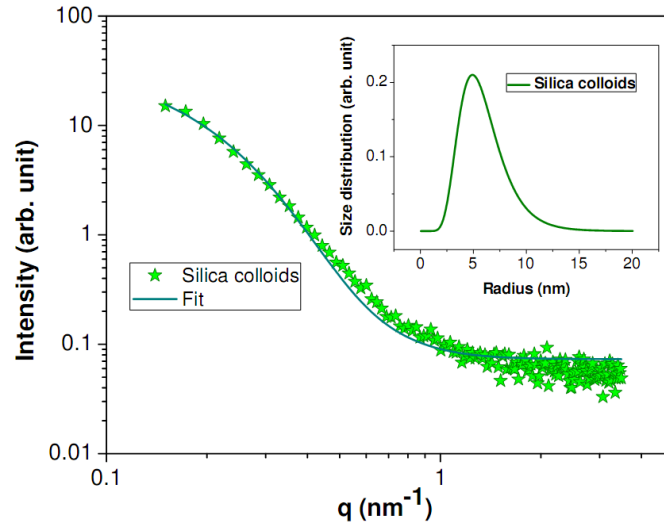


**Fig. 4.9** SANS profile from diluted virgin silica colloidal dispersion. The size distribution of the NPs is shown in the inset.

The scattering data from diluted (2wt %) silica dispersion is depicted in Fig. 4.9. Estimated size distribution of colloidal particles is shown in the inset.

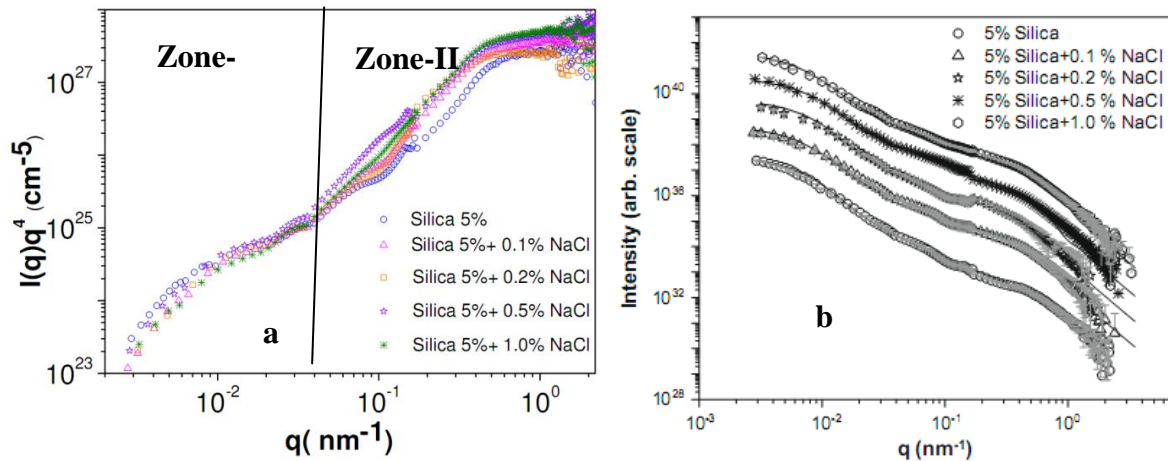


**Fig. 4.10** SANS profiles of the self-assembled grains are shown in Porod representation. (b) Fit of the scattering model to the combined scattering data. Solid lines show the fit. The profiles are shifted vertically in order to show the fits clearly.

Although SEM gives overall shape of the grains, it can't give information about the inter-particle correlation of constituent particles for which SANS measurement is required. SANS

experiment has been performed using MSANS and pinhole collimation based instrument at the Guide Tube Laboratory of Dhruva reactor, Mumbai, India. Combined data from both the two facilities, for assembled-grain powder samples, are depicted in Fig. 4.10.

### 4.2.3. Results and discussions

It is discernible from the SEM micrographs (Fig. 4.8) that the assembled grains are spherical in shape for all salt concentration although little polydispersity in size of the assembled grains could not be avoided due to some unavoidable fluctuations during the ultrasonic atomization process<sup>13,229</sup>.

From Fig. 4.10, it is evident that scattering profiles for samples P<sub>0.1</sub>-P<sub>1.0</sub> are significantly different than that of P<sub>0.0</sub> sample, particularly in intermediate and large q range. This clearly indicates that even though the external morphology remains unaltered (spherical), the internal arrangement of NPs inside the grains gets significantly modified with addition of electrolyte. It is observed that scattering profiles follow power law behavior ( $\sim q^{-D_m}$  where  $D_m$  is the fractal dimension) in a wide q range of  $\sim 10^{-2}$  to  $10^{-1}$  nm<sup>-1</sup> for the P<sub>0.1</sub>, - P<sub>1.0</sub> indicating the fractal like correlation between silica NPs.

From Fig. 4.10a, it is discernible that for all the samples, SANS profiles within the accessible q range ( $\sim 0.003$ - $2$  nm<sup>-1</sup>) may be subdivided into two distinct zones. Zone-I (for q range  $\sim 0.003$  to  $0.2$  nm<sup>-1</sup>) primarily bears the information about larger structure (i.e., information about overall assembled grains) while Zone-II (for q range  $\sim 0.2$  to  $2$  nm<sup>-1</sup>) mainly bears the information about silica NPs that constitutes each grain. It is worthy to mention that in recent past, the model for analyzing scattering data from spray dried grains has been developed<sup>242,13,15,232,233</sup>. Further, it is noteworthy that such model assumes that the final grains are produced via isotropic shrinkage of the initial droplet and have constant packing fraction

of the constituent NPs. For such two level structures, expression of scattering intensity may be written as <sup>13,15,232,233 242</sup>

$$I(q) = \frac{(\phi_S \Delta \rho_S^2 I_S(q) + v_g \Delta \rho_g^2 P_g(q))}{\phi_S} \quad (4.8)$$

where  $\phi_S$  is the volume fraction of silica NPs in a grain of volume  $v_g$ . If  $\rho_S$  is scattering length density of silica, then  $\Delta \rho_S = \rho_S - \rho_{int}$  ( $\rho_{int}$  being the scattering length density of interstices between silica NPs). As interstices between silica NPs is void (when electrolyte is removed),  $\rho_{int} = 0$  and hence  $\Delta \rho_S$  can be taken equal to  $\rho_S$ .  $\Delta \rho_g^2$  represents the average scattering contrast of the grains hence  $\Delta \rho_g = \phi_S \Delta \rho_S + \Delta \rho_{int}$ . As the medium in which grains are embedded and the medium of interstices are both void/air in this case,  $\Delta \rho_{int} = 0$  and thus  $\Delta \rho_g = \phi_S \Delta \rho_S$ . Here,  $P_g(q)$  is the normalized form factor of the grains.

$$P_g(q) = \frac{\int_0^\infty f_g^2(q, r) v_g^2(r) D_g(r) dr}{\int_0^\infty D_g(r) dr} \quad (4.9)$$

where  $f_g^2(q, R_{grain})$  represents the spherical form factor of the grains of radius  $R_{grain}$ .  $D_g(r)$  represents the size distribution of the assembled grains and is assumed as a lognormal distribution.

The first term in the numerator of the eq. 4.8 corresponds to the scattering from the colloidal particles in the grains. When the colloidal particles have a distribution in their size, then  $I_S(q)$  may be represented as following,

$$I_S(q) = \frac{\int_0^\infty P_S(q, r_{nano}) D_S(r_{nano}) v^2(r_{nano}) S(q, r_{nano}) dr_{nano}}{\int_0^\infty v(r_{nano}) D_S(r_{nano}) dr_{nano}} \quad (4.10)$$

$S(q, r_{nano})$  is the inter-particle structure factor.  $D_S(r_{nano})$  represents the size distribution of the

NPs.  $P_S(q, r_{\text{nano}})$  represents the normalized form factor of NPs with radius  $r_{\text{nano}}$ . For  $P_{0,0}$  sample, a sticky hard sphere type<sup>33,243</sup> potential, i.e., a repulsive hard sphere potential along with an attractive tail, could well explain the functionality of scattering profile. For,  $P_{0,1}$ , -  $P_{1,0}$  samples, where initial colloidal dispersion contained electrolyte of various concentration, sticky hard sphere type interaction could not explain the scattering data particularly in the intermediate  $q$  range. This is due to following fact. With addition of electrolyte, repulsive potential between silica NPs, that keep silica NPs stable, starts decreasing. This leads to small agglomerated clusters of silica NPs inside drying droplet. During the shrinkage and assembly processes, these clusters come closer and make larger clusters within droplet. Thus, inter-particle correlation gets modified. For  $P_{0,0}$ , i.e., for the case without electrolyte, self-assembly occurs by jamming of individual NPs in an isotropic manner. But, for the samples with addition of salts, self-assembly occurs by jamming of small flocculates instead of individual NPs. The structure factor may be approximated by of a fractal model for such agglomerated structure<sup>98,99</sup>. The fractal dimension has been estimated by fitting the scattering profiles for the  $P_{0,1}$ , -  $P_{1,0}$  specimens by taking fractal structure factor (eq.1.58). The fits of above models to the data are shown in Fig. 4.10b by solid lines. Parameters obtained from SANS analysis are tabulated in Table 4.2. The specific surface area ( $\Sigma_{\text{meso}}$ ) of the mesopores in the silica interstices in assembled grains may be calculated using eq. 4.3. From SANS results, it is seen that fractal dimension remains nearly 1.8 for the samples with added electrolyte and it does not vary much with amount of added salt.

**Table 4.2** Parameters, obtained from SANS analysis, are tabulated.

<b>Sample</b>	<b><math>\Sigma_{\text{meso}}</math> (<math>\text{m}^2/\text{gm}</math>)</b>	<b>Average size of silica colloids (nm)</b>	<b>Fractal dimension (<math>D_m</math>)</b>
P <sub>0.0</sub>	19±2	8.0±0.5	---
P <sub>0.1</sub>	26±2	8.0±0.5	1.8±0.1
P <sub>0.2</sub>	26±2	8.0±0.5	1.7±0.1
P <sub>0.5</sub>	31±2	8.0±0.5	1.9±0.1
P <sub>1.0</sub>	38±2	8.0±0.5	1.8±0.1

Due to continuous evaporation of solvent during the drying process, concentration of salt in a grain increases continuously as drying progresses. Up to a particular concentration of salt, aggregation structure of colloids depends on instantaneous salt concentration. If salt concentration crosses a particular maximum limit before particles are jammed, then fractal dimension may not change much after that. From Table 4.2, it is also seen that the specific surface area/effective available interfaces increases to some extent for samples where electrolyte has been added. This occurs because of following reason: the interparticle correlation gets modified with addition of electrolyte from hard sphere type to fractal type and thus some excess surface is exposed. When electrolyte is leached out from the grains after self-assembly, this gives rise to some more silica-void interfaces. The situation with and without addition of electrolyte is illustrated schematically in Fig. 4.11.

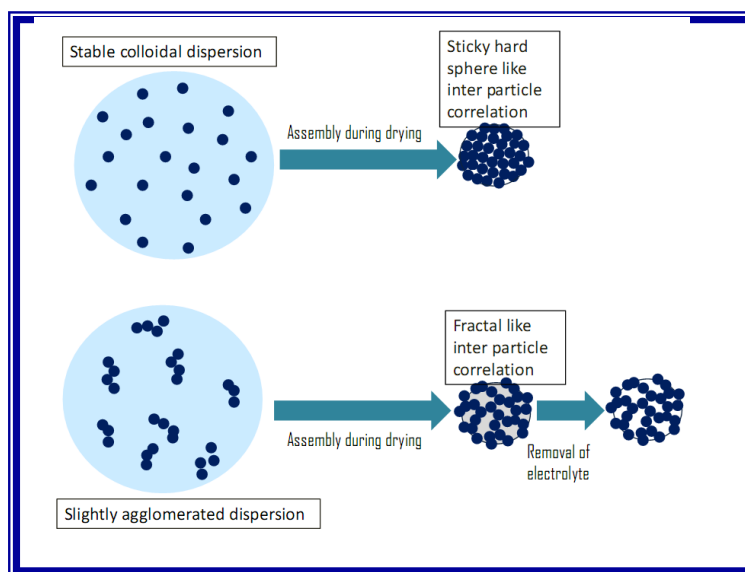


**Fig. 4.11** Schematic representation of the drying process of colloidal droplets, without and with presence of electrolyte, is shown.

#### 4.2.4. Conclusions

It has been shown that self assembly of NPs and their internal arrangement during droplet drying may be modified by addition of electrolyte in initial dispersion even at relatively slower rate. However, overall spherical shape of the grains remains unaltered. A sticky hard sphere type inter-particle correlation results in the absence of electrolyte while a fractal like correlation appears when electrolyte is present. Modifications of the inter-particle correlation in turn affect the available specific surface area of NPs-void interface.

# Hierarchical Nano-composites via Evaporation Induced Assembly under Buckling Regime

## 5.1. Origin of Buckling Phenomenon during Drying of Micrometric Colloidal Droplets

### 5.1.1. Introduction

Particle engineering in micrometric length scale is a relatively new field in science and technology that combines the knowledge of colloidal chemistry, nanotechnology, heat and mass transfer vis-à-vis the kinematical balance at fluid interfaces<sup>244</sup>. Spray drying<sup>12</sup> has found a special place in synthesizing hierarchically structured grains of NPs. The instability driven morphological transition, during drying of micrometric colloidal droplets, depends on several parameters that can be mainly classified into two categories. (i) Parameters related to physico-chemical properties of colloidal dispersion such as, initial concentration<sup>240</sup>, size of NPs<sup>13</sup>, interaction between the particles<sup>233</sup>, viscosity, surface tension. (ii) Parameters related to drying such as, drying temperature and time, droplet size. Depending on the above parameters, various morphologies of the dried grains, such as spherical<sup>13,231,233,240</sup>, doughnut<sup>13,231</sup>, are observed. However, origin of such complex morphological transition during EISA in fast drying regime<sup>240</sup> is not fully understood yet<sup>218</sup>.

In recent past, two hypotheses<sup>231,229</sup> have been proposed to explain possible mechanism for formation of doughnut like grains. In the first hypothesis<sup>231</sup>, it was assumed that structural instability of initial droplet leads to deformation leading to doughnut type of grains. As stability of liquid droplets depends on interplay between inertial force and surface

tension effects, it is likely that inertial effects try to deform the droplet, while interfacial tension acts to maintain the spherical shape. Quantitative measure of stability of droplet has been expressed by Bond number  $\beta$ , which is defined as  $\beta = \frac{4(\Delta\rho)gR^2}{\gamma}$ , where  $\Delta\rho$  is difference in densities of droplet and surrounding medium,  $g$  is the gravitational acceleration,  $R$  is radius of droplet and  $\gamma$  is interfacial tension. As  $\beta \rightarrow 0$  droplet remains spherical and it tends towards a flat shape as  $\beta$  increases. Apart from structural instability of initial droplets, it has also been assumed in this model that hydrodynamic instabilities during drying help in doughnut formation. It is worthy to mention that hydrodynamic instability depends on thermocapillary force ( $\Delta\gamma/\Delta T$ ), and Rayleigh number  $R_a$ , where  $T$  represents temperature<sup>231,251</sup>.

The second hypothesis in this direction is relatively recent<sup>229,225,245</sup>. This is based on the fact that colloidal droplet shows a combination of fluidic and elastic behaviour during drying. Experiments, on drying sessile droplets, have shed some light on this particular problem<sup>225,245</sup> suggesting that morphologies of buckled droplets can be interpreted using the theory of thin elastic shell.

### 5.1.2. Experimental

In present case, spray drying experiments have been performed in fast drying regime on stable 2 wt% silica colloidal dispersion using a spray dryer LU228<sup>246</sup>. The schematic of the spray dryer is shown in Fig. 5.1. The droplets were generated using compressed air spray nozzle. The feed rate was kept at 2 ml/min. The inlet temperature was kept at 170 °C. Average size of silica NPs is  $\sim 12$  nm<sup>233</sup>. To see the effects of droplet size on grain morphology, spray drying of 2 wt% silica colloids has been carried out for varying atomization pressure from 0.5 kg/cm<sup>2</sup> to 4.0 kg/cm<sup>2</sup>. The spray dried powders with

atomization pressure 0.5, 1.0, 2.0 and 4.0 kg/cm<sup>2</sup> are designated as Spt5, S1, S2 and S4, respectively.

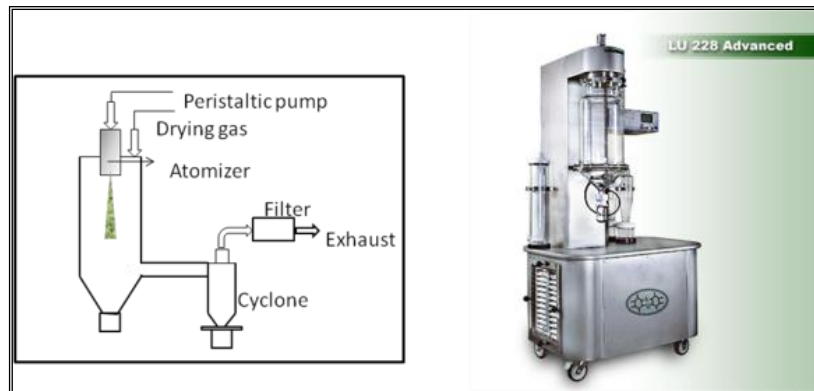


**Fig 5.1** Schematic of the LU 228 advance spray dryer.

The mesoscopic structure of the dried grains was probed using SEM. The micrographs for Spt5, S1, S2 and S4 samples are shown in Figs. 5.2.

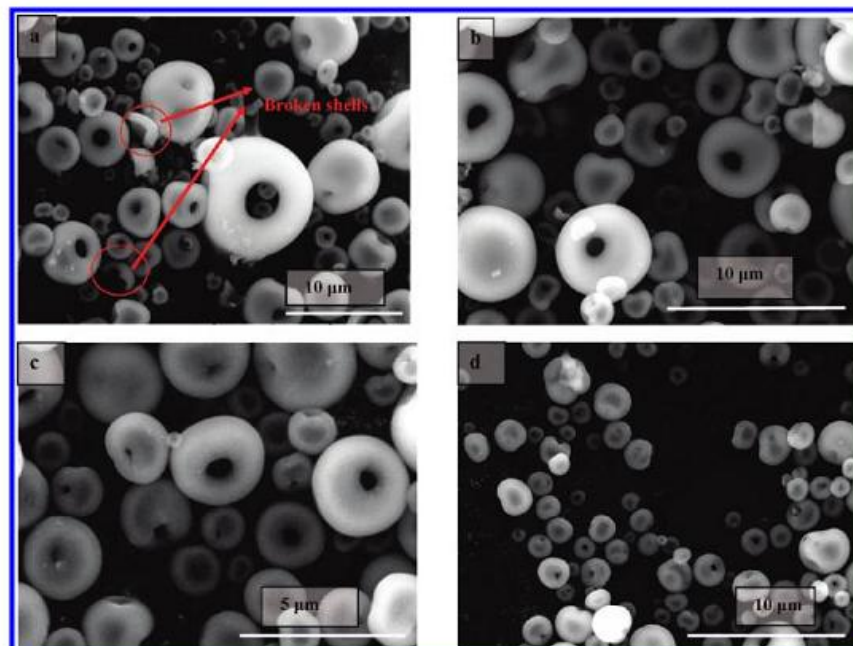


**Fig. 5.2** Morphology of the spray dried grains obtained by varying atomization pressure (a) 0.5 kg/cm<sup>2</sup> (b) 1.0 kg/cm<sup>2</sup> (c) 2.0 kg/cm<sup>2</sup> (d) 4.0 kg/cm<sup>2</sup>

SANS experiments have been performed using the facilities KWS 1<sup>247</sup> and KWS 3<sup>248</sup> at the high flux reactor FRM-II, Germany. Scattering profiles are depicted in Fig. 5.3.

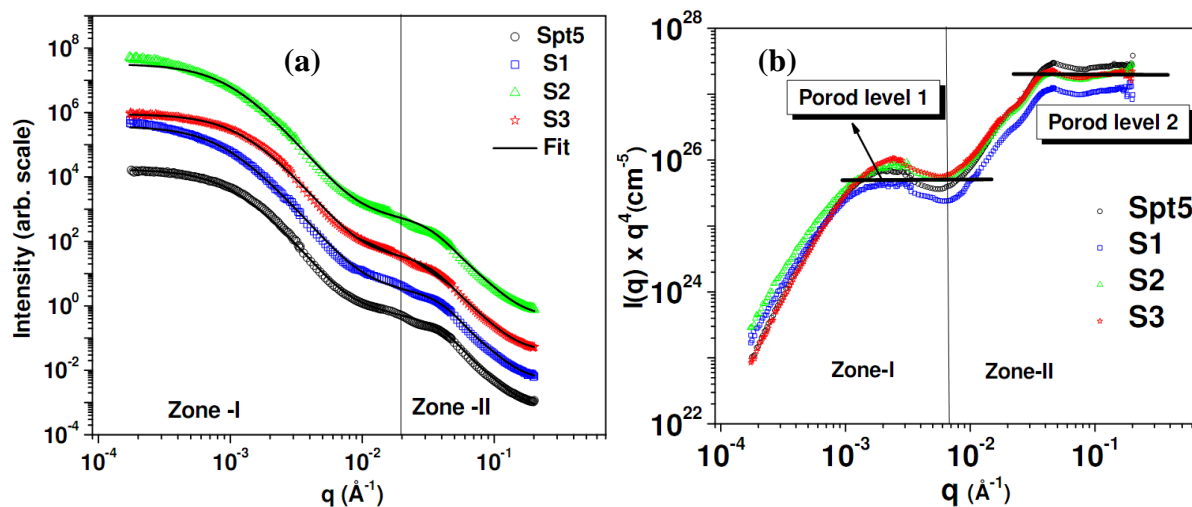


**Fig. 5.3** (a) SANS data for the specimens in double logarithmic scale. Solid lines represent fit to the data. Profiles have been shifted vertically for clarity. (b) SANS profiles for the specimens obtained at different specimens in Porod representation.

### 5.1.3. Results and discussion

From SEM micrographs, it is observed that grains possess doughnut like morphology. Further, from Fig. 5.1a, it is observed that some broken/fractured shells (marked in red circle) are also present for Spt5 specimen. From Fig. 5.1, it is evident that size of doughnut grains decreases with increasing atomization pressure. Size of central hole of doughnut decreases as a pressure is increased. Image analysis of grain has been performed by *ImageJ* software. Fig. 5.4 shows histogram of size of grains by analysis of SEM micrographs. It is observed that distribution of the grains extends to somewhat larger size at lower atomization pressure compared to that at higher pressure. It is also evident that grains possess significant polydispersity in their size for low atomization pressure.

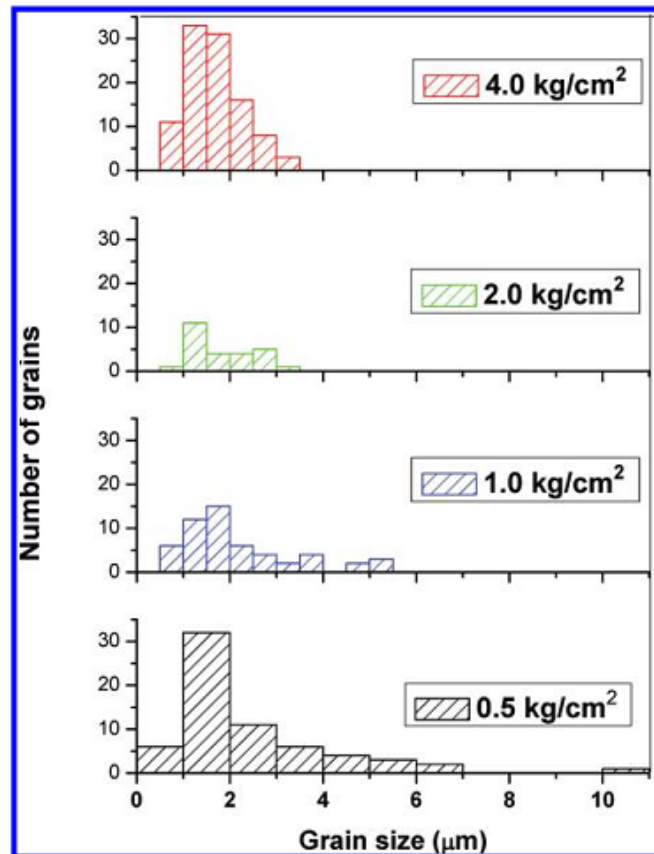


**Fig. 5.4** Histogram for size distribution of the spray dried grains at different atomization pressures by SEM micrograph analysis.

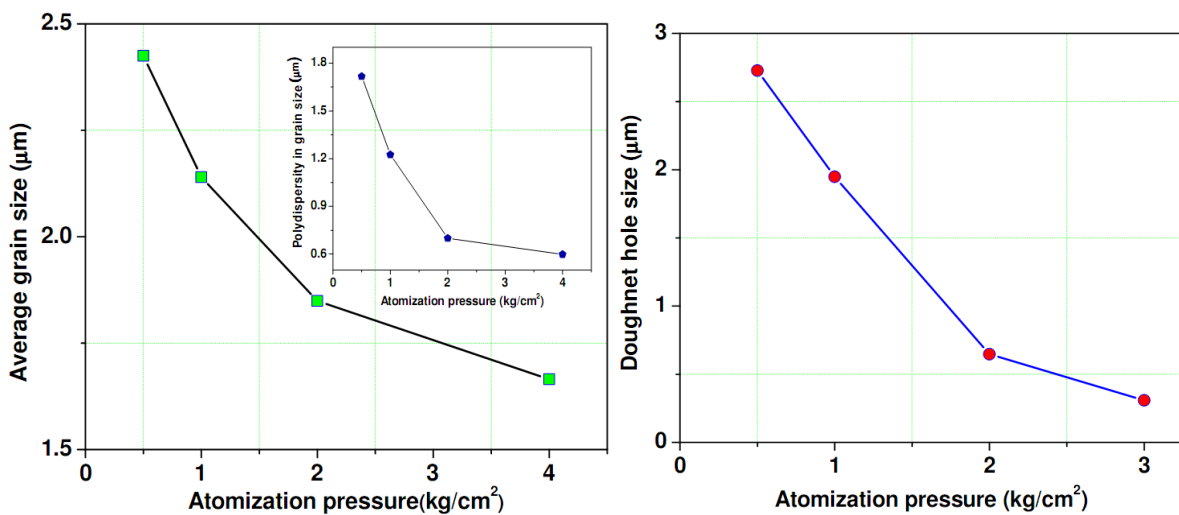


**Fig. 5.5** (a) Average size of the grains at different atomization pressures. The inset shows polydispersity in the size of the grains. (b) Variation of the size of central hole of doughnuts is depicted.

Average size of grains at different pressure has been depicted in Fig. 5.5a; inset of Fig. 5.5a shows polydispersity in grain size<sup>251</sup>. It is evident from Fig. 5.5b that size of central hole of doughnut decreases significantly with increase in atomization pressure. We define aspect ratio of doughnut as ratio of size of central hole to size of doughnut. It is related to degree of buckling. It is observed from Fig. 5.6a that aspect ratio of the doughnut decreases with atomization pressure.

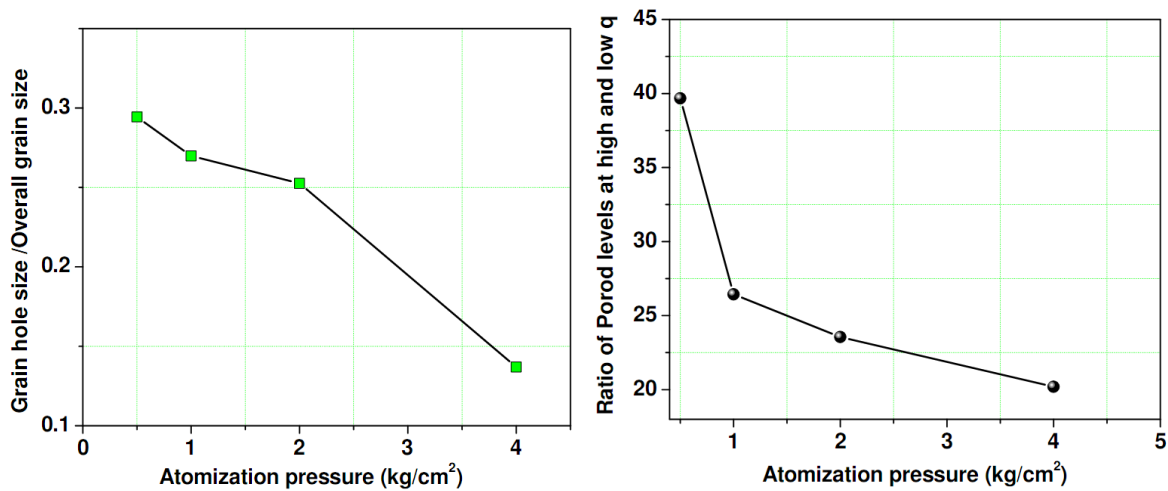


**Fig. 5.6** (a) The ratio of the size of doughnut hole to the overall size of grain with atomization pressure is shown. (b) The ratio of Porod levels at high and low  $q$  as a function of atomization pressure.

In order to probe internal structure of assembled grains, SANS measurements have been carried out. Fig. 5.3a indicates that scattering data consist of two distinct zones. Zone-I represents scattering contribution from overall grains whereas zone-II represents scattering contribution from constituent silica NPs. In present case due to existence of two level structures of grains, two distinct Porod levels are observed (Fig. 5.3b). Porod level at high  $q$  represents interstices surface area ( $S_i$ ) that originates due to jammed silica NPs inside grains. The other Porod level at the low  $q$  region represents grain surface area ( $S_g$ ). It is observed from Fig. 5.6b that ratio of two Porod levels, i.e., ratio of  $S_i$  to  $S_g$ , decreases with increasing

atomization pressure. This ratio may be treated as another measure of degree of buckling during drying. It is evident from SEM analysis that size of grains decreases with pressure resulting smaller surface area of grains. Further, shape of the grains tends towards spherical shape as pressure is increased leading to further reduction in overall surface area of grain. However, this could lead to increase in ratio of Porod levels if surface area of NP-interstices remains constant. However, opposite behavior of the ratio of Porod level is observed which indicates that surface area of NP-interstices is not a constant but depends on atomization pressure. The interstitial surface area  $S_i$  decreases faster as compared to grain surface area  $S_g$ . This indicates that nature of jamming of NPs inside grains varies with pressure. The jamming of NPs is not uniform throughout the grains at low atomization pressure leading to large interstitial surface area. This kind of non uniform jamming of the NPs may be regarded as anisotropic jamming. As atomization pressure increases, jamming of NPs approaches towards uniform or isotropic in nature leading to smaller interstitial surface area. As mentioned earlier (Fig. 5.1a), broken shells are observed for Spt5 specimen which suggests anisotropic jamming of NPs during drying at low atomization pressure. Broken shells are not observed at higher pressure where grains are less buckled indicating relatively more isotropic jamming throughout a grain.

The SANS data have also been modeled in view of two level structure of grains for which the scattering intensity may be expressed as

$$I(q) = I_1(q) + I_2(q) \quad (5.1)$$

where  $I_1(q)$  represents the scattering contribution due to overall grains. In present case, scattering contribution from doughnut grains has been represented by a Debye-Bueche type term<sup>19,249</sup>.

$$I_1(q) = C_0 \left[ \frac{1}{1 + q\xi^2} \right]^m \quad (5.2)$$

where  $\xi$  is typical correlation length of scatterer,  $m$  is Porod exponent and is typically 2 for objects with a sharp boundary.  $I_2(q)$  is scattering contribution from jammed silica NPs within the grains. The expression for  $I_2(q)$  may be written as below if an interacting polydisperse spherical particle model is assumed under local monodisperse approximation<sup>250</sup>

$$I_2(q) = \frac{C_1 \int P(q, r) r^6 D(r, r_0, \sigma) S(q, r) \left( \frac{4\pi}{3} \right) dr}{\int r^3 D(r, r_0, \sigma) dr} \quad (5.3)$$

where  $P(q, r)$  is spherical form factor,  $D(r, r_0, \sigma)$  is lognormal size distribution of jammed silica NPs with a median  $r_0$  and polydispersity index  $\sigma$ . Jamming behaviour during drying of colloidal droplet give the exact idea about interaction between jammed NPs<sup>251</sup>. In present case,  $S(q, r)$  is adopted as sticky hard sphere. The fit of the above model to the SANS data is shown in Fig.5.3a.

Let us understand the origin of doughnut morphology. Size of droplets and atomization pressure are related by an empirical formula<sup>12</sup>. Size of droplets from two fluid nozzle decreases with increase in pressure<sup>12,251</sup>. Since, size of grain size is proportional to initial droplet size hence size of grain decreases with increasing pressure. Thus, reduction of average grains size with pressure may be understood in terms of reduction of droplet size with pressure. However, transformation of grain morphology from spherical to doughnut is to be understood on the basis of existing hypothesis.

In present case, typical size of droplets may be estimated by using conservation of silica NPs in droplets during drying if an isotropic shrinkage of droplets is assumed during drying<sup>240</sup>. Typical droplet size for present case is approximately  $10 \mu\text{m}$ <sup>251</sup>. With this estimate

of droplet size, extent of deformation of initial droplets due to inertial instability can be estimated by calculating Bond number  $\beta$  by assuming that variation in surface tension with NP concentration remains relatively insignificant<sup>254</sup>. The Bond number  $\beta$  for 10  $\mu\text{m}$  droplet is estimated<sup>251</sup> to be  $1.4 \times 10^{-5}$ , which is quite small as compared to unity. Thus, possibility of instability of initial droplet due to inertial deformation is ruled out in present case. Similarly, this fact may also be verified by using the concept of Leidenfrost drops<sup>255, 251</sup>.

According to first hypothesis droplet instability, during drying which arises due to hydrodynamic instability<sup>256</sup>, depends on thermocapillary force ( $\Delta\gamma/\Delta T$ ) and Rayleigh number  $R_a$ . It is known in literature<sup>257</sup> that Rayleigh number  $R_a$  and Reynolds number  $R_e$  are related by a power law. Reynolds number for present spray drying condition turns out to be less than one for a micrometric droplet leading to smaller Rayleigh number  $R_a$ . At this juncture, it is important to note that during drying of colloidal droplets, various processes are diffusion of colloidal particles, solvent diffusion and heat transport in droplet. Different characteristic time may be assigned to different processes. Larger the characteristic time, slower is the processes. During drying of the micrometric droplet, characteristic time for heat conduction through droplet is very small as compared to those for other processes<sup>258-260</sup>. This implies that temperature of droplet reaches steady state before other processes. Thus, thermocapillary force, which arises due to temperature gradient, may be neglected during drying of micrometric droplets. Hence, it is evident that origin of doughnut type grains in spray drying of micrometric droplets is not significantly related to hydrodynamic and inertial instabilities.

Other hypothesis, proposed by Taspis et al., has been assumed for possible explanation of present experimental results. According to this hypothesis, shell formation during drying of colloidal droplets and its behaviour in response to capillary force play crucial roles in deciding morphology of dried grains. At very initial stage of drying, a viscoelastic shell forms and droplet shrinks isotropically. As drying proceeds, new particles

join the shell and at the same time the droplet tend to shrink. However, this leads to a rearrangement of the NPs, which depends on the force balance between colloidal particles. It is interesting to note that formation of shell and its thickness during drying depend on the drying time  $\tau_{dry}$  and mixing time  $\tau_{mix}$ . The two characteristic time scales are related by Peclet number  $P_e$  ( $\tau_{mix}/\tau_{dry}=R^2/D\tau_{dry}$ ). Peclet number is considered as dimensionless mass transport number that characterizes relative importance of diffusion and convection<sup>261</sup>. If the drying of the droplet is very slow,  $P_e \ll 1$ , colloids get enough time to diffuse through droplet leading to uniform colloidal concentration through out droplet. Hence, formation of shell in slow drying regime is less likely and droplets shrink isotropically leading to spherical dense grains. If drying of droplet is very quick,  $P_e \gg 1$ , NPs do not have sufficient time to diffuse from surface to center of droplet and instead accumulate near drying front of droplet<sup>262</sup>. As droplet evaporates, and particles accumulate on the free surface, capillary forces will draw NPs together and ultimately van der Waals type forces<sup>263-265</sup> can lock them in place. At the end of this process evaporating front transforms into a shell enclosing remaining solution. Further, liquid evaporates from interstices of the shell and remaining NPs joins inner surface of the shell<sup>266</sup>. A menisci form between NPs leading to capillary pressure on the shell. Initially, shell behaves as viscoelastic shell and isotropic shrinkage of droplet occurs. A situation arises, when rheological nature of shell undergoes a transition from viscoelastic to elastic. In this case the droplets do not shrink but buckle leading to doughnut type of morphology.

Peclet number  $P_e$ , for present drying condition is estimated<sup>251</sup> to be 3.5. Thus, drying experiments resides into fast drying regime. Doughnut type of grain morphology is expected for drying of 2wt% silica colloids in present experimental condition. It is interesting to note that shell thickness decreases with increasing Peclet number in fast drying regime<sup>251</sup>. Thinner shell during drying of droplet is more vulnerable to buckling and hence may result to a doughnut grains under capillary pressure. For larger atomization pressure, droplet size is

smaller resulting in smaller Peclet number although drying is still in fast drying regime. In this case shell thickness will be larger as compared to that in the previous case leading to less buckling. This in turn results into formation of doughnut with smaller hole size. It has been observed from Fig. 5.6a that normalized strength of buckling decreases with increasing atomization pressure which is clearly understood by the hypothesis described above. When atomization pressure has been  $0.5 \text{ kg/cm}^2$ , broken/fractured grains have been observed, as the shell thickness was lowest and some of them could not sustain the capillary stress and gets fractured. A schematic of proposed mechanism based on shell formation theory for different atomization pressure is shown in Fig. 5.7.

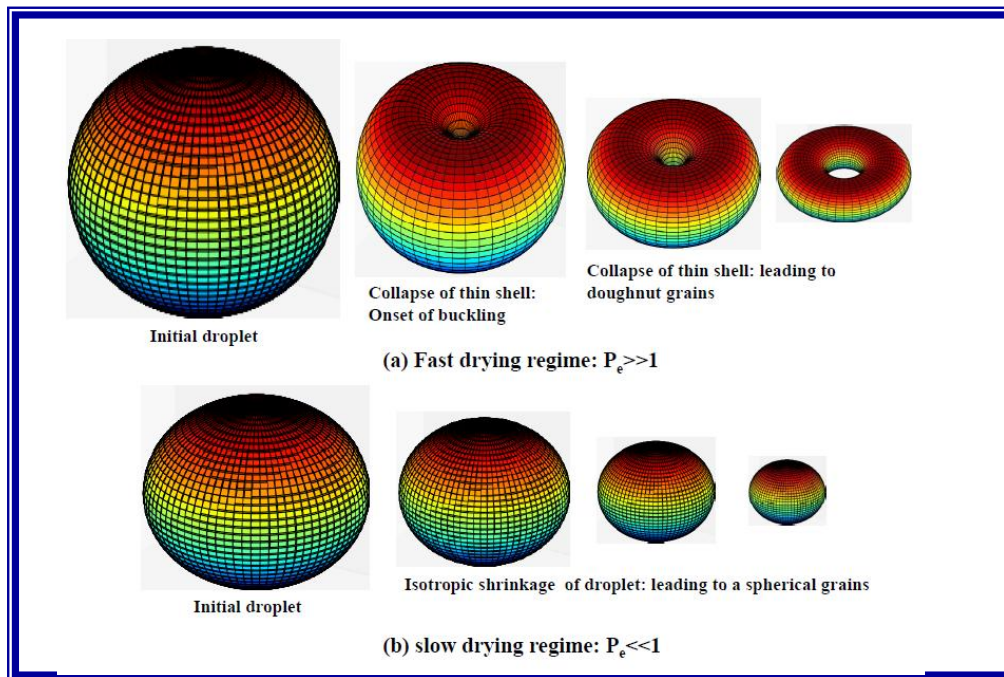


**Fig. 5.7** The mechanism for formation of doughnuts and spherical grains from spherical droplet in different drying regimes.

#### 5.1.4. Conclusions

Buckling induced morphological transformation of micrometric liquid droplets to doughnut like grains during evaporation induced self assembly (EISA) of NPs has been observed.

Doughnut characteristics depend on initial droplet size. The possible mechanisms of formation of such doughnut like grains during drying of micrometric droplets have been differentiated on the basis of two existing hypotheses. The hypothesis based on inertial instability of initial droplet and hydrodynamic instability fails to explain the experimental results. Hypothesis based on formation of shell of jammed NPs at air water interface and its buckling explains experimental results wells.

## **5.2. Control of Buckling in Colloidal Droplets during Evaporation Induced Assembly of Nano-particles**

### **5.2.1. Introduction**

Recent advances in area of self-assembly of NPs have encouraged for exploring various synthesis techniques in fabrication of micrometer sized grains with tailored morphology. In particular, anisotropic grains have been the subject of various studies in recent years. Such anisotropic micrometric grains can be obtained through different approaches, for example, either by deformation of spherical colloidal droplets during drying<sup>267-269</sup> or by forming clusters of NPs<sup>270-273</sup>. It has been demonstrated that such grains are potential candidates to generate anisotropic colloidal crystals<sup>270,274,275</sup>. Hollow anisotropic grains are particularly interesting for variety of applications such as drug delivery, catalysis, biotechnology and contrast agents for ultrasound or echographic imaging<sup>276,277</sup>. Microemulsion templated colloidal assembly<sup>278-283</sup> and spray drying<sup>12,13,15,218,232,233,284-288</sup> are most widely utilized techniques for fabrication of hierarchically structured micrometer sized grains.

It is shown in previous section that origin of buckled grains is attributed to the mechanical behaviour of elastic shell formed under capillary stress during drying of colloidal droplets<sup>251</sup>. Deformation of a spherical shell under external pressure has been investigated recently, both experimentally and numerically<sup>289-291</sup> due to the pertinent engineering

situations as well as biomechanics point of view. It is worthy to mention that mechanical deformation of thin elastic sheet of graphitic oxide<sup>292</sup>, polymerized Langmuir monolayer<sup>293</sup> or cytoskeletons of biological membranes<sup>294</sup> has been well studied in past. However, curved shells exhibit quite different elastic behaviour under external pressure because of the coupling between stretching and bending effects<sup>295</sup>. This interplay between bending and stretching leads to a reduced flexibility of shell<sup>225,296-298</sup>.

Some experimental and theoretical works<sup>229,245,299-304</sup> show complex geometry (wrinkled or dimpled) of grains due to buckling of shell formed during drying. The morphology of spherical shell under external pressure is a result of the minimization of the energies due to extensional and bending deformations. For larger deformation, extensional deformation is not energetically favorable and bending deformation is preferred. It is important to mention here that for small deformations, potential energy of buckled state is higher as compared to that for unbuckled state and vice versa<sup>301</sup>. It has been shown that for a homogenous spherical elastic shell, two modes of deformation may be combined by the Föppl-von Kármán (FvK) number  $\gamma$ . Recently, it has been shown by simulations that higher  $\gamma$  coupled with high rate of compression may lead to multiple numbers of the indentations on the shell leading to buckyball type of morphology<sup>299-300</sup>.

Elastic shell, formed during drying of colloidal droplet, may be treated as an experimental model for shell under external pressure. It is interesting to note that nature of shell buckling can be controlled by altering pressure on shell or by introducing inhomogeneity in shell. In real systems, shells are not always homogenous such as in engineering materials or soft materials or living cells etc. They always possess some degree of inhomogeneity. Effect of shell inhomogeneity on buckling phenomenon has not been well studied because of its complexity and needs attention.

### 5.2.2. Experiments

Drying experiments have been carried out in fast drying regime using LU228 spray dryer. 0.5, 1.0, 2.0, 3.0 gm of PEG400 (Poly ethylene glycol MW: 400) were mixed one by one with 100 ml of 2 wt% silica colloids and stirred well. Similarly, 0.5, 1.0 and 2.0 gm of PEG1450 (Poly ethylene glycol MW: 1450) were mixed with 2 wt% silica colloids. Spray dried powder specimens were calcined at 500°C for 4 hrs in order to remove the polymer from assembled grains. Spray dried specimens obtained for PEG400, are designated as S1 in general and S1pt5, S1p1, S1p2 and S1p3 for 0.5, 1.0, 2.0 and 3.0 wt%, respectively in particular. Similarly, specimens, obtained from spray drying of dispersion containing PEG1450, are designated as S2pt5, S2p1, S2p2 and S2p6 for 0.5, 1.0, 2.0 and 6.0 wt%, respectively (S2 in general). SEM micrograph of grains, obtained for 2wt% silica only, is shown in Fig. 5.8. Micrographs of calcined specimens for S1 and S2 specimens are shown in Fig. 5.9 and 5.10, respectively. Removal of polymer from assembled grains has been monitored by Thermogravimetric analysis (TGA) and Differential thermal analysis (DTA)<sup>305</sup>. TGA-DTA curve, for the removal of PEG400 and PEG1450 polymers from assembled grains, have been shown in Fig. 5.11.

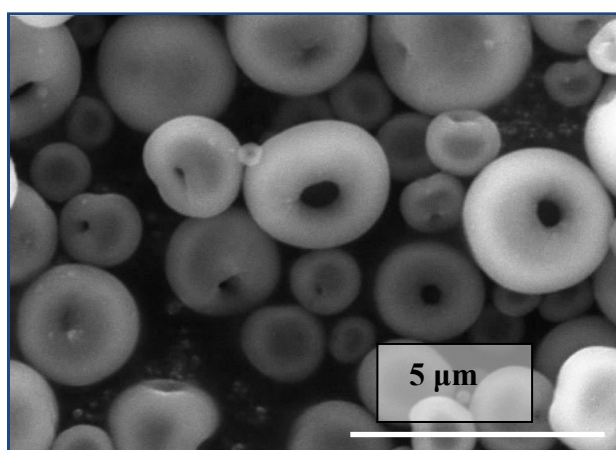


**Fig. 5.8** SEM micrograph of the self-assembled grains obtained for drying of only 2 wt% silica dispersion.

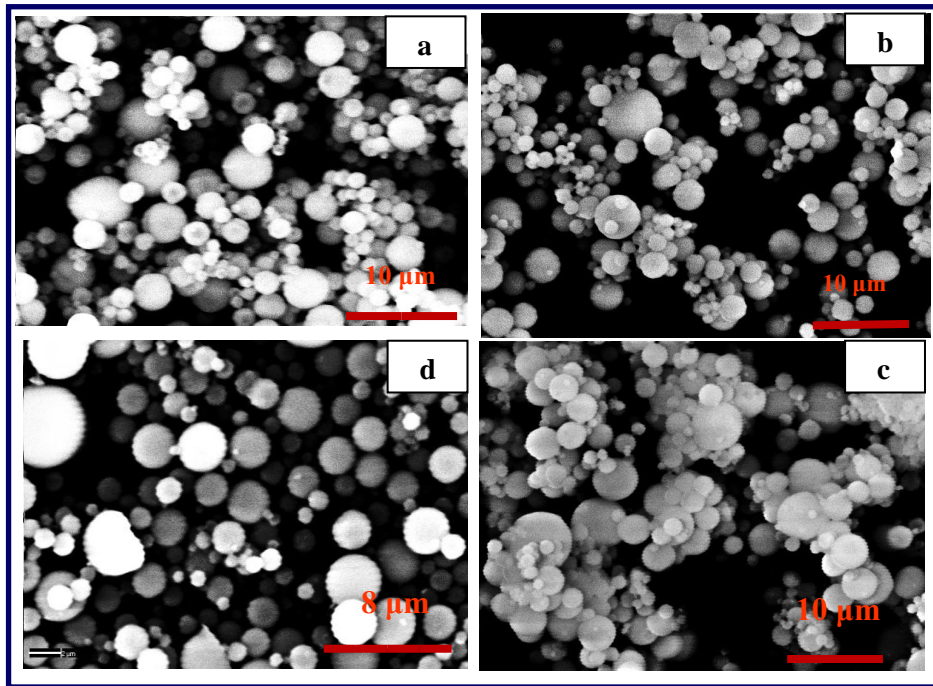


**Fig. 5.9** SEM micrographs of calcined specimens of (a) S1pt5 (b) S1p1 (c) S1p2 (d) S1p3.

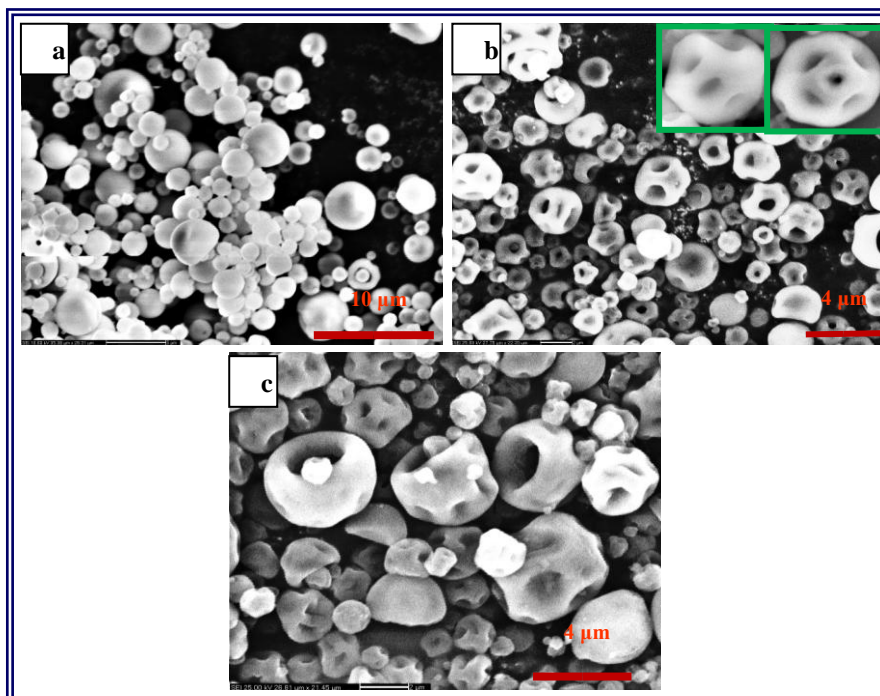
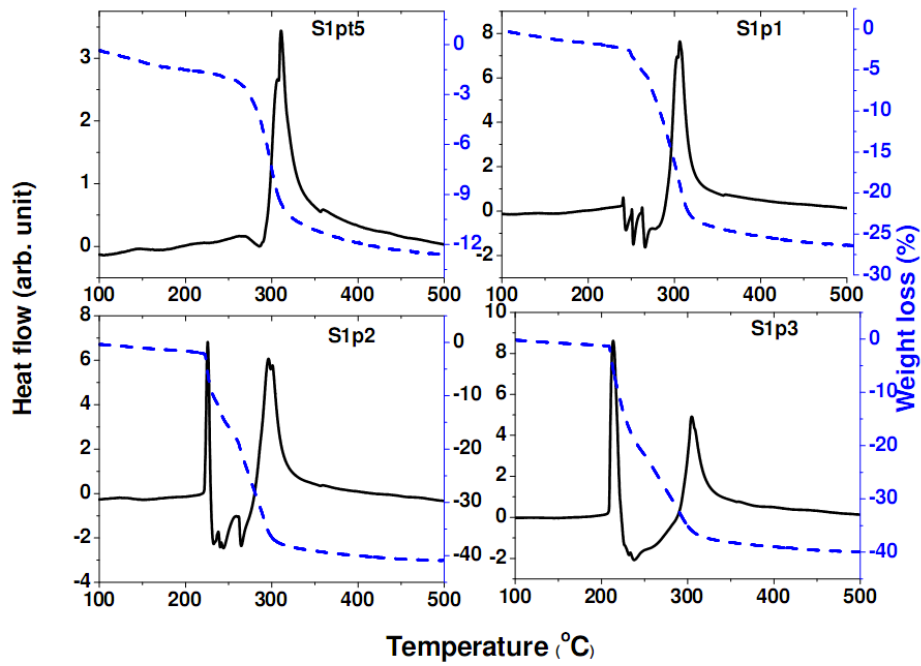
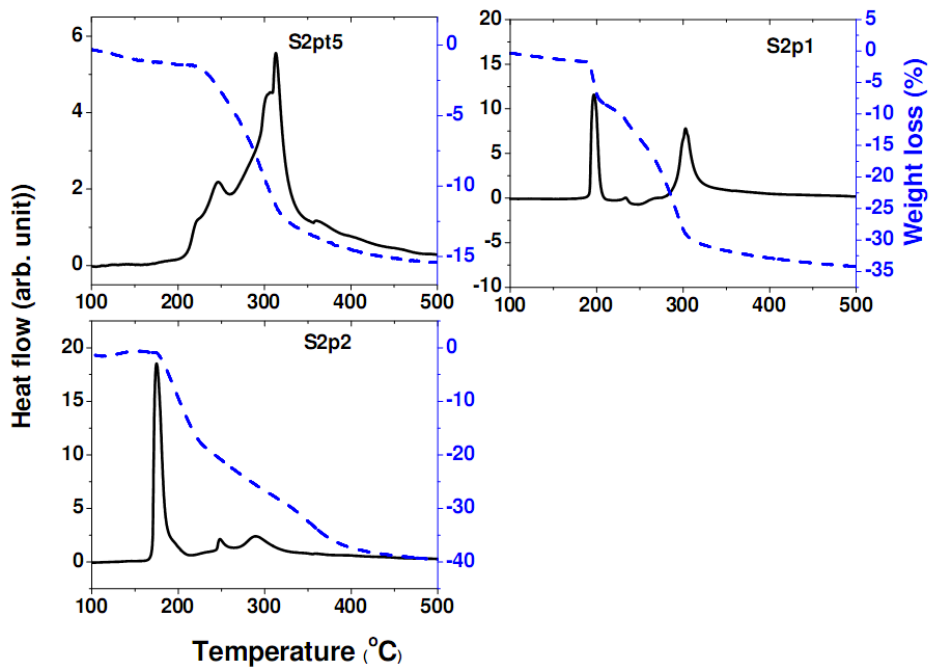


**Fig. 5.10** SEM micrographs of calcined specimens of (a) S2pt5 (b) S2p1 (c) S2p2.



(a)



(b)

**Fig. 5.11** (a) Heat flow and weight loss curves for spray dried grains for varying PEG 400 concentrations. (b) Heat flow and weight loss curve for the spray dried grains for varying PEG1450 concentrations.

SANS experiments have been performed on KWS1 and KWS3 instruments at the high flux reactor FRM-II, Germany (Fig. 5.12).

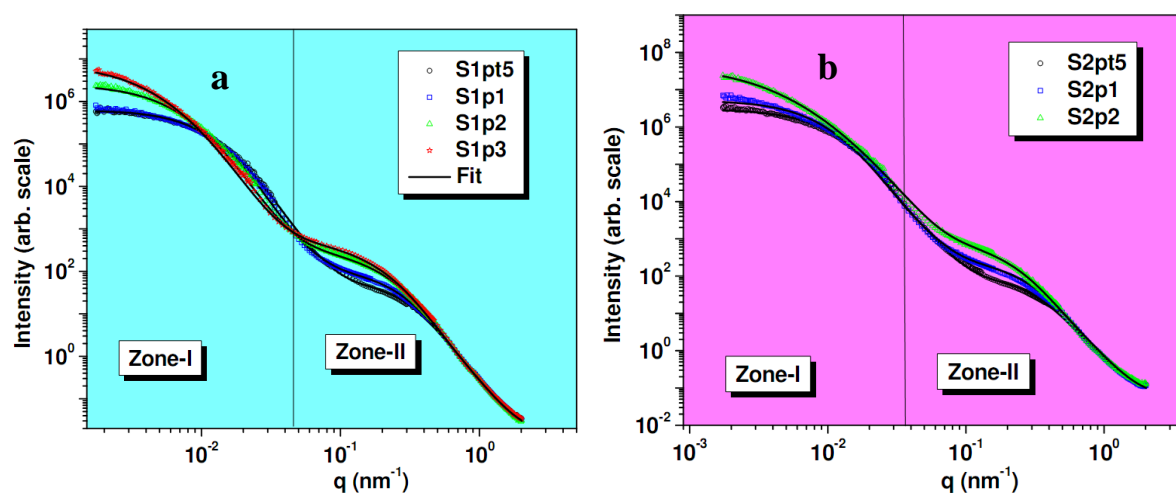


**Fig. 5.12** Normalized SANS profiles of calcined assembled silica grains obtained for different concentrations of (a) PEG400 (b) PEG1450. The solid lines are fit of model to the data.

It is to be noted that normalization of SANS profiles of calcined specimens has been performed at  $q = 0.72 \text{ nm}^{-1}$  in order to compare the functionality of scattering profiles<sup>305</sup>.

### 5.2.3. Results and discussion

From SEM micrographs (Fig. 5.8), it is evident that grains, obtained from spray drying of only 2 wt% silica colloids, possess doughnut morphology. However, grains, obtained from dispersion modified by PEG400, possess spherical morphology as depicted in Fig. 5.9. It is found from Fig. 5.9a that spherical grains with small dimple have been observed for S1pt5 specimen. This dimple disappears when PEG400 concentration is increased to 1, 2 and 3 wt%. Spherical grain morphology without dimple has been observed for S2pt5 (Fig. 5.10a). As PEG1450 concentration is increased further to 1 wt%, morphology of grains undergoes a shape transition from spherical to buckyball (Fig. 5.10b). The morphology of the grains has

well defined multiple indentations on nearly spherical matrix. Similar grain morphology has also been observed for S2p2 specimens with an increase in size of indentations (Fig. 5.10c).

It is observed that heat flow and weight loss curves for S1 and S2 grains are quite different. From Fig. 5.11a, it is found that for S1p5 and S1p1 specimens, an exothermic peak appears nearly at 300°C due to calcination of PEG. Some weaker endothermic peaks like structure are also observed before this exothermic peak. When concentration of PEG400 is increased to 2 and 3 wt%, additional exothermic peak appears at relatively lower temperature. This exothermic peak is not preceded by any endothermic peak. It is known that removal of trapped and free polymer shows different thermogravimetric behavior<sup>306</sup>. Free polymers manifest exothermic peak at relatively low temperature. However, for trapped polymers, exothermic peak appears at relatively higher temperature as it requires larger amount of energy for dissociation. The presence of endothermic peak, before the exothermic peak due to trapped polymers, indicates that some amount of heat is required to desorb the attached polymers. Smaller endothermic peak indicates the non-covalent nature of interaction between silica and polymer. In present case, polymers may get attached on silica NPs via physisorption or through hydrogen bond because of presence of –OH groups on silica colloids. Weight loss curves, during removal of polymer, show a consistent behaviour with calculated weight loss. Fig.5.11b shows thermo gravimetric behaviour of S2 grains. It is evident that exothermic peak due to free PEG1450 appears even at 1 wt% concentration while appearance of exothermic peak in case of PEG400 was at 2 wt%.

TG analysis of PEG incorporated grains provide crucial information regarding interaction of PEG and silica NPs. IR measurement indicates<sup>305</sup> presence of the Si-OH functional groups on its surface even after calcinations at 500°C, heat flow curves indicate the existence of both trapped as well as free polymers in grains. Based on these results, it is

believed that PEG interacts with silica NPs via Si-OH groups and gets absorbed on silica NPs. These polymers covered NPs get assembled in a random jamming process during drying of droplet. Thus, coated polymers in this case are trapped in interstices of jammed NPs and manifest exothermic peak at higher temperature. When concentration of polymer is increased to higher weight percent, absorption of polymer on NPs gets saturated and additional PEG polymers become free and may also form smaller aggregates. It is also evident from heat flow curve that for high molecular weight polymer, free polymer appears at lower concentration as compared to that of low molecular weight polymer. It shows that absorption of polymer on NPs saturates at lower concentration for higher molecular weight.

Scattering measurements provide information of internal morphology of grains. It is evident from Fig. 5.12 that a wide  $q$  range enables us to examine two level structures of grains. The scattered intensity from two level structure is modeled as  $I(q) = I_1(q) + I_2(q)$  where  $I_1(q)$  is scattering contribution from overall grains. Scattered intensity from overall grains  $I_1(q)$  is modeled in the light of polydisperse spheres having lognormal distribution (eq. 2.4).  $I_2(q)$  is scattering contribution from jammed polydisperse silica NPs having volume fraction  $\Phi$  within grains. Expression for  $I_2(q)$  may be assumed as an interacting polydisperse spherical particle model.

The two level structures model is successful to fit scattering profiles for S1p5 and S1p1. Scattering profiles of S1p2 and S1p3 could not be fitted by realistic parameters without considering additional scattering contribution in Zone-II (as scattering in Zone-II is increasing with increasing polymer concentration) which originates from templated pores by PEG aggregates (Fig. 5.12). Similarly, scattering profiles for S2 specimens could not be modeled using two level structures model. The additional scattering contribution  $I_3(q)$  from pores templated by PEG aggregates is also modeled as ensemble of polydisperse pore having

lognormal distribution (eq. 2.4) with polydispersity index  $\sigma$ . Volume weighted averaged grain size distribution for S1 and S2 specimens have been depicted in Fig. 5.13 and its inset, respectively.

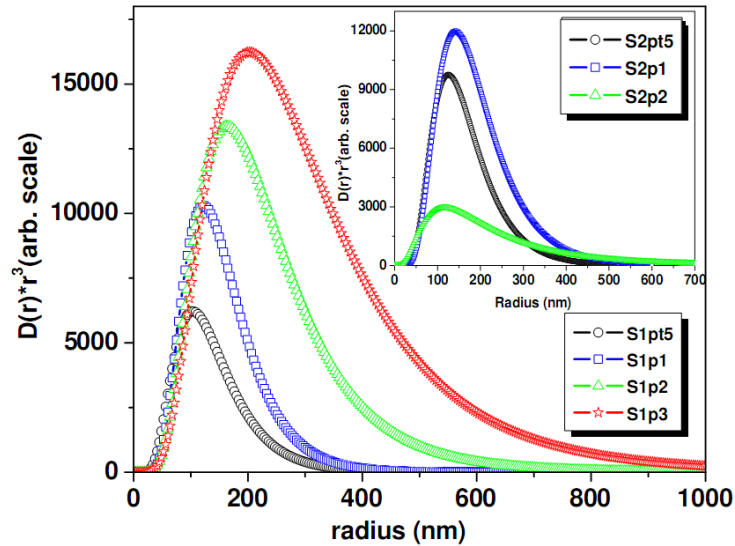


**Fig. 5.13** Pore size distribution for S1p2 and S1p3 calcined specimens is depicted. Inset shows the pore size distribution for S2p1 and S2p2 specimens. It is to be noted that these pores are templated by the free PEG aggregates.

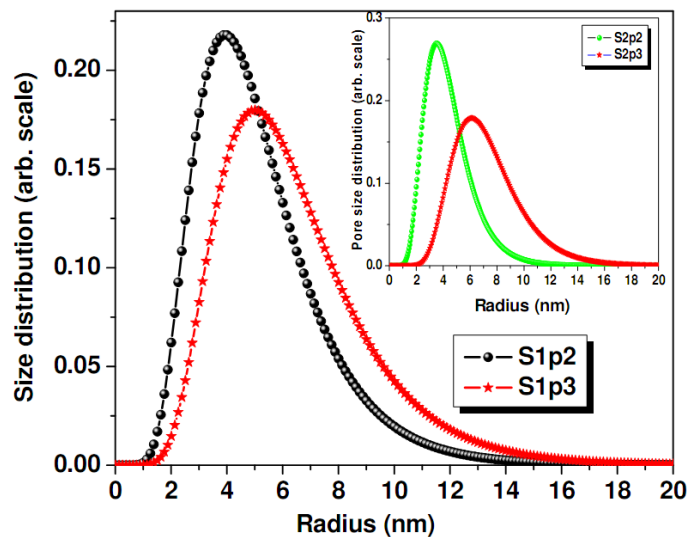


**Fig. 5.14** Pore size distribution for S1p2 and S1p3 calcined specimens, as obtained from the SANS analysis. Inset shows the pore size distribution for S2p1 and S2p2 specimens.

Pore size distribution, as estimated by SANS analysis, is depicted in Fig. 5.14. It is evident from Fig. 5.14 that typical size of PEG templated pores is 10 nm hence these pores can not be seen in SEM micrographs due to resolution limitation. Existence of such small pores in calcined specimens is evident from existence of free PEG aggregates in non-calcined samples through TGA. It is to be noted that size of PEG templated pores is comparable to silica NPs size and hence should not be confused with hole size of buckyball as their size is in order of micrometer.

Average radius of silica NPs is found<sup>305</sup> to be 5.8 nm with polydispersity index 0.43. Although, size distribution of NPs remains constant, local packing fraction  $\Phi$  of NPs does not remain constant at higher weight fraction of PEG400. For S1pt5 grains, local packing fraction  $\Phi$  of NPs is 0.60 and it decreases to 0.50 when PEG400 concentration is increased to 1 wt%. It remains constant for further higher concentration. Similarly, local packing fraction  $\Phi$  was nearly 0.60 for S2pt5 specimens and decreases to 0.5 when concentration is increased to 1wt%. The pore size distributions for S2 specimens are shown in inset of Fig. 5.14. Some parameters obtained by SANS analysis for PEG400 and PEG1450 are tabulated in Table 5.1 and 5.2, respectively.

**Table 5.1** The fitting parameters obtained from SANS data analysis for calcined S1 specimens.

Specimen (calcined)	Volume fraction ( $\Phi$ ) of jammed silica NPs	Pore size distribution parameters templated by free PEG aggregates	
		Average radius (nm)	Polydispersity index( $\sigma$ )
S1pt5	0.58	<i>No contribution</i>	
S1p1	0.49	<i>No contribution</i>	
S1p2	0.49	5.2	0.42
S1p3	0.49	6.4	0.40

**Table 5.2** *The fitting parameters obtained from SANS data analysis for calcined S2 specimens.*

Specimen (calcined)	Volume fraction ( $\Phi$ ) of jammed silica NPs	Pore size distribution parameters templated by free PEG aggregates	
		Average radius (nm)	Polydispersity Index ( $\sigma$ )
S2pt5	0.60	<i>No Contribution</i>	
S2p1	0.50	4.4	0.39
S2p2	0.50	7.3	0.34

As mentioned earlier, grains for only 2 wt% silica colloids possess doughnut morphology. However, spherical morphology is achieved on just addition of PEG400 polymer in 2wt% silica colloids. Slightly dimpled spherical morphology is observed for S1pt5 specimens. The arrest of buckling phenomenon on addition of PEG400 polymer may be understood as follows.

Capillary pressure on the shell formed during droplet drying, originates due to menisci formed in gaps between NPs at shell. This capillary pressure drives the deformation of shell. Pressure difference across the menisci is  $2\gamma/r_M$  (capillary pressure), where  $r_M$  is the local radius of curvature. Stress on the shell due to capillary pressure may be controlled by modification of colloidal particle size. At this juncture, it is important to mention that a critical pressure  $p_c = 4Y_0 h / R_c^2$  is required to induce the buckling of a homogenous shell<sup>300</sup>. If stress due to capillary pressures exceeds the critical pressure, shell buckles. Buckled grain with single indentation (doughnut grains) is observed for the case with only silica colloids. When PEG is added to silica colloids, it interacts with silica NPs via hydrogen bond and gets adsorbed on NPs to form a coating. Due to polymer coating, silica NPs could not come closer as compared to that in case of only silica NPs case. Thus, local curvature of menisci  $r_M$  is

relatively large in this case resulting in smaller capillary pressure, which is not sufficient to induce buckling. For 0.5 wt% of PEG400, buckling of shell is not fully arrested and dimpled grains are observed. Coating of polymers on NPs increases when concentration is increased to 1 wt% leading to lower packing fraction of NPs as was observed from SANS analysis. Thus, increase in coating amount on NPs leads to further reduction of capillary pressure resulting in spherical grains without any dimples. If concentration of PEG400 is increased further to 2 and 3 wt%, coating of polymer saturates and free polymers in form of aggregate appears as supported by TGA-DTA curve. Since, size of PEG aggregates is similar to that of silica NPs size; they become part of shell. Thus, shell formed during drying is not homogenous as far as its rigidity is concerned. However, for small molecular weight polymer (PEG400) number of aggregates is not significant even for 3 wt%. If molecular weight of PEG is increased from 400 to 1450 (approximately 4 times) free PEG appears even at 1 wt%. It was observed from SEM micrographs that assembled grains of S2p1 and S2p2 are of buckyball type morphology, which is quite intriguing observation. It is to be noted that addition of polymer of low molecular weight, as in present case, does not modify the viscosity of initial dispersion significantly<sup>307</sup>. Also, drying parameters remained identical for both the cases, i.e., for only silica colloid and polymer treated colloid. It is argued earlier that capillary pressure on the shell decreases on addition of polymer. Also, relative shell thickness ( $h/R_c$ ) may increase on addition of polymer due to presence of free PEG aggregates on shell at higher concentration. This will lead to lower  $\gamma$  value and smaller external pressure as compared to those for un-modified silica colloids case. Thus, according to elastic homogenous spherical shell theory, buckling should have been arrested in case of S2p1 and S2p2 specimens in contrast to present observation. Hence, in present scenario, theory of homogenous elastic spherical shell fails to explain origin of buckyball type morphology for S2p1 and S2p2 specimens. However, if inhomogeneity on shell is invoked, the present

experimental observation may be explained satisfactorily. Elastic shell, formed during assembly, will comprise of both silica and soft PEG aggregates as they are of comparable sizes. In this process, shell becomes inhomogeneous as far as their shear modulus is concerned. It is important to mention that deformation of shell under external pressure also depends on Young modulus of the shell. PEG aggregates on surface of shell act as centre for buckling. Also, critical pressure for this kind of inhomogeneous shell will be lower as compared to that of the homogenous shell of silica. It was observed that although free PEG aggregates in case of S1p2 and S1p3 are available, but their number is lesser as compared to that for S2p1 and S2p2 case due to higher molecular weight. Thus, buckling could not be induced for the shell having less number of PEG aggregates. Hence, the origin of such buckyball holes on the grains is attributed to buckling of inhomogeneous shell.

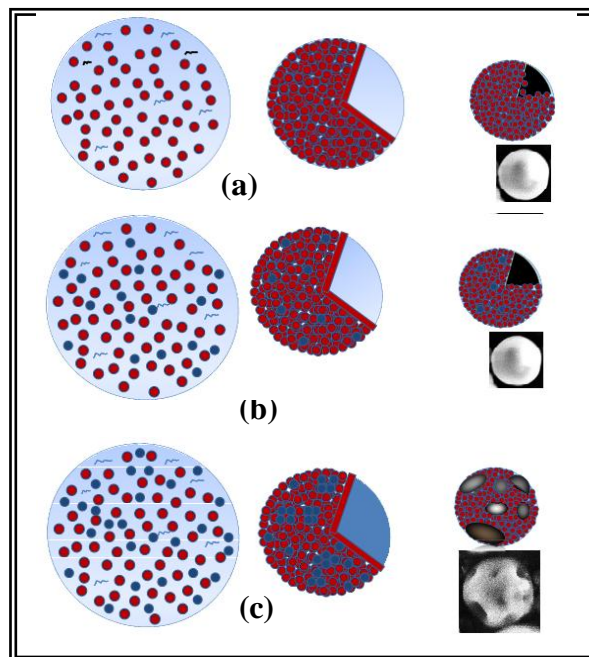


**Fig. 5.15** The schematic shows drying of droplets containing (a) silica colloids coated with polymer, no PEG aggregate (b) silica colloids coated with polymer, PEG aggregates are small in number (c) silica colloids coated with polymer, PEG aggregates are larger in number.

A schematic regarding the mechanism for the origin of the buckyball type grains has been depicted in Fig. 5.15.

#### **5.2.4. Conclusions**

It has been shown that phenomenon of morphological transformation to doughnut like shape during drying of droplets containing single type of colloid can be comprehended in terms of buckling theory of elastic homogenous spherical shell. Further, such buckling phenomenon can be arrested by covering NPs by poly ethylene glycol. Buckyball type morphology of grains could be realized for higher molecular weight and concentration of the polymer. Origin of such buckled grains could not be explained by theory of elastic homogenous shell for present experimental condition. SANS results show appearance of soft PEG aggregates at higher polymer concentration. It is revealed that a threshold number of soft PEG rich zones on shell are necessary to induce buckling. Relatively small elastic modulus of soft zones induces buckling at various centers resulting into buckyball type of grains.

### **5.3. One Step Fabrication of Thermally Stable TiO<sub>2</sub>/SiO<sub>2</sub> Nanocomposite Microspheres by Evaporation Induced Self-assembly**

#### **5.3.1. Introduction**

Nanostructured Titania (TiO<sub>2</sub>) is used in a wide range of applications, such as photocatalysis, separations, sensor devices, paints and dye-sensitized solar cells<sup>308,309</sup>. The properties of TiO<sub>2</sub> NPs depend on their crystal structure, size and morphology<sup>310-312</sup>. For practical applications, it is important to design a TiO<sub>2</sub> based functional material having improved efficiency as far as its photocatalytic properties are concerned. TiO<sub>2</sub> exists in three main phases: anatase, brookite and rutile. It is reported that anatase form has higher photoactivity than those in rutile form<sup>313-316</sup>. Under ambient conditions, macro-crystalline rutile is thermodynamically

stable in comparison to macro-crystalline anatase or brookite<sup>317</sup>. However, the thermodynamic stability depends on particle-size. For particle diameter below ~ 14 nm, anatase phase is more stable than rutile phase<sup>317</sup>. If TiO<sub>2</sub> nano-crystals are heated, crystal growth leads to alteration of phase stabilities and, ultimately, conversion of anatase to rutile takes place. Such, polymorphic transformation of anatase to rutile phase is considered to be one of the drawbacks that limits the photocatalytic activity<sup>318-321</sup>.

In order to get a TiO<sub>2</sub> based photocatalyst, having improved properties, a method is desired to develop meso/macro porous TiO<sub>2</sub>/SiO<sub>2</sub> micrometric grains. In past, mesoporous TiO<sub>2</sub> composites have been synthesized by sol-gel method<sup>322</sup>. However, this method results in an inhomogeneous phase distribution due to macroscopic reactions, leading to non-optimal performance. Therefore, it is essential to develop a process for rapid and controlled preparation of TiO<sub>2</sub>/SiO<sub>2</sub> based nanocomposites.

Meso/macro porous micrometric grains can be prepared from spray drying of micrometric droplets having nanosized TiO<sub>2</sub> and SiO<sub>2</sub> colloids. Fabrication of complex composite assemblies from drops containing mixture of two or more different type of colloids is not well studied in particular for the case of colloids consisting of two different species with different size and polydispersity of the primary particles.

### **5.3.2. Experimental methods**

Spray drying experiments have been performed on 2 wt% SiO<sub>2</sub> (Ludox HS-40) and 2 wt% TiO<sub>2</sub> dispersion using a spray dryer LU 228 in fast drying regime. SiO<sub>2</sub> and TiO<sub>2</sub> dispersions were mixed with ratio of 0.5, 1.0 and 2.0 weight percent keeping overall solid content constant. The specimens obtained from spray drying of 2 wt% SiO<sub>2</sub> and TiO<sub>2</sub> colloids were named as SI and TI, respectively. The specimens, obtained after spray drying of mixed

dispersions having  $\text{TiO}_2$  to  $\text{SiO}_2$  weight ratio as 2.0, 1.0 and 0.5, were designated as TiSi2, TiSi1 and TiSi0.5, respectively.

Virgin dispersions of  $\text{SiO}_2$  and  $\text{TiO}_2$  have been characterized by laboratory based SAXS instrument. SAXS experiments have also been performed on freshly prepared specimen of  $\text{SiO}_2$  and aged specimens of  $\text{SiO}_2$ ,  $\text{TiO}_2$  and its composites grains. Further, SANS experiments have been carried out on KWS 1 and KWS 3 at FRM II, Germany. Thermal stability of assembled grains has been monitored by TGA and DTA. The microscopic characterization of composite grains has been performed using a diffractometer using  $\text{CuK}\alpha$  source in  $\theta$ - $\theta$  geometry with 2 deg/min scanning speed.

### 5.3.3. Results and discussion

Micrograph of SI and TI grains are depicted in Figs. 5.16a, 5.16b, respectively.

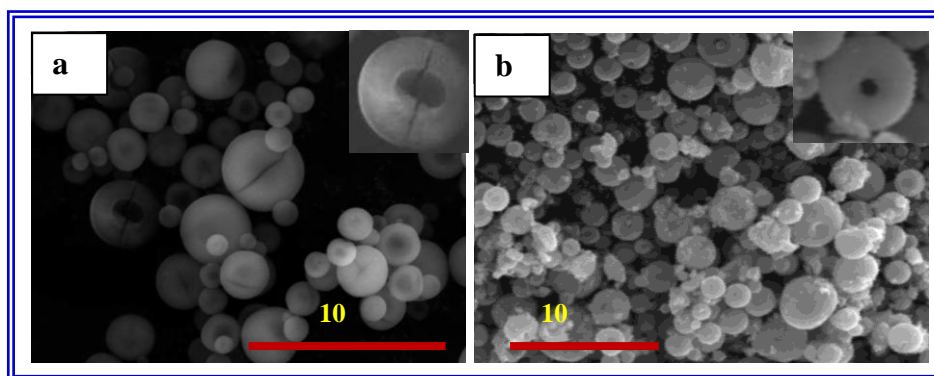


**Fig. 5.16** The micrographs of assembled grains consist of (a) only  $\text{SiO}_2$  NPs, inset show the cross sectional view of the hollow grains (b) only  $\text{TiO}_2$  NPs, inset of shows the doughnut type of grains.

It is observed from SEM micrographs (Fig. 5.16a) that grains of SI specimen possess spherical morphology. Hollow grains with large shell thickness are evident from the fractured grains. It is discernible from micrograph (Fig. 5.16b) that  $\text{TiO}_2$  grains are somewhat doughnut

shaped. Micrographs of grains obtained for mixed dispersion of  $\text{TiO}_2$  and  $\text{SiO}_2$  are shown in Fig. 5.17. Spherical grains are observed for the composite grains.

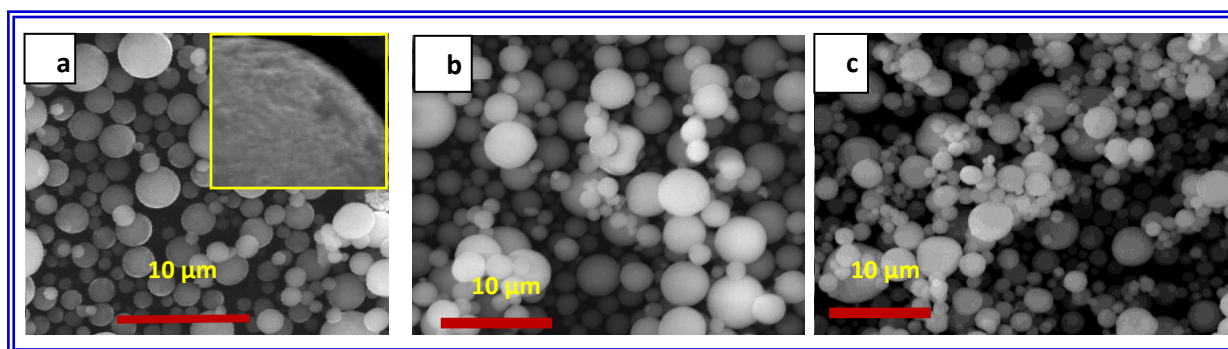


**Fig. 5.17** The micrographs of assembled grains consist of mixed colloids in weight ratio of (a)  $\text{TiO}_2/\text{SiO}_2=2.0$ ., Inset shows a magnified grains, the rough surface of grains indicate that the presence of bigger NPs on the surface (b)  $\text{TiO}_2/\text{SiO}_2=1.0$  (c)  $\text{TiO}_2/\text{SiO}_2=0.5$ .

In order to estimate size of  $\text{SiO}_2$  and  $\text{TiO}_2$  NPs in dispersions, SAXS experiments have been performed individually on 2wt%  $\text{SiO}_2$ , 2wt%  $\text{TiO}_2$  and mixed dispersion as well (Fig. 5.18a).

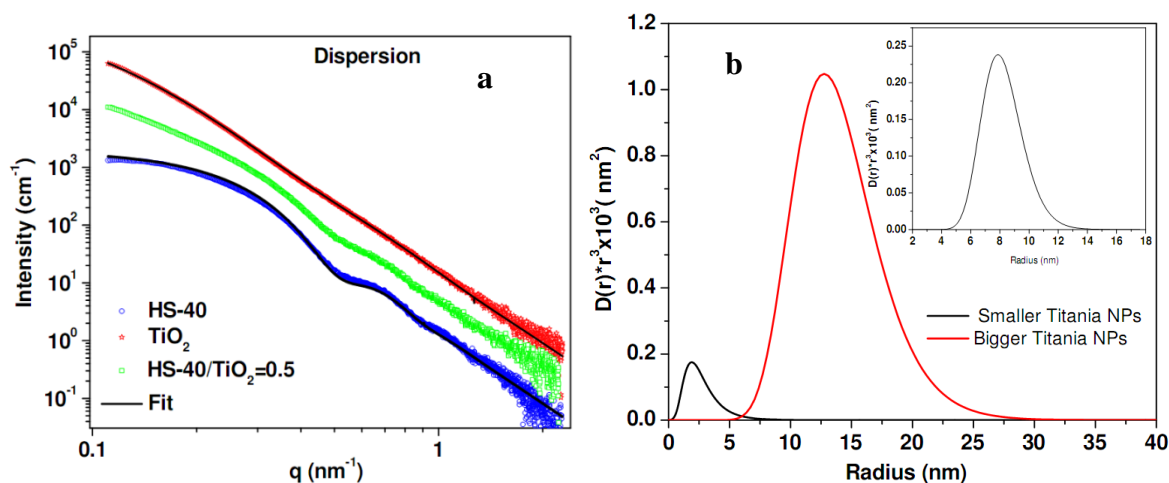


**Fig. 5.18** (a) SAXS profiles of the  $\text{SiO}_2$  and  $\text{TiO}_2$  dispersion. SAXS profiles of the mixed dispersion having  $\text{SiO}_2$  and  $\text{TiO}_2$  in equal proportion. The lines represent the model fit to the data. (b) Bimodal size distribution of the  $\text{TiO}_2$  NPs is shown. Inset shows the  $\text{SiO}_2$  radius distribution.

It is observed from scattering experiments that interaction between SiO<sub>2</sub> and TiO<sub>2</sub> NPs in mixed dispersion remains insignificant. It is apparent from Fig. 5.18a that SAXS profile of mixed dispersion is mimicked by adding individual SAXS profiles of SiO<sub>2</sub> and TiO<sub>2</sub> NPs with appropriate weighting factor without invoking any extra structure factor. SAXS profiles for dispersion have been analyzed by assuming ensemble of polydisperse spheres. Volume weighted radius distributions of NPs in 2 wt% TiO<sub>2</sub> and SiO<sub>2</sub> dispersions have been shown in Fig. 5.18b. It is observed that TiO<sub>2</sub> NPs possess a bimodal type size distribution. Average radius of the smaller TiO<sub>2</sub> NPs has been found to be 3.1 nm having 0.8 nm polydispersity (standard deviation). Similarly, average radius of the bigger NPs is 8.5 nm bearing 4.5 nm polydispersity. Size distribution of SiO<sub>2</sub> NPs is depicted in the inset of Fig. 5.18b. Average radius of SiO<sub>2</sub> NPs is found to be 8.2 nm with a polydispersity 1.0 nm. It important to mention here that size distribution of TiO<sub>2</sub> NPs possesses an extensive tail in higher radius size. However, size distribution of SiO<sub>2</sub> NPs is relatively narrow and do not possess broad tail in contrast to the size distribution of TiO<sub>2</sub> NPs.

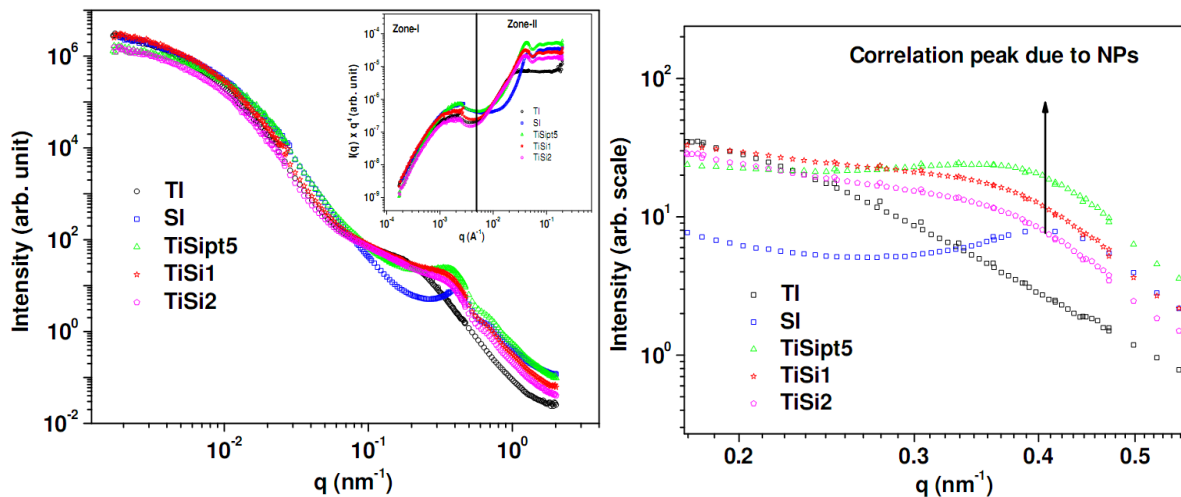


**Fig. 5.19** (a) SANS profiles of the assembled composite grains. Inset shows the profiles in Porod representation (b) SANS profiles of the assembled composite grains in a magnified view.

Combined SANS profiles of assembled grains have been shown in Fig.5.19a. Existence of two Porod levels is evident from the inset of the Fig. 5.19a. It is evident from the figure that assembled grains possess hierarchical length scale structure. In order to see the variation in correlation peak due to the jammed SiO<sub>2</sub> NPs, SANS data of composite grains have also been depicted in zoomed q range of 0.1 to 0.9 nm<sup>-1</sup> (Fig. 5.19b). The correlation of SiO<sub>2</sub> NPs in assembled grains is manifested in scattering profile at q~0.45 nm<sup>-1</sup> as peak. Due to narrow polydispersity of SiO<sub>2</sub> NPs, oscillations of form factor are also visible in scattering profile of SiO<sub>2</sub> grains. It is also evident that scattering profile of TI specimens does not show any prominent peak because of significant polydispersity in size of TiO<sub>2</sub> NPs. The correlation peak corresponding to SiO<sub>2</sub> NPs gets broadened for composite grains with addition of TiO<sub>2</sub> NPs. The broadening of correlation peak is related to volume fraction of SiO<sub>2</sub> NPs in composite grains. Higher the broadening of the peak, lower is the packing fraction of silica NPs. This observation can be understood in terms of homogenous mixing of TiO<sub>2</sub> and SiO<sub>2</sub> NPs. The local packing fraction of SiO<sub>2</sub> NPs gets reduced due to presence of TiO<sub>2</sub> NPs in vicinity, which is also reflected in the slight shift of the correlation peak towards lower q. The broadening of the correlation peak increases with increase in concentration of TiO<sub>2</sub> NPs.

SAXS profiles for freshly prepared SiO<sub>2</sub> grains, aged SiO<sub>2</sub>, TiO<sub>2</sub> and its composite grains have been depicted in Fig. 5.20 in Porod representation (I(q)q<sup>4</sup> vs. q). Silica correlation peak in assembled grains is shown in the inset of Fig. 5.20. Observations from SAXS results corroborate with the SANS results. SAXS profiles of composite grains have also been analyzed to get specific surface area due to jammed NPs. It is important to note that electron density for TiO<sub>2</sub> is approximately two times to that of SiO<sub>2</sub>. This results into higher Porod level for TI grains as compared to that of SI grains. However, specific surface area of SI specimens is higher as compared to that for TI grains as estimated (Table 5.3).

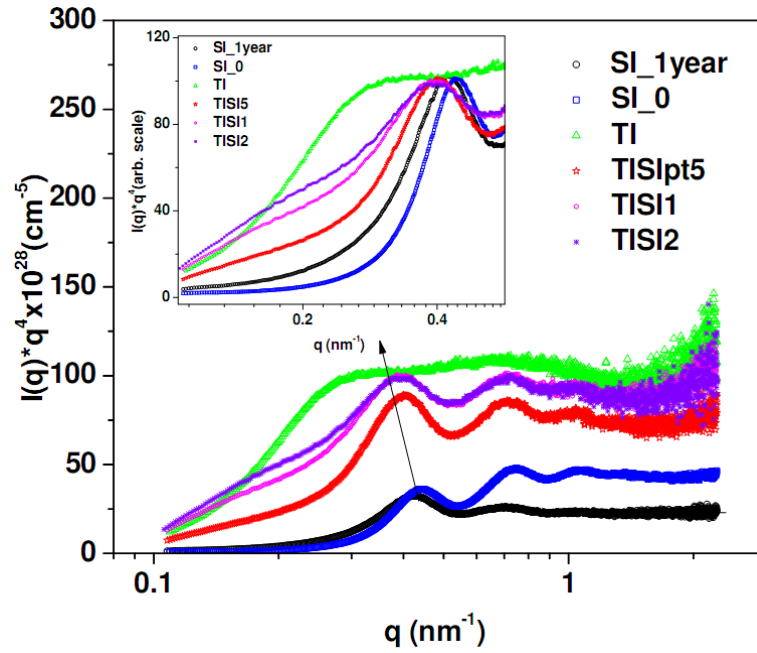


**Fig. 5.20** SAXS profiles of the assembled grains in Porod representation. Inset shows the magnified view of correlation peak.

**Table 5.3** The parameters obtained from SANS/SAXS analysis.

Sample	Specific surface area (m <sup>2</sup> /gm)	Silica NPs correlation peak position (nm <sup>-1</sup> )	Guinier radius of the grains (nm)
SI_t=0	118.8	0.445	281±6
SI_t=1year	62.6	0.420	—
TI	33.8	—	340±7
TISlpt5	85.7	0.399	258±7
TISI1	70.0	0.399	316±11
TISI2	52.7	0.399	293±7

SAXS experiments on freshly prepared SI specimen (SI\_t=0) and one year aged SI specimens (SI\_t=1year) reveal that specific surface area for aged SI specimen is significantly reduced as compared to that for fresh specimen. This observation indicates that smaller SiO<sub>2</sub>

NPs coalesced into bigger NPs at ambient condition over a long period of time in order to reduce specific surface area. From Table 5.3, it is evident that specific surface area of  $\text{TiO}_2/\text{SiO}_2$  composite grains lies between specific surface area of TI and  $\text{SI}_{t=0}$  specimens. It is interesting to note that specific surface area of  $\text{TiSi}_{t5}$ ,  $\text{TiSi}_{t1}$  specimens is higher as compared to aged SI specimen. It indicates that ageing effect (i.e., coalescence of  $\text{SiO}_2$  NPs) on the composite grain is not significant. Coalescence of  $\text{SiO}_2$  NPs is inhibited by presence of  $\text{TiO}_2$  NPs.

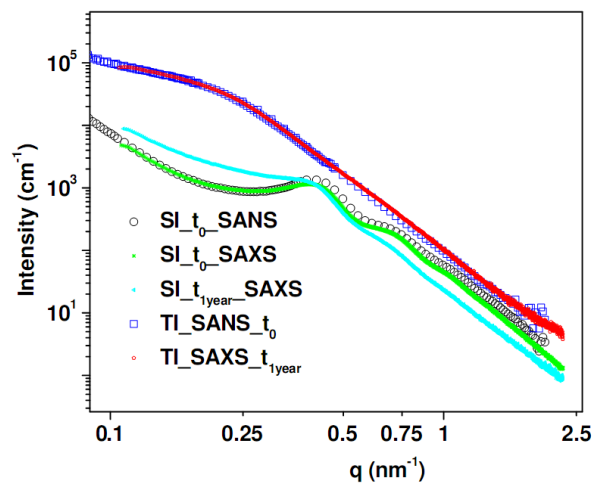


**Fig. 5.21** SANS/SAXS profiles of the self-assembled grains of  $\text{TiO}_2$  and  $\text{SiO}_2$ . The scattering profiles of assembled grains at two different times to compare the effect of aging on the grains.

SANS data collected for freshly prepared SI and TI specimens have been compared to the corresponding SAXS data of aged specimens (Fig. 5.21). SANS profiles have been shifted to match SAXS profiles at high  $q$ . It is evident from figure that SAXS and SANS profiles of fresh and aged TI specimens resemble reasonably well in overlapping  $q$  regime. It indicates that there is no aging effect on the  $\text{TiO}_2$  grains. The temporal stability of the  $\text{TiO}_2$  grains may be attributed to small specific surface area of the grains. Further, SAXS data of aged SI specimens do not match with SANS/SAXS profile of freshly prepared SI specimens.

These observations may be understood in terms of aging effect of SI grains due to high specific surface area of SI grains as discussed above.

Thermogravimetric results of composite grains have been depicted in Fig. 5.22. Weight loss curves of the grains show that there is no significant weight change up to 1000°C in all cases. The slight weight (~2 wt %) loss is due to evaporation of physically absorbed water from assembled grains during heat treatment. Heat flow curves for the all composite grains are mostly identical except presence of an additional small exothermic peak for TI specimens at ~750°C and it may be related to some crystalline phase transition of TiO<sub>2</sub>. However, no exothermic peak is observed for TiO<sub>2</sub>/SiO<sub>2</sub> composite grains.

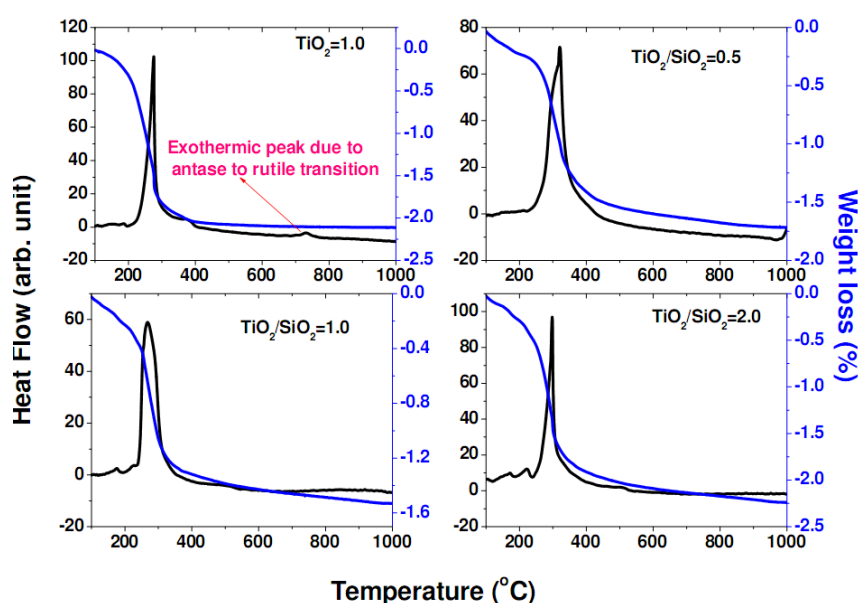


**Fig. 5.22** The heat flow and weight loss curves for composite grains with different TiO<sub>2</sub>/SiO<sub>2</sub> ratio.

To confirm the above results, structural characterization has been carried out by X-ray diffraction. The observed diffraction profile of TI specimens at room temperature have been compared with the anatase and rutile phase of TiO<sub>2</sub> corresponding to JCPDS card nos. 21-1272 and 21-1276, respectively. It is observed that TiO<sub>2</sub> NPs in TI grains exist in a mixed

phase comprised of both anatase and rutile phases. The diffraction profile of TISiPt5 grains has both crystalline  $\text{TiO}_2$  and amorphous  $\text{SiO}_2$  contribution with appropriate weight factor (Fig. 5.23a).

High temperature XRD on TI specimen reveals an anatase to rutile phase transformation below  $850^\circ\text{C}$  (Fig. 5.23a). It shows that assembled grains of only  $\text{TiO}_2$  NPs are not thermally stable as far its crystalline phase is concerned. The XRD profiles of TiSipt5 specimens at different temperatures (Fig. 5.23b) show an interesting observation. Anatase to rutile phase transformation is not observed below  $850^\circ\text{C}$  in contrast to that for only TI case.

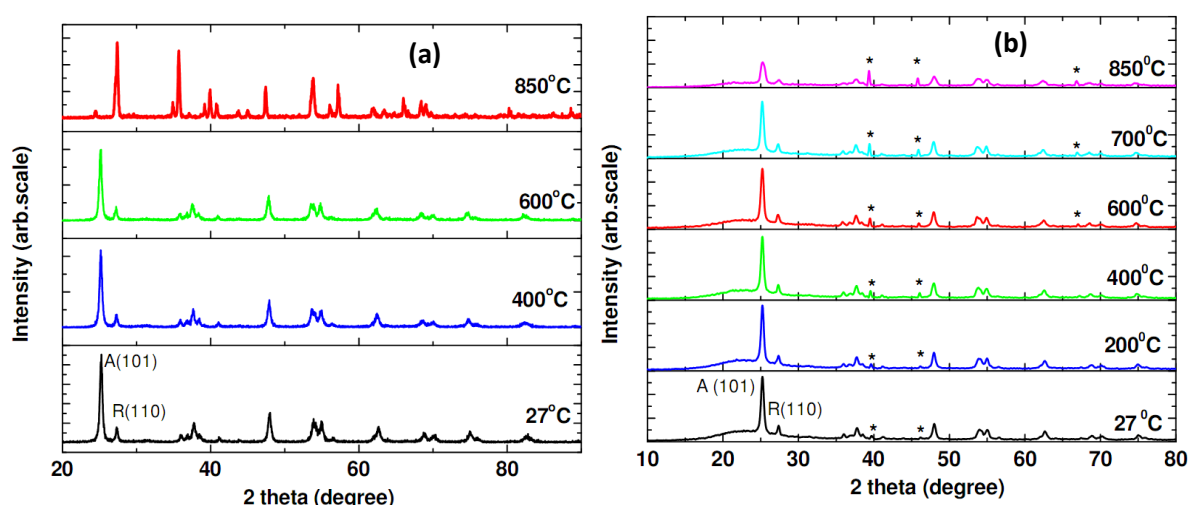


**Fig. 5.23** (a) The X-ray diffraction pattern of the TI specimens for different temperatures. (b) The X-ray diffraction pattern of the TiSipt5 specimens for different temperatures. The \* marked peaks originate from Pt sample holder and should not be considered in the present perspective.

The weight fraction of anatase ( $W_A$ ) and rutile ( $W_R$ ) in both the specimens were calculated from the Spurr equations<sup>87,323</sup> which is shown in chapter-2 as eq. 2.7. The fractions of anatase and rutile phases, at different temperatures, have been tabulated in Tables 5.4 and 5.5 for both the specimens. Mean crystallite size for anatase and rutile phases was calculated<sup>323</sup> from the

broadening of the X-ray reflections (101) crystallographic plane for anatase and (110) for rutile, using the Scherrer's formula<sup>50</sup>.

**Table 5.4** *The parameters obtained from analysis of XRD patterns for TI specimens.*

Temperature (°C)	Weight percent		Average anatase crystalline size (nm)	Average rutile crystallite size (nm)
	Anatase	Rutile		
27	85.2	14.8	19.4	23.5
400	84.5	15.4	19.3	23.1
600	83.9	16.1	19.0	22.7
850	7.4	92.6	-	21.5

**Table 5.5** *The parameters obtained from analysis of XRD patterns for TISIpt5 specimens.*

Temperature (°C)	Weight percent		Average anatase crystalline size (nm)	Average rutile crystallite size (nm)
	Anatase	Rutile		
27	82.4	17.6	18.6	26.7
200	84.0	16.0	19.7	24.6
400	83.0	17.0	20.2	25.3
600	83.4	16.6	18.5	22.4
700	83.1	16.9	17.7	24.0
850	81.2	18.8	16.3	23.0

It is evident from above tables that average weight fractions of anatase and rutile for TI specimens are approximately 85% and 15%, respectively. The crystallite size estimated from XRD analysis shows that average crystallites size of anatase and rutile are typically 19 nm

and 24 nm, respectively. It is interesting to note that the size distribution of TiO<sub>2</sub> NPs has a tail towards higher size. The average size of NPs is ~16 nm, which is closer to anatase crystallite size. However, tail part of the size distribution contains larger size particles of typical size 25 nm. Thus, the tail part of the distribution (higher size) possesses rutile NPs in contrast to average NPs which are in anatase phase.

In following section, a mechanism of formation of such novel composite via EISA will be explained.

Peclet number  $P_e$ , for present drying condition for 2 wt% silica (Ludox HS-40) dispersions is estimated<sup>323</sup> to be 3.6. This confirms that present drying condition falls under relatively fast drying regime. It is to be noted that all the physical conditions were kept invariant during drying of SiO<sub>2</sub>, TiO<sub>2</sub> and mixed dispersions. Peclet number for the drying of 2 wt% TiO<sub>2</sub> dispersion remains nearly same since average size of TiO<sub>2</sub> and SiO<sub>2</sub> NPs are comparable. However, it is important to mention here that Peclet number is inversely proportional to diffusion coefficient of NPs inside the drying droplet. Thus, Peclet number for bigger TiO<sub>2</sub> NPs which falls in the tail of size distribution turns out to be higher as compared to the smaller ones.

Relative shell thickness plays an important role in deciding the morphology of drying droplet and hence grain morphology. The capillary pressure drives the deformation of the shell. However, a critical pressure  $p_c = 4Y_0 \left( \frac{h}{R_c} \right)^2$  is required to induce the buckling of a homogenous shell<sup>300-301</sup>. Where  $h/R_c$  is the relative shell thickness and  $Y_0$  is the Young's modulus of the shell. If the stress on the shell due to capillary pressures exceeds the critical pressure, shell buckles. In case of SiO<sub>2</sub> dispersion, size distribution of NPs is quite narrow with mean radius 8.2 nm. During drying of 2 wt% SiO<sub>2</sub> dispersion, a shell forms and gets

thickened as drying proceeds. The relative shell thickness  $h/R_c$  is large enough and thus requires higher critical pressure. Capillary pressure, acting on the shell, is not sufficient to overcome the critical pressure required for buckling. However, formation of hollow grains is a possibility if water evaporates through the porous shell of jammed NPs. In present experiment, hollow spherical silica grain has been observed and is well understood by aforementioned mechanism. EISA during drying of the 2 wt%  $TiO_2$  dispersions is different due to higher polydispersity. The diffusion of bigger  $TiO_2$  NPs is smaller as compared to that of smaller NPs. During shrinkage of the drying droplet bigger NPs are less mobile towards core of the droplet. This leads to accumulation of NPs at drying front leading to shell formation in early stage as compared to the drying of the droplet containing  $SiO_2$  colloids resulting lower relative shell thickness. The critical pressure required to deform a shell having lower relative thickness is smaller. Thus the capillary pressure acting on the shell is sufficient to deform it. For mixed colloids of  $SiO_2$  and  $TiO_2$ , fraction of smaller NPs increases. The effective NPs size distribution becomes narrower as compared to only  $TiO_2$  dispersion. The relative shell thickness formed during drying of mixed colloidal droplet will be higher. Thus, the droplets of mixed dispersions do not buckle during drying and lead to spherical morphology of the grains.

It is to be noted that due to above mentioned EISA process of the stable mixed dispersion of the  $SiO_2$  and  $TiO_2$  of comparable size, uniform composite grains have been fabricated except surface layer of grains. On the surface layer of grains, bigger  $TiO_2$  NPs are present in a dominant way which is evident from inset of Fig. 5.19a.

It is clear from XRD analysis that rutile is stable phase for higher size of  $TiO_2$  NPs; however, for smaller  $TiO_2$  NPs anatase phase is more favorable<sup>324</sup>. At relatively small particle dimensions, the surface energy is an important part of the total energy and it has been found

that the surface energy of anatase is lower than those of rutile<sup>317,325</sup>. Anatase to rutile polymorphic phase transformation follows a nucleation-growth mechanism<sup>326</sup>. Upon thermal treatment, anatase crystallites grow until they reach a critical nuclei size. Once the crystallites size overcome the critical nuclei size, the rutile nucleation starts,<sup>327</sup> involving the breaking of anatase Ti–O bonds, followed by a cooperative motion of these atoms<sup>328</sup>. The anatase to rutile transformation of NPs in TI specimens may be well understood by the above mechanism. However, anatase to rutile phase transformation has not been observed in case of the composite grains. It may be understood by the mesoscopic morphology of composite grains. As TiO<sub>2</sub> NPs are uniformly jammed with SiO<sub>2</sub> NPs in the grains, growth process of TiO<sub>2</sub> NPs is inhibited and vice versa. Thus, size and hence, anatase phase of TiO<sub>2</sub> NPs remains constant with temperature in composite grains.

A schematic of the EISA mechanism of single colloidal droplet and mixed colloidal droplet is shown in Fig. 5.24.

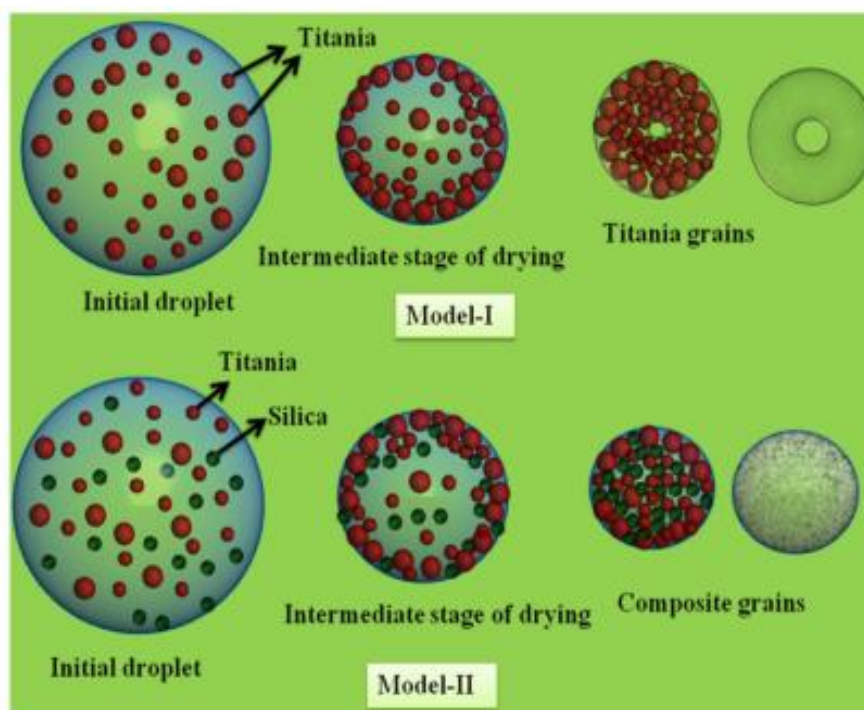


**Fig. 5.24** The schematic of the formation of assembled grains of TiO<sub>2</sub> NPs and composite grains.

#### **5.3.4. Conclusions**

TiO<sub>2</sub>/SiO<sub>2</sub> mesoporous microspheres have been synthesized by EISA of mixed colloids. Origin of different morphology of SiO<sub>2</sub>, TiO<sub>2</sub> and its composite grains has been related to average size and polydispersity of the NPs. SAXS and SANS experiments reveal that composite grains do not show aging effects in contrast to only SiO<sub>2</sub> grains and is related to specific surface area of grains. X-ray diffraction experiments show that composite grains are thermally stable against the anatase to rutile phase transition. This is attributed due to inhibition of growth of TiO<sub>2</sub> NPs due to confinement in SiO<sub>2</sub> matrix.

# **Buckling Induced Morphological Transformation of Droplets of Mixed Colloidal Suspensions during Evaporation Induced Self assembly**

## **6.1. Morphological Transformation of Droplets of Silica Colloids and *E-coli* Suspensions**

### **6.1.1. Introduction**

Morphological transformation has been realized experimentally for drying of droplets for single type of colloidal suspension<sup>13,229,329</sup>. However, understanding of such transformation in droplets that contain mixed colloids is not fully understood yet, both experimentally and theoretically. This is because of difference in their size, shape or elastic modulus. It is noteworthy to mention here that if initial droplets contain mixed colloids of organic and inorganic components, then porous grains may be synthesized by removal of organic template species from assembled grains. In the present section, the effect of incorporation of *E. coli* on sphere to doughnut like morphological transformation during the EISA of colloidal silica suspension is presented. It is interesting to mention that present study was motivated from the fact that the *E. coli* being soft and anisotropic in shape may facilitate buckling driven shape transformation by modifying the elastic modulus of the formed shell of jammed particles at the boundary of the drying droplets.

### 6.1.2. Experimental section

Mixed colloidal dispersion of 2wt% silica and varying *E. coli* (0%, 2%, 4% and 6% in weight) was prepared and spray drying was carried out using a spray dryer LU222 in fast drying regime. Removal of the imprinted materials was carried out by incineration in muffle furnace at 300 °C for 10 hrs. The powders with 0, 2, 4 and 6% of *E. coli* are labeled as E0, E2, E4 and E6, respectively.

### 6.1.3. Results and discussions

SEM micrographs for E0, E2, E4 and E6 specimens are shown in Fig. 6.1.

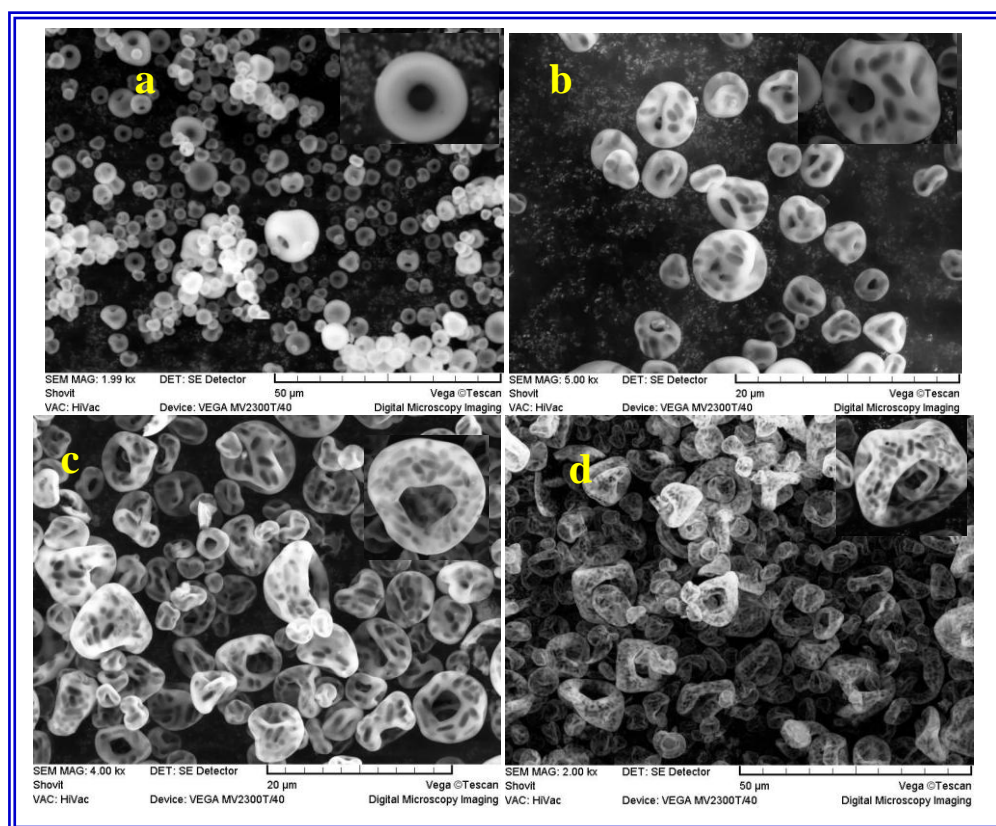


**Fig. 6.1** SEM micrograph of (a) Sample E0 (b) Sample E2 (c) sample E4 (d) sample E6

From SEM micrograph (Fig. 6.1a), it is evident that the assembled grains of the sample E0 are doughnut with almost no deformation. Further, relatively large multi-faced deformed doughnuts have been observed in case of grains with higher *E. coli* fractions (Figs. 6.1b-d).

It is also evident from micrographs that deformation/asymmetry increases with increasing volume fraction of the *E. coli*. These observations clearly indicate that the concentration of the *E. coli* in the initial liquid droplet plays an important role in deciding the distortion and morphology of central hole of the multi-faced doughnuts during the assembly.

SANS experiments on spray dried grains were performed using two instruments at the Guide Tube Laboratory of Dhruva reactor at Trombay, Mumbai, India. For the assembled grains, combined SANS data from both the above instruments are shown in Fig. 6.2 in double logarithmic scale. Inset depicts the data in Porod representation.

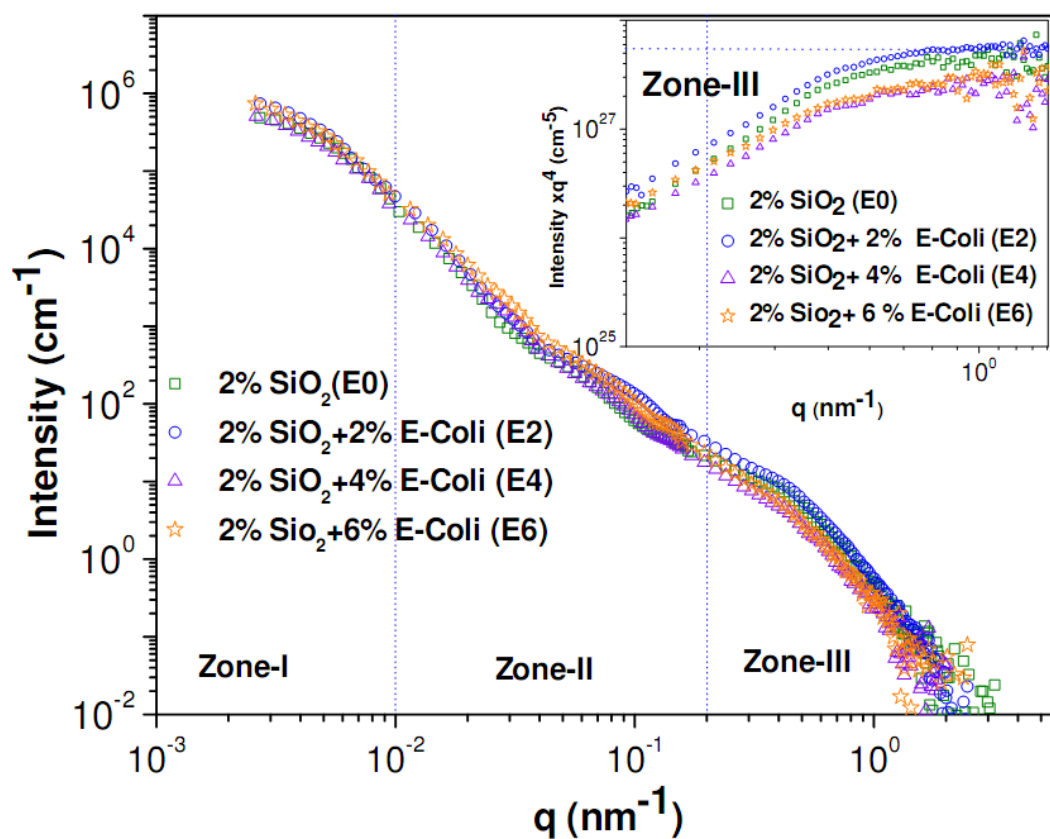


**Fig. 6.2** SANS data from self assembled macro/mesoporous silica grains plotted in double logarithmic scale. The inset shows the Zone-III of the profiles plotted in Porod representation.

The average size of the virgin silica colloids was found<sup>218</sup> to be ~12 nm. From Fig. 6.2, it is evident that for all the specimens, SANS profiles may be subdivided, for clarity, into three distinct zones, namely, Zone-I, Zone-II and Zone-III. Zone-I primarily bears the information about larger structure (a part of size distribution of assembled grains and also scattering from cylindrical macropores which are imprinted by *E. coli*). Zone-II mainly contains information about macropores templated by *E-coli*. Zone-III bears the signature of small silica colloids which constitute the solid skeleton of the grains. It is worth mentioning that the number of macropores in a grain increases with *E. coli* volume fraction, while the total amount of silica particles gets reduced from sample E0 to E6 leading to reduction in microporosity (if it is assumed that the initial droplet size is constant).

At this juncture, it is important to mention that quantitative analysis of SANS data, by fitting the whole profile, becomes significantly complex for systems with structures in hierarchical length scales. In addition, further complications creep in because of following factors: (i) Firstly, the grains are not spherical in nature and possess a significant size and shape distribution. (ii) Secondly, most of the grains seem to be hollow and are not isotropic in nature. (iii) Macropores are not spherical but cylindrical in nature. (iv) Ratio of size of grains to the size of cylindrical macropore is not significantly high. However, an empirical approach has been adopted to fit the experimental profiles and discussed in detail elsewhere<sup>218</sup>.

In following section, deformations of doughnuts due to increasing concentration of *E. coli* have been discussed. For present experimental conditions, Peclet number  $P_e$  is estimated<sup>218</sup> to be 1.2 for droplet containing only silica colloids and 124.7 for droplet containing only *E. coli*. Hence, addition of *E. coli* effectively increases the Peclet number vis-à-vis the instability of drying droplet. Size, shape and elastic modulus of the particles in the droplets are important factors as far as buckling deformations are concerned. As the

Peclet number is more for bigger particles, the deformation during buckling is more when *E. coli* is present. *E. coli* being a bacteria is much softer (Longitudinal Young's modulus  $\sim 25$  Mpa and circumferential Young's modulus  $\sim 75$  MPa density  $\sim 1.1 \text{ gm/cm}^3$ )<sup>330</sup> than silica ( $\sim 75000$  MPa, density  $\sim 2.5 \text{ gm/cm}^3$ ). Thus, incorporation of bacterial component results in decrease in elastic constants vis-à-vis enhancement of buckling probability of the formed shell of NPs at boundary of drying droplets. Further, non spherical shape of *E. coli* causes somewhat anisotropic variation of capillary forces at different zones of shell resulting to multi invagination zone on surface of shell. This enhances the deformation during buckling and dimpled multi-faced deformed doughnuts grains are realized. The evolution of the droplet during drying has been presented more in Fig. 6.3.

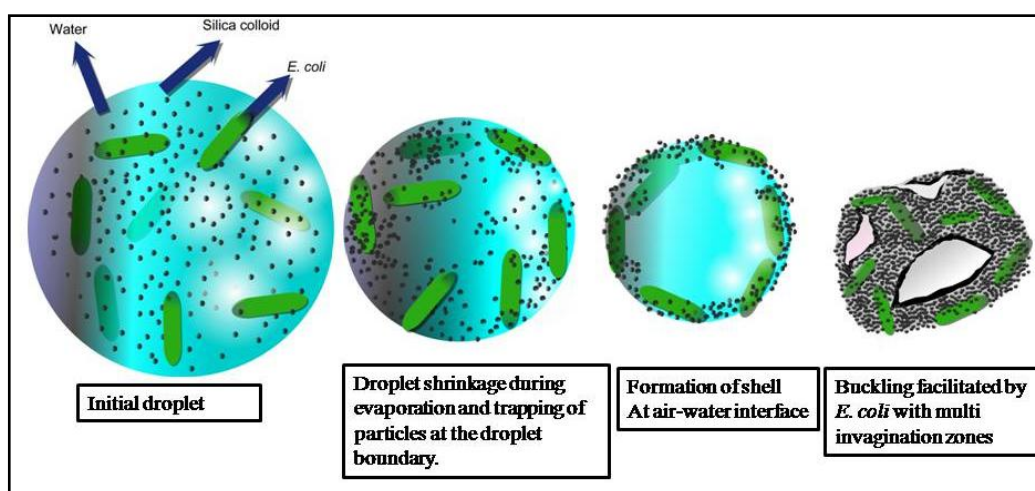


**Fig. 6.3** A schematic representation of possible evolutions of structures during drying of a droplet in presence of *E. coli* is depicted.

#### 6.1.4. Conclusions

Morphological transition of micrometric droplet of mixed colloidal suspension during EISA with incorporation of soft anisotropic particle is experimentally demonstrated. It has been indicated that reduction in elastic modulus of the formed shell, by incorporation of soft anisotropic component, at air water interface facilitates buckling and deformation.

Hierarchically structured doughnut shaped micrometric silica grains, with cylindrical macropores and mesopores in silica interstices is realized by this process.

## **6.2. Arrest of Morphological Transformation during EISA of Mixed Colloids by Charge Tuning**

### **6.2.1. Introduction**

The physical origin of buckling instabilities<sup>229,230,245,251</sup> has been dealt with for a suspension of single and mixed colloids. However, such instability for a multi-component system has not been fully understood so far<sup>218</sup>. Further, a method to arrest such morphological transformation is yet to be proposed. In this section, it has been demonstrated that buckling instabilities during drying of droplets of mixed colloidal suspension can be arrested by tuning surface charge on the colloidal components. Present investigation also indicates that effective elastic modulus of the particles exposed at air-water interface play an important role in controlling buckling deformation. Further, it has also been demonstrated that buckling criteria for drying droplets of mixed colloidal particles remain beyond the existing buckling hypothesis<sup>229</sup>.

### **6.2.2. Experimental**

In order to tune the repulsive force between colloidal particles, *E. coli* cells were treated to impart a polycationic charge on cell surface<sup>331</sup> using polyethylenimine (PEI) (Average MW~7.5x10<sup>5</sup>). It has been verified<sup>285</sup> by Ostwald method that specific viscosity of 2% PEI solution with respect to pure water is 1.5 only. The effective viscosity will be even smaller after removal of excess PEI. Zeta potentials for *E. coli* suspensions with varying PEI coating (0.2, 1.0, 2.0 %) at surface of *E. coli* were found to be -8.4 (Case-II), +14.6 mV (Case-III) and +19.6 mV (Case-IV), respectively. This confirms that adsorbed layer of PEI on *E. coli*

surface reduces negative charge and eventually reverses the polarity of surface charge on *E. coli*, depending on amount of polymer coated.

Spray drying experiments have been carried out with silica and PEI coated *E. coli* mixed colloidal suspension in fast drying regime. Mass fraction of silica and *E. coli* in the initial suspension was 2 wt % and 6 wt %. The spray dried specimens were calcined at 300 °C for 10 hrs to remove organic moieties. Zeta potential for individual silica and virgin *E. coli* suspensions were found to be -43.2 mV and -30.0 mV, respectively. Same for the mixed suspension of silica and *E. coli* was -58.6 mV. The micrographs of calcined spray dried grains are depicted in Fig. 6.4. SANS measurement have been performed at KWS-1, KWS-3 (at FRM-II, Germany) and S18 (at ILL, France)<sup>332</sup>.

### 6.2.3. Results and discussion

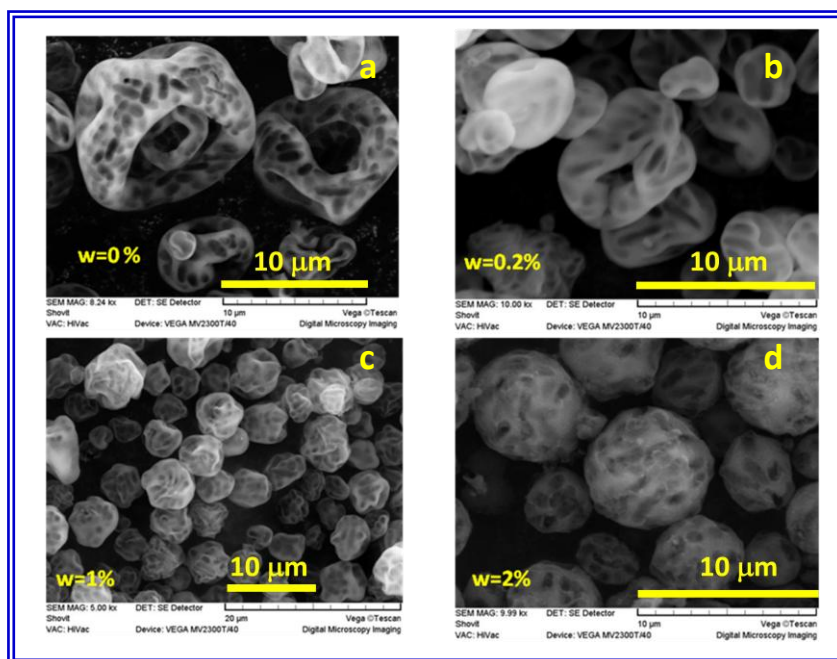


**Fig. 6.4** SEM micrograph of the composite grains (a) *E. coli* is not covered with poly-cationic PEI (b) *E. coli* coated with 0.2 % PEI (c) *E. coli* coated with 1.0 % PEI (d) *E. coli* coated with 2.0 % PEI.

Peclet number  $P_e$  for present experimental conditions is estimated<sup>285</sup> as 1.2 for a droplet containing only silica colloid. The same turns out<sup>285</sup> to be 125 for droplet containing only *E. coli*.

It is interesting to note from zeta potential measurements that both silica and virgin *E. coli* possess charge of similar polarity (-ve) and thus form a repulsive system. It is clearly evident from the SEM micrographs that amplitude of buckling has been maximum in the Case-I, i.e., when the repulsive force between the *E. coli* and silica is maximum. However, buckling amplitude reduces with decrease in repulsive stabilization force (by coating poly-cationic PEI on *E. coli*). Gradually, buckling becomes insignificant and eventually vanishes when system becomes somewhat attractive by reversing the polarity of surface charge of *E. coli* (zeta potential for silica is -43.2 mV and 2 % PEI coated *E. coli* is +19.6 mV). According to the existing hypothesis<sup>229, 251</sup> morphological transformations should have been occurred in other way, i.e., the grains should have been more hollow and deformed when the stabilization force is reduced by making the system slightly attractive. This observation motivated us to search for mechanism of buckling and its arrest in case of EISA of mixed colloids. At this juncture, it is to be noted that duration of each spray drying experiment has been nearly half an hour and there was no visible flocculation or phase separation of the colloids within this time interval even for maximum attractive system (2% PEI coated *E. coli*).

It is important to mention that *E. coli* is much soft (Longitudinal Young's modulus ~25 Mpa and circumferential Young's modulus ~75 MPa, density ~1.1 gm/cm<sup>3</sup>)<sup>330</sup> than silica (~75,000 MPa, density ~2.0 gm/cm<sup>3</sup>). In fact, present investigation was also motivated by the query whether buckling could be arrested by modifying effective elastic strength of the shell at air water interface during drying. When *E. coli* is not coated with PEI, i.e., for the Case-I, repulsive stabilization force is maximum between silica and *E. coli*. Thus, air-

water interface of the droplets is equally exposed to both silica as well as *E. coli*. As elastic constant of *E. coli* is significantly small compared to that of silica, the droplet is more prone to buckling as compared to that for the case where air water interface is exposed only to silica. When PEI is coated on *E. coli*, negative charge of virgin *E. coli* gets reduced and gradually attains positive polarity at higher PEI concentration. In such an environment, silica NPs, which are much smaller than *E. coli*, form a particle-cloud around *E. coli*. Thus, during drying, air water interface is mostly exposed to silica and thus the amplitude of buckling gets diminished. It is also supported by micrograph in Fig. 6.4d. The cylindrical pores in grains, templated by *E. coli*, look somewhat blurred because of the fact that *E. coli* gets mostly covered with silica NPs. Thus, buckling could be arrested by not exposing *E. coli*, the softer component, directly to the air-water interface.

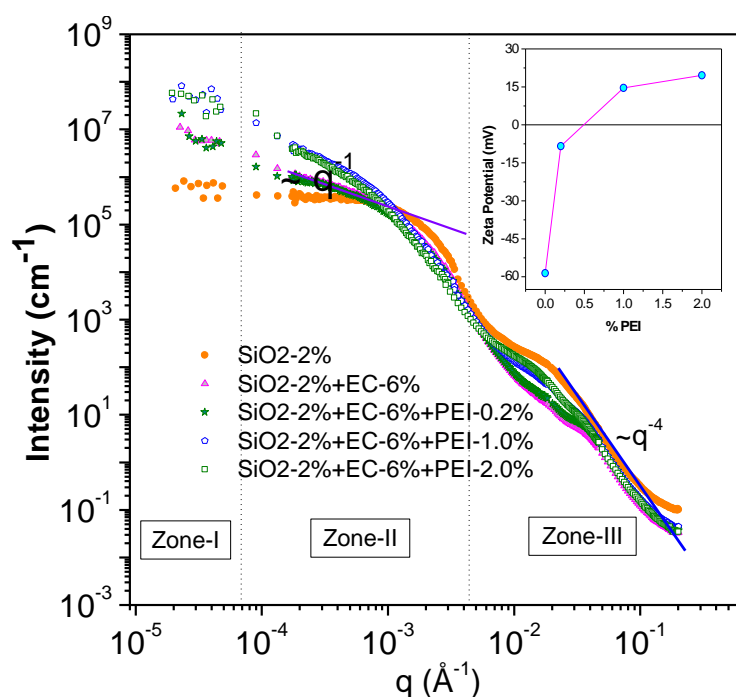


**Fig. 6.5** SANS data from the hierarchically structured assembled grains. Three different length scales in the assembled grains are obvious from the scattering data. It is observed from the data that the correlation of the particles inside the grains gets modified with change in the surface charge of *E-coli*.

As the arrest of buckling is strongly associated with modification of hierarchical structure of assembled grains, the same has also been verified by using SANS measurements. The SANS profiles of spray dried samples are plotted in Fig. 6.5. It is apprehensible that assembled grains possess structure in three different length scales due to presence of (i) silica NPs, (ii) pores templated by *E. coli* and (iii) overall assembled grains. Three distinct zones in scattering profiles, zone-III, zone-II and zone-I, respectively bear the signatures of the above mentioned length scales in the grain, respectively. It is obvious from Fig. 6.5 that functionality of scattering profiles gets modified with addition of *E. coli* and also by further charge modification. The  $q^{-1}$  behaviour of scattering profile in zone-II indicates the presence of cylindrical macropores templated by *E. coli*. It is to be noted that such region with  $q^{-1}$  dependence of scattering data was absent for sample without *E. coli*. It is interesting to observe from scattering profiles that intensity in zone-III reduces significantly when unmodified *E. coli* is added to silica suspension. With increase in amount of added PEI, intensity in zone-III starts increasing again. This signifies appearance of relatively more compact grains in Cases-II, III and IV than Case-I.

In a quantitative way, scattering intensity from such hierarchical grains may be approximated by additive contributions of scattering components from three different length scales<sup>218,233,242,285</sup>:

$$I(q) = C_s \Delta\rho_s^2 I_s(q) + C_p \Delta\rho_{\text{pore}}^2 I_{\text{pore}}(q) + C_g \Delta\rho_g^2 I_g(q) + B \quad (6.1)$$

$\Delta\rho_s = \rho_s - \rho_{\text{int}}$  ( $\rho_s$  is the scattering length density of silica and  $\rho_{\text{int}}$  being the scattering length density of interstices between silica NPs). As interstice between silica NPs is air,  $\rho_{\text{int}} \sim 0$ . Here,  $\Delta\rho_g$  represents average scattering contrast of grains, hence  $\Delta\rho_g = \phi_s \Delta\rho_s + \Delta\rho_{\text{int}}$ . As the medium in which grains are embedded and medium of interstices are both air in this case,  $\Delta\rho_{\text{int}} = 0$  and thus  $\Delta\rho_g = \phi_s \Delta\rho_s$ . B represents background. After calcination of grains most of

the organic moieties leave the grains and hence, in the present case,  $\Delta\rho_{\text{pore}}$  has been taken as  $\Delta\rho_{\text{s}}$  itself.  $C_{\text{s}}$ ,  $C_{\text{p}}$  and  $C_{\text{g}}$  are respectively, scale factors for scattering contribution from silica, pore and grain.  $I_{\text{s}}(q)$  is the scattering contribution from the silica particles.  $I_{\text{s}}(q)$  has been assuming an interacting polydisperse spherical particle model. Expression for  $I_{\text{pore}}(q)$  due the presence of templated macropores is similar to that of  $I_{\text{s}}(q)$  except the fact that a cylindrical form factor for macropores has been used (to account for  $q^{-1}$  behaviour in zone-II, a signature of presence of cylindrical pores). Scattering contribution  $I_{\text{g}}(q)$  from overall grains, is manifested in zone-I . A polydisperse spherical particle model was assumed for this term. It has been shown<sup>285</sup> that the above described model fit the experimental data quite well .The estimated parameters from fitting of model to scattering profiles are tabulated in Table 6.1.

**Table 6.1** Structural parameters obtained from SANS analysis

Sample	Assembled grain size distribution		Templated cylindrical macro pore		
	Mean radius ( $R_{\text{grain}}$ ) (nm)	$\frac{\Delta R_{\text{grain}}}{R_{\text{grain}}}$	Length ( $L_{\text{pore}}$ ) (nm)	Average radius ( $R_{\text{pore}}$ ) (nm)	$\frac{\Delta R_{\text{pore}}}{R_{\text{pore}}}$
Only Silica	200	0.099	-	-	
Silica+EC	2394	0.658	2000	102	0.205
Silica+EC+PEI0.2	2266	0.533	2050	115	0.209
Silica+EC+PEI1.0	2266	0.533	2600	167	0.305
Silica+EC+PEI2.0	2159	0.531	2600	167	0.305

It is seen from Table 6.1 that mean size of grains increases significantly in presence of *E. coli* as grains become hollow and buckled. Further, mean size and the polydispersity get somewhat reduced when charge on *E. coli* is modified by PEI as grains become relatively

more compact. It is also seen that grain radius decreases slightly with increases in addition of PEI that occurs because of some compaction in internal structure.

It appears at first sight that arrest of morphological transformation may be either due to charge effect or modification in viscoelastic behavior when PEI is added. However, these two possibilities are differentiated in following way, in order to reach a plausible conclusion. First of all, it should be noted that excess or unbound PEI that did not get coated on *E. coli* was removed by washing. As mentioned earlier that it was verified that the specific viscosity of 2% PEI solution with respect to pure water is 1.5. After removal of excess PEI, it would be even smaller. Thus, there should not be any significant increase in viscosity with PEI coating. We think that such morphological transformation gets arrested through effective coverage of larger and softer colloidal components by smaller and harder components by proper tuning of the surface charges. A plausible mechanism is represented schematically in Fig. 6.6.

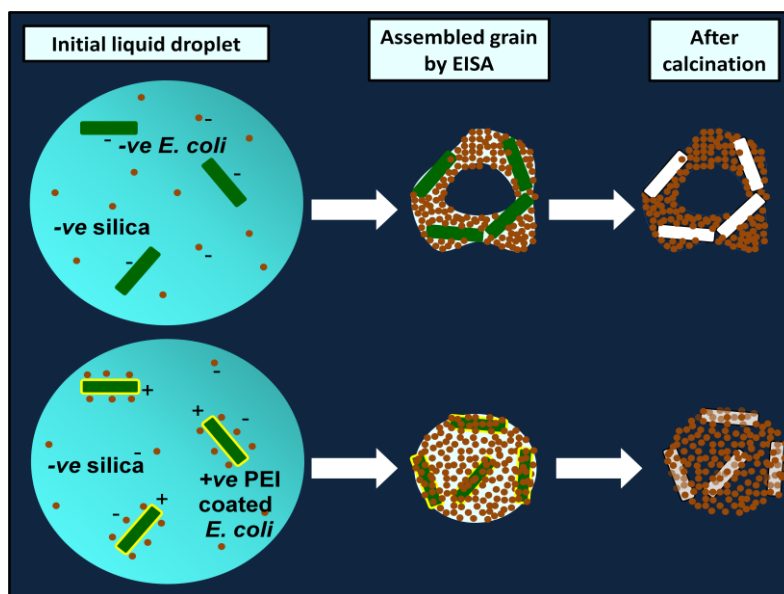


**Fig. 6.6** Schematic representation of the assembly process of silica and *E. coli*. (a) Both silica and *E. coli* have negative surface charges. (b) Silica is negative as earlier case but *E. coli* surface is coated with PEI to impart positive charge on *E. coli* surface.

#### **6.2.4. Conclusions**

It is revealed that buckling driven sphere to deformed-doughnut like morphological transformation of mixed colloidal suspension droplets during EISA can be arrested through effective coverage of larger and softer colloidal components by smaller and harder components by proper tuning of surface charges. Such observations on EISA of mixed colloids are beyond the existing hypothesis of buckling of colloidal suspension droplets that contain only one type of colloid.

### **6.3. Nanocomposite Silica Surfactant Microcapsules by Evaporation Induced Self Assembly: Tuning the Morphological Buckling by Modifying Viscosity and Surface Charge**

#### **6.3.1. Introduction**

In recent years, porous and hollow microcapsules are attracting continuous interest in science and technology<sup>333-340</sup>. This is because of the fact that such hollow capsules are potential candidates for various applications such as, drug delivery, catalysis, photonic crystal, chromatography, protection of biologically active agents, pigments, coatings, waste removal, dye-sensitized solar cells etc. Several strategies such as hetero phase polymerization, self-assembly, layer-by-layer assembly and spray drying have been adopted to synthesize hollow capsules comprising of polymeric or ceramic materials<sup>341-342</sup>. In this regard, spray drying has been proved to be an efficient, fast and one step process to realize micrometric and sub-micrometric capsules/grains.

In previous section, it has been shown that morphological transformation of mixed colloidal suspension droplets during EISA can be arrested through an effective coverage of the bigger and softer colloidal components by the smaller and harder components by suitable

tuning of surface charge. Such intriguing results prompted us to further investigate the role of surface charge of colloids and viscosity of the formulation during EISA of mixed colloids comprising of both hard and soft colloids.

Surfactants, in aqueous solutions, have the ability to modify the surface charge of inorganic materials via adsorption and at the same time these molecules self assemble to form soft colloidal structures such as micelles, worm-like micelles, vesicles etc. Here, we used micelles, formed by anionic surfactant SDS, as the soft matrix. The size of these micelles is smaller than harder component, i.e., silica NPs. Microstructural transitions in micellar solutions can be achieved via surface charge modulation, which in turn affect the macroscopic properties of the fluid, such as viscosity. In recent past, it was observed that hydrotropic electrolyte, in low concentration, modifies the surface charge of anionic micelles significantly and also imparts substantial changes in rheological behaviour of fluid<sup>332</sup>. Further, it has been shown that such addition of hydrotropic electrolyte, even at low concentrations, to anionic micelles promotes a transition from spherical to worm-like micelles through strong binding of hydrophobic cation to anionic micelles<sup>333</sup>.

The present investigation is a step to improvise the understanding on how inter-particle interaction/surface charge and viscosity of medium affect morphological transformation during drying of spray colloidal droplets.

### **6.3.2. Experimental**

Mixed dispersions of 2 wt% silica, 2 wt% Sodium dodecyl sulfate (SDS) for varying concentration of Aniline Hydro Chloride (AHC) (0, 10, 20, 30 and 50 mM) were prepared for spray drying purpose. Spray drying of dispersion has been performed using LU228 spray dryer under fast drying regime. Spray dried grains were also washed carefully with methanol or calcined in order to expel the organic moieties from the grains<sup>334</sup>.

Rheological properties of dispersions have been measured by a rheometer (Anton Parr Physica MCR 101) using double gap concentric cylinder geometry (DG 26.7) with a Peltier temperature control. Shear rate was varied from 0.1 to 200 s<sup>-1</sup>. The pH values for silica dispersion and mixed silica-SDS dispersion were 9.7 and 9.4, respectively. The pH value for dispersion with 10, 20, 30 and 40 mM AHC concentration were 7.8, 5.7, 5.2 and 4.5, respectively.

SANS measurement were performed on non-calcined self-assembled grains at JCNS, FRM-II, Germany, using KWS-1 and KWS-3. SAXS measurements on non-calcined grains have also been carried using a laboratory based SAXS instrument.

### 6.3.3. Results and discussion

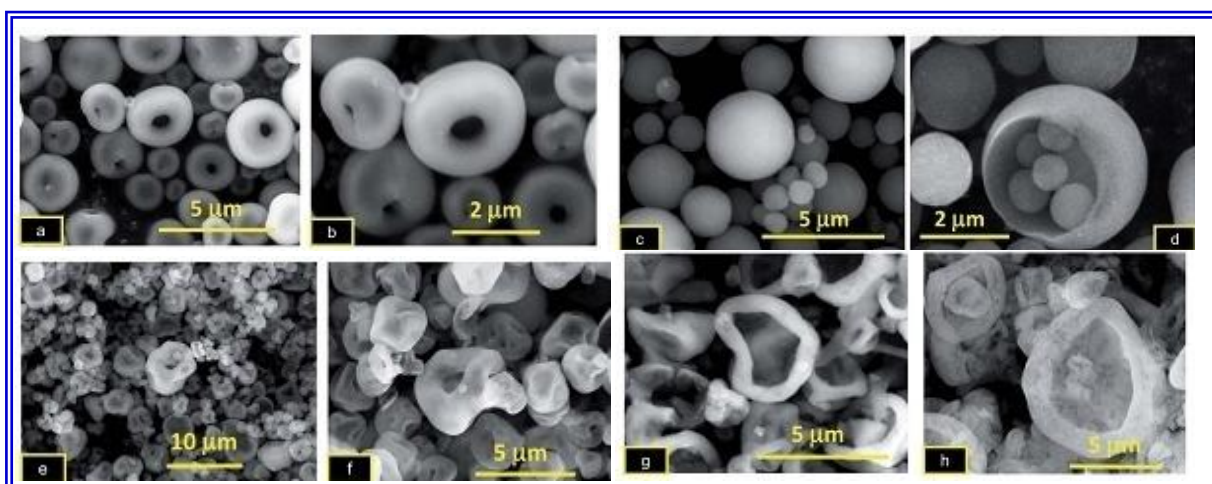


**Fig. 6.7** SEM micrographs of the assembled grains. (a, b) Doughnut like capsules prepared from only silica colloids. (c) Spherical capsules synthesized with silica colloids and SDS in absence of AHC. (d) Same as (c) but after removal of organic moieties. (e) Deformed doughnut like capsules synthesized with silica, SDS and 20 mM AHC. (f) Same as (e) but after removal of organic moieties. (g) Mushroom like grains synthesized with silica, SDS and 50 mM AHC. (h) Same as (g) but after removal of organic moieties.

SEM micrographs of assembled capsules are shown in Fig. 6.7. It is evident from micrographs (Figs. 6.7a, 6.7b) that microcapsules, as obtained from spray drying of silica dispersion alone, are smooth doughnuts with prominent central hole. However, addition of SDS micelles in dispersions results in spherical microcapsules. From Fig. 6.6d, it is observed that after removal of SDS, these microcapsules become indeed hollow with relatively thin shell. Interestingly, significant deformation in grain morphology starts when AHC is added to silica-SDS dispersion. At 50 mM of AHC concentration, spherical droplets during drying get deformed significantly and eventually form mushroom-like structure (Figs. 6.7g, 6.7h) of the assembled grains.

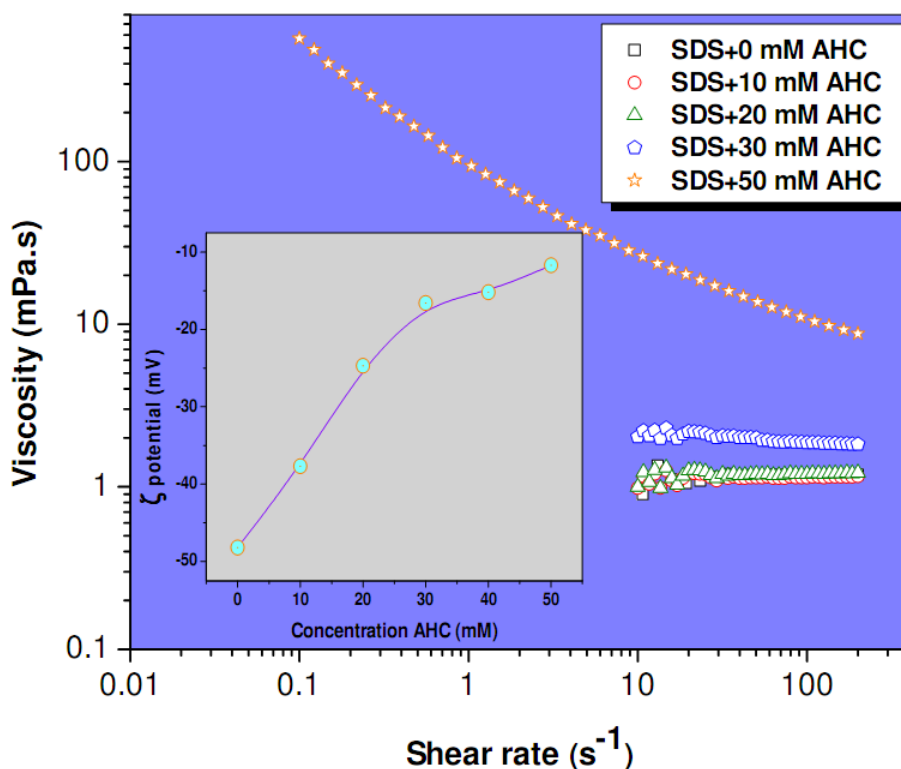


**Fig. 6.8** Rheological response of the dispersions prior to the drying is shown. The inset shows the variation of the  $\zeta$  potential with AHC concentration.

Here, it should be mentioned that although the amount of AHC has been limited to 50 mM, the addition of this hydrotropic additive affects the physico-chemical properties of the

dispersion significantly in two ways. It reduces the effective  $\zeta$  potential (inset of Fig. 6.8) and modifies the viscosity (Fig. 6.8) of dispersion basically due to changes in micelle structure and arrangement<sup>332,333</sup>. In absence of AHC, the  $\zeta$  potential remains highly negative (-50 mV). However, magnitude of surface charge decreases in a continuous fashion with addition of AHC suggesting co-adsorption of AHC with SDS. Although the reduction in viscosity is marginal at low concentrations up to 20 mM of AHC, a significant increase in viscosity is observed at 50 mM AHC (Fig. 6.8).

Peclet number  $P_e$  in present experimental condition is estimated<sup>334</sup> as  $\sim 4$ , which is more than unity. Formation of hollow shell during self assembly is possible in such a case and is also indicated by hollow micro-capsules in Fig. 6.7d. Although in intermediate stage of drying, droplets remain viscous in nature, they become elastic during course of drying because of formation of a dense shell at air-water interface. Thickness and nature of the shell, formed during drying droplet, are important parameters as far as morphology of the grains is concerned. These parameters in turn determine the magnitude of required stress to drive the deformation of the shell. It has been observed that addition of just 2 wt % SDS arrests buckling and produces microcapsules with nearly spherical shape. At the same time, it is revealed from SEM micrograph that these spherical grains are hollow in nature. This implies that addition of SDS in silica dispersion somehow hinders or retards buckling process. It is to be mentioned that SDS in water forms nearly-globular micelles at concentration of 1.4% (i.e., 50 mM) in water. In absence of any hydrotropic electrolyte, these micelles are spherical in nature. With the addition of hydrotropic electrolyte, like AHC, PTHC etc., spherical micelles become elongated leading to rod/worm like micelles are manifested<sup>332,333</sup>. Typical size of spherical SDS micelles remains in range of 3 - 4 nm, which is smaller than silica NPs ( $\sim 10-15$  nm). As micelles are significantly smaller than silica NPs, they could diffuse faster towards core away from air water interface than silica NPs. This

results in formation of microcapsules with silica rich outer shell and micelle rich inner shell. Peclet number corresponding to micelles remains smaller than that of silica NPs. This leads to formation of relatively thick shell (silica mostly at outer shell and micelles at inner shell) leading to arrest buckling resulting spherical grains. Removal of trapped surfactant aggregates gives rise to hollow microcapsules.

With addition of AHC, rheological properties of dispersion get altered and deformation of grains creeps in. Further, internal structure and correlation of constituent colloids also get modified. In present investigation, we try to understand that how inter-particle interaction/surface charges and viscosity affects morphological transformation during drying. In order to probe internal structure of grains, SANS/SAXS experiments have been performed on non-calcined grains.

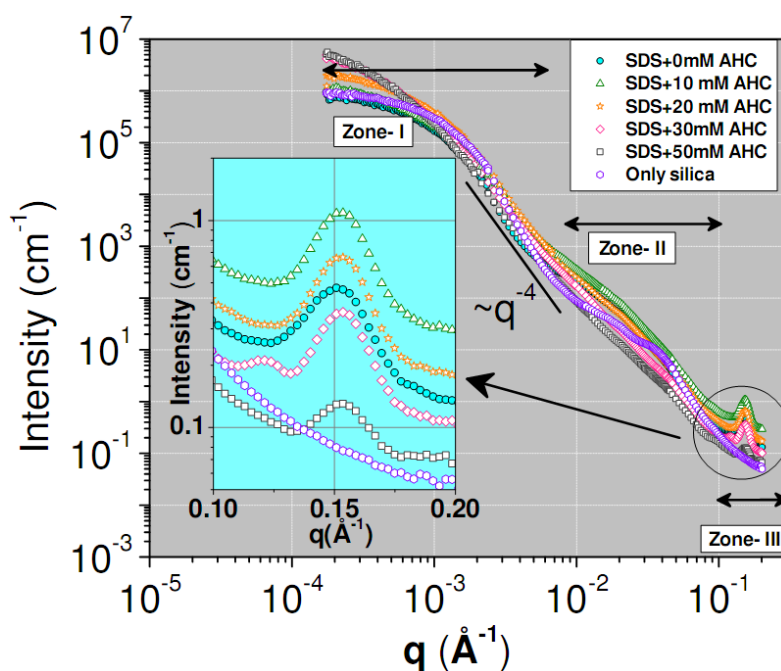


**Fig. 6.9** SANS data for the assembled non-calcined silica-SDS microcapsules are depicted. Inset shows zoomed view of the zone-III which reflects the correlation between the jammed micelles.

It is discernible that morphology of microcapsules changes drastically at higher AHC concentration. This suggests that addition of AHC not only alters the microstructure of micelles at small length scales but also affects overall morphology. Interestingly, prominent peak in Zone-III appears due to micellar correlation when SDS is added along-with silica. The peak height gets modified with increase in AHC concentration, particularly with addition of 50 mM of AHC.

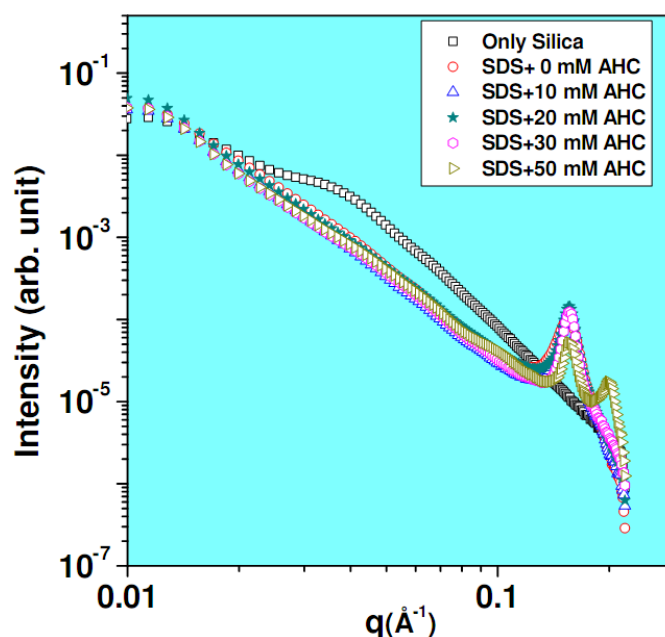


**Fig. 6.10** SAXS pattern from the non-calcined assembled microcapsules. Peak at around  $q \sim 0.15 \text{ \AA}^{-1}$  is observed when SDS is present. A double peak manifests at highest AHC concentration (50 mM).

These modifications are also supported by SAXS data (Fig. 6.10). In addition, SAXS data show an appearance of a second peak at highest AHC concentration due to ordered arrangement of micelles. A reduction in height of first peak, at highest AHC concentration, is observed from both SAXS and SANS data.

Scattering intensity from such hierarchical grains may be approximated by additive contributions of scattering components from three different length scales<sup>285,334</sup> and can be represented as:

$$I(q) = I_{\text{grain}}(q) + I_{\text{Silica}}(q) + I_{\text{micelle}}(q) + B \quad (6.1)$$

$I_{\text{grain}}$ ,  $I_{\text{Silica}}$  and  $I_{\text{micelle}}$  are respective intensities from overall grain, jammed silica NPs and micelles. An ensemble of polydisperse spheres model has been adopted for  $I_{\text{grain}}$  and an ensemble of interacting polydisperse sphere has been adopted for  $I_{\text{Silica}}$  and  $I_{\text{micelle}}$ . Since, length scale of grains and silica NPs are widely separated and thus data in Zones-I and II can be analyzed in light of the above model taking into consideration of first two terms of the eq. 6.1. To avoid complexity, analysis of Zone-III has been dealt separately. It has been observed<sup>334</sup> that above model fits data well.

A hard sphere type interaction has been considered between the micelles. It has been mentioned earlier that a significant modification occurs in peak shape for addition of 50 mM AHC. A second peak at  $q \sim 0.2 \text{ nm}^{-1}$  appears and height of the main peak at  $q \sim 0.15 \text{ nm}^{-1}$  decreases. This indicates that morphology of jammed micelles in assembled grains gets modified significantly at high AHC concentration. The average micelle size was found to be  $\sim 4.6 \text{ nm}$  and local volume fraction of the micelles was found to be  $\sim 0.6$ . For the sample with 50 mM AHC, ratio of the position of first peak to that of second peak is found to be nearly 1.34. It is to be noted that for a hexagonal arrangement above ratio should have been 1.73 while that for a lamellar arrangement should have been 2.0. It is important to discuss here that earlier studies indicated<sup>335</sup> that morphological transformation from cylindrical micelles to bi-layers does not take place abruptly but through a sequence of intermediate shapes leading to a sequence of so-called intermediate phases between hexagonal and lamellar phases. Such intermediate cubic phases are also indicated in literature<sup>336</sup>. Interestingly, for

cubic phase the ratio of inter planer spacing value for (100) reflection to that of (110) reflection corresponds to  $\sim 1.4$ , which matches reasonably well with the ratio that has been observed experimentally in present case. It should be noted that long micelles, formed in aqueous suspension at 50mM AHC, are randomly oriented. However, upon drying the micelles get aligned and forms cubically packed system.

It is interesting to observe from Figs. 6.7g, 6.7h that mushroom like grains also contain local zones (as seen from different contrast in SEM image of a grain in Figs. 6.7g, 6.7h) which are micelle rich (or due to templated pores in calcined grains). Such distinct local zones are not observed for the cases with lower AHC content. This implies that at high AHC concentration, micelles form some larger assembly among themselves resulting higher Peclet number. Viscosity of initial suspension is also high leading to further increase in Peclet number. The increase in effective Peclet number enhances buckling probability and finally results in mushroom like grains. It is quite evident from Fig. 6.7 d that spherical grains, for only SDS-silica case, are hollow and there is no signature of templated pore on the surface of grains when micelles are removed. This suggests that the SDS remains mostly at the inner surface of the shell of microcapsules while the silica forms outer surface of the shell. After calcinations the SDS leaves the grain and hollow grains are realized.

It is interesting to note that the microcapsules were buckled doughnut shaped for the case of only silica and buckling gets arrested when SDS is mixed with silica. This can be explained as follows. During drying of droplets with only silica, the difference between shear modulus at shell and inner part of droplet is larger than the situation where SDS micelles reside at the core of droplet and silica at the air-water interface. Relatively less difference in shear modulus between shell and core retards buckling phenomenon in later case. Further, doughnut shape in case of only silica was significantly smoother as compared

to that in case of increased AHC concentration. This is because of appearance of heterogeneity of shear modulus at shell. At larger concentration of AHC, micelles deviate from spherical shape and tend to arrange as elongated cylinders which effectively reduce their diffusion coefficient. Because of lesser rate of diffusion, some part of micelles resides at shell leading to heterogeneous shell. Micelles rich zone, being softer than silica, is more prone to induce invagination zones on surface leading to deformed doughnuts with multi invagination zones. A plausible mechanism is represented schematically in Fig. 6.11.

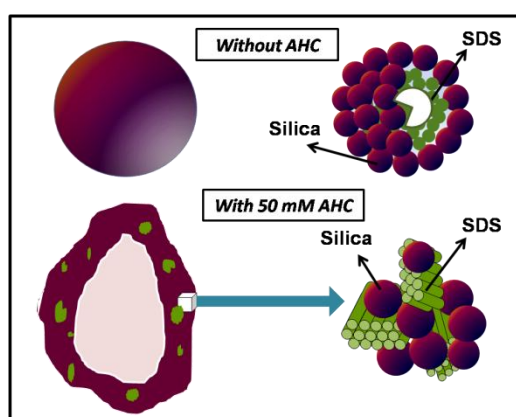


**Fig. 6.11** Schematic diagram shows two different mechanisms with no AHC and with large amount of AHC. At large AHC concentration, the ordering of cylindrical micelles during self-assembly occurs through an intermediate cubic phase between hexagonal and lamellar.

#### 6.3.4. Conclusions

In summary, hollow silica microcapsules were synthesized using EISA of silica colloids and SDS micelles with varying hydrophilic AHC. Ordering of surfactant in assembled microcapsules is demonstrated by SANS/SAXS measurements. A chronological pathway of morphological transition to hollow spherical shell, deformed doughnut and mushroom like morphology of microcapsules could be obtained by systematic tuning of viscosity of virgin suspension and surface charge on constituent colloidal particles.

### Summary and Conclusions

In present thesis, it has been demonstrated that the pertinent length scales in nano-ceramics and nano-composites exist in 1-1000 nm. SAS technique is an ideal bulk-sensitive probe to investigate such length scales. Neutrons and X-rays are two complementary probes as far as SAS technique is concerned. The advantage and disadvantage of the neutrons and X-rays as a probe has been discussed. The theory of SAS is well established and some important glimpse has been provided in the first chapter of the thesis.

Different kinds of the SAXS and SANS instruments have also been described briefly in first chapter. SANS is low flux and low resolution technique however it is important technique to probe soft matter due to low  $Z$  and isotope sensitivity. Kinetics of dynamical systems in milliseconds range can be only probed by synchrotron SAXS. The double crystal based instruments can be used to access higher length scale in the nano-ceramics.

In present thesis two aspects of the nano-ceramics have been studied. First aspect deals with SAS investigation on sintering behavior of aggregates which results due to uncontrolled aggregation of NPs. Second aspect deals with SAS investigation of controlled assembly of NPs via evaporation induced self-assembly (EISA). The major outcome of the thesis is summarized below:

It has been shown that pore morphology in NiO nano-ceramics aggregates gets modified under sintering. Existence of pore structures in two wide separated lengths has been shown. It is established that the bigger pores size gets significantly modified during sintering as

compared to the smaller pores. SAS investigation on  $\text{YCrO}_3$  nano-ceramic shows reduction in polydispersity in pore size under sintering. Dielectric response showed a strong dependence on pore characteristics. The modification in pore morphology has been attributed to mass transport by atomistic diffusion during sintering. The mesoscopic and microscopic structures, under heat treatment, have been studied for NiO doped  $\text{TiO}_2$  submicrospheres which were synthesized by spray hydrolysis technique. It has been established that initial phase of  $\text{TiO}_2$  is anatase due its small size. Rutile phase appear beyond  $600^\circ\text{C}$  due to growth of NPs beyond 14 nm size. It has been shown that doped  $\text{TiO}_2$  is good substrate candidate for synthesis of carbon nanotubes.

Sintering behaviors of fractal aggregates such as YAG ( $\text{Y}_3\text{Al}_5\text{O}_{12}$ ), doped Ceria ( $\text{Ce}_{0.50}\text{Nd}_{0.50}\text{O}_{1.75}$ ) have been investigated. It has been shown that YAG aggregates possess mass fractal nature while doped Ceria possess surface fractal nature. The experimental results have been understood using Monte Carlo simulation. The main effect of thermal relaxation under annealing of YAG fractal cluster is coarsening of fractal structure keeping the fractal dimension invariant. The Monte Carlo based computer simulation establishes that smoothening of fractal rough surface under sintering occurs due to the diffusion transport of materials from regions of higher local roughness to the lower one. Similarly, Monte Carlo simulation on 2 dimension DLA cluster has been performed to understand evolution of fractal morphology during cement hydration as was observed by USANS measurements.

EISA of NPs have been carried out in slow and fast drying regime depending on the Peclet number  $P_e$  (slow drying ( $P_e \ll 1$ ) or fast drying ( $P_e \gg 1$ )). The spray drying experiment in slow drying regime on silica colloids with varying concentration shows that overall morphology of assembled grains remains spherical for all concentrations. However, packing of NPs in assembled grains depends on initial concentration. It has also been shown that

assembly of NPs and their internal arrangement during drying can be modified by addition of electrolyte in initial dispersion. The modification of the inter-particle correlation in turn affects the available specific surface area of the nanoparticle-void interface.

Buckling induced morphological transformation of colloidal droplets to doughnut like grains during EISA of NPs under fast drying regime has been shown. The possible mechanism of formation of such doughnut like grains during drying of micrometric droplets has been differentiated on the basis of two existing hypotheses. It has been shown that the hypothesis based on the formation and buckling of shell of jammed NPs at air-water interface explains the morphological transformation. It has been depicted that such buckling phenomenon can be arrested by covering the NPs by poly ethylene glycol polymer. However, for higher molecular weight and concentration of the polymer, buckyball type morphology of the grains is realized. The origin of such buckled grains could not be explained by theory of homogenous spherical elastic shell for the present experimental condition. It has been found that soft zones due to PEG aggregates make the shell inhomogeneous. The soft zones having relatively small elastic modulus induces buckling at various centers of the shell resulting into buckyball type of grains. The EISA of mixed colloids has also been utilized to fabricate stable  $\text{TiO}_2/\text{SiO}_2$  mesoporous microspheres. The composite grains are thermally stable against anatase to rutile phase transition due to inhibition of growth of  $\text{TiO}_2$  NPs in  $\text{SiO}_2$  matrix.

Morphological transition of droplet of mixed colloidal suspension during EISA with incorporation of soft anisotropic particle (*e-coli*) has been demonstrated. It has been elucidated that reduction in elastic modulus of the formed shell, by incorporation of soft anisotropic colloids, at the air water interface facilitates the buckling leading to large

deformations. It is unveiled that such buckling can be arrested through effective coverage of anisotropic softer colloids by smaller silica NPs by proper tuning of the surface charges.

Hollow microcapsules have been synthesized using EISA of silica colloids and SDS micelles by tuning viscosity of initial suspension and surface charge on the colloids using hydrotropic aniline hydrochloride. Ordering of surfactant in the assembled microcapsules is demonstrated from SAXS/SANS measurements. A chronological pathway of morphological transition during drying to hollow spherical shell, deformed doughnut and mushroom like morphology of the microcapsules have been depicted.

### **Future Scope of the work**

Present thesis addresses issues related to sintering behavior of aggregates due to uncontrolled aggregation of NPs. However, more experiments, in-particular, high temperature *in-situ* SAXS/SANS measurements will be useful to address the kinetics of sintering in nano-ceramics. In order to understand the underlying diffusion mechanisms, Monte Carlo simulations on three dimension clusters are called for.

The present thesis also shed some lights on the controlled assembly of the NPs via EISA for various physico-chemical parameters. Further, the present work opens up an effective experimental as well as a theoretical route towards the comprehensive understanding of the buckling phenomenon during EISA of mixed colloids. It has been shown that the presence of soft bacteria and polymer can induce the buckling of the shell during drying. Quantitative measurement of Young Modulus  $Y_0$  of the shell is a challenging task. It is difficult to measure the shell stiffness during spray drying experiment. However, experiment on single drying droplet may help in measuring  $Y_0$  with time and will be attempted in future. A theoretical approach towards the simulation of the inhomogeneous elastic spherical shell under external pressure is quite complex problem and needs further

attention. In order to address the buckling phenomenon for single and mixed colloids *in-situ* SAXS/SANS experiments is called for. Experiment on drying of single colloidal droplet is quite important to understand the different mechanisms involved during EISA. *In-situ* viscosity measurement of the drying droplet would also be helpful. In future, various experiments such as scattering, viscosity, zeta potential and stiffness on drying of single droplet will be sought.

It will be useful if some other crucial parameters, e.g., charge and stiffness of the colloid may be accounted during EISA in order to achieve more general Peclet number based model for prediction of buckling.

*In-situ* SAS experiment will also be attempted in near future to see the removal of the organic component such as SDS, PEG, *E-coli* from the assembled composite grains.

## REFERENCES

- [1] C. B. Murray, C. R. Kagan, M. G. Bawendi *Annu. Rev. Matter Sci.* **30** (2006) 545
- [2] G-M Chow, N. Ivanova Noskova, *Nano-structured Materials Science and Technology*. Dordrecht: Kluwer Academic publishers (1998).
- [3] L. Mazzola *Nature biotechnology* **21** (2003) 1137
- [4] R. Paul, J. Wolfe, P. Hebert, M. Sinkula *Nature Biotechnology* **20** (2003) 277
- [5] [http://en.wikipedia.org/wiki/List\\_of\\_nanotechnology\\_applications](http://en.wikipedia.org/wiki/List_of_nanotechnology_applications)
- [6] Larry L. Hench, Jon K. West *Chem. Rev.* **90** (1) (1990) 33–72
- [7] R. W. Siegel “*Physics of New Materials*” edited by F. E. Fujita (Springer-Verlag, Heidelberg) (1994) 65
- [8] J. Karch, R. Birringer, H. Gleiter *Nature* **330** (1987) 556
- [9] W. D. Kingery, H. K. Bowden, D.R. Uhlmann, *Introduction to Ceramics*. Sec ed. Wiley Series on the Science and Technology of the Materials. 1976, New York: John Wiley & sons. 1032
- [10] G. M. Whitesides, B. Grzybowski *Science* **295** (2002) 2418
- [11] R. D. Kamien *Science* **299** (2003) 1671
- [12] K. Master *Spray Drying Handbook*, 5th ed.; Longman Scientific & Technical: England, 1991
- [13] D. Sen, S. Mazumder, J. S. Melo, Arshad Khan, S. Bhattacharya and S. F. D’Souza, *Langmuir* **25** (2009) 6690
- [14] N. Tsapis, D. Bennett, B. Jackson, D. A. Weitz and D. A. Edwards *Proc. Natl. Acad. Sci. USA* **99** (2002) 12005
- [15] D. Sen, O. Spalla, L. Belloni, T. Charpentier, A. Thill *Langmuir* **22** (2006) 3798

- [16] A. Guinier, G. Fournet, B. C. Walker and L. K. Yudowith in “*Small Angle Scattering of X-Rays*” Wiley, New York (1955)
- [17] G. Prorod *Small-Angle X-ray Scattering*. O. Kratky and O. Glatter, editors. Academic Press (London, 1982).
- [18] B. Hammouda “*Probing Nanoscale Structures –The SANS Toolbox*”  
["http://www.ncnr.nist.gov/staff/hammouda/the\\_SANS\\_toolbox.pdf"](http://www.ncnr.nist.gov/staff/hammouda/the_SANS_toolbox.pdf)
- A. F. Craievich “*Small-angle X-ray scattering by nanostructured materials.*” Handbook of Sol-Gel Science and Technology, Vol II Chapter 8, Kluwer Publishers (2005)
- [19] P. Debye and A. M. Bueche *J. Appl. Phys.* **20** (1949) 518
- [20] G. Porod. *Kolloid Z* **124** (1951) 83
- [21] S. Ciccariello *J. Appl. Cryst.* **24** (1991) 509
- [22] W. Ruland *J. Appl. Cryst.* **4** (1971) 70
- [23] S. Ciccariello *J. Appl. Cryst.* **35** (2002) 304
- [24] C. G. Shull and L.C. Roess *J. Appl. Phys.* **18** (1947) 295
- [25] Lord Rayleigh *Proc. Roy. Soc. London, Ser. A* **84** (1911) 25-38
- [26] A. Guinier *Ann. Phys.* **12** (1939) 161-237
- [27] G. Fournet *Bull. Soc. Fr. Mineral. Crist.* **74** (1951) 39-113
- [28] G. Beaucage *J. Appl. Cryst.* **28** (1995) 717
- [29] J. P. Hansen and I. R. McDonald “*Theory of Simple Liquids*” Academic Press, London (1986)
- [30] L.S. Ornstein and F. Zernike *Phys. Z.* **19** (1918) 134
- [31] J. K. Percus, G. J. Yevick *Phys. Rev.* **110** (1958) 1
- [32] J. H. Hayter and J. Penfold *Molecular Physics* **42** (1981) 109-118
- [33] R. J. Baxter *J. Chem. Phys.* **49** (1968) 2770-2774

- [34] S.K. Sinha, T. Freltoft and J. Kjems in “*Kinetics of Aggregation and Gelation*” Editors F. Family and D.P. Landau, pp. 87-90. North Holland (Amsterdam, 1984)
- [35] S. H. Chen and J. Teixeira *Phys. Rev. Lett.* **57** (1986) 2583
- [36a] S. Mazumder, BARC Newsletter, Founder’s Day Special Issue, October, 2010, 1-5
- [36b] <http://nmi3.eu/neutron-research/techniques-for-/structural-research/large-scale-structures.html>
- [36] S. Mazumder, D. Sen, T. Saravanan, P. R. Vijayaraghavan *J. Neutron Res.* **9** (2001) 39
- [37] S. Mazumder, D. Sen, T. Saravanan, P. R. Vijayaraghavan *Current Science* **81** (2001) 257
- [38] G. D. Wignall *J. Appl. Cryst.* **24** (1991) 479-484
- [39] V. Ramkrishnan *J. Appl. Cryst.* **18** (1985) 42-46
- [40] G. D. Wignall, D. K. Christen and V. Ramkrishnan *J. Appl. Cryst.* **21** (1988) 438-451
- [41] P. W. Schmidt and R. Height *Acta. Crystallogr.* **13** (1960) 480
- [42] J. A. Lake *J. Appl. Cryst.* **23** (1967) 191
- [43] L. Bosio, J. Teixeira and M.-C. Bellissent-Funel *Phys. Rev. A* **39** (1989) 6612-6613
- [44] D. Vollath and D. V. Szabo *Nanostruct. Mater.* **4** (1994) 927
- [45] U. Keiderling, A. Moller, A. Wiedenmann, M. Winterer and H. Hahn *Phys. B.* **874** (2000) 276
- [46] U. Keiderling, A. Wiedenmann, V. Srdic, M. Winterer and H. Hahn *J. Appl. Crystallo.* **33** (2000) 483
- [47] A. K. Patra, J. Bahadur, S. Mazumder, Sathi Nair, R. D. Purohit and A. K. Tyagi *J. Nanosc. Nanotech* **8** (2007) 1-6
- [48] J. Bahadur, D. Sen, S. Mazumder and S. Ramanathan *Journal of Solid State Chemistry* **181** (2008) 1227–1235.
- [49] P.J. McMahon, S.D. Moss *J. Appl. Cryst.* **32** (1999) 956.

- [50] Klug, H. P.; Alexander, E. L. in “*X-ray diffraction procedures for polycrystalline and amorphous materials*” 2nd ed. New York, USA: J. Wiley and Sons; 1974. p. 960
- [51] W. Weibull *J. Appl. Mech.-Trans. ASME* **18(3)** (1951) 293-297
- [52] C. R. Serrao, A. K. Kundu, S. B. Krupanidhi, U. V. Waghmare and C. N. R. Rao *Phys. Rev. B* **72** (2005) 220101(R)
- [53] V. E. Wood and A. E. Austin in “*Magnetoelectric Interaction Phenomena in Crystals*” ed. A. J. Freeman and H. Schmid (London: Gordon and Breach) 1975
- [54] C. R. Bowen and D. P. Almond *Materials Science and Technology*, **22(6)**, 719
- [55] S. J. Penn, N. M. Alford, A. Templeton, X. Wang, M. Xu, M. Reece and K. Schrapel *J. Am. Ceram. Soc.* **80** (1997) 1885
- [56] M. Valant and D. Suvorov *Mater. Chem. Phys.* **79** (2003) 104
- [57] N. M. Alford and S. J. Penn *J. Appl. Phys.* **80** (1996) 5895
- [58] J. C. Maxwell *A Treatise on Electricity and Magnetism* vol 1 (New York: Dover) (1954).
- [59] W. Wagner *Arch. Elektrotech.* **2** (1914) 371
- [60] V. Bedekar, R. Shukla and A. K. Tyagi *Nanotechnology* **18** (2007) 155706
- [61] V. K. Aswal and P. S. Goyal *Current Science* **79** (2000) 947.
- [62] S. Mazumder and A. Sequeira *J. Appl. Crystallogr.* **25** (1992) 221
- [63] S. Mazumder, B. Jayaswal, A. Sequeira *Physica B* **122** (1998) 241–243
- [64] S. Mazumder and A. Sequeira *Phys. Rev. B* **41** (1990) 6272
- [65] D. Sen, J. Bahadur, S. Mazumder *Eur. Phys. J-B* **71** (2009) 75-84
- [66] J. Bahadur, D. Sen, S. Mazumder, R. Shukla and A. K. Tyagi *J. Phys.: Condens. Matter* **20** (2008) 345201
- [68] A. K. Jonscher *Dielectric Relaxation in Solids* (London: Chelsea Dielectrics Press) 1983
- [69] A. K. Jonscher, F. Meca and H. M. Millany *J. Phy. C: Solid State phys.* **12** (1979) L293.

- [70] D. Sen, J. Bahadur, S. Mazumder, V. Bedekar and A. K. Tyagi *J. Phys.: Condens. Matter* **20** (2008) 035103
- [71] R. Hilfer *Physica Scripta*. **T44** (1992) 51
- [72] J. R. Hearst and P. H. Nelson “*Well Logging for Physical Properties*” (McGraw Hill, New York 1985)
- [73] G. V. Keller and P. H. Licastro *U.S. Geol. Surv. Bull.* **10528** (1959) 257
- [74] G. V. Keller in: “*Handbook of Physical Properties of Rock*” (Edited by R. A. Carmichael) (CRC Press, Boca Raton 1982), p. 217
- [75] D. Sen, T. Mahata, A. K. Patra, S. Mazumder and B. P. Sharma *J. Phys.: Condens. Matter* **16** (2004) 6229
- [76] A. Hagfeldt, M. Grätzel *Chem. Rev* **95** (1995) 49-68
- [77] B. O’Regan and M. Grätzel *Nature* **353** (1991) 737-740
- [78] A. L. Linsebigler, G. Lu, J. T. Yates *Chem. Rev.* **95** (1995) 735-758
- [79] B. Ohtani, Y. Ogawa, S. Nishimoto *J. Phys. Chem. B* **101** (1997) 3746-3752
- [80] A. Niklasson, C.G. Granqvist *J. Mater. Chem.* **17** (2007) 127
- [81] W. Shangguan, *Sci. Technol. Adv. Mater.* **8** (2007) 76
- [82] S. Nagamine, A. Sugioka, Y. Konishi *Materials Letters* **61** (2007) 444–447
- [83] S. Nagaoka, Y. Hamasaki, S. Ishihara, M. Nagata, K. Iio, C. Nagasawa, H. Ihara *J. Mol. Catal. A: Chem.* **177** (2002) 255–263
- [84] B. Ahmmad, Y. Kusumoto, Md. S. Islam *Adv. Powd. Tech.* **21** (2010) 292–297
- [85] J. Bahadur, D. Sen, J. Prakash, Ripandeep Singh, B. Paul and S. Mazumder and D. Sathiyamoorthy *AIP Conf. Proc.* **1447** (2012) 281-282
- [86] Ripandeep Singh, D. Sen, J. Bahadur, and S. Mazumder *AIP Conf. Proc.* **1447** (2012) 301-302
- [87] R. A. Spurr and H. Myers *Anal. Chem.* **29** (1957) 760–62

- [88] J. Bahadur, D. Sen, S. Mazumder, J. Parkash, D. Sathiyamoorthy, R. Venugopalan *Journal of Nanoscience and nanotechnology* **10** (2010) 2963–2971
- [89] D. Sen, K. Dasgupta J. Bahadur, S. Mazumder and D. Sathiyamoorthy *PRAMANA-journal of physics* **71** (2008) 971-977
- [90] B.B Mandelbrot “*The Fractal Geometry of Nature*”. Freeman, New York. Mandelbrot B.B. 1977 “*Fractals, Form and dimension*”; San Francisco: Freeman, 1982
- [91] D. Sen, S. Mazumder, S. Tarafdar *Journal of Materials Science* **37** (2002) 941– 947
- [92] A. P. Radlinski, E. Z. Radlinska, M. Agamalian, G. D. Wignall, P. Linder and O. G. Randl *Phys. Rev. Lett.* **82** (1999) 3078
- [93] D. Sen, S. Mazumder, R.Chitra and K. S. Chandrasekaran *J. Mater. Sci.* **36** (2001) 909
- [94] H. D. Bale and P.W. Schmidt *Phys. Rev. Lett.* **53** (1984) 596
- [95] S. Mazumder, D. Sen, A. K. Patra, S. A. Khadilkar, R. M. Cursetji, R. Loidl, M. Baron, and H. Rauch *Phys. Rev. Lett.* **93** (2004) 255704
- [96] S. Mazumder, D. Sen, and A. K. Patra, S. A. Khadilkar and R. M. Cursetji, R. Loidl, M. Baron and H. Rauch *Phys. Rev. B* **72** (2005) 224208
- [97] P. W. Schimidt *J. Appl. Cryst.* **24** (1991) 414
- [98] J. Texeira *J. Appl. Cryst.*, **21** (1988) 781-785
- [99] T. Freltoft, J. K. Kjems and S. K. Sinha *Phys. Rev. B* **33** (1986) 269
- [100] J.W. S. Rayleigh *Proc. London Math. Soc.* **10** (1879) 4
- [101] S. Chandrasekhar *Hydrodynamics and Hydrodynamic Stability*, Oxford University, New York, 1961.
- [102] J. Eggers *Rev. Mod. Phys.* **69** (1997) 865
- [103] W.W. Mullins *J. Appl. Phys.* **28** (1957) 333
- [104] F. A. Nichols and W.W. Mullins *J. Appl. Phys.* **36** (1965) 1826
- [105] F. A. Nichols and W.W. Mullins *Trans. Metall. Soc. AIME* **233** (1965) 1840

- [106] D'Arcy Thompspon "*On the Growth and Form*" Cambridge University Press, Cambridge, England, 1961.
- [107] J. S. Langer *Rev. Mod. Phys.* **52** (1980) 1
- [108] W.W. Mullins and R. F. Sekerka *J. Appl. Phys.* **34** (1963) 323
- [109] *Fractals and Disordered Systems* edited by A. Bunde and S. Havlin ,Springer-Verlag, New York 1991
- [110] *The Fractal Approach to Heterogeneous Chemistry* edited by D. Avnir, Wiley, New York 1989
- [111] R. Q. Hwang, J. Schroder, C. Gunther and R. J. Behm *Phys. Rev. Lett.* **67** (1991) 3279
- [112] R. Sempere, D. Bourret, T. Woignier, J. Phalippou and R. Jullien *Phys. Rev. Lett.* **71** (1993) 3307
- [113] T. Irisawa, M. Uwaha and Y. Saito *Europhys. Lett.* **30** (1995) 139
- [114] N. Olivi-Tran, R. Thouy and R. Jullien *J. Phys. I* **6** (1996) 557
- [115] R. Thouy, N. Olivi-Tran and R. Jullien *Phys. Rev. B* **56** (1997) 5321
- [116] M. Conti, B. Meerson and P. V. Sasorov *Phys. Rev. Lett.* **80** (1998) 4693
- [117] A. Schmidt-Ott *J. Aerosol Sci.* **19** (1988) 553
- [118] P. Huang, B. J. Turpin, M. J. Piphoo, D. B. Kittelson and P. H. McMurry *J. Aerosol Sci.* **25** (1994) 447
- [119] R. Jullien and P. Meakin *J. Colloid Interface Sci.* **127** (1989) 265
- [120] C. Brechignac, P. Cahuzac, F. Carlier, C. Colliex, J. Le Roux, A. Masson, B.Yoon and U.Landman *Phys. Rev. Lett.* **88** (2002) 196103
- [121] E. Sharon, M. G. Moore, W. D. McCormick and H. L. Swinney *Phys. Rev. Lett.* **91** (2003) 205504
- [122] M. Conti, A. Lipshtat and B. Meerson *Phys. Rev. E* **69** (2004) 031406
- [123] R. C. Flagan and M. M. Lunden *Mater. Sci. Eng. A* **204** (1995) 113

- [124] E. J. Lehtinen, R. S. Windeler and S. K. Friedlander *J. Aerosol Sci.* **27** (1996) 883
- [125] D. W. Schaefer, B. J. Olivier, C. Ashley, G. Beaucage, D. Richter, B. Farago, B. Frick and D. A. Fischer *J. Non-Cryst. Solids* **172/173** (1994) 647
- [126] N. Olivi-Tran, R. Jullien and G. W. Cohen-Solal *Europhys. Lett.* **30** (1995) 393
- [127] N. Olivi-Tran and R. Jullien *Phys. Rev. B* **52** (1995) 258
- [128] N. Olivi-Tran and R. Jullien *J. Sol–Gel Sci. Technol.* **8** (1997) 813
- [129] S. Mazumder, R. Loidl and H. Rauch *Phys. Rev. B* **76** (2007) 064205
- [130] D. Sen, S. Mazumder and J. Bahadur *Phys. Rev. B* **79** (2009) 134207
- [131] G. Yang and P. Biswas *J. Colloid and Interface Sci.* **211** (1999) 142
- [132] W. Koch and S. K. Friedlander *J. Colloid Interface Sci.* **140** (1990) 419
- [133] A. Kobata, K. Kusakabe and S. Morooka *J. AIChE* **37** (1991) 347
- [134] J. Bahadur, S. Mazumder, D. Sen, S. Ramanathan *J. Phys.: Condens. Matter* **22** (2010) 195107
- [135] J. Maul, E. Marosits, C. Sudek, T. Berg and U. Ott *Phys. Rev. B* **72** (2005) 245401
- [136] T. A. Witten, L. M. Sander *Phys. Rev. Lett.* **47** (1981) 1400
- [137] P. Meakin *Phys. Rev. Lett.* **51** (1983) 1119
- [138] R. Thouy, R. Jullien *J. Phys. A: Math. Gen.* **27** (1994) 2953
- [139] R. Thouy, R. Jullien *J. Phys.* **16** (1996) 1365
- [140] P. Meakin and F. Family *Phys. Rev. A* **38** (1988) 2110
- [141] A. P. Weber and S. K. Friedlander *J. Aerosol Sci.* **28** (1997) 179
- [142] Y. Maki, M. Matsuda and T. Kudo *U.S. Patent No.3, 607,424* (1971)
- [143] V. Bedekar and A. K. Tyagi *J. Nanosci. Nanotechnol.* **7** (2007) 1–7
- [144] Y. S. Cho, H. D. Glicksman and V. R.W. Amarakoon *Encyclopedia of Nanoscience and Nanotechnology*, edited by H.S. Nalwa, 2004 American Scientific Publishers, Vol.1, p.727

- [145] E.M. Logothetis *National Symposium on Ceramics on the Service of Men*, Washington, DC (1976)
- [146] J. Lambard, P. Lesieur, T. Zemb *J. Phys. I France* **2** (1992) 1191-1213
- [147] D. F.R Mildner and P. L. Hall *J. Phys. D* **19** (1986) 1535
- [148] S.R. Bhatia *Current Opinion in Colloid & Interface Science* **9** (2005) 404-411
- [149] S. A. Shah, Y.L. Chen, S. Ramakrishnan, K.S. Schweizer, C.F. Zukoski *J. Phys., Condens. Matter* **15** (2003) 4751-4778
- [150] K. K. Mon *Phys. Rev. Lett.* **57** (7) (1986) 866-868
- [151] Family Fereydoon *J. Phys. A: Math. Gen.* **19** (1986) L441-L446
- [152] E. Aharonov and D. Rothman *J. Geophys. Res.* **101** (1996) 2973-2987
- [153] S. Hans-Joachim, Al-Zaitone Belal, C. Artelt, W. Peukert *Chemical Engineering Science* **61** (2006) 293 – 305.
- [154] D. Saupe “*Random Fractals Algorithms*” in *The Science of Fractal images*, H.O. Peitgen, D. saupe (Eds) Springer-Verlag, new york, pp. -71-136 (1988).
- [155] M. Hennion, D. Ronzaud and P. Guyot *Acta Metall.* **30** (1982) 599
- [156] S. Komura, K. Osamura, H. Fujii and T. Takeda *Phys. Rev. B* **30** (1984) 2944
- [157] S. Katano and M. Iizumi *Phys. Rev. Lett.* **52** (1984) 835
- [158] S. Komura, K. Osamura, H. Fujii and T. Takeda *Phys. Rev. B* **31** (1985) 1278
- [159] M. Furusaka, Y. Ishikawa and M. Mera *Phys. Rev. Lett.* **54** (1985) 2611
- [160] O. Lyon and J. P. Simon *Phys. Rev. B* **35** (1987) 5164
- [161] B. Rodmacq, M. Maret, J. Laugier, L. Billard and A. Chamberod *Phys. Rev. B* **38** (1988) 1105
- [162] R. D. Lorentz, A. Bienenstock and T. I. Morrison *Phys. Rev. B* **49** (1994) 3172
- [163] M. J. Regan and A. Bienenstock *Phys. Rev. B* **51** (1995) 12170

- [164] S. Mazumder, D. Sen, I. S. Batra, R. Tewari, G. K. Dey, S. Banerjee, A. Sequeira, H. Amenitsch and S. Bernstorff *Phys. Rev. B* **60** (1999) 822
- [165] R. Tewari, S. Mazumder, I. S. Batra, G. K. Dey and S. Banerjee *Acta Metall.* **48** (2000) 1187
- [166] D. Sen, S. Mazumder, R. Tewari, P. K. De, H. Amenitsch and S. Bernstorff *J. Alloys Compd.* **308** (2000) 250
- [167] M. Kriechbaum, G. Degovics, J. Tritthart and P. Laggner *Prog. Colloid Polym. Sci.* **79** (1989) 101
- [168] A. Heinemann, H. Hermann, K. Wetzig, F. Haeussler, H. Baumbach and M. Kroening *J. Mater. Sci. Lett.* **18** (1999) 1413
- [169] R. A. Livingston, D. A. Neumann, A. J. Allen, S. A. Fitzgerald, and R. Berliner *Neutron News* **11** (4) (2000) 18
- [170] C.V. Santilli, S. H. Pulcinelli and A. F. Craievich *Phys. Rev. B* **51** (1995) 8801
- [171] A. Chakrabarti, R. Toral, J. D. Gunton and M. Muthukumar *Phys. Rev. Lett.* **63** (1989) 2072
- [172] B. Dunweg and K. Kremer *Phys. Rev. Lett.* **66** (1991) 2996
- [173] M. Takenaka and T. Hashimoto *Phys. Rev. E* **48** (1993) R647
- [174] G. Brown and A. Chakrabarti *Phys. Rev. E* **48** (1993) 3705
- [175] G. Krausch, C. A. Dai, E. J. Kramer, and F. S. Bates *Phys. Rev. Lett.* **71** (1993) 3669
- [176] M. Rubinstein, R. H. Colby, and A. V. Dobrynin *Phys. Rev. Lett.* **73** (1994) 2776
- [177] S. Bastea and J. L. Lebowitz *Phys. Rev. Lett.* **78** (1997) 3499
- [178] W. R. White and P. Wiltzius *Phys. Rev. Lett.* **75** (1995) 3012
- [179] S. R. Shannon and T. C. Choy *Phys. Rev. Lett.* **79** (1997) 1455
- [180] P. W. Zhu, J. W. White, and J. E. Epperson *Phys. Rev. E* **62** (2000) 8234

- [181] E. Falck, O. Punkkinen, I. Vattulainen, and T. Ala-Nissila *Phys. Rev. E* **68** (2003) 050102 (R)
- [182] C. O. Kim and W. L. Johnson *Phys. Rev. B* **23** (1981) 143
- [183] A. F. Craievich and J. M. Sanchez *Phys. Rev. Lett.* **47** (1981) 1308
- [184] A. F. Craievich, J. M. Sanchez, and C. E. Williams *Phys. Rev. B* **34** (1986) 2762
- [185] S. Sen and J. F. Stebbins *Phys. Rev. B* **50** (1994) 822
- [186] A. Wiedenmann and Jun-Ming Liu *Solid State Commun.* **100** (1996) 331
- [187] A. Malik, A. R. Sandy, L. B. Lurio, G. B. Stephenson, S. G. J. Mochrie, I. McNulty, and M. Sutton *Phys. Rev. Lett.* **81** (1998) 5832
- [188] J. H. He and E. Ma *Phys. Rev. B* **64** (2001) 144206
- [189] A. Chakrabarti *Phys. Rev. Lett.* **69** (1992) 1548
- [190] J. C. Lee *Phys. Rev. B* **46** (1992) 8648
- [191] C. K. Chan *Phys. Rev. Lett.* **72** (1994) 2915
- [192] J. Jacob, A. Kumar, S. Asokan, D. Sen, R. Chitra, and S. Mazumder *Chem. Phys. Lett.* **304** (1999) 180
- [193] C. M. Knobler and N. C. Wong *J. Phys. Chem.* **85** (1981) 1972
- [194] Y. C. Chou and W. I. Goldberg *Phys. Rev. A* **23** (1981) 858
- [195] D. N. Sinha and J. K. Hoffer *Physica B & C* **107** (1981) 155
- [196] J. Tritthart, F. Haußler *Cement and Concrete Research* **33** (2003) 1063-1070
- [197] H. M. Jeanings *Cement and Concrete Research* **30** (2000) 101-116
- [198] D. Winslow, J. M. Bukowski and J. F. Young *Cement and Concrete Research* **25** (1995) 147-156
- [199] M. Kind *Chem. Eng. Proc.* **38** (1999) 405
- [200] E. Matijevic *Chem. Mater.* **5** (1993) 412
- [201] A. Sayari *Chem. Mater.* **8** (1996) 1840

- [202] A. Corma *Chem. Rev.* **97** (1997) 2373
- [203] A. P. Wright, M. E. Davis *Chem. Rev.* **102** (2002) 3589
- [204] D.E. Devos, M. Dams, B. F. Sels, P. A. Jacobs *Chem. Rev.* **102** (2002) 3615
- [205] M. Grun, A. A. Kurganov, S. Schacht, F. Schuth, K. K. Unger *J. Chromatogr. A* **740** (1996) 1
- [206] K. W. Gallis, J. T Araujo, K. J. Duff, J. G. Moore, C. C. Landry *Adv. Mater.* **11** (1999) 1452
- [207] K. K. Unger, D. Kumar, M. Grun, G. Buchel, S. Ludtke, T. Adam, K. Schumacher, S. Renker *J. Chromatogr. A* **892** (2000) 47
- [208] C. Boissiere, M. Kummel, M. Persin, A. Labot, E. Prouzet *Adv. Funct. Mater.* **11** (2001) 129
- [209] C.-Y. Lai, B. G. Trewyn, D. M. Jefthinija, K. Jefthinija, S. Xu, S. Jefthinija, V. S.-Y. Lin *J. Am. Chem. Soc.* **125** (2003) 4451
- [210] T. Buranda, J. Huang, G. V. Ramarao, L. K. Ista, R. S. Larson, T. L. Ward, L. A. Sklar, G. P. Lopez *Langmuir* **19** (2003) 1654
- [211] Q. Huo, J. Feng, F. Schuth, G. D Stucky *Chem. Mater.* **9** (1997) 14
- [212] G. Ozin *Adv. Mater.* **4** (1992) 612
- [213] S. Mann, G. A. Ozin *Nature* **382** (1996) 313
- [214] H.-P. Lin, C.-Y. Mou *Science* **273** (1996) 765
- [215] H. Yang, N. Coombs, G. A. Ozin *Nature* **386** (1997) 692
- [216] S. Mann, S. L. Burkett, S. A. Davis, C. E. Fowler, N. H. Mendelson, S. D. Sims, D. Walsh, N. Whilton *Chem. Mater.* **9** (1997) 2300
- [217] U. Ciesla, F. Schuth *Microporous Mesoporous Mater.* **27** (1999) 131
- [218] D. Sen, J. S. Melo, J. Bahadur, S. Mazumder, S. Bhattacharya, G. Ghosh, D. Dutta and S.F. D' Souza *Eur. Phys. J. E* **1. 31** (2010) 393- 402

- [219] J. J. E. Moreau, L. Vellutini, M. W. C. Man, C. Bied, J. L. Bantignies, P. Dieudonne, J. L. Sauvajol *J. Am. Chem. Soc.* **123** (2001) 7957
- [220] G. J. A. A. Soler-Illia, C. Sanchez, B. Lebeau, J. Patarin *Chem. Rev.* **102** (2002) 4093
- [221] F. Schuth, W. Schmidt *Adv. Mater.* **14** (2002) 629
- [222] A. Stein *Adv. Mater.* **15** (2003) 763
- [223] I. W. Hamley *Angew. Chem. Int. Ed.* **42** (2003) 1692
- [224] H. Xu, S. Melle, K. Golemanov, G. Fuller *Langmuir* **21** (2005) 10016
- [225] L. Pauchard, C. Allain *Europhys. Lett.* **62** (2003) 897
- [226] L. Pauchard, C. Allain *Phys. Rev. E* **68** (2003) 052801
- [227] Y. Gorand, L. Pauchard, G. Calligari, J. P. Hulin, C. Allain *Langmuir* **20** (2004), 5138
- [228] R. S. Subramanian, R. J. Larsen, H. A. Stone *Langmuir* **21** (2005) 4526
- [229] N. Tsapis, E. R. Dufresne, S. S. Sinha, C. S. Riera, J. W. Hutchinson, L. Mahadevan, D. A. Weitz *Phys. Rev. Lett.* **94** (2005) 018302
- [230] N. Tsapis, D. Bennett, B. Jackson, D. A. Weitz, D. A. Edwards *Proc. Natl. Acad. Sci. U.S.A* **72** (2002) 12001
- [231] F. Iskandar, L. Gradon, K. Okuyama *J. Colloid Interface Sci.* **265** (2003) 296
- [232] D. Sen, O. Spalla, T. Spalla, P. Haltebourg, T. Thill *Langmuir* **23** (2007) 4296
- [233] D. Sen, Arshad Khan, J. Bahadur, S. Mazumder, B.K. Sapra *J. Colloid Interface Sci.* **347** (2010) 25-30
- [234] A. Khan, D. Sen, P. Kothalkar, B. K. Sapra, S. Mazumder and Y. S. Mayya *Drying Technology* **30** (2012) 679–686
- [235] Jan Skov Pedersen *Adv. Colloid Interface Sci.* **70** (1997) 171-210 (*and the references therein*)
- [236] O. Kratky and G. Porod *Rec. Trav. Chim. Pays-Bas*, **68** (1949) 1106-1122
- [237] O. Spalla, S. Lyonnard and F. Testard *J. Appl. Cryst.* **36** (2003), 338

- [238] A. Zbigniew, J. Barbara, K. Marta *J. Colloid Interface Sci.* **273** (2004) 668
- [239] C. G. de Kruif, E. M. F. van Iersel, A. Vrij *J. Chem. Phys.* **83** (1985) 9
- [240] J. Bahadur, D. Sen, S. Mazumder, Bhaskar Paul, Arshad Khan, G. Ghosh *J. Colloid and Interface Sci.* **351** (2010) 357–364
- [241] J. Bahadur, D. Sen, S. Mazumder, Bhaskar Paul, Arshad Khan *International Journal of Nanoscience* **10** (2011) 995-999
- [242] A. Thill, O. Spalla *J. Colloid and Interface Sci.* **291** (2005) 477–488
- [243] S.V.G. Menon, C. Manohar, K.J. Srinivas Rao *Chem. Phys.* **95** (1991) 9186-9190
- [244] Reinhard Vehring *Pharmaceutical Research* **2008**, 25, 5
- [245] L. Pauchard and Y. Couder *Europhys. Lett.* **66** (2004) 667
- [246] <http://www.labultima.com/lu228.htm>
- [247] H. Frielinghaus, et al., *JCNS Experimental Report* 2007/2008
- [248] G. Goerigk and Z. Varga *J. Appl. Cryst.* **44** (2011) 337
- [249] P. Debye, H.R. Anderson, Jr. and H. Brumberger *J. Appl. Phys.* **28** (1957) 679
- [250] J. S. Pedersen *J. Appl. Cryst.* **7** (1994) 595
- [251] J. Bahadur, D. Sen, S. Mazumder, S. Bhattacharya, Henrich Frielinghaus, Günter Goerigk *Langmuir* **27** (13) (2011) 8404–8414
- [252] K. J. Konsztowicz, G. Maksym, T. Maksym, H. W. King, W. F. Caley and E. Vargha-Butler *Forming Sci. Technol. Ceram.* **26** (1990) 46
- [253] T. Okubo *J. of Colloid and Interface Sci.* **171** (1995) 55
- [254] A. Biance, C. Clanet, D. Quere *Phys. Fluids* **15** (2003) 6
- [255] J. G. Leidenfrost, *De Aquae Communis Nonnullis Qualitatibus Tractatus, Duisburg,* 1756
- [256] M. A. Pelacho, A.I Garcimartin and J. Burguete *Phys. Rev. E* **62** (2000) 477
- [257] X. L. Qiu and P. Tong *Phys. Rev. Lett.* **87** (2001) 094501

- [258] G. V. Jayanthi, S. C. Zhang, and Gary L. Messing *Aerosol Science and Technology* **19** (1993) 478
- [259] D. H. Charlesworth and W. R. Jr. Marshall *AIChE J.* **6** (1960) 9
- [260] J. H. Seinfeld, *Atmospheric Chemistry and Physics of Air Pollution*. John Wiley & Sons, New York, 1986.
- [261] A. D. Stroock, S. K. W. Dertinger, A. Ajdari, I. Mezic, H. A. Stone and G. M. Whitesides *Science* **295** (2002) 647
- [262] P. Pieranski *Phys. Rev. Lett.* **45** (1980) 569
- [263] O. D. Velev, K. Furusawa and K. Nagayama *Langmuir* **12** (1996) 2374
- [264] O. D. Velev, K. Furusawa and K. Nagayama *Langmuir* **12** (1996) 2385
- [265] O. D. Velev, K. Furusawa and K. Nagayama *Langmuir* **13** (1997) 1856
- [266] J.-C. Lin and J. W. Gentry *Aerosol Sci. Technol.* **37** (2003) 15
- [267] A. Fernandez-Nieves, G. Cristobal, V. Garces-Chavez, G. C. Spalding, K. Dholakia, D.A. Weitz *Adv. Mater.* **17** (2005) 680
- [268] I.O. Shklyarevskiy, P. Jonkheijm, P. C. M. Christianen, A. P. H. J. Shenning, E.W. Meijer, O. Henze, A.F.M. Kilbinger, W. J. Feast, A. Del Guerzo, J.-P. Desvergne, J.C. Maan *J. Am. Chem. Soc.* **127** (2005) 1112
- [269] T. van Dillen, A. Polman, C.M. van Kats, A. van Blaaderen *Appl. Phys. Lett.* **83** (2003) 4315
- [270] Y. Yin, Y. Lu, B. Gates, Y. Xia *J. Am. Chem. Soc.* **123** (2001) 8718
- [271] V. N. Manoharan, M. T. Elsesser, D. J. Pine *Science* **301** (2003) 483
- [272] P.M. Johnson, C.M. van Kats, A. van Blaaderen *Langmuir* **21** (2005) 11510
- [273] D. Zerrouki, B. Rotenberg, S. Abramson et al. *Langmuir* **22** (2006) 57
- [274] T. van Dillen, A. van Blaaderen, A. Polman *Mater. Today*, **7**(7-8) (2004) 40
- [275] C. M. Liddel, C. J. Summers *Adv. Mater.* **15** (2003) 1715

- [276] N.C. Nanda, R. Schlieff, Eds., *in Advances in Echo Imaging Using Contrast Enhancement* Kluwer Academic Publishers, Dordrecht, 1993.
- [277] P. Marmottant, S. van der Meer, M. Emmer, M. Versluis, N. de Jong, S. Hilgenfeldt, D. Lohse *J. Acoustical Soc. Am.* **118** (2005) 3499
- [278] A. D. Dinsmore, M. F. Hsu, M. G. Nikolaides, M. Marquez, A. R. Bausch, D. A. Weitz *Science* **298** (2002) 1006.
- [279] A. Imhof, D. J. Pine, *Nature* **389** (1997) 948
- [280] D. M. Kuncicky, O. D. Velev *Langmuir* **24** (2008) 1371
- [281] J. R. Millman, K. H. Bhatt, B. G. Prevo, O. D. Velev, *Nat. Mater.* **4** (2005) 98
- [282] K.-H. Roh, D. C. Martin, J. Lahann *Nat. Mater.* **4** (2005) 759
- [283] O. D. Velev, A.M. Lenhoff, E. W. Kaler *Science* **287** (2000) 2240
- [284] Iskandar, F., Mikrajuddin, K. Okuyama *Nano Letters* **2** (4) (2002) 389–392
- [285] D. Sen, J. S. Melo, J. Bahadur, S. Mazumder, S. Bhattacharya, S. F. D’Souza, H. Frielinghaus, G. Goerigk, R. Loidl *Soft Matter* **7** (2011) 5423
- [286] S. Lyonnard, J. R. Bartlett, E. Sizgek, K. S. Finnie, T. Zemb, J. L. Woolfrey *Langmuir* **18** (2002) 10386-10397
- [287] S. Y. Lee, L. Gradon, S. Janeczko, F. Iskandar, K. Okuyama *ACS Nano* **4** (8) (2010) 4717
- [288] S. Y. Lee, W. Widiyastuti, F. Iskandar, K. Okuyama, L. Grado *Aerosol Science and Technology* **43** (2009) 1184
- [289] I.L. Ivanovska, P.J. de Pablo, B. Ibarra, G. Sgalari, F.C. MacKintosh, J.L. Carrasccosa, C.F. Schmidt, G. J. L. Wuite *Proc. Natl. Acad. Sci. U.S.A.* **101** (2004) 7600
- [290] J. P. Michel, I.L. Ivanovska, M. M. Gibbons, W.S. Klug, C.M. Knobler, G. J. L. Wuite, C.F. Schmidt *Proc. Natl. Acad. Sci. U.S.A.* **103** (2006) 6184
- [291] A. Fery, R. Weinkamer *Polymer* **48** (2007) 7221

- [292] M. S. Spector, E. Naranjo, S. Chiruvolu, J. A. Zasadzinski *Phys. Rev. Lett.* **73** (1994) 2867
- [293] A. Saint-Jalmes, F. Gallet, *Eur. Phys. J. B* **2** (1998) 489
- [294] C. F. Schmidt, K. Svoboda, N. Lei, I. B. Petsche, L. E. Berman, C. R. Safinya, G. S. Grest *Science* **259** (1993) 952
- [295] L. D. Landau, E. M. Lifshitz *Theory of Elasticity* (Oxford: Pergamon) 1986.
- [296] S. Komura, R. Lipowsky *J. Physique II* **2** (1992) 1563
- [297] T. A. Witten, H. Li, *Europhys. Lett.* **23** (1993) 51
- [298] U. S. Schwarz, S. Komura, S. A. Safran, *Europhys. Lett.* **50** (2000) 762
- [299] C. Quilliet, C. Zoldesi, C. Riera, A. van Blaaderen, A. Imhof, *Eur. Phys. J. E* **27** (2008) 13–20
- [300] G.A. Vliegenthart, G. Gompper, *New Journal of Physics* **13** (2011) 045020
- [301] B. Li, F. Jia, Y. Cao, X. Feng, H. Gao, *Phys. Rev. Lett.* **106** (2011) 234301
- [302] Y. Sugiyama, Ryan J. Larsen, Jin-Woong Kim, David A. Weitz, *Langmuir* **22** (2006) 6024
- [303] W. S. Cheow, S. Li, K. Hadinoto *chemical engineering research and design* **8** (2010) 673
- [304] S. Sacanna, T. M. William Irvine, L. Pine Rossi, J. David *Soft Matter* **7** (2011) 1631
- [305] J. Bahadur, D. Sen, S. Mazumder, B. Paul, H. Bhatt, S. G. Singh, *Langmuir* **28** (2012) 1914–1923
- [306] H. Elimelech, D. Avnir *Chem. Mater.* **20** (2008) 2224–2227
- [307] M. Kamibayashi, H. Ogura, Y. Otsubo *Ind. Eng. Chem. Res.* **45** (2006) 6899–6905
- [308] X. Chen, S. S. Mao *Chem. Rev.* **107** (2007) 2891
- [309] M. R. Hoffmann, S. T. Martin; W. Choi, D. W. Bahnemann *Chem. Rev.* **95** (1995) 69
- [310] E. Matijevic *Langmuir* **2** (1986) 12

- [311] E. A. Barringer, H. K. Bowen *Langmuir* **1** (1985) 414
- [312] J. H. Jean, T. A. Ring *Langmuir* **2** (1986) 251
- [313] S.I. Nishimoto, S.B. Ohtani, H. Kajiwara, T. Kagiya *J. Chem. Soc. Faraday Trans. 1* **81** (1985) 61
- [314] A. Sclafani, L. Palmisano, M. Schiavello *J. Phys. Chem.* **94** (1990) 829
- [315] G.X. Yang, H.R. Zhuang, P. Biswas *Nanostruct. Mater.* **7** (1996) 675
- [316] M.K. Akhtar, X.O. Yun, S. E. Pratsinis *AIChE J.* **1991**, 37 1561
- [317] H. Zhang, J. F. Banfield *J. Mater. Chem.* **8** (1998) 2073
- [318] P. Yang, D. Zhao, D. I. Margolese, B. F. Chmelka, G. D. Stucky *Nature* **396** (1998) 152
- [319] D. M. Antonelli, J. Y. Ying *Angew. Chem., Int. Ed. Eng.* **34** (1995) 2014
- [320] X. Z. Fu, L. A. Clark, Q. Yang *Environ. Sci. Technol.* **30** (2) (1996) 647
- [321] C. Anderson, A. J. Bard *J. Phys. Chem. B* **101** (1997) 2611
- [322] Y. Li, W. N. Wang, Z. L. Zhan, M. H. Woo, C. Y. Wu and P. Biswas *Appl. Catal., B* **100** (2011) 386–392
- [323] J. Bahadur, D. Sen, S. Mazumder, P. U. Sastry, B. Paul, H. Bhatt, S. G. Singh, *Langmuir* **28** (2012) 11343–11353
- [324] M. Anderson, J. Giesermann and Q. Xu *J. Membr. Sci.*, **39** (1988) 243
- [325] H. Zhang and J. Banfield *J. Phys. Chem. B* **104** (2000) 3481
- [326] R. D. Shannon, J. A. Pask *J Am Ceram Soc.* **48**(8) (1965) 391
- [327] K. Kumar *Scr. Metall. Mater.* **32** (1995) 873
- [328] R. D. Shannon, J. A. Pask *Am Miner* **49** (1964) 1707
- [329] G. Marty and N. Tsapis, *Eur. Phys. J. E* **27** (2008) 213–219
- [330] G. Lan, C.W. Wolgemuth, S.X. Sun, *PNAS*, **104** (2007) 16110–16115
- [331] J. S. Melo and S.F. D'Souza *World J. Microbiol Biotechnol.* **15** (1999) 17-21

- [332] G. Garg, P. A. Hassan, V. K. Aswal and S. K. Kulshreshtha *J. Phys. Chem B*, **109** (2005) 1340
- [333] P. A. Hassan, Srinivasa R. Raghavan, and Eric W. Kaler, *Langmuir* **18** (2002) 2543-2548
- [334] D. Sen, J. Bahadur, S. Mazumder, G. Verma, P. A. Hassan, S. Bhattacharya, K. Vijay and P. Doshi *Soft Matter* **8** (2012) 1955–1963
- [335] M.C. Holmes, M.S. Leaver in Bicontinuous liquid crystals; M.L. Lynch, P.T. Spicer, Eds.; *Surfactant Science Series*, Volume 127, CRC Press: Boca Raton, FL, 2005; pp 15–39
- [336] V. Luzzati, *In Biological Membrane*, D. Chapman, Eds.; Academic Press: London and New York, p71, 1968.

## LIST OF PUBLICATIONS

1. One Step Fabrication of Thermally Stable TiO<sub>2</sub>/SiO<sub>2</sub> Nanocomposite Microspheres by Evaporation Induced Self-assembly, **J. Bahadur**, D. Sen, S. Mazumder, P. U. Sastry, B. Paul, H. Bhatt, S. G. Singh, *Langmuir* 28, 11343–11353 (2012).
2. Control of Buckling in Colloidal Droplets during Evaporation Induced Assembly of Nano-particles, **J. Bahadur**, D. Sen, S. Mazumder, B. Paul, H. Bhatt, S. G. Singh, *Langmuir*, 28, 1914–1923 (2012).
3. Origin of buckling phenomenon during drying of micrometric colloidal droplets, **J. Bahadur**, D. Sen, S. Mazumder, S. Bhattacharya, H. Frielinghaus, G. Goerigk, *Langmuir* 27 (13), 8404–8414 (2011) .
4. Formation of hollow spherical and doughnut microcapsules by evaporation induced self-Assembly of nanoparticles: Effects of particle size and polydispersity, D. Sen, **J. Bahadur**, S. Mazumder, S. Bhattacharya, *Soft Matter*, 8, 10036–10044 (2012).
5. Nanocomposite silica surfactant microcapsules by evaporation induced self assembly: tuning the morphological buckling by modifying viscosity and surface charge, D. Sen, **J. Bahadur**, S. Mazumder, G. Verma, P. A. Hassan, S. Bhattacharya, K. Vijay and P. Doshi *Soft Matter*, 8, 1955–1963 (2012).
6. Arrest of morphological transformation during evaporation-induced self-assembly of mixed colloids in micrometric droplets by charge tuning D. Sen, J. S. Melo, **J. Bahadur**, S. Mazumder, S. Bhattacharya, S. F. D'Souza, H. Frielinghaus, G. Goerigk and R. Loidl, *Soft Matter*, 7 (11), 5423 – 5429 (2011).

7. Evaporation-induced self assembly of nanoparticles in non-buckling regime: Volume fraction dependent packing, **J. Bahadur**, D. Sen, S. Mazumder, Bhaskar Paul, Arshad Khan, G. Ghosh *J. Colloid and Interface Sci.* 351 357–364 (2010).
8. Buckling driven morphological transformation of droplets of a mixed colloidal suspension during evaporation induced self assembly by spray drying D. Sen, J. S. Melo, **J. Bahadur**, S. Mazumder, S. Bhattacharya, G. Ghosh, D. Dutta and S.F. D' Souza *Eur. Phys. J. E*, 31, 393, 402 (2010).
9. Use of small-angle neutron scattering to investigate modifications of internal structure in self-assembled grains of nanoparticles synthesized by spray drying D. Sen, Arshad Khan, **J. Bahadur**, S. Mazumder, B.K. Sapra, *J. Colloid and Interface Sci.*, 347, 25-30 (2010).
10. Evolution of a fractal system with conserved order parameter under thermal annealing **J. Bahadur**, S. Mazumder, D. Sen, S. Ramanathan, *J. Phys.: Condens. Matter*, 22 195107 (2010).
11. Non-Debye to Debye transition of ac dielectric response in YCrO<sub>3</sub> nanoceramic under sintering: effect of pore structure **J Bahadur**, D Sen, S Mazumder, R Shukla and A K Tyagi, *J. Phys.: Condens. Matter*, 20, 345201 (2008).
12. Effect of Heat Treatment on Pore Structure in Nano-Crystalline NiO: A Small Angle Neutron Scattering Study **J. Bahadur**, D. Sen, S. Mazumder and S. Ramanathan *Journal of Solid State Chemistry*, 181, 1227–1235 (2008).
13. Smoothing of the non-Euclidean surface of Nd<sub>2</sub>O<sub>3</sub> doped CeO<sub>2</sub> nano-ceramic grain under sintering: An ultra-small-angle X-ray scattering investigation and a computer simulation study D. Sen, **J. Bahadur**, S. Mazumder, V. Bedekar and A.K. Tyagi, *J. Phys.: Condens. Matter*, 20 035103, (2008) (COVER PAGE ARTICLE).

14. Nonlinearity and isotope effect in temporal evolution of mesoscopic structure during hydration of cement S. Mazumder, D. Sen, **J. Bahadur**, J. Klepp, H. Rauch, Jose Teixeira *Phy. Rev. B*, 82, 064203 (2010).
15. Temporal evolution of characteristic length and fractal dimension for a non-Euclidean system D. Sen, S. Mazumder, and **J. Bahadur**, *Phy. Rev. B*, 79, 134207 (2009).
16. \*Influence of annealing on structure and optical properties of Mn-substituted ZnO nanoparticles B. Roy, O. Mondal, D. Sen, **J. Bahadur**, S. Mazumder and M. Pal *J. Appl. Cryst.*, 44, 991–998 (2011).
17. \*Effects of calcination on microscopic and mesoscopic structures in Ca and Sr doped nanocrystalline Lanthanum Chromites H. Bhatt, **J. Bahadur**, M. N Deo, S. Ramanathan, K. K Pandey, D. Sen, S. Mazumder, S. M Sharma *Journal of Solid State Chemistry*, 184, 204–213 (2011).
18. \*Structural characterization of manganese-substituted nano-crystalline zinc oxide using small-angle neutron scattering and high-resolution transmission electron microscopy B. Roy, B. Karmakar, **J. Bahadur**, S. Mazumder, D. Sen and M. Pal *J. Appl. Cryst.*, 42, 1085–1091 (2009).
19. \*Extraction of single scattering profile from multiple small-angle scattering data utilizing basis function set D. Sen, **J. Bahadur**, S. Mazumder *Eur. Phys. J-B*, 71, 75-84 (2009).
20. \*Decoration of carbon nanotubes with metal nanoparticles by wet chemical method: A small-angle neutron scattering study **J Bahadur**, D Sen, S Mazumder, Jyoti Parkash , D Sathiyamoorthy, R Venugopalan *Journal of Nanoscience and nanotechnology*, 10, 2963–2971 (2010).

21. \*Small-Angle Neutron Scattering Investigations on sintering behavior of combustion synthesized  $\text{La}_{0.8}\text{Sr}_{0.2}\text{CrO}_3$ , A. K. Patra, **J. Bahadur**, S. Mazumder, Sathi Nair, R. D. Purohit and A. K. Tyagi, *J. of Nanoscience and Nanotechnology*, 8, 1–6 (2007).
22. \*Isotope effect in temporal evolution of mesoscopic structure during hydration of cement, S. Mazumder, D. Sen and **J. Bahadur**, J. Klepp, H. Rauch and José Teixeira *ILL Annual Report*, 36-37 (2010).
23. \*The isotope effect in hydration of cement S. Mazumder, D. Sen, **J. Bahadur**, J. Klepp, H. Rauch and J. Teixeira, *LLB Annual Report* 34-35 (2010).

\*Publications not included in the thesis.